

APPROACHES FOR REAL-TIME FREQUENCY DEPENDENT REDUCED  
ORDER MODELING AND WIDE-AREA CONTROL OF MODERN POWER  
GRID

by

Abilash Thakallapelli

A dissertation submitted to the faculty of  
The University of North Carolina at Charlotte  
in partial fulfillment of the requirements  
for the degree of Doctor of Philosophy in  
Electrical Engineering

Charlotte

2018

Approved by:

---

Dr. Sukumar Kamalasan

---

Dr. Yogendra Kakad

---

Dr. Valentina Cecchi

---

Dr. Maciej Noras



## ABSTRACT

ABILASH THAKALLAPELLI. Approaches for real-time frequency dependent reduced order modeling and wide-area control of modern power grid. (Under the direction of DR. SUKUMAR KAMALASADAN)

In this dissertation, approaches for measurement based real-time wide-area damping controllers (WADC), are studied for renewable energy integrated power grid. For this, first, a model-free algorithm for multi-input-multi-output (MIMO) transfer function identification of the power system is presented. The MIMO identification is based on actual measurements which can monitor changes in the grid as opposed to conventional methods that are based on the small-signal analysis. An optimal control loop for WADC is estimated using the identified MIMO system. The WADC design is based on the discrete linear quadratic regulator (DLQR) and Kalman filtering for real-time damping of inter-area oscillations. This methodology is then modified by incorporating an online coherency properly characterizes real-time changes. The WADC architecture is then decentralized using the Alternating Direction Method of Multipliers (ADMM). Further, for large-scale power system implementation, Frequency-Dependent Network Equivalent (FDNE) are designed that can aggregate the power grid based on the study area and external area classified utilizing the grid property of special complexity. The FDNE is used for two applications a) Pitch Control of Wind Farms and b) Reducing the grid model to implement the proposed WADC. The architecture is tested and validated on a RTDS/RSCAD and MATLAB real-time co-simulation platform using two-area and IEEE 39 bus power system models.

## ACKNOWLEDGEMENTS

I would like to express my sincere gratitude to my advisor, Dr. Sukumar Kamalasan who provided me with an opportunity to be a part of his research team and honed my skills as a researcher and an individual. I would also like to appreciate the time and support provided by the advising committee of Dr. Yogendra Kakad, Dr. Valentina Cecchi, and Dr. Maciej Noras.

I sincerely thank UNC Charlotte for offering me GASP which aided in continuing the course smoothly. Also, I would like to thank EPIC for providing the right atmosphere and research assistantship for performing research.

I would like to thank students of UNC Charlotte and in particular PEISL lab who supported directly or indirectly on this work.

## DEDICATION

*To Nature: Ever aspiring me to serve better.*

## TABLE OF CONTENTS

LIST OF FIGURES	xii
LIST OF TABLES	xix
CHAPTER 1: INTRODUCTION	1
1.1. Modern Power Grid Modeling and Control Challenges	1
1.2. Research Gap and Proposed Work	2
1.3. Wide-Area Control Overview	2
1.3.1. Inter-Area Mode Estimation	3
1.3.2. Coherency Group Determination	5
1.3.3. Identifying Optimal Wide-Area Control Loop	6
1.3.4. WADC Design	6
1.4. Reduced Order Modeling Overview	7
1.4.1. Low Frequency Equivalent (TSA)	9
1.4.2. High Frequency Equivalents	11
1.5. Power System Control Applications using Reduced Order Model	11
1.6. Research Contributions	11
1.7. Dissertation Organization	13
CHAPTER 2: MODEL-FREE WIDE AREA DAMPING OF INTER-AREA OSCILLATIONS BASED ON MIMO IDENTIFICATION	15
2.1. Introduction	16
2.2. Dividing Power System Based on Coherency	18
2.2.1. Coherency grouping of two-area system model	19
2.2.2. Coherency grouping of IEEE 39 bus system	19

	vii
2.3. Model-free MIMO Identification	20
2.3.1. MIMO transfer function from state space matrices	21
2.3.2. Model-free MIMO identification considering mutual coupling	26
2.4. Real-time implementation of MIMO identification	30
2.4.1. MIMO Identification two-area system	30
2.4.2. MIMO Identification of 39-bus system	33
2.5. Optimal Wide Area Control Loop Selection	35
2.5.1. Identifying the optimal control loop for two-area system	36
2.5.2. Identifying the optimal control loop for 39 bus system	37
2.6. Model-free DLQR and Kalman filter design	39
2.6.1. Discrete-time linear quadratic regulator	39
2.6.2. Kalman filtering based state estimation	41
2.7. Simulation Results	42
2.7.1. Simulation results of two-area system	42
2.7.2. Simulation results of 39 bus system	45
2.7.3. Case:1	45
2.7.4. Case:2	46
2.8. Summary	49
CHAPTER 3: COHERENCY AND ONLINE SIGNAL SELECTION BASED WIDE AREA CONTROL OF WIND INTEGRATED POWER GRID	53
3.1. Introduction	53

3.2. Proposed Framework for the Online Wide Area Controller	56
3.2.1. Proposed coherency grouping algorithm	57
3.2.2. MIMO Identification	64
3.2.3. Order reduction	65
3.2.4. Signal selection	66
3.2.5. WAC design architecture	67
3.3. Simulation Results	67
3.3.1. Implementation test results using two-area system	67
3.3.2. Implementation test results on IEEE 39-bus system	70
3.4. Summary	74
CHAPTER 4: ALTERNATING DIRECTION METHOD OF MULTIPLIERS (ADMM) BASED DISTRIBUTED APPROACH FOR WIDE-AREA CONTROL	77
4.1. Introduction	77
4.2. Proposed Approach and Problem Formulation	80
4.2.1. Dividing Large Scale Network into Areas	80
4.2.2. Proposed Architecture for Signal Selection	82
4.2.3. Wide Area Damping Controller Design	91
4.3. Experimental Setup for Implementing the Proposed Signal Selection Method	92
4.4. Implementation Test Results	93
4.4.1. Implementation test results using two-area system	94
4.4.2. Implementation test results using 39-bus system	96
4.5. Summary	100

CHAPTER 5: DEVELOPMENT AND APPLICABILITY OF ONLINE PASSIVITY ENFORCED WIDE-BAND MULTI-PORT EQUIVALENTS FOR HYBRID TRANSIENT SIMULATION	112
5.1. Introduction	112
5.2. Proposed Methodology	115
5.2.1. Aggregation of External Area for TSA type modeling and Real-time Integration	116
5.2.2. Study and analysis of TSA type equivalent modeling	119
5.2.3. FDNE Formulation and Real-time simulator Integration	121
5.2.4. Study and analysis of FDNE type equivalent modeling	132
5.2.5. Implementing TSA and FDNE on two area power system	133
5.3. Implementation Test on Interconnected Power Grid	136
5.4. Application of Reduced Order Model for Wide Area Control	139
5.4.1. Reduced Model Validation for IEEE 68 system	142
5.4.2. Simulation Results of Wide Area Control	143
5.5. Summary	149
CHAPTER 6: SENSORLESS REAL-TIME REDUCED ORDER MODEL-BASED ADAPTIVE MAXIMUM POWER TRACKING PITCH CONTROLLER FOR GRID-CONNECTED WIND TURBINES	152
6.1. Introduction	153
6.2. Wind Turbine and Generator Modeling	156
6.2.1. The Wind Turbine	157
6.2.2. The Coefficient of Performance	157

6.2.3.	Wind Generator	158
6.2.4.	Maximum Power Point Tracking (MPPT)	159
6.3.	Frequency-Dependent Reduced Order Modeling of Power Grid	159
6.4.	Proposed Adaptive Pitch Controller	161
6.4.1.	Recursive Least Square Identification	161
6.4.2.	Calculating Gains of the Controller	165
6.5.	Implementation of the Proposed Controller	167
6.6.	Experimental Test Bed and Results	168
6.6.1.	Validation of the algorithm using Kundur's test system	169
6.6.2.	Validation of the algorithm with IEEE 39-bus test system	174
6.7.	Summary	178
CHAPTER 7: DISTRIBUTED COHERENCY GROUPING OF GENERATORS BASED ON SPECTRAL CLUSTERING USING MEASUREMENTS		180
7.1.	Introduction	181
7.2.	Proposed Algorithm	183
7.2.1.	Optimal number of clusters	183
7.2.2.	Clustering of generators at local control centers	185
7.2.3.	Clustering of local cluster centers at global control center	188
7.3.	Implementation of the Proposed Algorithm	189
7.4.	Experimental Setup	191

	xi
7.5. Implementation Test Results	192
7.5.1. Estimation of Optimal Number of Clusters	193
7.5.2. Distributed Coherency Grouping	195
7.6. Summary	203
CHAPTER 8: CONCLUSION	206
8.1. Concluding Remarks	206
8.2. Future Work Directions	207
REFERENCES	208

## LIST OF FIGURES

FIGURE 2.1: Architecture for proposed WADC	19
FIGURE 2.2: Two-area power system model	20
FIGURE 2.3: Speed deviation (rad/s) (two-area system)	21
FIGURE 2.4: 39-bus power system model	22
FIGURE 2.5: Speed Deviation (Group-1)	22
FIGURE 2.6: Speed Deviation (Group-2)	23
FIGURE 2.7: Speed Deviation (Group-3)	23
FIGURE 2.8: Input and output measurements	26
FIGURE 2.9: Real-time experimental setup	31
FIGURE 2.10: Speed deviation of generators(rad/s)	32
FIGURE 2.11: FFT analysis of $\Delta\omega_1$	33
FIGURE 2.12: 39 bus speed deviation (rad/s)	34
FIGURE 2.13: FFT analysis of $\Delta\omega_5$ (Case:1)	34
FIGURE 2.14: FFT analysis of $\Delta\omega_5$ (Case:2)	35
FIGURE 2.15: WADC architecture	39
FIGURE 2.16: Optimal control loop for two-area system	43
FIGURE 2.17: Generator-2 speed deviation (rad/s)	44
FIGURE 2.18: Generator-4 speed deviation (rad/s)	44
FIGURE 2.19: WADC output signal	45
FIGURE 2.20: Generator-3 speed deviation (rad/s)	46
FIGURE 2.21: Generator-4 speed deviation (rad/s)	47

FIGURE 2.22: Generator-9 speed deviation (rad/s)	47
FIGURE 2.23: Generator-10 speed deviation (rad/s)	48
FIGURE 2.24: WADC output signal	48
FIGURE 2.25: Generator-3 speed deviation (rad/s)	49
FIGURE 2.26: Generator-7 speed deviation (rad/s)	50
FIGURE 2.27: Generator-8 speed deviation (rad/s)	50
FIGURE 2.28: Generator-10 speed deviation (rad/s)	51
FIGURE 2.29: WADC output signal	51
FIGURE 3.1: The architecture of proposed framework	56
FIGURE 3.2: Flow chart of the proposed coherency grouping algorithm.	59
FIGURE 3.3: Two-area study system model.	60
FIGURE 3.4: IEEE-39 bus test system model (Fault on Bus-14).	61
FIGURE 3.5: Coherency group-1	62
FIGURE 3.6: Coherency group-2	62
FIGURE 3.7: Coherency group-3	63
FIGURE 3.8: Coherency group-4	63
FIGURE 3.9: Coherency grouping for different operating conditions.	64
FIGURE 3.10: Experimental test bed.	68
FIGURE 3.11: Wind Speed.	69
FIGURE 3.12: WTG Active Power.	69
FIGURE 3.13: Relative speed of generator 2 w.r.t generator 3.	70
FIGURE 3.14: Relative speed of generator 1 w.r.t generator 4.	70
FIGURE 3.15: Relative speed of generator 2 w.r.t generator 4.	71

FIGURE 3.16: WAC input signal to generator 1 and 3.	71
FIGURE 3.17: Wind Speed.	73
FIGURE 3.18: WTG Active Power.	73
FIGURE 3.19: Relative speed of generator 5 w.r.t generator 2.	74
FIGURE 3.20: Relative speed of generator 7 w.r.t generator 2.	74
FIGURE 3.21: Relative speed of generator 8 w.r.t generator 2.	75
FIGURE 3.22: WAC input signal to generator 2, 7, and 8	75
FIGURE 4.1: Proposed distributed architecture for wide area control.	81
FIGURE 4.2: Flowchart of overall methodology.	81
FIGURE 4.3: Input signal for transfer function estimation.	83
FIGURE 4.4: Wide area control implementation.	92
FIGURE 4.5: Flowchart for WADC design.	93
FIGURE 4.6: Experimental test bed.	102
FIGURE 4.7: Two area test system.	103
FIGURE 4.8: IEEE-39 bus test system model.	103
FIGURE 4.9: Tie-line power flow (Bus7-Bus8-Bus9).	104
FIGURE 4.10: Relative speed between generator-1 and generator-2.	104
FIGURE 4.11: Relative speed between generator-3 and generator-2.	105
FIGURE 4.12: Active power deviation through tie-line (Bus7-Bus8-Bus9).	105
FIGURE 4.13: Wide area control signal to generator-3.	106
FIGURE 4.14: Control Loops for IEEE-39 Bus (Bus-14 fault).	106
FIGURE 4.15: Active power deviation (Bus17-Bus18).	107
FIGURE 4.16: Active power deviation (Bus1-Bus39).	107

FIGURE 4.17: Relative speed between generator 2 and generator 4.	108
FIGURE 4.18: Relative speed between generator 2 and generator 6.	108
FIGURE 4.19: Wide area control output with PSS.	109
FIGURE 4.20: Active power deviation (Bus1-Bus39).	109
FIGURE 4.21: Active power deviation (Bus17-Bus18).	110
FIGURE 4.22: Relative speed between generator 2 and generator 4.	110
FIGURE 4.23: Relative speed between generator 2 and generator 6.	111
FIGURE 4.24: Wide area control output with PSS.	111
FIGURE 5.1: The conceptual and functional flowchart for TSA type modeling	116
FIGURE 5.2: Proposed dynamic equivalent of two area system	120
FIGURE 5.3: The relative speed of Gen.2 w.r.t Gen.1	121
FIGURE 5.4: Active power flow from bus 10 to bus 9	122
FIGURE 5.5: The conceptual and functional flowchart for FDNE modeling	123
FIGURE 5.6: Admittance vs frequency of external area (two area system)	127
FIGURE 5.7: The eigenvalue of real-part of admittance matrix (1-port)	131
FIGURE 5.8: Relative speed of Gen.2 w.r.t Gen.1	132
FIGURE 5.9: Active power flow from bus 10 to bus 9 (Boundary Bus)	133
FIGURE 5.10: Implementation flowchart for TSA and FDNE type models.	134
FIGURE 5.11: Relative speed of Gen.2 w.r.t Gen.1	135
FIGURE 5.12: Active power flow from bus 10 to bus 9 (Boundary Bus Power)	136
FIGURE 5.13: IEEE 39 bus test system	137

FIGURE 5.14: Admittance vs frequency of external area (39 Bus System)	138
FIGURE 5.15: The corrected eigenvalue of real-part of admittance matrix (3-port)	138
FIGURE 5.16: Bus 26 Active Power	139
FIGURE 5.17: Bus 17 Voltage	139
FIGURE 5.18: Relative speed of generator gen.1 w.r.t gen.2	140
FIGURE 5.19: IEEE 68 bus system	141
FIGURE 5.20: The equivalent representation of 68 bus system	142
FIGURE 5.21: Generator-7 speed (rad/s)	143
FIGURE 5.22: Generator-9 speed (rad/s)	144
FIGURE 5.23: Boundary bus voltage (Bus-61) (rad/s)	144
FIGURE 5.24: Generator-2 speed deviation (rad/s)	146
FIGURE 5.25: Generator-7 speed deviation (rad/s)	146
FIGURE 5.26: Generator-9 speed deviation (rad/s)	147
FIGURE 5.27: WADC output signal	147
FIGURE 5.28: Generator-2 speed deviation (rad/s)	149
FIGURE 5.29: Generator-6 speed deviation (rad/s)	149
FIGURE 5.30: Generator-9 speed deviation (rad/s)	150
FIGURE 5.31: WADC output signal	150
FIGURE 6.1: Wind turbine characteristics.	158
FIGURE 6.2: FDNE and TSA block diagram for a power network.	161
FIGURE 6.3: Proposed dynamic equivalent of two-area test system.	162
FIGURE 6.4: Proposed STR Controller.	167

FIGURE 6.5: Flowchart for $\omega_{ref}$ calculation.	169
FIGURE 6.6: Flowchart of the proposed controller.	170
FIGURE 6.7: Experiment setup in RTDS.	172
FIGURE 6.8: FDNE validation	173
FIGURE 6.9: Wind Speed and DFIG Active Power	174
FIGURE 6.10: DFIG rotor speed and relative speed comparison.	175
FIGURE 6.11: Pitch angle and mechanical torque comparison.	175
FIGURE 6.12: STR and conventional PI controller gains.	176
FIGURE 6.13: IEEE 39-Bus system.	177
FIGURE 6.14: Wind speed and PCC voltage comparison.	178
FIGURE 6.15: DFIG rotor speed and active power comparison.	178
FIGURE 6.16: Relative speed and mechanical torque comparison.	179
FIGURE 7.1: Flow chart of spectral clustering algorithm.	186
FIGURE 7.2: Implementation of the proposed algorithm.	187
FIGURE 7.3: Real-time experimental setup.	189
FIGURE 7.4: IEEE 39 bus system.	190
FIGURE 7.5: Generator speeds	191
FIGURE 7.6: Optimal number of clusters (Case: 1).	193
FIGURE 7.7: Optimal number of clusters (Case: 2).	194
FIGURE 7.8: Optimal number of clusters (Case: 3).	195
FIGURE 7.9: Coherency group-1 (Case:1).	198
FIGURE 7.10: Coherency group-2 (Case:1).	198
FIGURE 7.11: Coherency group-3 (Case:1).	199

FIGURE 7.12: Coherency group-1 (Case:2).	200
FIGURE 7.13: Coherency group-3 (Case:2).	201
FIGURE 7.14: Coherency group-4 (Case:2).	201
FIGURE 7.15: Coherency group-2 (Case:3).	203
FIGURE 7.16: Coherency group-3 (Case:3).	204
FIGURE 7.17: Coherency group-4 (Case:3).	204

## LIST OF TABLES

TABLE 2.1: Coherency grouping of power system models	20
TABLE 2.2: Inter-area mode comparison	32
TABLE 2.3: Optimal wide-area control loop based on normalized residue analysis	37
TABLE 2.4: Optimal control loop for IEEE 39-bus (fault on bus-14)	38
TABLE 2.5: Optimal control loop for IEEE 39-bus (fault on bus-19)	38
TABLE 2.6: Estimated LQR gains ( $K$ ) for two-area system	40
TABLE 2.7: Estimated LQR gains ( $K$ ) for IEEE 39 bus system (Case:1)	41
TABLE 2.8: Estimated LQR gains ( $K$ ) for IEEE 39 bus system (Case:2)	41
TABLE 2.9: Performance metrics for two-area system	43
TABLE 2.10: Area under the curve for two-area system	43
TABLE 2.11: Area under the curve metric (39 bus system case:1)	46
TABLE 2.12: Area under the curve metric (39 bus system case:2)	49
TABLE 3.1: Comparison of coherency grouping methods	60
TABLE 3.2: Coherency grouping of IEEE-39 bus system (spectral clustering) fault on bus-14	64
TABLE 3.3: Coherency grouping of IEEE-39 bus system (spectral clustering) fault on bus-19	65
TABLE 3.4: Coherency grouping of IEEE-39 bus system (spectral clustering) fault on bus-6	65
TABLE 3.5: Control loop based on residue approach	65
TABLE 3.6: IEEE 39-bus control loop (fault on bus-14)	72
TABLE 4.1: Coherency grouping of generators	94

TABLE 4.2: Residue analysis of two-area system	95
TABLE 4.3: IEEE 39-bus control loop (fault on bus-14)	96
TABLE 4.4: Controller performance comparison (fault on bus-14)	97
TABLE 4.5: IEEE 39-bus control loop (fault on bus-25)	98
TABLE 4.6: Controller performance comparison (fault on bus-25)	99
TABLE 4.7: Relative error comparison	100
TABLE 5.1: Coherency grouping of generators for IEEE 39 bus system	117
TABLE 5.2: Comparison of reduced (EMT+TSA) and original (EMT) models	121
TABLE 5.3: FDNE formulation comparison	127
TABLE 5.4: Comparison of reduced (EMT+FDNE) and original (EMT) models	133
TABLE 5.5: Comparison of reduced order (FDNE only) models	135
TABLE 5.6: Comparison of reduced (EMT+FDNE+TSA) and original (EMT) models	136
TABLE 5.7: Comparison of reduced (EMT+FDNE+TSA) and original (EMT) models	137
TABLE 5.8: Comparison of reduced 68 bus, IEEE 39 and 68 bus models	143
TABLE 5.9: IEEE 39-bus control loop (fault on bus-66)	145
TABLE 5.10: Damping improvement comparison (Case:1)	145
TABLE 5.11: IEEE 39-bus control loop (fault on bus-19)	148
TABLE 5.12: Damping improvement comparison (Case:2)	148
TABLE 6.1: Simulation parameters of wind turbine	171
TABLE 6.2: Simulation parameters of DFIG	171

TABLE 7.1: Distributed clustering (Case:1)	197
TABLE 7.2: Distributed clustering (Case:2)	200
TABLE 7.3: Distributed clustering (Case:3)	203

## CHAPTER 1: INTRODUCTION

### 1.1 Modern Power Grid Modeling and Control Challenges

Interconnected power system exhibit oscillatory response after a disturbance in the system. If the frequency of these oscillations is in the range of 0.1 to 1 Hz, then these are called inter-area oscillations and have to be estimated and damped effectively to avoid power system reliability issues. The damping of inter-area oscillations can be achieved using a Wide Area Damping Controller (WADC). The input to the controller is the most observable signal, and the controller output is sent to the most controllable generator. Thus designed controller has to be validated before implementing in the field, for this real-time electromagnetic simulation (EMT) based power grid models are required.

Detailed Electro-Magnetic Transient (EMT), based grid models with dynamic models of Synchronous Machines and DFIG, are required for the accurate design of power system dynamic controllers considering grid transient effects. Such a model-based design for large power grid proves to be impractical due to computational complexity. Earlier, several model order reduction based on linearized models have been developed, but such models are shown to be effective in mitigating only the low-frequency oscillations. For including wide frequency bands, a possible extension is to develop EMT based models in which part of the power grid (study area) for which control is

to be designed is modeled in detail and the remainder of the network (external area) as an aggregated source. In this type of modeling, the external area is modeled as a combination of low and high-frequency equivalents to cover a wide range of frequency spectrum. The generated reduced order model of the power systems can be used for control of the modern power grid.

## 1.2 Research Gap and Proposed Work

State-of-the-art research in power system control applications are based on modal analysis, and thus the designed controllers will operate around a specific operating point. With increased renewable energy penetration, operating point changes continuously, and as a result, offline tuned controllers may not work efficiently. To fill this gap, this dissertation also introduces novel methods of designing real-time centralized and decentralized control which auto-tunes whenever operating point changes.

State-of-the-art research on power grid model reduction techniques are based on linearized models, but these models are based on offline methods such as curve fitting, and the computational effort required to achieve the desired accuracy is very high. In this dissertation, a new approach is proposed for frequency dependent reduced order modeling based on online recursive square online identification with less computational effort and increased accuracy. Validation results are compared with results from earlier methods.

## 1.3 Wide-Area Control Overview

For reliable operation, electro-mechanical oscillations which arise in large interconnected power systems due to disturbance should be damped promptly. The electro-

mechanical oscillations of generators with respect to remaining part of the system are called local modes, whereas groups of generators oscillating together against other groups are called inter-area modes [5]. The frequency of inter-area oscillations is between 0.1-1.0 Hz. Higher penetration of renewable energy resources and variable loads makes the inter-connected power systems to operate close to limits. This condition increases the stress on the power system and can deteriorate the inherent damping of the system. Thus inter-area oscillation damping is even more critical and challenging in the modern power grid. Unfortunately, inter-area modes are not observable/controllable from generator local measurements and the effectiveness of conventional power system stabilizer (PSS) in damping of inter-area modes is thus limited [114]. The damping of inter-area oscillations can be achieved through wide-area control architecture. The wide-area control architecture involves the following steps:

- Inter-area mode estimation
- Coherency group determination
- Identifying optimal wide-area control loop
- Design of WADC

### 1.3.1 Inter-Area Mode Estimation

The interconnected power system after a disturbance exhibit inter-area oscillations of frequency in the range 0.1 to 1Hz. The inter-area modes can be estimated using either modal based or measurement based approaches.

### 1.3.1.1 Model Based Approach

In modal based approach power system is linearized at an operating point and the corresponding state-space matrices of the system are analyzed for evaluating the inter-area modes. The state space model of the system is represented as follows:

$$\dot{x} = Ax + Bu \quad (1.1)$$

$$y = Cx + Du \quad (1.2)$$

where  $A$ ,  $B$ ,  $C$ , and  $D$  are the state, control, output, and feed-forward matrices,  $x$  denotes state,  $y$  denotes output, and  $u$  is the input. The state space model given by (2.1) and (2.2) are formulated after linearizing the system at a particular operating point. If the system operating point changes then the system have to be linearized again. Linearizing a sophisticated power system every time as the operating point changes is tedious and the availability of accurate power system model which represents the current state is not be guaranteed.

### 1.3.1.2 Measurement Based Approach

To overcome the disadvantages of the model-based methods, in this approach the measurement data is used for identification of power system [67, 96, 131–133]. References [131, 133] shows the application of system identification for estimating electromechanical modes and mode shapes. Subspace state model of the system has also been designed for different operating conditions of the power system by using subspace state-space system identification (N4SID) method [132], or recursive adaptive stochastic subspace identification (RASSI) method [96]. However, obtaining a sub-

space state-space model is computationally challenging; also most of these methods do not consider the effect of coupling between different input/output combinations while estimating the MIMO system.

### 1.3.2 Coherency Group Determination

The coherent group of generators information is required for effective wide-area control of the power system such that each group will have one WADC. The identification of a coherent group of generators can be achieved through two methods: 1) Modal based and 2) Measurement-based methods.

#### 1.3.2.1 Modal Based Approach

In model-based approaches, [20] proposed a method for coherency grouping based on weak-link and slow coherency methods. In [55] used relation factors and [16] Krylov subspace to identify coherent groups of generators. However model-based methods are based on the linearized power system model at a particular operating point, and the accuracy of grouping depends on the accuracy of the model.

#### 1.3.2.2 Measurement Based Approach

The model based methods are solely dependent on measurements these methods are independent of contingencies, accurate network parameters, or detailed dynamic model. Recently PMU based measurements are used for coherency identification and the current research methodologies are focusing in this direction [66]. Coherency identification based on wavelet phase difference [11], spectrum analysis [113], graph theory [90], principal component analysis (PCA) [83], independent component analysis (ICA) [9], agglomerative hierarchical clustering (HC) [105], Projection Pursuit

(PP) [49], Fast Fourier transform [50], Hilbert-Huang transform [97], energy function based [45], artificial neural networks [4], self-organizing maps [83], and k-means clustering [25] are reported in literature. Since these methods are based on measurements, it automatically considers and adapts to changes in system operating conditions. However excessive computational burden and bandwidth requirements limit the success of existing coherency grouping based on measured data.

### 1.3.3 Identifying Optimal Wide-Area Control Loop

The optimal wide-area control loop identification is required to find out which control loop is more effective in damping inter-area mode. Several methodologies to identify and damp inter-area oscillations considering optimal wide area control loop (input/output signal selection) are reported in the literature. This include, residue analysis [53, 57, 62], relative gain array (RGA) [71], combined residue and RGA method [61], and geometric measure of joint observability/controllability [31, 78]. However, these methods are formulated using state-space matrices obtained through linearizing the system at a particular operating point and analyzing modes at that point which cannot be implemented in real-life as power system is non-linear and dynamic.

### 1.3.4 WADC Design

Conventional damping controllers are designed considering specific operating conditions that are typical for the power system [48]. The effectiveness of such controllers decreases when the actual operating conditions of the power system deviate from the specified conditions used for the design of such damping controllers. With the increase

in integration of renewable energy to the grid, the operating conditions of power grid change more frequently especially due to the variability in the power output of these renewable resources. Under such variable operating conditions, local robust damping controllers fail to perform well. For example, in [13, 118, 134] a robust damping controller is designed considering a dominant operating condition with bounded uncertainty to make the controller effective to use under varying operating conditions. As the design is considering a dominant frequency at one operating condition, the performance of these controllers may not be optimal as the operating condition deviates from the dominant one.

#### 1.4 Reduced Order Modeling Overview

In electromagnetic (EMT) simulation, the power system is modeled in detail to know the effect of transients arising due to switching, resonance, etc. With the penetration of renewable energy sources like wind and the photovoltaic system, the impact of power electronic components should be studied using EMT simulation. The integration step size of EMT simulation is in  $\mu s$ . In TSA type simulation, only dynamic components like generators, turbines, and governors are modeled in detail. With TSA type simulation effect of transients on electromagnetic oscillations can be observed. The integration time step of TSA models is large, which makes TSA simulation faster than EMT simulation.

Detailed modeling of the large power system for real-time EMT simulation requires large amounts of computational time, and detailed modeling of such large complex network is impractical. Since advanced real-time simulation run on parallel

computing, with an increase in the size of network more processors are required for computation which increases the overall cost. To reduce computational time and the number of processors needed only part of the network to be studied (study area) in which transient phenomenon occurs or to investigate the effect of power electronic devices is modeled in detail, and the rest of the network (external area) is reduced and modeled as an equivalent.

One way to reduce computational effort is to model the external area as TSA type representing the network with simple inductances derived from short circuit impedances at the terminal buses evaluated at power frequency. However, representing the network at fundamental frequency will ignore high-frequency transient phenomenon whose frequency ranges from zero to several kHz. To consider high-frequency transient phenomenon FDNE must be considered to take care of a wide range of frequencies.

If the external area is modeled only as FDNE, the effect of high-frequency transients on generator dynamics cannot be observed since all generators are replaced by voltage sources; hence the electromechanical oscillations are ignored. To cover both electromechanical (low frequency) and high-frequency behavior, the external area should be modeled as TSA in parallel with FDNE. The frequency dependent reduced order modeling involves the following steps:

- Developing low-frequency equivalent (TSA) of the external area
- Developing high-frequency equivalent (FDNE) of the external area

### 1.4.1 Low Frequency Equivalent (TSA)

These models are used in transient stability simulation studies. TSA type models are used when there is limited computing facilities. Currently, with the advent of fast computers, the full model is simulated. The need for low-frequency equivalent is still relevant since the effect of transients and power electronic devices on electro-mechanical oscillations is studied using EMT type simulations. In transient stability simulations, the generators and associated controllers are modeled using nonlinear differential equations whereas, the network is modeled using algebraic equations at the fundamental frequency. The entire power system is modeled as differential and algebraic equations (DAE) [8]. With the input to the  $n^{th}$  generator as terminal voltage  $V_n$ , controller input  $E_n$  and output of the generator is current  $I_n$ , generator differential equations can be written in state space form as:

$$\dot{X}_n = AX_n + Bu_n \quad (1.3)$$

$$I_n = CX_n + Du_n \quad (1.4)$$

where  $u_n = [V_n \ E_n]^T$ ,  $X_n$  is state vector associated with  $n^{th}$  generator, and  $A$  is state matrix.

The primary objective of low-frequency equivalents is to retain the low frequency oscillations (electromechanical modes) which are relatively less damped. Aggregating generators reduce the computational time and reducing buses thus retaining only modes of interest in the dynamic model. In literature approaches for generator aggregation are classified into three types, 1) Model based, 2) Coherency based, and 3)

Measurement based.

#### 1.4.1.1 Modal Based

In this method the linearized state-space model of the power system is obtained at an operating point written as (7.1). Then the state matrix is analyzed to estimate the frequency and damping factor. The overall response of the system is determined considering only less damped modes as highly damped modes decay faster [7, 24, 26, 27, 112].

#### 1.4.1.2 Coherency Based

In this approach, first generators are grouped based on coherency grouping methods [32, 76, 116]. Then the generator buses, generators and their associated controllers are aggregated [33]. The final step in this method is to reduce the load buses. A software program DYNRED for dynamic reduction of large power grids is developed by EPRI [87, 89]. The coherency grouping by analyzing the state matrix is reported in [123]. In [17] and [75] a combination of a modal and coherency based approach is presented. In [75] weak couplings that exist in the state matrix,  $[A]$  is used to identify weak coupling between machines.

#### 1.4.1.3 Measurement or Simulation Based

In measurement based approach either measurements from the real power system or from simulations are used to identify the power system model using system identification techniques [51, 52, 104, 122]. A least-squares algorithm is used to identify the system in [122]. Similar approach to identify the power system model is also reported in [52, 104]. The recorded disturbances are analyzed to estimate the power system

model is reported in [51].

#### 1.4.2 High Frequency Equivalents

The pioneering work in curve fitting reported in [60] used the non-linear least squares technique to fit coefficients of a rational polynomial matrix to the observation data. Improvements to this technique are presented in [94, 102, 103, 119]. A low order rational function model is proposed in [69]. The ill-conditioning problems of FDNE are addressed in [79, 80].

The original work in FDNE reported in [29, 30, 72] used lumped equivalent parameter models to synthesize the frequency dependent admittance of the external network. Further, time domain approaches like Prony Analysis [47] and digital filtering technique [98, 99] are used to formulate the FDNE [8]. The recent FDNE formulations based on vector fitting technique are reported in [28, 40–44].

### 1.5 Power System Control Applications using Reduced Order Model

The obtained reduced order model of the power systems can be used for power system control applications like pitch control of grid-connected wind turbines, wide area control, etc.

### 1.6 Research Contributions

Following are the research contributions which facilitates new methods for wide-area control, reduced order modeling of powers systems and power system control:

- A novel method for designing WADC based on a discrete Linear Quadratic Regulator (DLQR) and Kalman filtering based state-estimation that can be

applied for real-time damping of inter-area oscillations of wind integrated power grid is developed. The main advantages of the proposed architecture are a) online coherency grouping that accurately characterizes real-time changes in the power grid b) online wide-area signal selection based on residue method for proper selection of the WADC signals.

- A novel method for wide-area input-output signal selection based control using ADMM is developed. In this approach, the interconnected power system is divided into areas and then using measured data, a black-box transfer function model is estimated locally for each area based on Lagrange multipliers. These local area controllers communicate with the central controller to estimate a global transfer function model of the power system. Based on the estimated global transfer function, the residue corresponding to inter-area mode is calculated. This provides information of optimal wide area control loop. Residue and corresponding eigenvalue information is used for wide-area damping controller design.
- A novel algorithm for developing single and multi-port FDNE based on an on-line recursive least squares (RLS) identification algorithm is developed, which identifies the input admittance matrix in z-domain and also modeling of reduced power systems as a combination of TSA and FDNE in real-time digital simulators. The advantage of this method is the reduced computational burden.
- An algorithm for real-time reduced order model based adaptive pitch controller for grid interconnected wind turbines is developed. The advantage of the pro-

posed reduced order model based pitch-control architecture is that the method minimizes the damage caused by mechanical fatigue of the wind turbine and at the same time ensures that the grid voltage and power are stable and balanced at all operating conditions.

- An algorithm for distributed coherency grouping of generators based on spectral clustering is proposed. In this method initially generators of each area are clustered locally, and the optimal number of clusters are identified using Elbow method. The cluster centers corresponding to each group are transmitted to the global control center and at the global control center these centers from all local control centers are grouped which gives the indices of global clusters. The global indices are transmitted to the local area for regrouping based on global indices.

## 1.7 Dissertation Organization

This dissertation is organized as follows:

- Chapter 1: This chapter provides overview of the proposed research on centralized and decentralized power system control and applications of the reduced order modeling of the power systems. It summarizes the research contributions
- Chapter 2: This chapter presents an algorithm for model-free MIMO identification, also discusses the wide-area damping controller design based on DLQR and Kalman filtering.
- Chapter 3: The centralized algorithm for wide-area control is further improved

by incorporating online-coherency grouping into the routine and implementing on wind integrated power grid.

- Chapter 4: In this chapter the centralized MIMO identification is decentralized based on Alternating Direction Method of Multipliers (ADMM).
- Chapter 5: This chapter discusses the algorithm and methodology for reduced order modeling of the power system and validation test cases.
- Chapter 6: This chapter discusses a novel method for pitch angle control of variable-speed WTG connected to a reduced order model of large power grid based on adaptive Self Tuning Regulator (STR) control.
- Chapter 7: This chapter discusses the application of reduced order model for wide-area control.
- Chapter 8: This chapter discusses the methodology for distributed coherency grouping of generators.
- Chapter 9: This chapter concludes dissertation and discusses about future research work

In Chapter 2 model-free wide-area damping of inter-area oscillations based on MIMO identification is proposed.

## CHAPTER 2: MODEL-FREE WIDE AREA DAMPING OF INTER-AREA OSCILLATIONS BASED ON MIMO IDENTIFICATION

Interconnected power system exhibit oscillatory response after a disturbance in the system. If the frequency of these oscillations is in the range of 0.1 to 1 Hz, then these are called inter-area oscillations and have to be estimated and damped effectively to avoid power system reliability issues. The damping of inter-area oscillations can be achieved using a Wide Area Damping Controller (WADC), the input to the controller is the most observable signal, and the controller output is sent to the most controllable generator. To this effect, this chapter presents a model-free novel algorithm for multi-input-multi-output (MIMO) transfer function identification of the power system to estimate the frequency of the oscillations. Based on the MIMO transfer function the optimal control loop for WADC is estimated. The WADC design is based on the discrete linear quadratic regulator (DLQR) and Kalman filtering for real-time damping of inter-area oscillations. The MIMO identification is based on actual measurements so the proposed method can accurately monitor changes in the power grid whereas the conventional methods are based on small-signal analysis of a linearized model of a complex system which does not consider changing operating conditions of the grid. The overall algorithm is implemented and validated on a RTDS/RSCAD<sup>®</sup> and MATLAB<sup>®</sup> real-time co-simulation platform using two-area and IEEE 39 bus power system models.

## 2.1 Introduction

The increase in the penetration of renewable energy sources and deregulation made the power system to operate near its rated operating limits. Under these circumstances, if there is a disturbance in the system, this could affect the power system reliability and security. The oscillatory response which arises due to such disturbances have to be damped effectively, and these oscillations are of two types 1) Local oscillations, and 2) Inter-area oscillations. The local oscillations have frequencies higher than 1 Hz, and inter-area oscillations frequency lies in the range of 0.1 to 1 Hz [56]. In the case of inter-area oscillations the generators in one coherent area swing together against other area generators [20]. The inter-area oscillations limit the power transfer capability across the tie-lines and may destabilize the power system [84] if not damped effectively.

In literature, as discussed in Sections 1.3.1.1 and 1.3.3 several methodologies for inter-area mode estimation and control-loop selection are based on linearizing the system at an operating point and analyzing the state space matrices obtained after that. If the system operating point changes then the control-loop obtained at a different operating point may not be valid, and a new control-loop is to be estimated based on the current operating point. However, linearizing the complex power system model every time as the operating point changes is tedious and an accurate model of the power system for the current operating point may not always be readily available.

To overcome the drawbacks of linearization based methods, the measurement based methods are adapted. Using the measurements directly the MIMO model of the power

system is estimated without the need for a detailed model of the power system. Since the changing dynamics/operating points of the system are captured in the measurement data, the MIMO model thus obtained can be used for mode and control loop estimation. The measurement-based methodologies gained interest with the advent of phasor measurement unit (PMUs), communication infrastructure. Several measurement based methods are discussed in Section 1.3.1.2, but some of these methods did not consider the mutual coupling between different control loops and estimating optimal wide-area control loop is not addressed.

To this effect, a novel model-free MIMO system identification technique for wide-area control considering mutual coupling between different control loops is presented this chapter, the identified MIMO system is used for 1) inter-area frequency estimation, 2) optimal control loop estimation, and 3) design of wide area controller. In this initially, the power system is divided into areas based on coherency grouping such that each area has one WADC to damp inter-area oscillations [83]. Then MIMO identification is performed to estimate an optimal control loop to damp the inter-area mode of interest. Finally, WADC is designed based on the model-free discrete linear quadratic regulator (DLQR) and Kalman filtering (KF) techniques. The efficacy of the proposed architecture is verified by implementing on a RTDS/RSCAD and MATLAB real-time testbed using two-area and IEEE 39 bus [46] power system models.

To summarize, the major contributions in this chapter are:

- Developed a real-time co-simulation test bed for model-free MIMO considering

mutual coupling between different control loops.

- Performing residue analysis on the identified MIMO transfer function to estimate the optimal control loop for wide-area control.
- Designed a WADC based on DLQR and KF techniques which use the extracted state space matrices from identified MIMO system.

The rest of the chapter is organized as follows: In Section 2.2 dividing power system based on coherency is discussed. In Section 2.3, model-free MIMO identification is discussed and Section 2.4 discusses about real-time implementation of MIMO identification. Section 2.5 discusses about optimal wide area control loop selection. Section 2.6 discusses model-free DLQR and Kalman filter design. Section 2.7 discusses simulation results and Section 2.8 summarizes the chapter.

## 2.2 Dividing Power System Based on Coherency

In reality, power system comprises of different physical areas and are interconnected through tie-lines, to realize this the power system test models under consideration are divided into areas based on slow coherency grouping of generators which is based on linearized power system model. The division of the power system into areas are required to assign WADC to each of the control areas. The details regarding slow coherency grouping of generators are reported in [95] so further details are not discussed here. This algorithm is implemented on two-area power system (Fig. 1(a)) as well as IEEE 39 bus (Fig. 2.4) power system models. Fig. 2.1 shows the architecture of the proposed WADC.

### 2.2.1 Coherency grouping of two-area system model

On applying the slow coherency grouping method to the two-area power system model, it is found that generators 1 and 2 are in one area and the remaining generators are in other areas. To validate this grouping from the actual response of the system a 3-ph fault is created at 4s for a duration of 0.05s on bus-8 and generators inter-area dynamics are observed. Fig. 2.3 shows the speed deviation of generators from its rated speed (i.e.,  $2\pi f$ , where  $f$  is the fundamental frequency in Hz) and it can be seen that generators 1,2 swing against generators 3 and 4. Based on this grouping the test model is divided into two areas (groups) as shown in Fig .1(a) and Table 2.1.

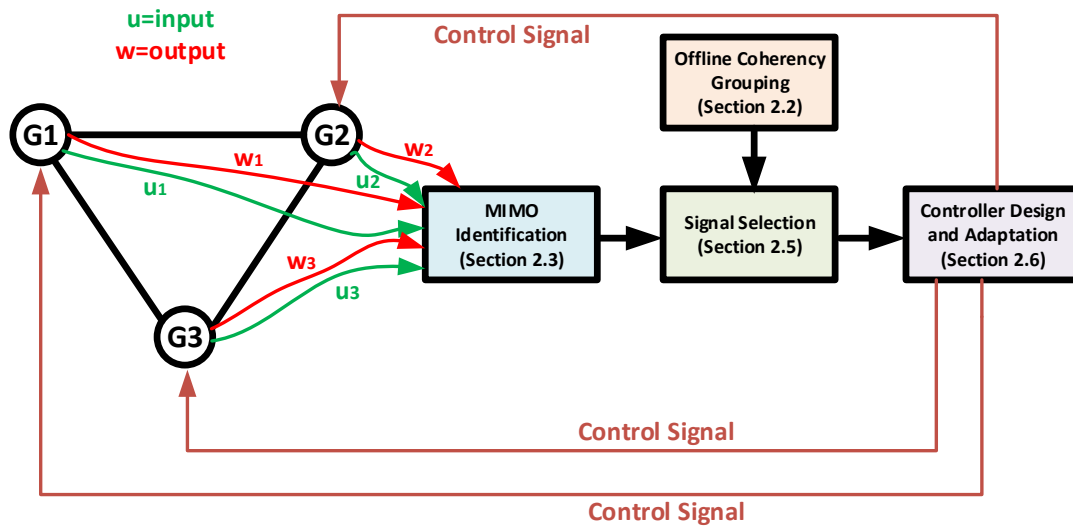


Fig. 2.1. Architecture for proposed WADC

### 2.2.2 Coherency grouping of IEEE 39 bus system

Further to divide the IEEE 39 bus system (Fig. 2.4) into realistic areas, the slow coherency grouping technique is used here, and the coherent groups of generators

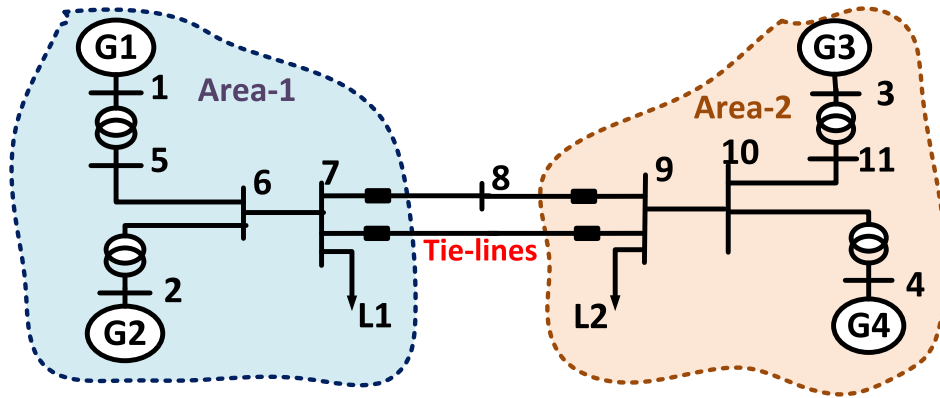


Fig. 2.2. Two-area power system model

Table 2.1  
Coherency grouping of power system models

Test System	Slow Coherency
Two Area	Group-1: 1,2
	Group-2: 3,4
IEEE 39-BUS	Group-1: 4,5,6,7
	Group-2: 1,8,9
	Group-3: 2,3
	Group-4: 10

obtained are as shown in Table 2.1. To show the grouping of generators from generator dynamics, a 3-ph fault is created on Bus-14 at 4s for a duration of 0.1s. Fig. 4.3, Fig. 2.6, and Fig. 4.4 shows the speed deviations of generators in groups-1, 2, and 3 respectively.

### 2.3 Model-free MIMO Identification

Most of the physical world systems are MIMO, and the dynamics of these systems traditionally are analyzed using linearized model at an operating point and estimating modes and mode shapes from the state space matrices thus obtained after linearization. However, linearizing a complex system requires an accurate model which

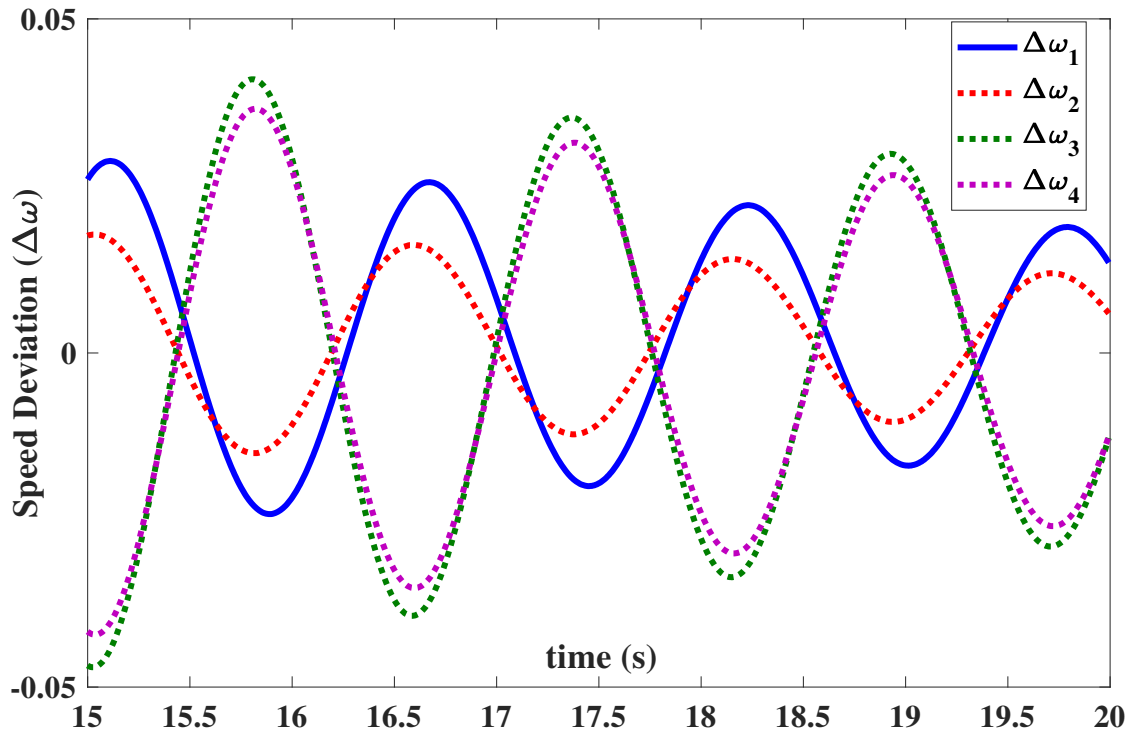


Fig. 2.3. Speed deviation (rad/s) (two-area system)

represents the current operating point of the system and achieving the exact model may not always be possible. To overcome this, the MIMO identification should be model-free without loss of accuracy in identified models. This can be achieved using measured data, and while formulating MIMO system transfer functions the effects between different input/output combinations should be considered. The need for considering mutual coupling effect is as shown using a physical example in Section 2.3.1.

### 2.3.1 MIMO transfer function from state space matrices

Consider a system with two inputs,  $u_1$  and  $u_2$ , and two outputs,  $y_1$  and  $y_2$  and the system is represented by differential equation [1] as follows:

$$y_1'' + a_1 y_1' + a_0(y_1 + y_2) = u_1(t) \quad (2.1)$$

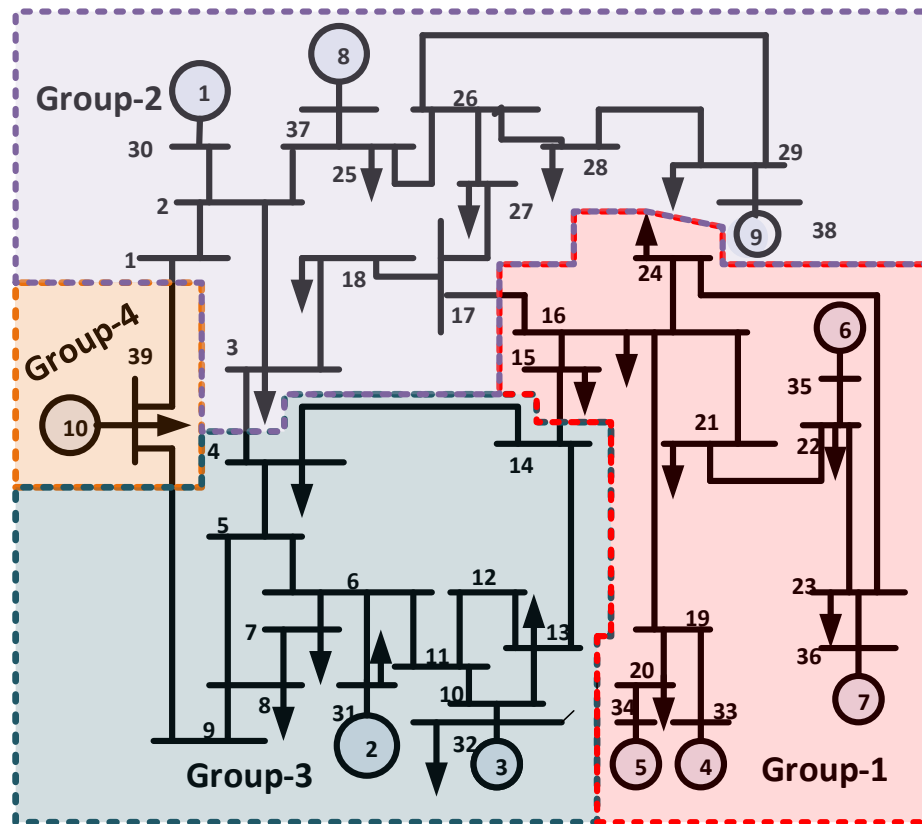


Fig. 2.4. 39-bus power system model

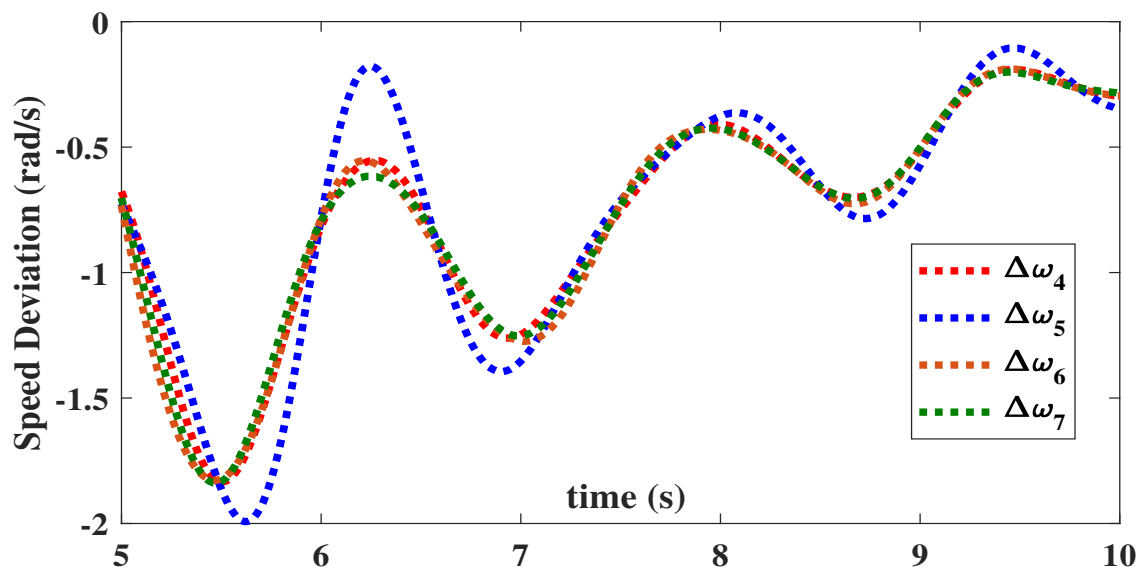


Fig. 2.5. Speed Deviation (Group-1)

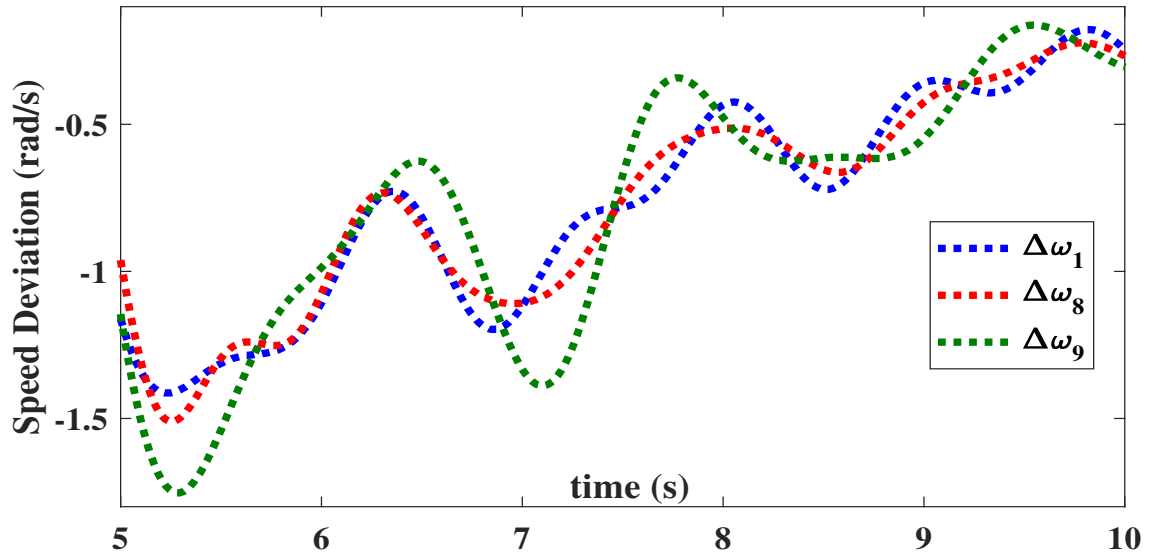


Fig. 2.6. Speed Deviation (Group-2)

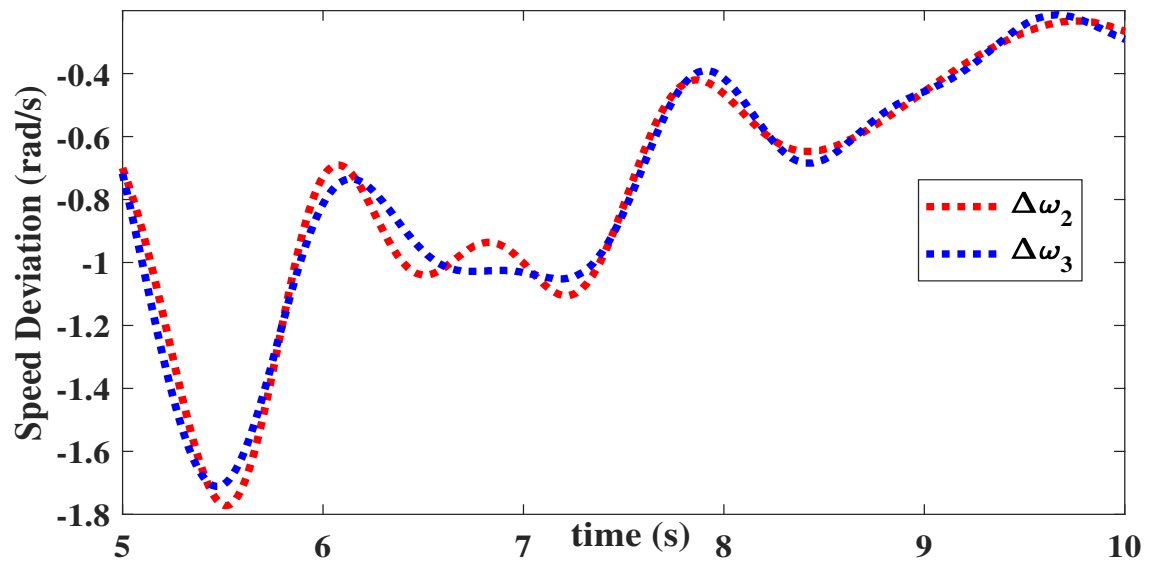


Fig. 2.7. Speed Deviation (Group-3)

$$y_2' + a_2(y_2 - y_1) = u_2(t) \quad (2.2)$$

where superscripts  $y'$  and  $y''$  indicates first and second order differential equations respectively. Now formulating state space matrices from (2.1) and (2.2) gives:

$$x_1 = y_1 \quad (2.3)$$

$$x_4 = y_2 = x_3' \quad (2.4)$$

$$x_1' = y_1' = x_2 \quad (2.5)$$

$$x_2' = -a_1 x_2 - a_0(x_1 + x_4) + u_1(t) \quad (2.6)$$

$$x_4' = -a_2(x_4 - x_1) + u_2(t) \quad (2.7)$$

Now rearranging (2.3) to (2.7) to get state space equations.

$$x' = \underbrace{\begin{bmatrix} 0 & 1 & 0 & 0 \\ -a_0 & -a_1 & 0 & -a_0 \\ 0 & 0 & 0 & 1 \\ a_2 & 0 & 0 & -a_2 \end{bmatrix}}_{\mathbf{A}} x + \underbrace{\begin{bmatrix} 0 & 0 \\ 1 & 0 \\ 0 & 0 \\ 0 & 1 \end{bmatrix}}_{\mathbf{B}} \begin{bmatrix} u_1 \\ u_2 \end{bmatrix} \quad (2.8)$$

$$\begin{bmatrix} y_1 \\ y_2 \end{bmatrix} = \underbrace{\begin{bmatrix} 1 & 0 & 0 & 0 \\ 0 & 0 & 0 & 1 \end{bmatrix}}_{\mathbf{C}} x \quad (2.9)$$

Converting (2.8) and (2.9) into transfer function format yields:

$$G(s) = \mathbf{C}(s\mathbf{I} - \mathbf{A})^{-1}\mathbf{B} = \begin{bmatrix} G_{11}(s) & G_{12}(s) \\ G_{21}(s) & G_{22}(s) \end{bmatrix} \quad (2.10)$$

where  $\mathbf{I}$  is the identity matrix and

$$\begin{aligned} G_{11}(s) &= \frac{s + a_2}{s^3 + (a_1 + a_2)s^2 + (a_0 + a_1a_2)s + 2a_0a_2} \\ G_{12}(s) &= \frac{-a_0}{s^3 + (a_1 + a_2)s^2 + (a_0 + a_1a_2)s + 2a_0a_2} \\ G_{21}(s) &= \frac{a_2}{s^3 + (a_1 + a_2)s^2 + (a_0 + a_1a_2)s + 2a_0a_2} \\ G_{22}(s) &= \frac{s^2 + a_1s + a_0}{s^3 + (a_1 + a_2)s^2 + (a_0 + a_1a_2)s + 2a_0a_2} \end{aligned}$$

Equation (2.10) can be represented in discrete time domain by replacing  $s$  with  $\frac{2(1-z^{-1})}{T_s(1+z^{-1})}$  (tustin approximation), where  $T_s$  is the sampling time.

$$G(z^{-1}) = \begin{bmatrix} G_{11}(z^{-1}) & G_{12}(z^{-1}) \\ G_{21}(z^{-1}) & G_{22}(z^{-1}) \end{bmatrix} \quad (2.11)$$

The objective here is to identify the MIMO transfer function as shown in (2.10) and (2.11) using the measurement data without the information of the model. One way to determine the MIMO is to identify different input/output combinations separately, but this approach does not include mutual coupling between loops. If we observe the individual transfer function of (2.10) all the transfer functions have same denominator coefficients (i.e., eigenvalues of the system) while numerator coefficients differ this is to ensure mutual coupling between loops in MIMO system. So our objective is to formulate a MIMO identification which uses input/output measurement data and have the same denominator coefficients but different numerator coefficients.

### 2.3.2 Model-free MIMO identification considering mutual coupling

For model-free MIMO identification of the system, the available parameters are the input and output measurements. In the power system perspective, the input data  $u_p$  is the voltage reference to the exciter of the synchronous machine, and the output is the speed deviation,  $\Delta\omega_m$ . The input/output measurement channel is as illustrated in Fig. 4.9. The EMT based real-time simulator is in discrete-domain the MIMO formulation of the power system is also in the discrete time domain with  $p$  inputs and  $m$  outputs is given by (2.12). The individual transfer function corresponding to each input/output loop is estimated using the proposed methodology for MIMO identification considering the mutual coupling between different loops.

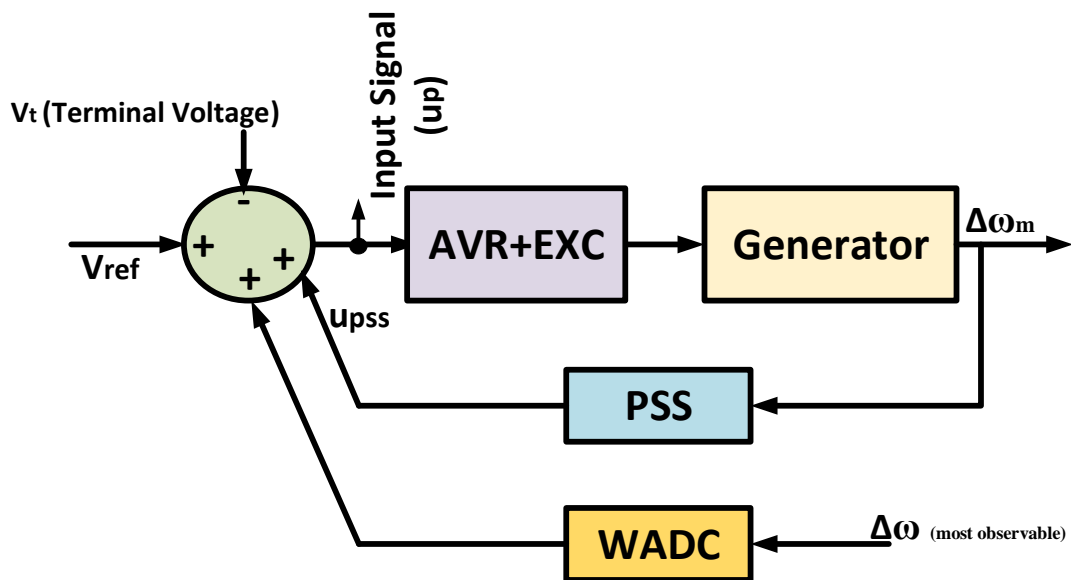


Fig. 2.8. Input and output measurements

$$\Delta\omega(z^{-1}) = G(z^{-1})U(z^{-1}) \quad (2.12)$$

where

$$\Delta\omega(z^{-1}) = \begin{bmatrix} \Delta\omega_1(z^{-1}) \\ \cdot \\ \cdot \\ \Delta\omega_m(z^{-1}) \end{bmatrix}, U(z^{-1}) = \begin{bmatrix} u_1(z^{-1}) \\ \cdot \\ \cdot \\ u_p(z^{-1}) \end{bmatrix}$$

$$G(z^{-1}) = \begin{bmatrix} G_{11}(z^{-1}) & \cdot & \cdot & G_{1p}(z^{-1}) \\ \cdot & \cdot & \cdot & \cdot \\ \cdot & \cdot & \cdot & \cdot \\ G_{m1}(z^{-1}) & \cdot & \cdot & G_{mp}(z^{-1}) \end{bmatrix}$$

The individual transfer functions of the MIMO system can be represented as shown in (2.13).

$$G_{mp}(z^{-1}) = \frac{\Delta\omega_m(z^{-1})}{u_p(z^{-1})} = \frac{b_0^h + b_1^h z^{-1} + \dots + b_k^h z^{-k}}{1 + a_1 z^{-1} + a_2 z^{-2} + \dots + a_k z^{-k}} \quad (2.13)$$

where  $u_p$  and  $\Delta\omega_m$  are the input and output signal data,  $h$  is the element number in the matrix, and  $k$  is the order of transfer function. The (2.13) is formulated in a way such that can be seen that for all transfer functions the denominator coefficients are same but numerator coefficients differ, this is to ensure that mutual coupling is ensured while identifying the MIMO system. The MIMO system is identified as shown in the following steps:

### 2.3.2.1 Step-1

The equation (2.12) is rewritten for  $N$  observation window length as shown in (2.14).

$$X_{His}^h = X_{Num}^h + X_{Den}^h \quad (2.14)$$

where

$$X_{His}^h = \begin{bmatrix} \Delta\omega_m(z) \\ \cdot \\ \cdot \\ \Delta\omega_m(z - N + 1) \end{bmatrix}$$

$$X_{Num}^h = \begin{bmatrix} u_p(z - 1) & \cdot & u_p(z - k) \\ \cdot & \cdot & \cdot \\ \cdot & \cdot & \cdot \\ u_p(z - N) & \cdot & u_p(z - N + 1 - k) \end{bmatrix} \begin{bmatrix} b_0^h \\ \cdot \\ \cdot \\ b_k^h \end{bmatrix}$$

$$X_{Den}^h = \begin{bmatrix} \Delta\omega_m(z - 1) & \cdot & \Delta\omega_m(z - k) \\ \cdot & \cdot & \cdot \\ \cdot & \cdot & \cdot \\ \Delta\omega_m(z - N) & \cdot & \Delta\omega_m(z - N + 1 - k) \end{bmatrix} \begin{bmatrix} a_1 \\ \cdot \\ \cdot \\ a_k \end{bmatrix}$$

### 2.3.2.2 Step-2

For all input/output loops, concatenate  $X_{His}^h$  and is represented as (2.15)

$$\begin{bmatrix} X_{His}^1 \\ X_{His}^2 \\ \cdot \\ X_{His}^h \end{bmatrix} = \begin{bmatrix} X_{Num}^1 \\ X_{Num}^2 \\ \cdot \\ X_{Num}^h \end{bmatrix} + \begin{bmatrix} X_{\Delta\omega}^1 \\ X_{\Delta\omega}^2 \\ \cdot \\ X_{\Delta\omega}^h \end{bmatrix} \begin{bmatrix} a_1 \\ \cdot \\ \cdot \\ a_k \end{bmatrix} \quad (2.15)$$

### 2.3.2.3 Step-3

Calculate denominator coefficients and numerator coefficients iteratively. For this, in the first iteration numerator coefficients are initialized. Then the denominator coefficients  $(a_1, a_2 \dots a_k)$  are calculated by applying the least squares technique to (2.16). Further the numerator coefficients  $(b_0^h, b_1^h \dots b_k^h)$  are calculated again as shown in (2.17)

$$\begin{bmatrix} \mathbf{X}_{\Delta\omega}^1 \\ \mathbf{X}_{\Delta\omega}^2 \\ \cdot \\ \mathbf{X}_{\Delta\omega}^h \end{bmatrix} \begin{bmatrix} a_1 \\ \cdot \\ \cdot \\ a_k \end{bmatrix} = \begin{bmatrix} \mathbf{X}_{His}^1 \\ \mathbf{X}_{His}^2 \\ \cdot \\ \mathbf{X}_{His}^h \end{bmatrix} - \begin{bmatrix} \mathbf{X}_{Num}^1 \\ \mathbf{X}_{Num}^2 \\ \cdot \\ \mathbf{X}_{Num}^h \end{bmatrix} \quad (2.16)$$

$$\begin{bmatrix} \mathbf{X}_{up}^h \end{bmatrix} \begin{bmatrix} b_0^h \\ \cdot \\ \cdot \\ b_k^h \end{bmatrix} = \begin{bmatrix} \mathbf{X}_{His}^h \end{bmatrix} - \begin{bmatrix} \mathbf{X}_{\Delta\omega}^h \end{bmatrix} \begin{bmatrix} a_1 \\ \cdot \\ \cdot \\ a_k \end{bmatrix} \quad (2.17)$$

The numerator and denominator are calculated iteratively until the desired tolerance is achieved such that  $\|([\mathbf{X}_{His}^h - (\mathbf{X}_{Num}^h + \mathbf{X}_{Den}^h)])\| \leq 0.0001$ . The MIMO identification flow is shown in Algorithm 2.1.

---

**Algorithm 2.1** MIMO Identification-Algorithm
 

---

```

1) Initialize numerator coefficients  $(b_0^h, b_1^h \dots b_k^h)$  of (9)
while  $tol \leq 0.0001$  do
  a) Calculate denominator coefficients  $(a_1, a_2 \dots a_k)$  (12)
  b) Using denominator coefficients obtained in previous step, calculate numerator
  coefficients (13)
  c)  $tol = norm([\mathbf{X}_{His}^h - (\mathbf{X}_{Num}^h + \mathbf{X}_{Den}^h)])$ 
end while

```

---

## 2.4 Real-time implementation of MIMO identification

The proposed MIMO identification of the power system is implemented on a RTDS/RSCAD and MATLAB co-simulation test bed as shown in Fig. 8(a). The power system is modeled in RTDS/RSCAD, and the MIMO identification algorithm is implemented in MATLAB. The RTDS/RSCAD sends the measurement data to MATLAB for processing through GTNET-Socket connection [2]. The data received on MATLAB end is processed for MIMO identification, apart from MIMO identification MATLAB also uses the identified transfer functions to estimate an optimal control loop and send the control signal back to the power system model is RTDS. Since this approach is implemented using RTDS, the real-life time scenario is emulated and the designed controllers can be tested using this co-simulation platform before implementing in the field.

### 2.4.1 MIMO Identification two-area system

The two-area power system model (Fig. 1(a)) is initially identified to validate the proposed algorithm. The measurement data  $u_m$  and  $\Delta\omega_m$  of all generators are transmitted to MATLAB with a sampling time of 0.0064s. Then further to reduce the computational effort the data available is down-sampled by a factor 10 so that

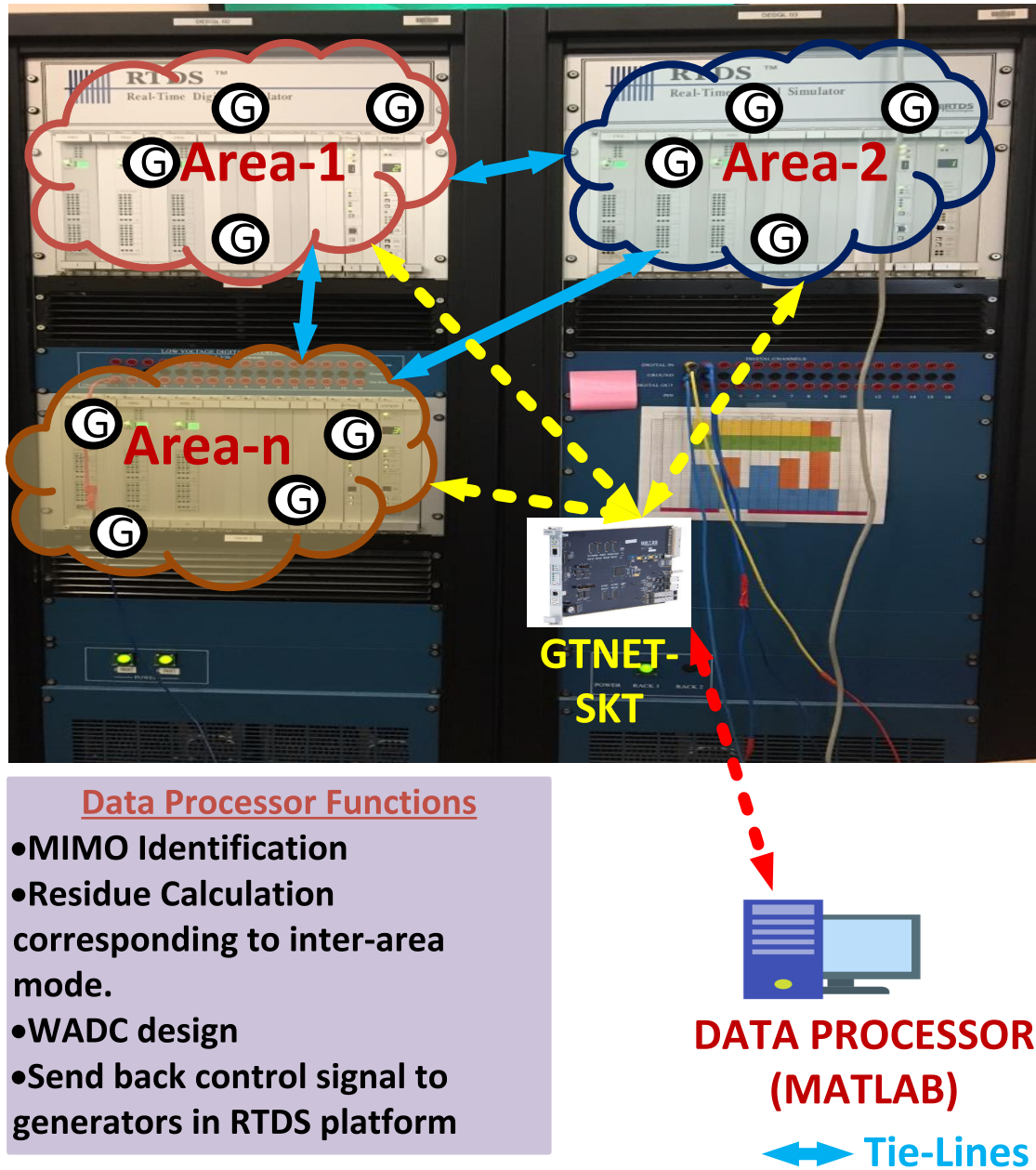


Fig. 2.9. Real-time experimental setup

the new sampling time will be 0.064s. The new sampling time after down-sampling is used in the conversion of discrete to continuous time domain as well as estimation of inter-area modes. To validate the effectiveness of the proposed MIMO identification algorithm in estimating the inter-area modes, a 3-ph fault is created on Bus-8 at 4s for

a duration of 0.05s. The speed deviation after the fault is shown in Fig. 2.10. From Fig. 2.10 the approximate frequency of oscillations from visual inspection is 0.6803Hz and from application of Fast Fourier Transform (FFT) algorithm on  $\Delta\omega_1$  data, the inter-area frequency is 0.6793Hz (see Fig. 2.11). The frequency obtained from the proposed algorithm considering mutual coupling is 0.6619Hz. Table 2.2 shows the inter-area mode comparison.

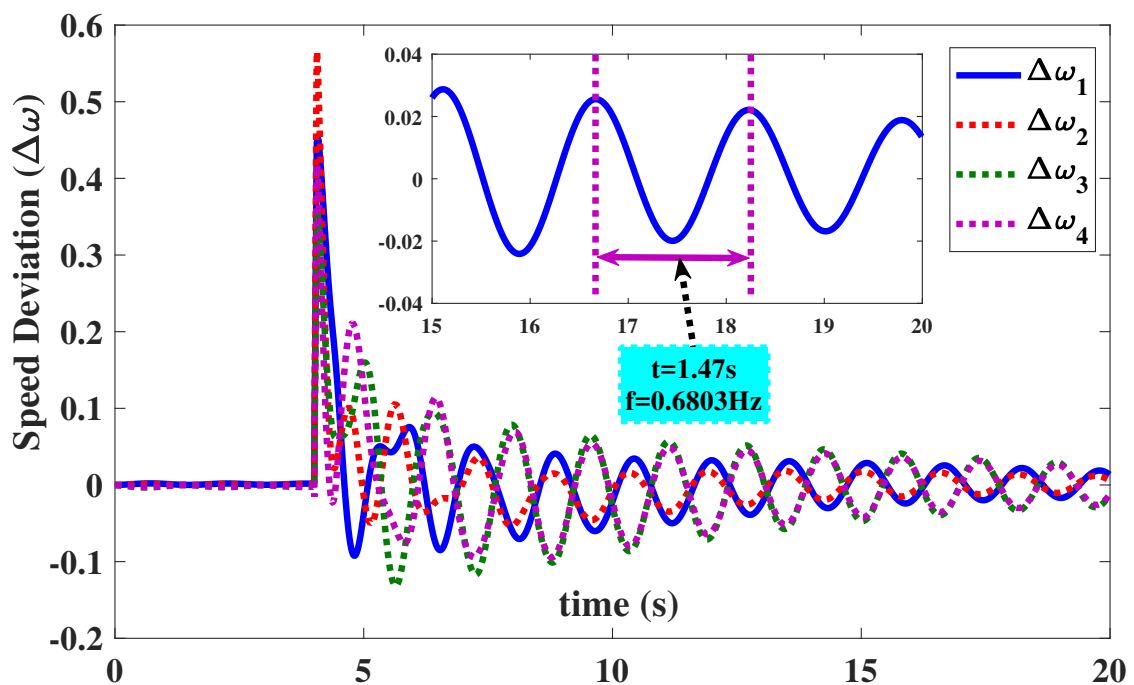


Fig. 2.10. Speed deviation of generators(rad/s)

Table 2.2  
Inter-area mode comparison

Test System	MIMO Identification	FFT
Two Area	0.6694Hz	0.6793Hz
IEEE 39-BUS	Case-1: 0.6077Hz	Case-1: 0.5919Hz
	Case-2: 0.6631Hz	Case-2: 0.6658Hz

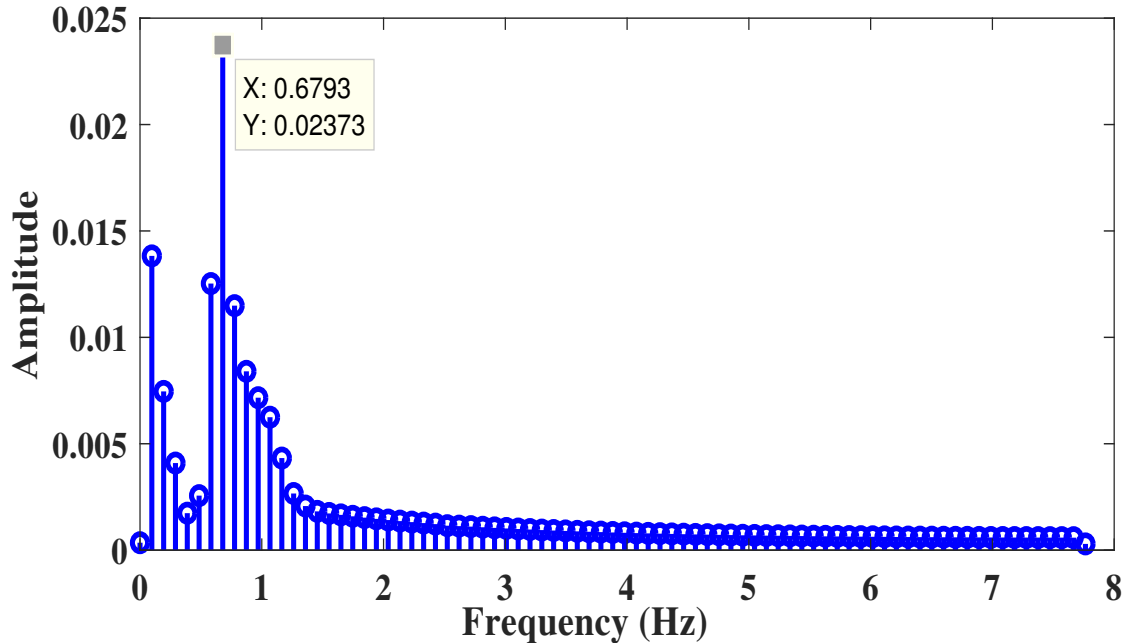


Fig. 2.11. FFT analysis of  $\Delta\omega_1$

#### 2.4.2 MIMO Identification of 39-bus system

Further to validate the MIMO identification of IEEE 39 bus system is used. Two subsequent disturbance cases at different locations as shown in Fig. 2.12 are simulated.

##### 2.4.2.1 Case:1

In this case, a 3-ph fault is created at 14s for a duration of 0.1s on bus-14. In this case, also the data sampling time is 0.0064s and transmitted to MATLAB. After receiving at the MATLAB end, the data is down-sampled by 10 to reduce the computation time and burden. From Table 2.2 it can be seen that from proposed method the estimated inter-area frequency is 0.6077Hz whereas from FFT analysis of generator-5 speed( $\Delta\omega_5$ ) data the inter-area frequency obtained is 0.5919Hz (Fig. 4.13).

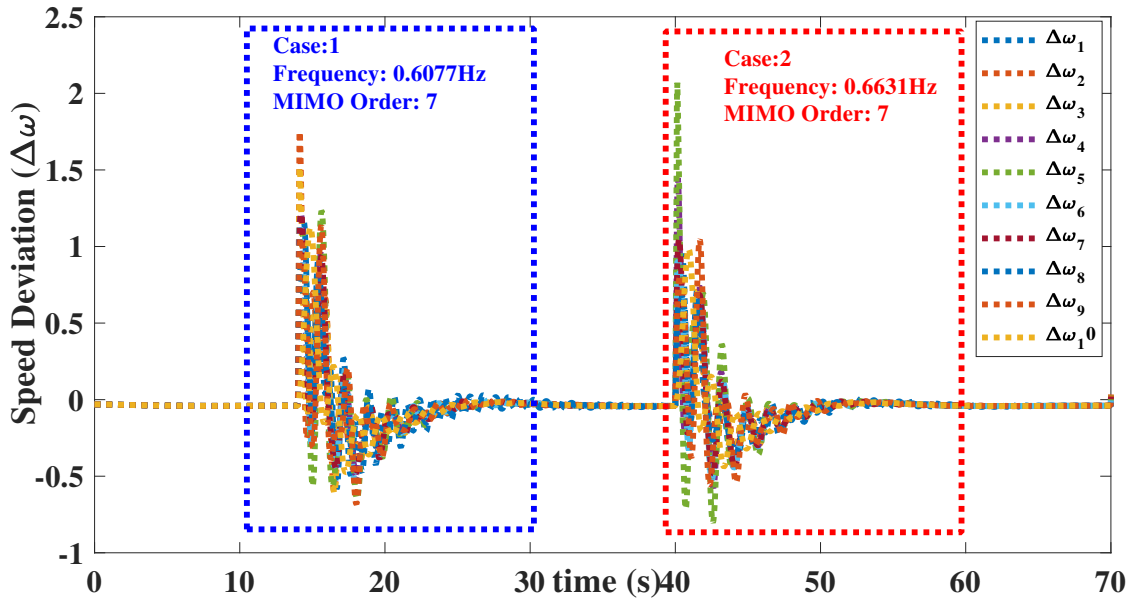


Fig. 2.12. 39 bus speed deviation (rad/s)

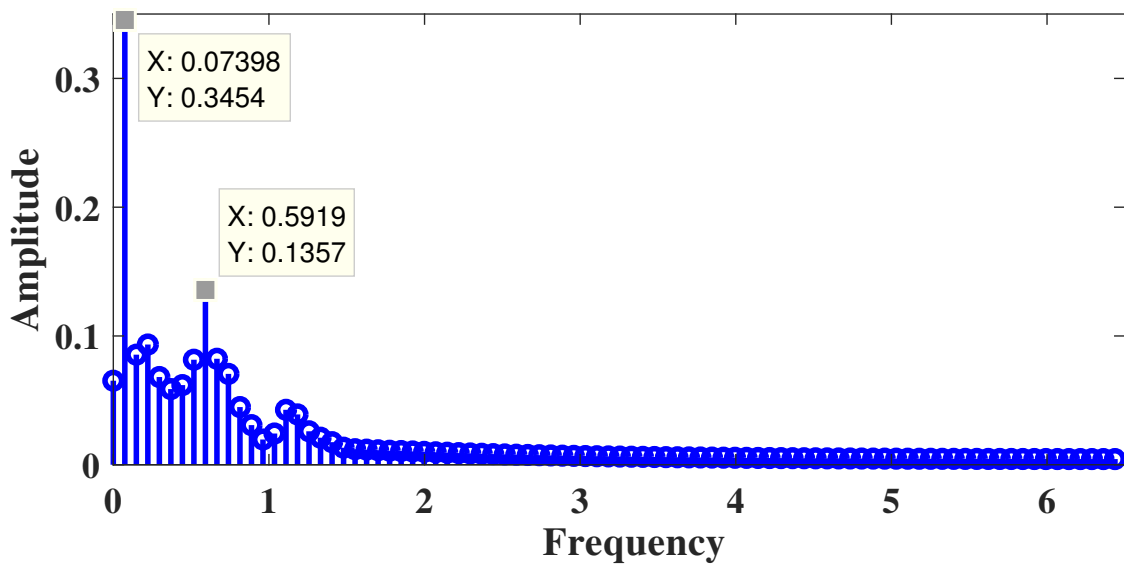


Fig. 2.13. FFT analysis of  $\Delta\omega_5$  (Case:1)

#### 2.4.2.2 Case:2

Further, in this case, a 3-ph fault is created at 39.5s for a duration of 0.1s on bus-19. In this case, also the data sampling time is 0.0064s and transmitted to MATLAB. After receiving at the MATLAB end, the data is down-sampled by 10 to reduce the

computation time and burden. From Table 2.2 it can be seen that from proposed method the estimated inter-area frequency is 0.6631Hz whereas from FFT analysis of generator-5 speed( $\Delta\omega_5$ ) data the inter-area frequency obtained is 0.6658Hz (Fig. 2.14).

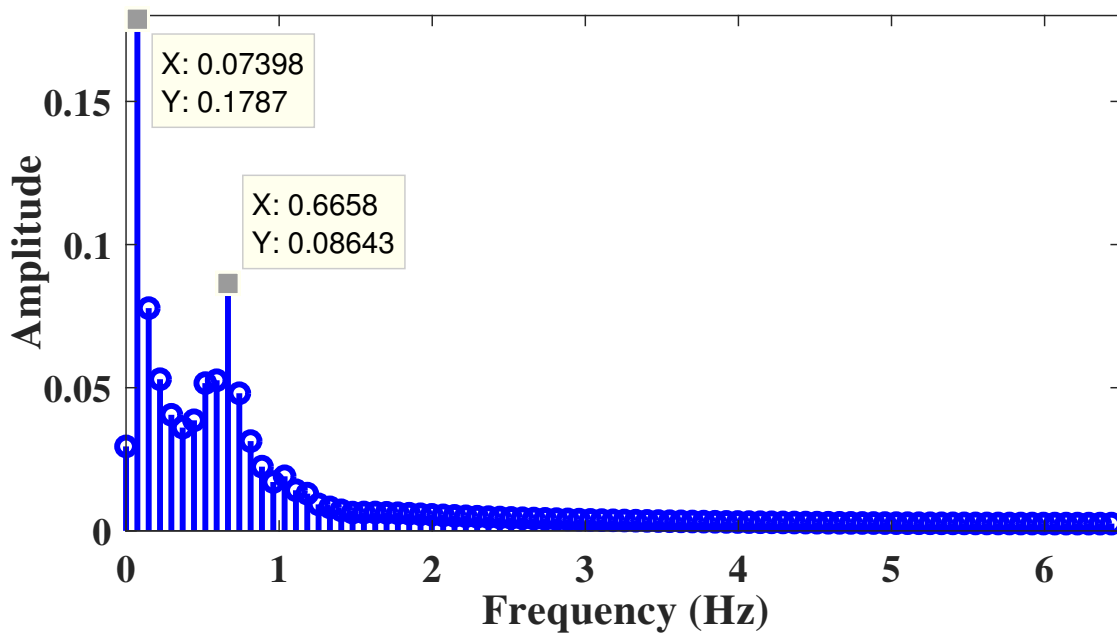


Fig. 2.14. FFT analysis of  $\Delta\omega_5$  (Case:2)

## 2.5 Optimal Wide Area Control Loop Selection

After estimating the inter-area mode, the objective is to damp that oscillation using WADC. However, in the MIMO power system model, there are different input/output control loop combinations, it is inevitable to estimate the most optimal control loop with which we can damp inter-area oscillations. This can be achieved by analyzing residues of the identified MIMO transfer functions corresponding to inter-area modes of interest [109]. For this (2.13) is converted to continuous time domain format and rewritten in partial fraction expansion form as shown in (2.18).

$$\mathbf{G}_{mp}(s) = \frac{\Delta\omega_m(s)}{\mathbf{u}_p(s)} = \frac{\mathbf{r}_{mp}(\mathbf{1})}{s - \mathbf{p}_1} + \frac{\mathbf{r}_{mp}(\mathbf{2})}{s - \mathbf{p}_2} + \dots + \frac{\mathbf{r}_{mp}(\mathbf{j})}{s - \mathbf{p}_j} + \mathbf{k}_{mp}(s) \quad (2.18)$$

where  $p$  and  $r_{mp}$  are the poles and residues of the transfer function  $G_{mp}(s)$ . The residue ( $r_{mp}(j)$ ) corresponding to inter-area mode ( $p_j$ ) gives the information of the optimal control loop. For a mode  $p_j$ , the value of residue gives how controllable is the output  $\Delta\omega_m$  and how observable is the input  $u_p$ , overall how strong is the control loop to damp oscillations. From this then it can be concluded that the control loop which has larger residue is optimal.

### 2.5.1 Identifying the optimal control loop for two-area system

From Table 2.2 dominant inter-area mode for two-area power system model is 0.6694Hz. The residue analysis corresponding to the inter-area mode of frequency 0.6694Hz is shown in Table 2.3. From Table 2.3 it can be seen that for Area-1 the maximum value of residue is for  $\Delta\omega_3 \rightarrow u_2$  loop and in Area-2 the maximum values of residue is for  $\Delta\omega_3 \rightarrow u_4$  loop. From this, for Area-1 which consists of generators 1 and 2, the generator-2 is the most controllable and the speed deviation of generator-3 is the most observable and this combination is an optimal control loop for Area-1. Likewise, for Area-2 the generator-4 is the most controllable and speed deviation of generator-3 is the most observable and this combination is an optimal control loop for Area-2.

Table 2.3  
Optimal wide-area control loop based on normalized residue analysis

output/input	$u_1$	$u_2$	$u_3$	$u_4$
$\Delta\omega_1$	0.7695	0.4274	0.0188	0.5275
$\Delta\omega_2$	0.2838	0.5255	0.7124	0.3025
$\Delta\omega_3$	0.5568	<b>0.8274</b>	0.0159	<b>1.0</b>
$\Delta\omega_4$	0.1534	0.1404	0.2492	0.4395

## 2.5.2 Identifying the optimal control loop for 39 bus system

In the case of 39 bus system different cases are analyzed as discussed in Section 7.5.1.1 and 7.5.1.2 to illustrate how changes in operating conditions affect the inter-area modes and corresponding optimal control loops.

### 2.5.2.1 Case: 1

From Table 2.2 dominant inter-area mode for 39 bus system, case-1 is 0.6077Hz. The residue analysis corresponding to the inter-area mode of frequency 0.6077Hz is shown in Table 2.4. From Table 2.4 it can be seen that for Group-1 the generator-4 is the most controllable and the speed deviation of generator-9 is the most observable. For Group-2 the generator-9 is the most controllable and the speed deviation of generator-10 is the most observable. For Group-3 the generator-3 is the most controllable, and the speed deviation of generator-2 is the most observable, and finally, for Group-4 the generator-10 is the most controllable and the speed deviation of generator-6 is the most observable and this makes an optimal control for this case.

Table 2.4  
Optimal control loop for IEEE 39-bus (fault on bus-14)

	Control Loop	Residue
<i>Group – 1</i>	$\Delta\omega_9$ to $u_4$	0.7160
<i>Group – 2</i>	$\Delta\omega_{10}$ to $u_9$	0.7302
<i>Group – 3</i>	$\Delta\omega_2$ to $u_3$	0.3950
<i>Group – 4</i>	$\Delta\omega_6$ to $u_{10}$	1.0

### 2.5.2.2 Case: 2

From Table 2.2 dominant inter-area mode for 39 bus system, case-2 is 0.6631Hz. The residue analysis corresponding to the inter-area mode of frequency 0.6077Hz is shown in Table 2.5. From Table 2.5 it can be seen that for Group-1 the generator-7 is the most controllable and the speed deviation of generator-1 is the most observable. For Group-2 the generator-8 is the most controllable and the speed deviation of generator-4 is the most observable. For Group-3 the generator-3 is the most controllable, and the speed deviation of generator-9 is the most observable, and finally, for Group-4 the generator-10 is the most controllable and the speed deviation of generator-4 is the most observable and this makes an optimal control for this case.

Table 2.5  
Optimal control loop for IEEE 39-bus (fault on bus-19)

	Control Loop	Residue
<i>Group – 1</i>	$\Delta\omega_1$ to $u_7$	0.7911
<i>Group – 2</i>	$\Delta\omega_4$ to $u_8$	0.6864
<i>Group – 3</i>	$\Delta\omega_9$ to $u_3$	0.3465
<i>Group – 4</i>	$\Delta\omega_4$ to $u_{10}$	1.0

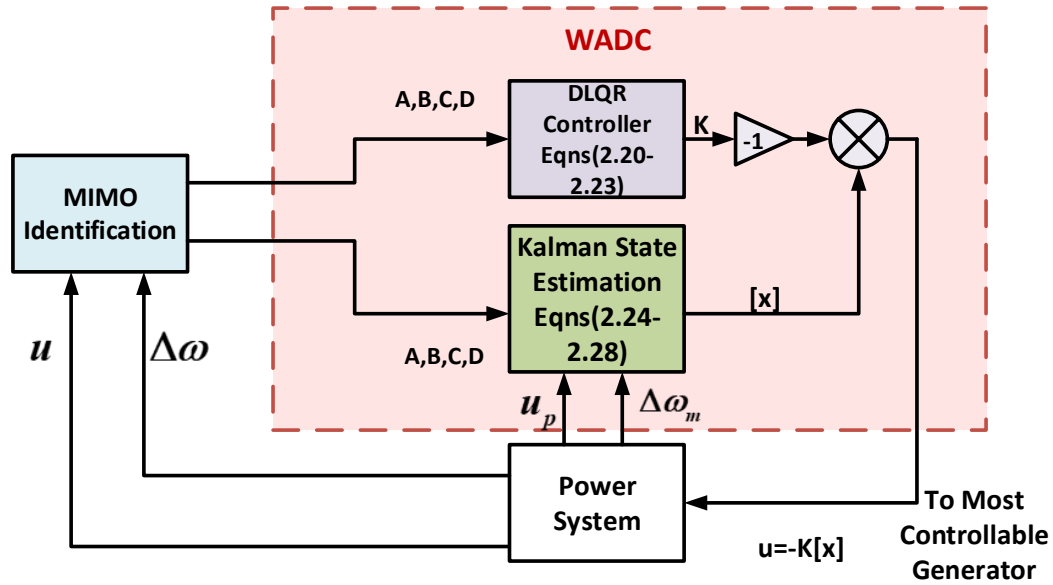


Fig. 2.15. WADC architecture

## 2.6 Model-free DLQR and Kalman filter design

The WADC design is based on DLQR and KF. The WADC design architecture is as shown in Fig. 2.15.

### 2.6.1 Discrete-time linear quadratic regulator

The DLQR based controller uses state-space matrices corresponding to the optimal control loop for calculating the control gain. For this the discrete state space model is extracted from the MIMO transfer functions (2.13) and represented as follows:

$$x_{k+1} = A_k x_k + B_k u_k \quad (2.19)$$

$$y_k = C_k x_k + D_k u_k$$

where  $A$ ,  $B$ ,  $C$ , and  $D$  are the state, input, output, and feedforward matrices respectively. The objective of the DLQR is to minimize the cost of the objective function

represented as (2.20), where  $R = \rho I (\rho > 0)$ ,  $Q = C_k^T C_k$  are the weight matrices and  $N$  is the number of samples. The cost function can be minimized by calculating optimal control gain  $K$  by solving (2.22)-(2.23). The  $P$  in (2.22) is the solution of the discrete algebraic Ricatti equations represented as (2.23). The optimal control signal is represented as (2.21) [127]. The optimal control signal is sent to most controllable generator estimated from residue analysis.

$$J = \sum_{k=0}^N (x_k^T Q x_k + u_k^T R u_k) \quad (2.20)$$

$$u_k = -K_k x_k \quad (2.21)$$

$$K_k = (R + B_k^T P_{k+1} B_k)^{-1} B_k^T P_{k+1} A_k \quad (2.22)$$

$$P_{k-1} = Q + A_k^T P_k A_k - A_k^T P_k B_k (R + B_k^T P_k B_k)^{-1} B_k^T P_k A_k \quad (2.23)$$

Table 2.6  
Estimated LQR gains ( $K$ ) for two-area system

Control Loop	Gain (K)
$\Delta\omega_3$ to $u_2$	[-0.0077 0.0379 -0.0022 0.0570 -0.1733 0.0416 0.0933]
$\Delta\omega_3$ to $u_4$	[0.1897 -0.0656 -0.1852 0.0454 -0.0402 -0.0300 0.1810]

For a 7<sup>th</sup> order control loops, Table 2.6 shows the estimated optimal control gains for two-area system. Table 2.7 and Table 2.8 shows the optimal control gains for 39-bus system Case 1 and 2 respectively.

Table 2.7  
Estimated LQR gains ( $K$ ) for IEEE 39 bus system (Case:1)

Control Loop	Gain ( $K$ )
$\Delta\omega_9$ to $u_4$	[0.0041 -0.0065 -0.0029 0.0295 -0.0407 0.0233 -0.0190]
$\Delta\omega_{10}$ to $u_9$	[-0.0467 0.1225 -0.2635 0.2954 -0.1783 0.0519 -0.0188]
$\Delta\omega_2$ to $u_3$	[0.3510 -0.4969 0.4490 0.0186 -0.2645 0.1415 -0.0743]
$\Delta\omega_6$ to $u_{10}$	[-0.0296 0.0884 -0.2031 0.2372 -0.1477 0.0448 -0.0188]

Table 2.8  
Estimated LQR gains ( $K$ ) for IEEE 39 bus system (Case:2)

Control Loop	Gain ( $K$ )
$\Delta\omega_1$ to $u_7$	[-0.1659 0.6799 -0.8777 0.5350 -0.3312 0.1834 -0.0405]
$\Delta\omega_4$ to $u_8$	[-0.0919 0.3275 -0.4145 0.2566 -0.1636 0.0935 -0.0207]
$\Delta\omega_9$ to $u_3$	[-0.0858 0.3297 -0.4227 0.2606 -0.1645 0.0931 -0.0207]
$\Delta\omega_4$ to $u_{10}$	[-0.0445 0.1546 -0.1984 0.1249 -0.0807 0.0465 -0.0104]

### 2.6.2 Kalman filtering based state estimation

The optimal control signal in (2.21) is the product of the optimal control gain and states of the system corresponding to the optimal control loop. Here, KF technique is adapted to estimate the states of the system. The state space model as shown in (2.19) is used to estimate the states. The predictor step and co-variance calculation is given by (2.24) and (2.25) respectively.

$$x_{k+1} = A_k x_k + B_k u_k \quad (2.24)$$

$$L_k = A_k L_{k-1} A_k^T + Q_k \quad (2.25)$$

where  $Q$  and  $L$  are co-variance of noise and state vector estimate respectively. The the Kalman gain factor ( $G$ ) is estimated as shown in (2.26)

$$G_k = L_k H_k^T (H_k L_k H_k^T + R_k)^{-1} \quad (2.26)$$

where  $R$  and  $H$  are co-variance of measurement noise and and the observation matrix respectively. Finally, the corrector step is represented as shown in (2.27) and (2.28).

$$x_k = x_{k+1} + G_k(z - Hx_k + 1) \quad (2.27)$$

$$L_k = L_{k+1} - K_k H_k L_{k+1} \quad (2.28)$$

Further details of kalman filtering based state estimation are reported in [126].

## 2.7 Simulation Results

The output of WADC is sent to the most controllable generator as shown in Fig. 2.15. The overall architecture is implemented to damp inter-area oscillations in two-area and IEEE 39 bus system models during various disturbances.

### 2.7.1 Simulation results of two-area system

The wide area control loop for the two-area system is as shown in Fig. 2.16. Fig. 2.17 shows the speed deviation of generator 2 with and without WADC. Fig. 2.18 shows the speed deviation of generator 4 with and without WADC. Fig. 2.19 shows the WADC output sent to generator 2 and 4. From the above figures, it can be observed that the with the proposed approach the oscillations are damped effectively. Table 2.9 shows the comparison of performance metrics with and without WADC.

The speed deviation value for generator-2 without WADC at 11s after disturbance is 0.01773 whereas with WADC the value is 0.0038. This indicates that there is 78.68% reduction in oscillation magnitude. In the same way for generator-4 there is 72.60% reduction in oscillation magnitude. Further area under the curve for the absolute value of oscillations is analyzed as shown in Table 2.10 and found that for generator-2 the area under the curve is 66% less with WADC and for generator-4 it is 56% less.

Table 2.9  
Performance metrics for two-area system

Variable	Without WADC	With WADC
Peak $\Delta\omega_2$ at 15s (Fig. 2.17)	0.01773	0.0038
Peak $\Delta\omega_4$ at 14.25s (Fig. 2.18)	0.0413	0.0113

Table 2.10  
Area under the curve for two-area system

Variable	Without WADC	With WADC
$\Delta\omega_2$ (Fig. 2.17)	0.4817	0.1638
$\Delta\omega_4$ (Fig. 2.18)	0.6959	0.3012

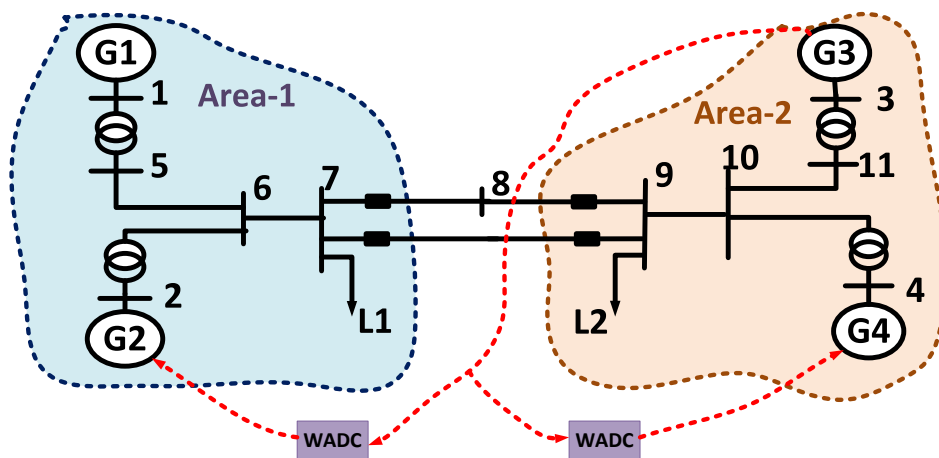


Fig. 2.16. Optimal control loop for two-area system

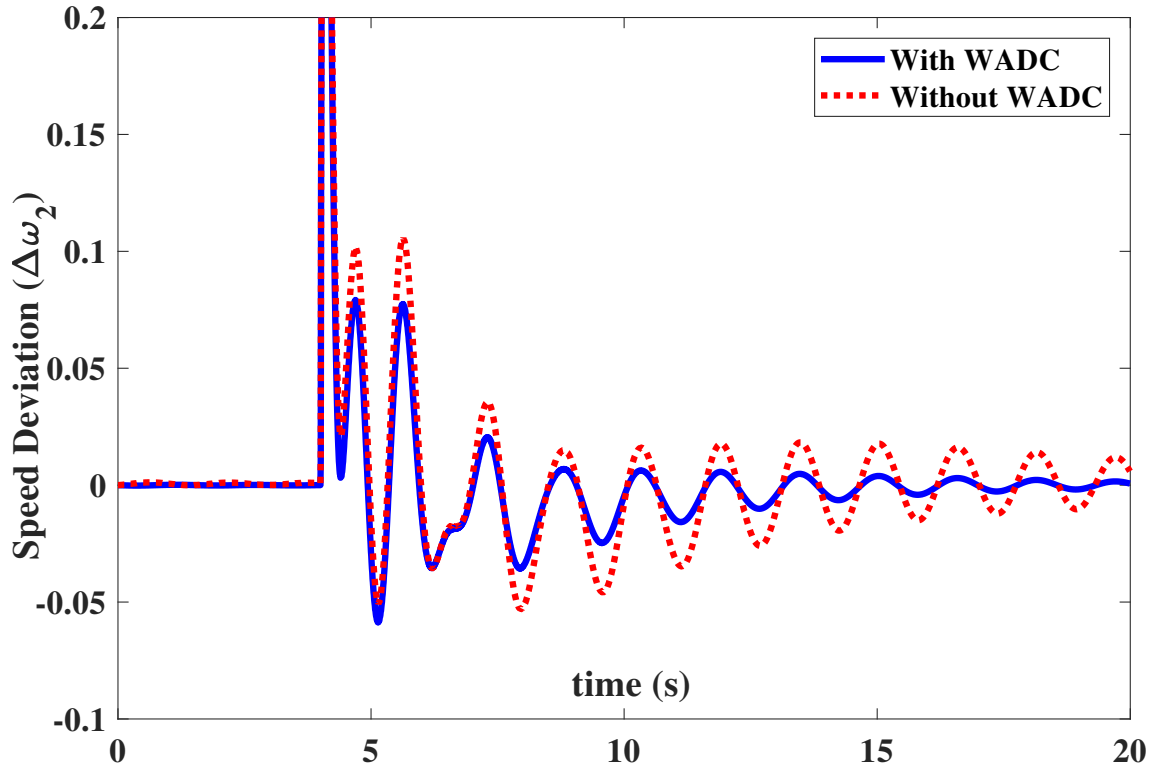


Fig. 2.17. Generator-2 speed deviation (rad/s)

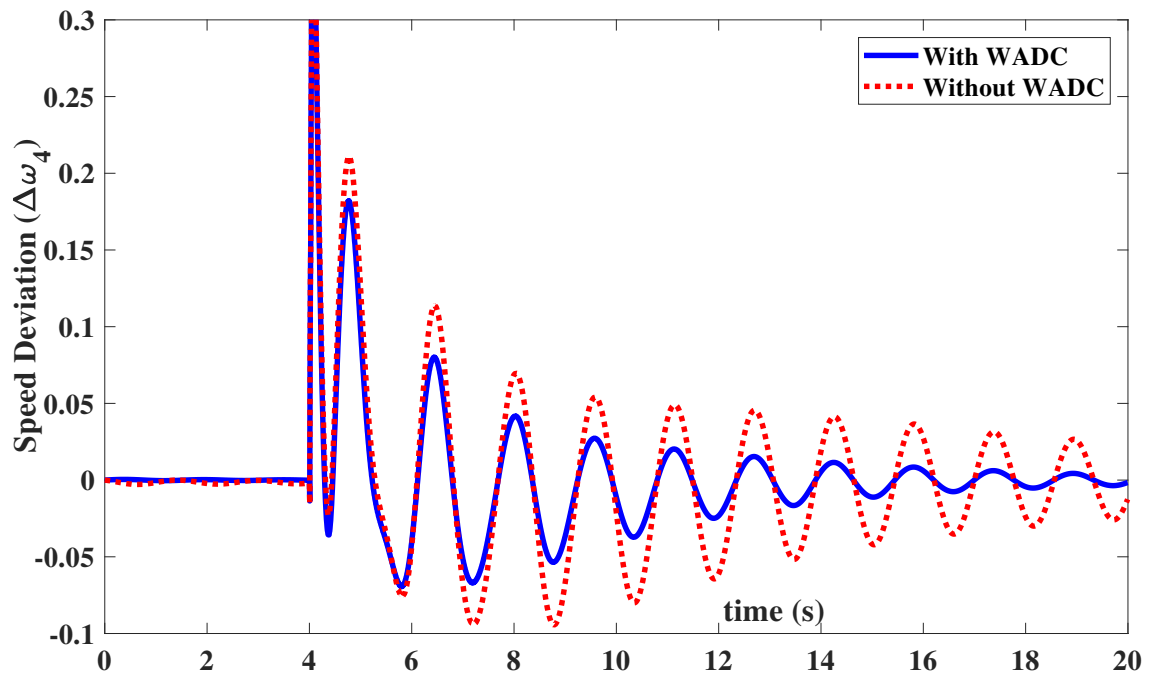


Fig. 2.18. Generator-4 speed deviation (rad/s)

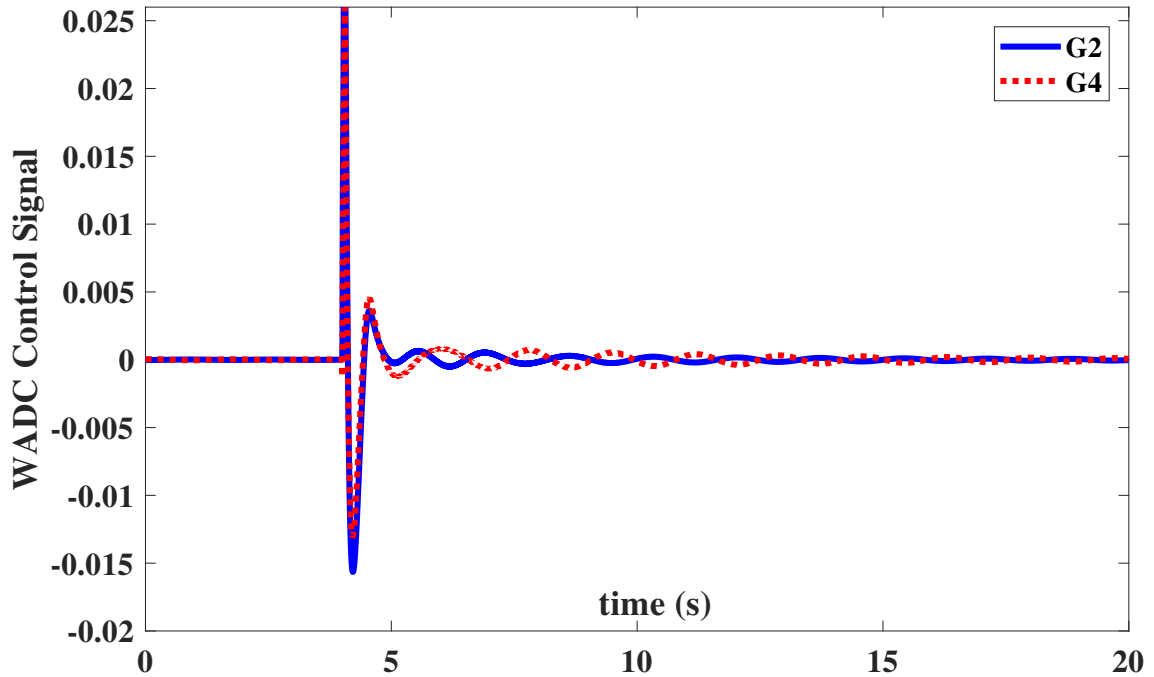


Fig. 2.19. WADC output signal

### 2.7.2 Simulation results of 39 bus system

For this system two cases are analyzed for different disturbances.

#### 2.7.3 Case:1

For the same disturbance scenario as discussed in Section 7.5.1.1, Fig. 2.20, Fig. 2.21, Fig. 2.22, and Fig. 2.23 shows the speed deviations of generator 3, 4, 9, and 10 with and without WADC respectively. Fig. 2.23 shows the WADC output sent to the most controllable generator. From the above figures, it can be seen that with the proposed approach the oscillations are damped effectively. The area under the curve for the absolute value of speed deviations are analyzed as shown in Table 2.11 and it is found that the area under the curve is reduced by 56%, 59%, 54%, and 60.56% with WADC for generators 3, 4, 9, and 10 respectively.

Table 2.11  
Area under the curve metric (39 bus system case:1)

Variable	Without WADC	With WADC
$\Delta\omega_3$ (Fig. 2.20)	6.4002	2.5803
$\Delta\omega_4$ (Fig. 2.21)	6.3374	2.7498
$\Delta\omega_9$ (Fig. 2.22)	6.4669	2.9669
$\Delta\omega_{10}$ (Fig. 2.23)	6.3081	2.4878

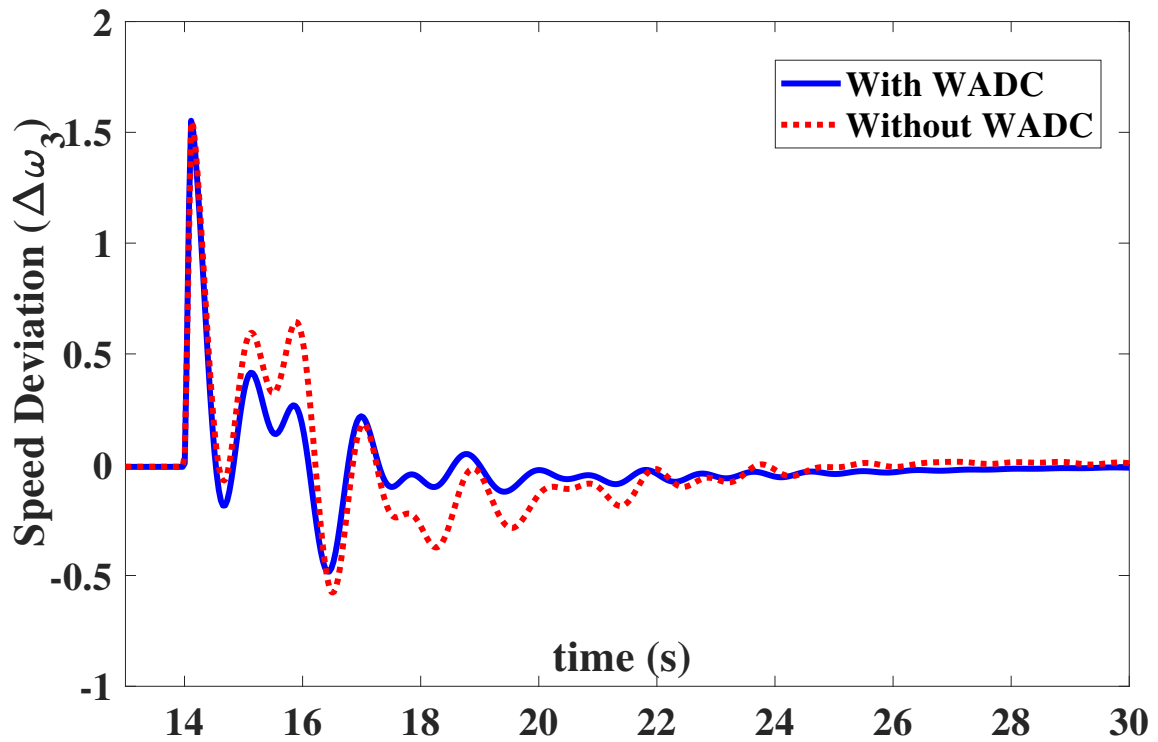


Fig. 2.20. Generator-3 speed deviation (rad/s)

#### 2.7.4 Case:2

For the same disturbance scenario as discussed in Section 7.5.1.2, Fig. 2.25, Fig. 2.26, Fig. 2.27, and Fig. 2.28 shows the speed deviations of generator 3, 7, 8, and 10 with and without WADC respectively. Fig. 2.29 shows the WADC output sent to the most controllable generator. From the above figures, it can be seen that the with the proposed approach the oscillations are damped effectively. The area under

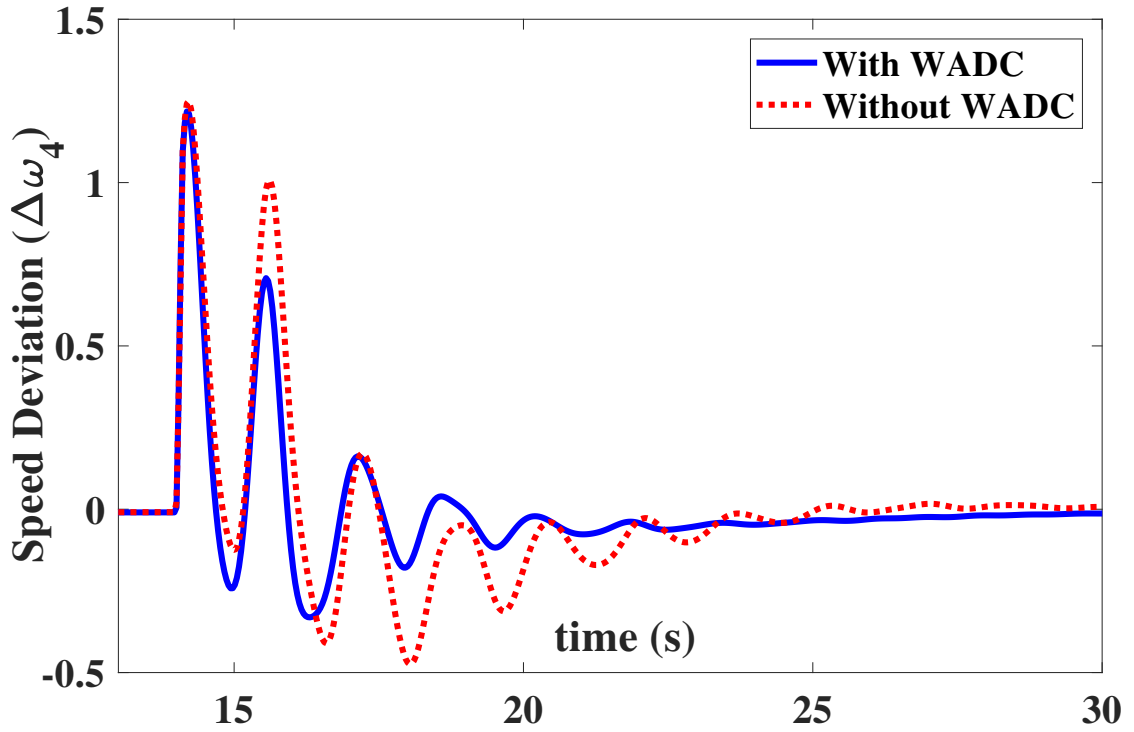


Fig. 2.21. Generator-4 speed deviation (rad/s)

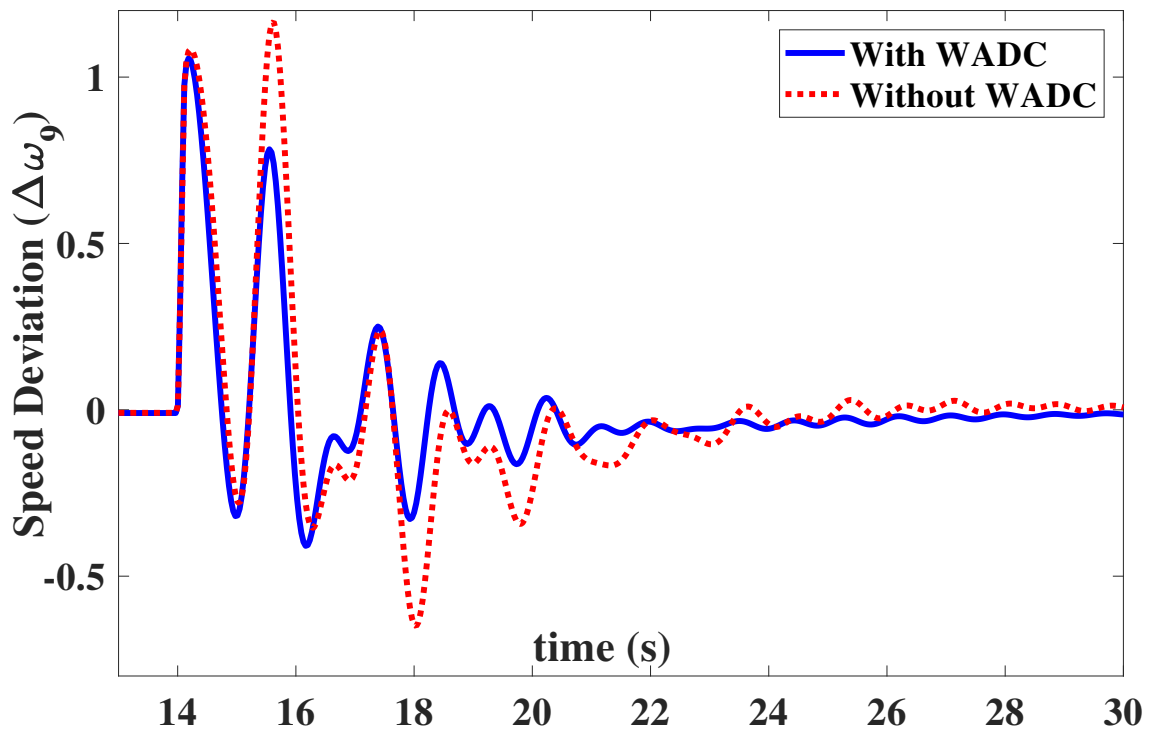


Fig. 2.22. Generator-9 speed deviation (rad/s)

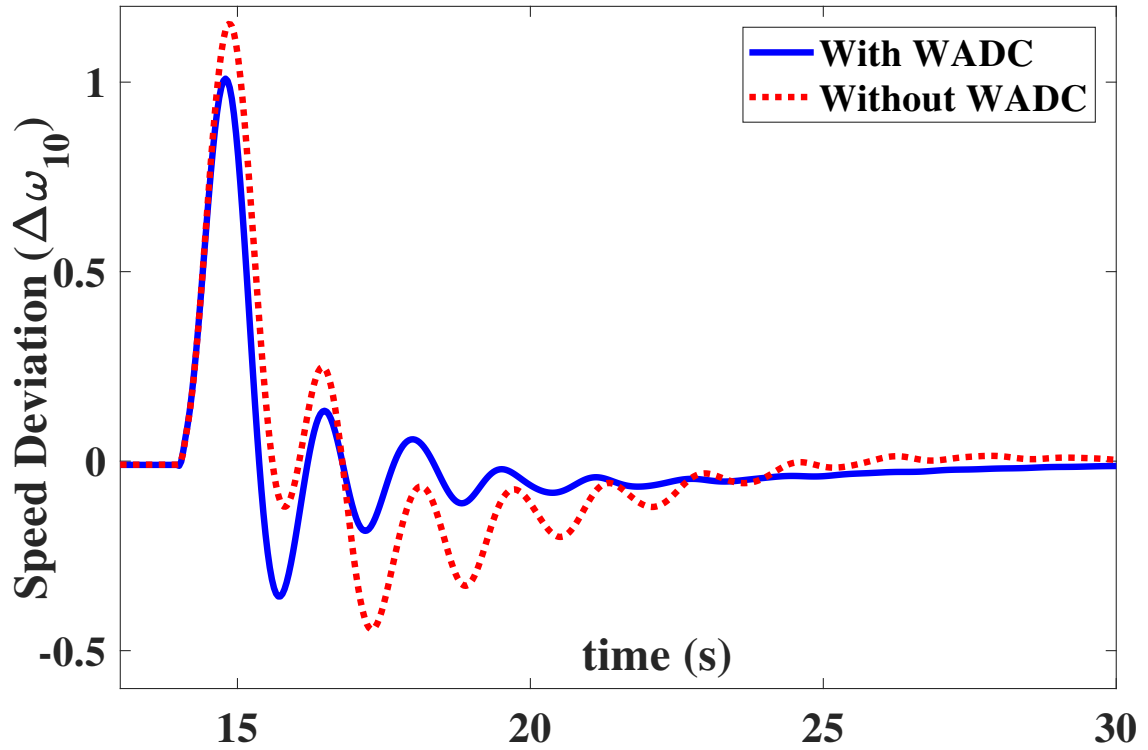


Fig. 2.23. Generator-10 speed deviation (rad/s)

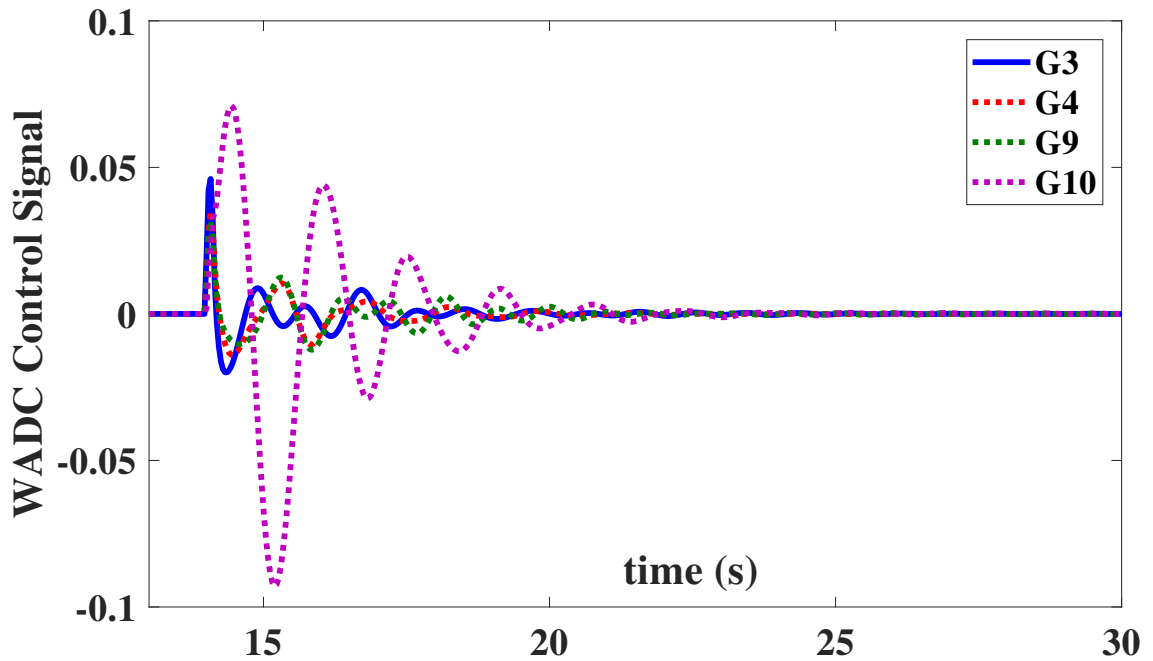


Fig. 2.24. WADC output signal

the curve for the absolute value of speed deviations are analyzed as shown in Table 2.12 and it is found that the area under the curve is reduced by 55%, 54%, 60%, and 56% with WADC for generators 3, 7, 8, and 10 respectively.

Table 2.12  
Area under the curve metric (39 bus system case:2)

Variable	Without WADC	With WADC
$\Delta\omega_3$ (Fig. 2.25)	3.477	1.5355
$\Delta\omega_7$ (Fig. 2.26)	3.746	1.7233
$\Delta\omega_8$ (Fig. 2.27)	3.3801	1.3258
$\Delta\omega_{10}$ (Fig. 2.28)	3.5383	1.5359

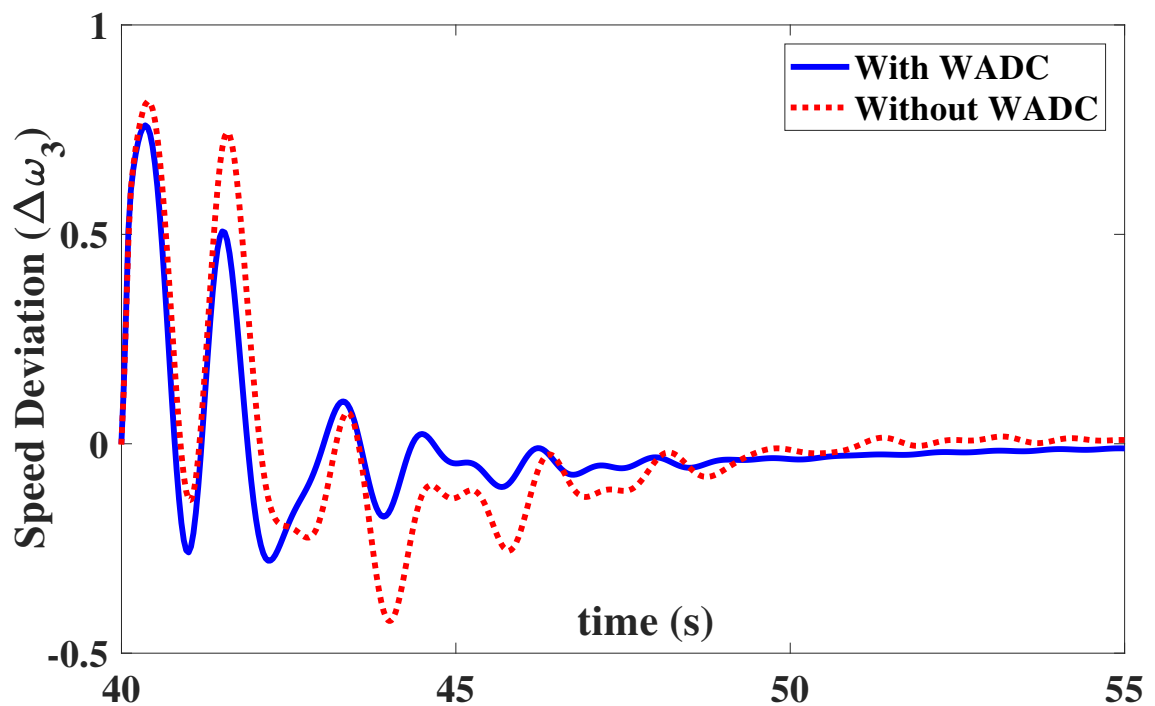


Fig. 2.25. Generator-3 speed deviation (rad/s)

## 2.8 Summary

The proposed method for model-free wide-area damping of inter-area oscillations based on MIMO identification overcome the drawbacks of earlier linearization based

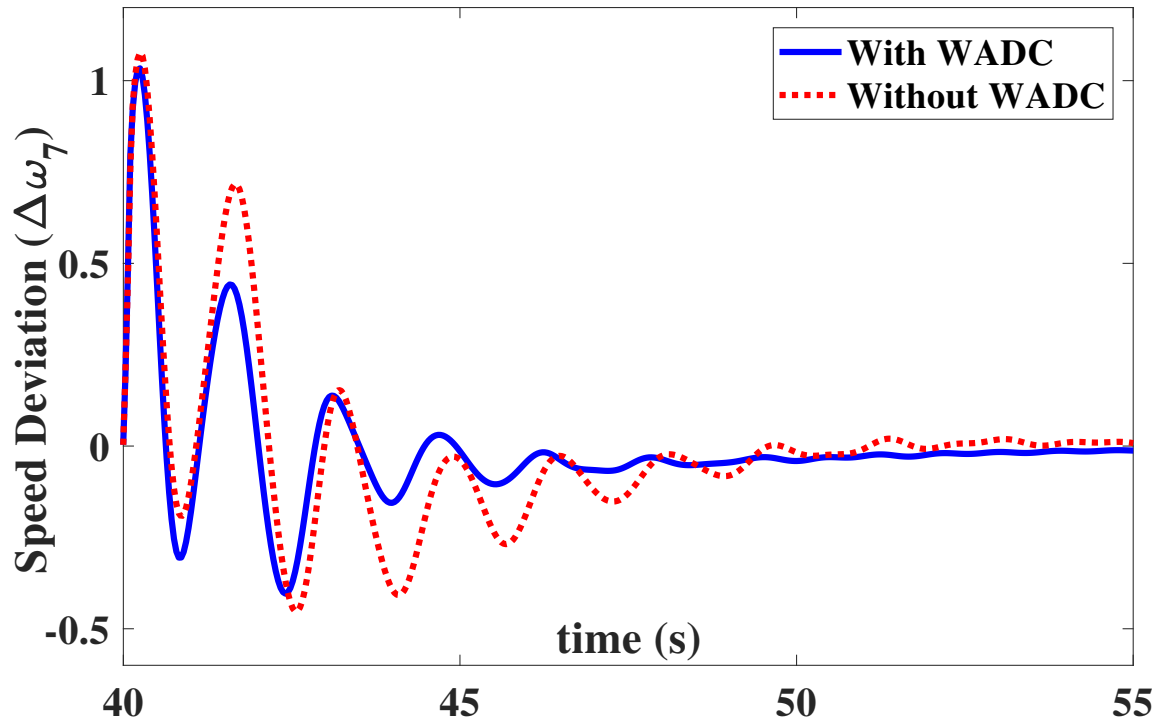


Fig. 2.26. Generator-7 speed deviation (rad/s)

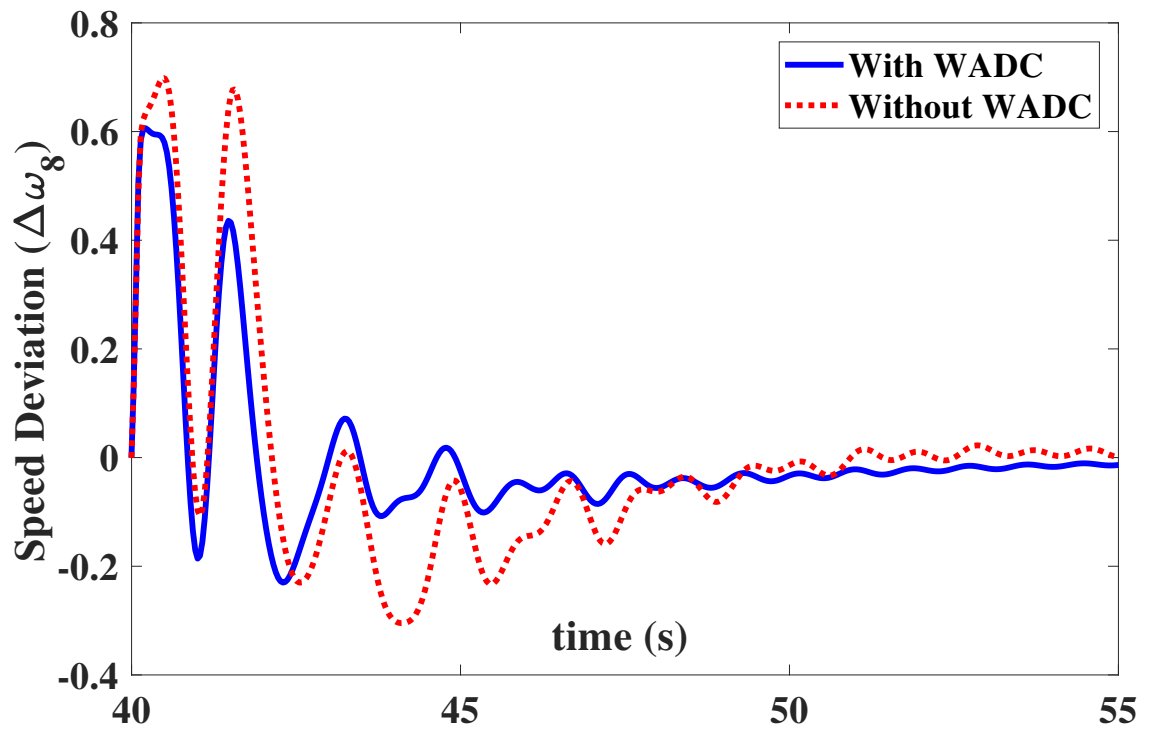


Fig. 2.27. Generator-8 speed deviation (rad/s)

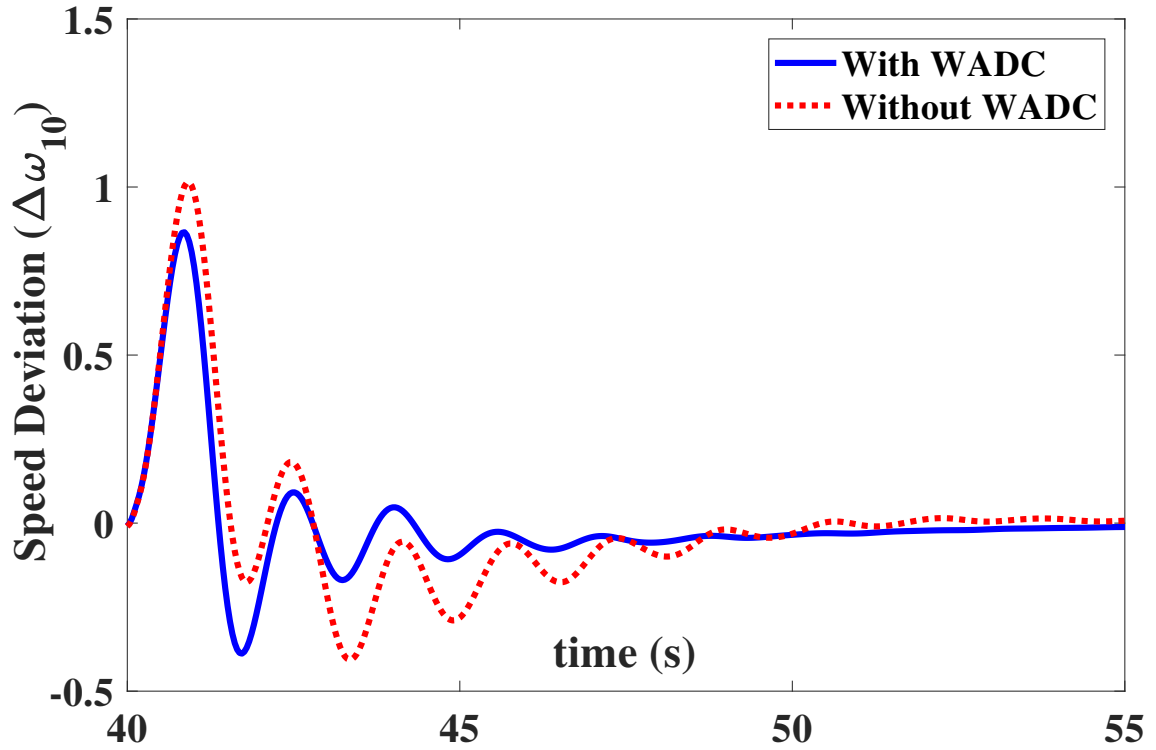


Fig. 2.28. Generator-10 speed deviation (rad/s)

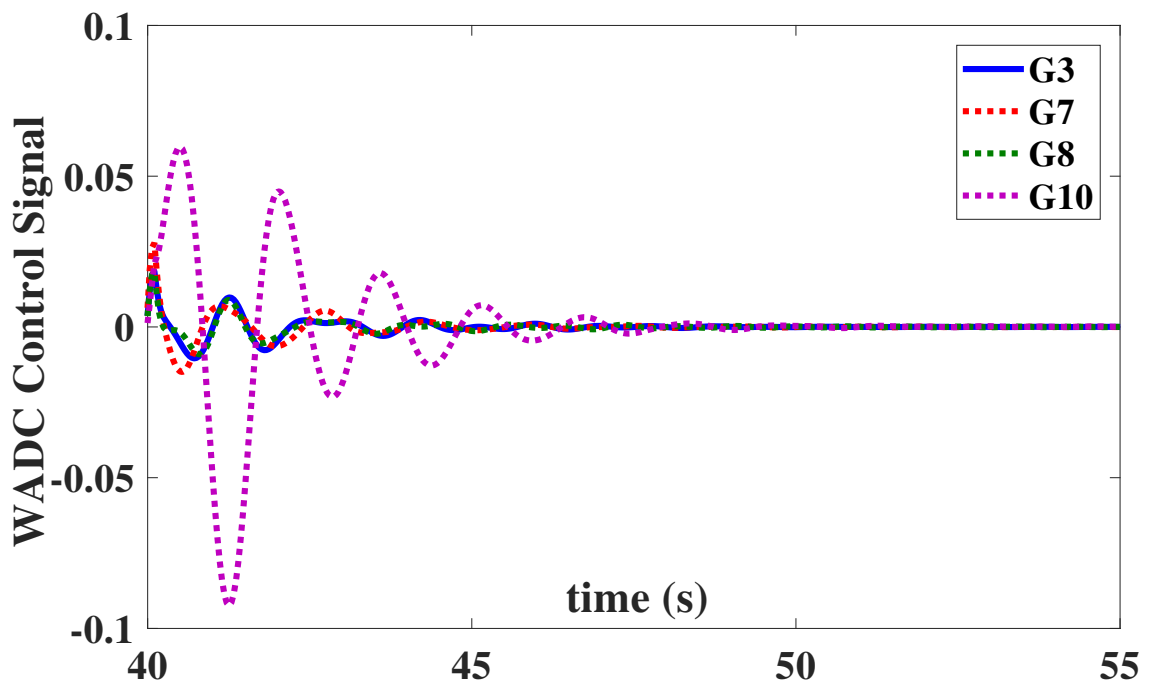


Fig. 2.29. WADC output signal

methods reported in the literature. In this approach, initially MIMO system transfer functions are identified, then the inter-area modes are estimated using the MIMO transfer functions. The optimal control loop required for WADC is estimated through residues corresponding to the inter-area mode of interest. Finally, the WADC is design based on a combination of DLQR and Kalman filtering algorithms. The efficacy of the proposed architecture is verified by implementing on two-area, and IEEE 39 bus power system models on RTDS/RSCAD and MATLAB based real-time co-simulation platform. In the next chapter, coherency and online signal selection based wide-area control of wind integrated power grid is proposed.

## CHAPTER 3: COHERENCY AND ONLINE SIGNAL SELECTION BASED WIDE AREA CONTROL OF WIND INTEGRATED POWER GRID

This chapter extends the design of WAC based on a discrete Linear Quadratic Regulator (DLQR) and Kalman filtering based state-estimation that can be applied for real-time damping of inter-area oscillations of wind integrated power grid. The main advantages of the proposed architecture are a) online coherency grouping that accurately characterizes real-time changes in the power grid, and b) online wide-area signal selection based on residue method for proper selection of the WAC signals. The proposed architecture can thus accurately monitors changes in the power grid and select the appropriate control signal for more effectively damping the inter-area oscillation when compared to the conventional local signal based Power System Stabilizers (PSS) or offline based WAC designs. The architecture is tested on a wind integrated two-area system and IEEE 39 bus system to show the capability of the proposed method.

### 3.1 Introduction

Interconnected power systems exhibit dominant inter-area oscillations with the frequency of oscillation between 0.1-0.8 Hz [56]. During inter-area oscillations, coherent generators tend to swing together in groups against other groups based on changes in system conditions [20]. Inter-area oscillations pose significant problems in the operation of the power system as it limits the power transfer capability of tie-lines and

also deteriorates power system security [84]. To suppress the inter-area oscillations, power system stabilizers (PSS) have been designed. PSS provides supplementary damping through synchronous generator exciters [91], high-voltage direct current (HVDC) links [12], and flexible alternating current transmission systems (FACTS) devices [121].

Conventional damping controllers are designed considering specific operating conditions that are typical for the power system [48]. The effectiveness of such controllers decreases when the actual operating conditions of the power system deviate from the specified conditions used for the design of such damping controllers. With the increase in integration of renewable energy to the grid, the operating conditions of power grid change more frequently especially due to the variability in the power output of these renewable resources. Under such variable operating conditions, local robust damping controllers fail to perform well. The conventional damping controllers reported in the literature are discussed in Section 1.3.4.

Due to the recent developments in wide-area measurement system (WAMS), adaptive damping controller design has drawn a lot of attention. Work performed in [68], [130] and development of algorithms for applying system identification techniques in power system [86] are critical in these aspect. However, most of the research till now is focused on the tuning of local adaptive controllers while the issue of coordination among all the controller is not addressed well yet. It is worth noting that both the adaptive design of local individual controller and the coordination between different controllers can be achieved simultaneously through a properly designed WAC.

There are two significant challenges in designing an effective real-time WAC. First,

there should be a robust method for obtaining a fast online model of the power system that can capture all low-frequency oscillation modes, and second, there should be an online method for selecting most observable and controllable signals for the control loop. For successfully managing these challenges, an online coherency grouping method is required, as such grouping reduces the number of signals to be monitored for the design of WAC [67]. The reduction in the number of signals decreases computation burden and at the same time facilitates online design and implementation of the WAC. The coherency grouping based on modal and measurement based methods are discussed in Section 1.3.2.1 and 1.3.2.2. Significant advances on applications of system identification on power system are also discussed in Section 1.3.1.2.

In this chapter [110], three major novel contributions are proposed. First, an online computationally robust coherency grouping of machines is performed based on spectral clustering which uses measurement signals for grouping. This method considers the current system operating condition. To overcome the computational burden and to reduce the execution time, only the slow eigenvalues of the Laplacian matrix are used for clustering. Second, the control/loop for WAC is selected based on residue analysis of gain matrix formulated online using MIMO identification which considers the changes in operating conditions of the system. Third, a novel controller is designed based on discrete LQR and state estimation using Kalman filtering. The efficacy of the proposed method is verified by evaluating the performance of the architecture to damp the inter-area oscillations on a WTG successfully integrated two-area and IEEE 39 bus system models in real-time using RSCAD/RTDS real-time digital simulator. To summarize, the major contributions of this work are:

- A new coherency grouping method based on online spectral clustering.
- A new method for online selection of wide-area control loop using MIMO identification.
- A novel method for WAC based on discrete LQR and state estimation using Kalman filtering.

The rest of the chapter is organized as follows: In Section 3.2 the proposed framework for the online WAC design is discussed. In Section 3.3, the results on a power grid using two-area test system and IEEE 39-bus system are discussed and Section 3.4 summarizes the chapter.

### 3.2 Proposed Framework for the Online Wide Area Controller

The proposed framework for the online WAC design involves the following steps: a) coherency grouping algorithm, b) signal selection algorithm for WAC based on residue approach and, c) WAC design algorithm. The architecture for the proposed framework is as shown in Fig. 3.5

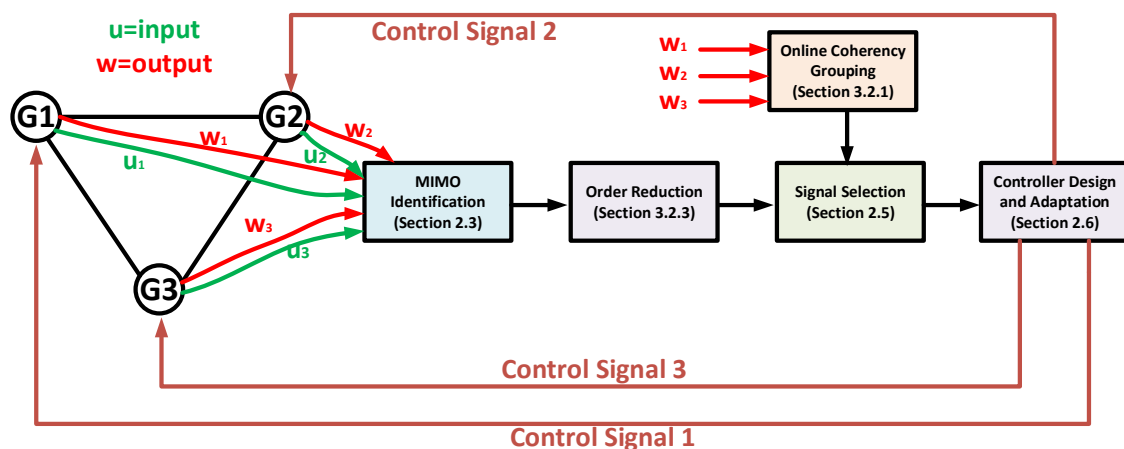


Fig. 3.1. The architecture of proposed framework

### 3.2.1 Proposed coherency grouping algorithm

In this approach coherency grouping of generators is performed based on spectral clustering using measured data points which is the speed of the generators. Data points  $x_1, x_2, \dots, x_n$  for a window length of  $n$  are considered for clustering. Further, using the data points a similarity matrix  $S \subseteq R^{nn}$  is formulated, where  $S_{ij}$  gives the relation between  $x_i$  and  $x_j$ . The similarity matrix information is used to group  $x_1, x_2, \dots, x_n$  into  $k$  clusters. The similarity matrix is based on a Gaussian function represented as in (7.1)

$$S_{ij} = e^{\left(-\frac{\|x_i - x_j\|}{2\sigma^2}\right)} \quad (3.1)$$

where  $\sigma$  is a scaling factor. Here  $S$  is dense and is of the order  $n \times n$ . The size of  $S$  increases with increase in the number of data points under consideration, but this slows the simulation speed. To increase the online clustering speed Nystrom method is used which uses sub-matrix of the dense matrix  $\mathbf{S}$ . Let a sub-matrix  $\mathbf{A}$  of the dense matrix  $\mathbf{S}$  can be represented as an  $l \times l$  matrix (where  $l \ll n$ ), sub-matrix  $\mathbf{B}$  as  $l \times (n - l)$  matrix, and  $\mathbf{C}$  as  $(n - l) \times (n - l)$  matrix. Upon rearranging the columns and rows  $\mathbf{S}$  can be represented as

$$\mathbf{S} = \begin{bmatrix} \mathbf{A} & \mathbf{B} \\ \mathbf{B}^T & \mathbf{C} \end{bmatrix}, \mathbf{W} = \begin{bmatrix} \mathbf{A} \\ \mathbf{B}^T \end{bmatrix} \quad (3.2)$$

where  $\mathbf{A} \subseteq R^{l \times l}$ ,  $\mathbf{B} \subseteq R^{l \times (n-l)}$ , and  $\mathbf{C} \subseteq R^{(n-l) \times (n-l)}$ .  $S$  is approximated by Nystrom method using  $A$  and  $B$ . The approximation  $S$  is given in (7.3)

$$\mathbf{S} \approx \bar{\mathbf{S}} = \begin{bmatrix} \mathbf{A} & \mathbf{B} \\ \mathbf{B}^T & \mathbf{B}^T \mathbf{A}^{-1} \mathbf{B} \end{bmatrix} \quad (3.3)$$

The normalized laplacian matrix using the approximated similarity matrix  $\mathbf{S}$  can then be represented as (7.4)

$$\bar{\mathbf{L}} = \mathbf{I} - \mathbf{D}^{-\frac{1}{2}} \bar{\mathbf{S}} \mathbf{D}^{-\frac{1}{2}} \quad (3.4)$$

where  $\mathbf{D} = \sum_{j=1}^n \bar{S}_{ij}$  is a diagonal matrix. The decomposition of  $\bar{\mathbf{L}}$  gives the eigenvalues and corresponding eigenvectors according to (7.5).

$$\bar{\mathbf{L}} = \bar{\mathbf{V}} \bar{\mathbf{\Sigma}} \bar{\mathbf{V}}^T \quad (3.5)$$

where  $\bar{\mathbf{\Sigma}}$  contains eigenvalues, and  $\bar{\mathbf{V}}$  are the corresponding eigenvectors. If  $j$  slow eigenvalues are considered, then the eigenvectors corresponding to  $j$  eigenvalues, written as an  $R^{n \times j}$  matrix can be formulated as in (7.6)

$$\bar{\mathbf{V}} = [\vec{v}_1, \vec{v}_2, \dots, \vec{v}_j] \quad (3.6)$$

where  $\vec{v}_i \subseteq R^n, i = 1, \dots, j$  and  $j$  is the number of eigenvectors. The normalized eigenvector matrix can then be written as

$$\mathbf{U}_{im} = \frac{\bar{\mathbf{V}}_{im}}{\sqrt{\sum_{r=1}^k \bar{\mathbf{V}}_{ir}^2}}, i = 1, \dots, n \quad \text{and} \quad m = 1, \dots, j \quad (3.7)$$

The  $n$  rows of  $\mathbf{U}$  can easily be clustered into groups using the k-means method (see Algorithm 1). In Algorithm-1 the inner-loop repeatedly assigns each set of entities

$u_i$  to the closest cluster center  $\mu_j$ , and recalculate the new cluster center ( $\mu_j$ ) based on the statistical mean of the data points assigned to it. More details of k-means method can be found in [19, 77].

---

**Algorithm 3.1** K-means Algorithm

---

1) Given  $\mathbf{U} = \{u_1, u_2, \dots, u_n\}$  (set of entities to be clustered)

2) Select  $k$  initial cluster centers  $\mu_1, \mu_2, \dots, \mu_k \in \mathbb{R}$ .

**repeat**

a) For every  $i$ , set  $c_i = \operatorname{argmin}_j \|u_i - \mu_j\|^2$

b) For every  $j$ , set  $\mu_j = \frac{\sum_{i=1}^n 1_{\{c_i=j\}} u_i}{\sum_{i=1}^n 1_{\{c_i=j\}}}$

**until** converged

---

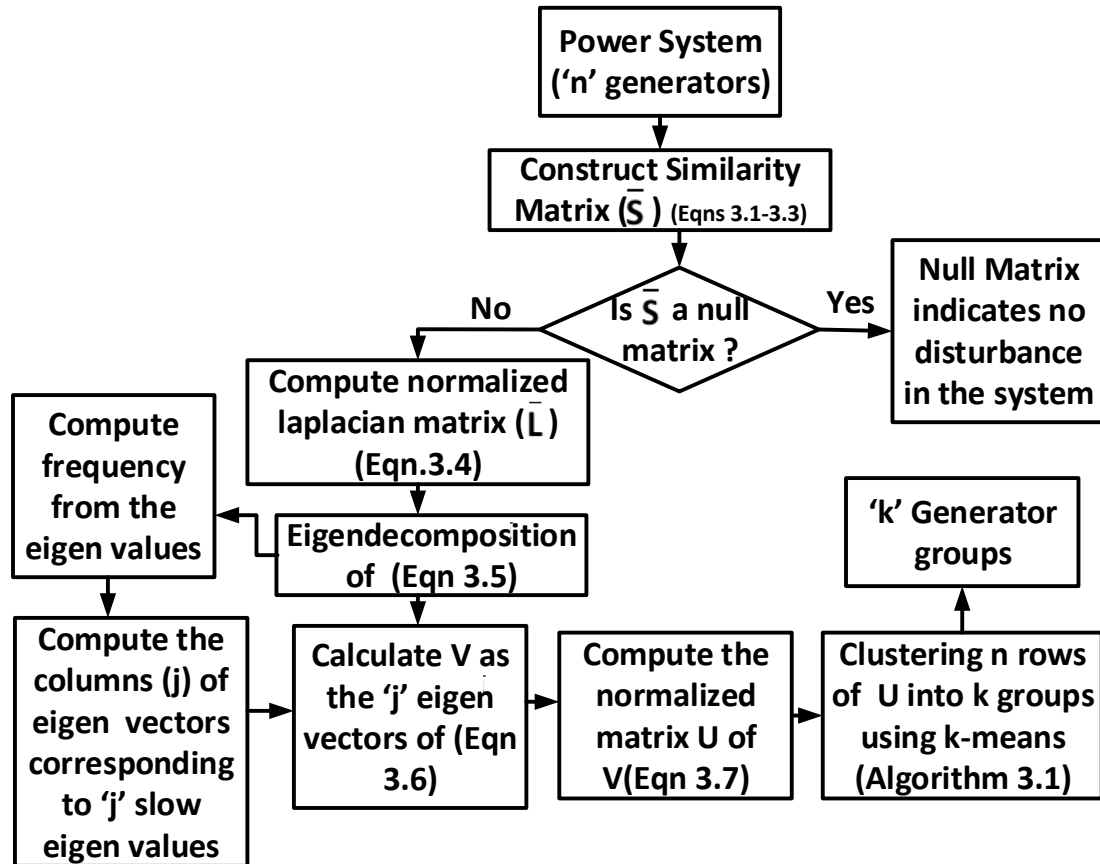


Fig. 3.2. Flow chart of the proposed coherency grouping algorithm.

Fig. 3.2 shows the flowchart of the proposed algorithm. The efficacy of the proposed algorithm is verified by implementing the architecture on Kundur two area (Fig. 3.3)

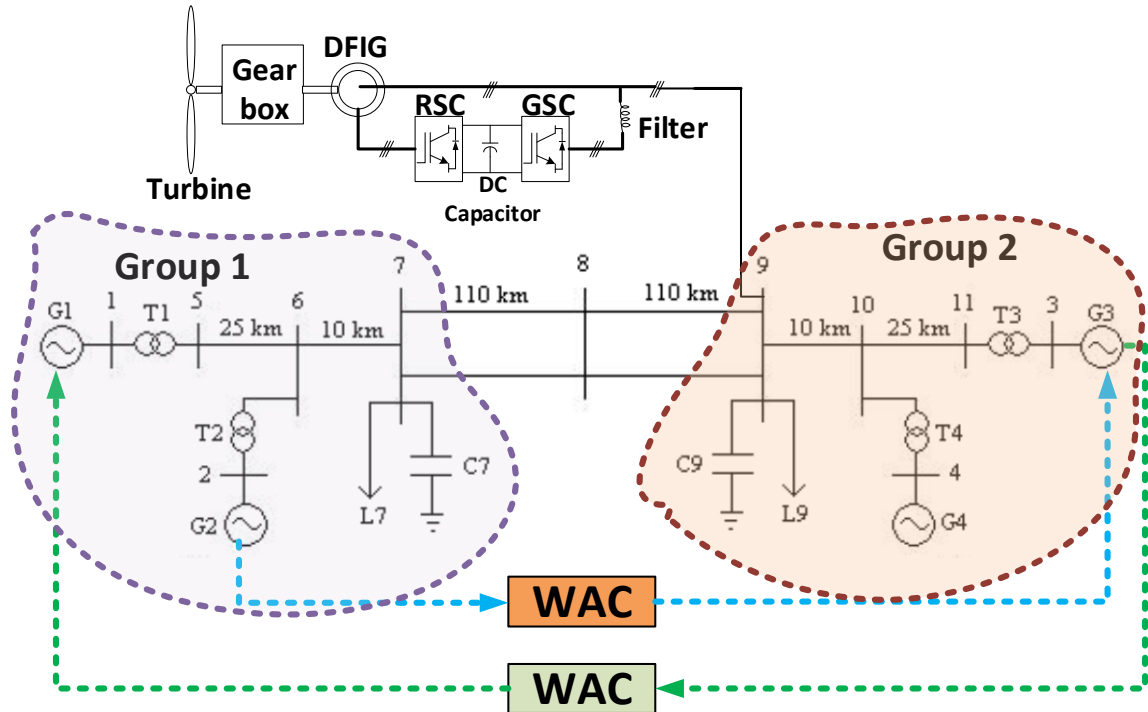


Fig. 3.3. Two-area study system model.

Table 3.1  
Comparison of coherency grouping methods

Test System	Slow Coherency	Spectral Clustering
Two Area	Group-1:1,2	Group-1:1,2
	Group-2:3,4	Group-2:3,4
	$t = 0.4826s$	$t = 0.021s$
IEEE 39-BUS	Group-1:4,5,6,7	Group-1:4,5,6,7,9
	Group-2:1,8,9	Group-2:1,8
	Group-3:2,3	Group-3:2,3
	Group-4:10	Group-4:10
	$t = 0.8138s$	$t = 0.0423s$

\* $t$  = Computational Time

and IEEE-39 bus power system models (Fig. 3.4), and then comparing the method with state-of-the-art offline, slow coherency based grouping. For the two-area system, a 3-ph fault is created on bus-9 for 0.1 sec. The coherent groups obtained based on

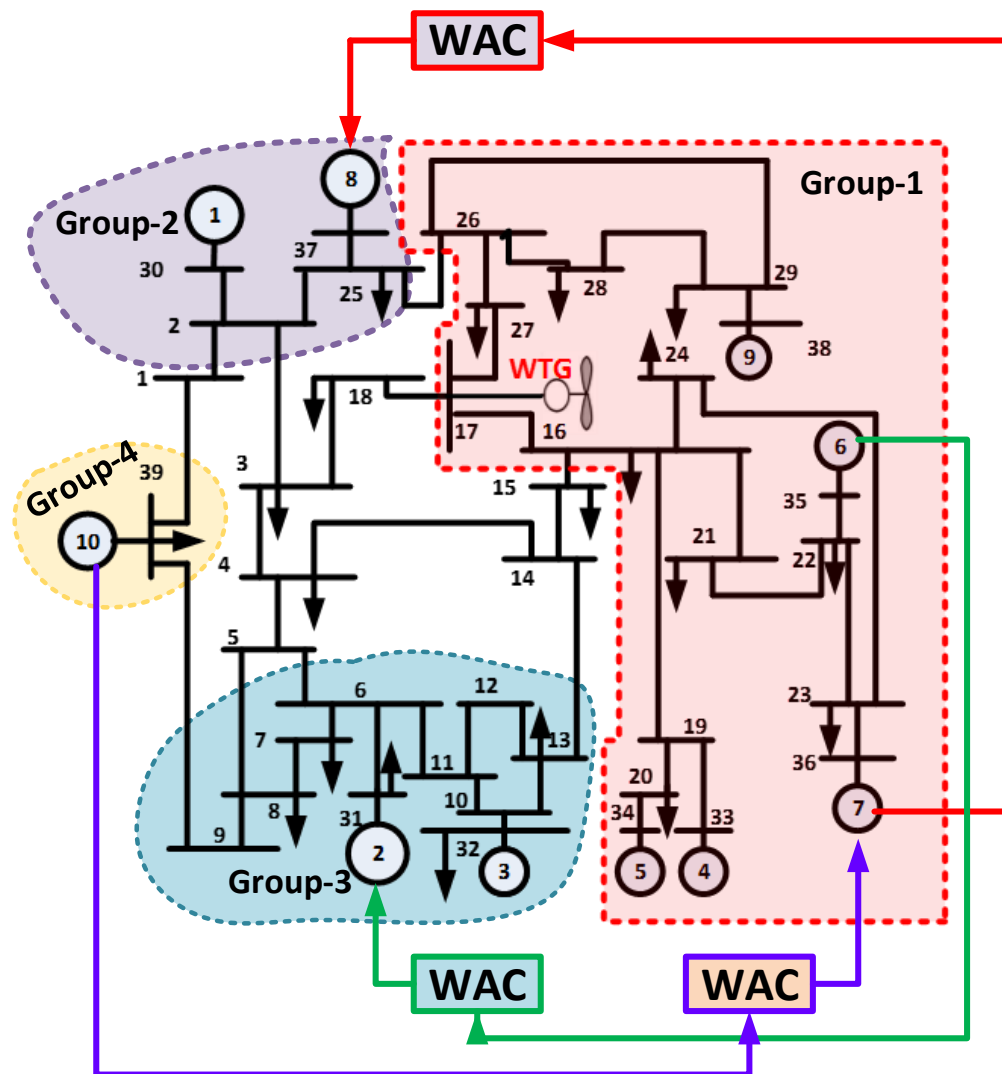


Fig. 3.4. IEEE-39 bus test system model (Fault on Bus-14).

the proposed algorithm and comparisons are shown in Table 3.1. It can be seen that the proposed online method provides the same grouping as an offline method but with lower computational time. Also, for IEEE 39 bus system, group 1 is different with generator 9 included in group 1. This is wrongly interpreted in the slow coherency method. Fig. 3.5 to Fig. 3.8 shows the comparison of coherency grouping for a fault on bus-14.

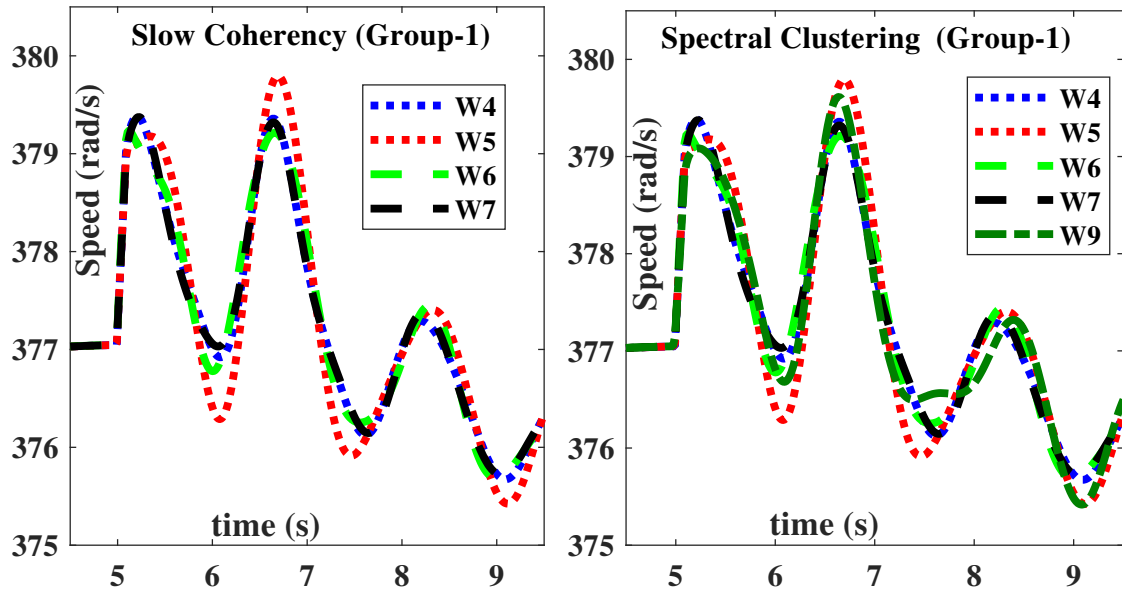


Fig. 3.5. Coherency group-1

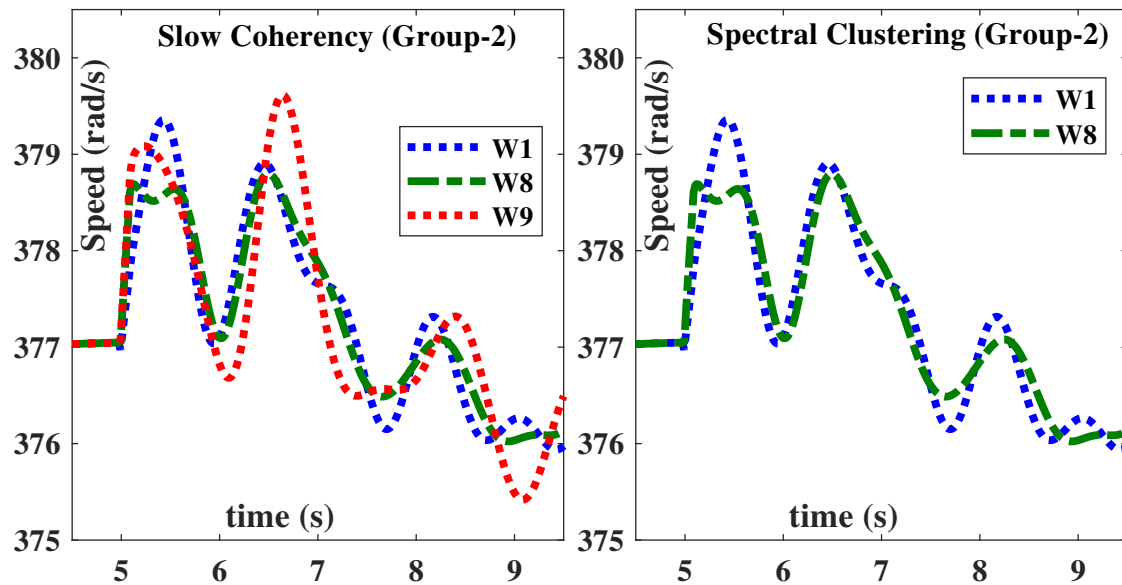


Fig. 3.6. Coherency group-2

Further to validate the algorithm for changing operating conditions in real-life, a sequence of disturbances are studied at various locations of the IEEE-39 bus system. For this, 3-ph faults are created for 0.1 sec at bus-14, bus-19, and bus-6 at 5, 31 and 61 sec respectively. Tables 3.2, 3.3, and 3.4 shows the coherency grouping comparison

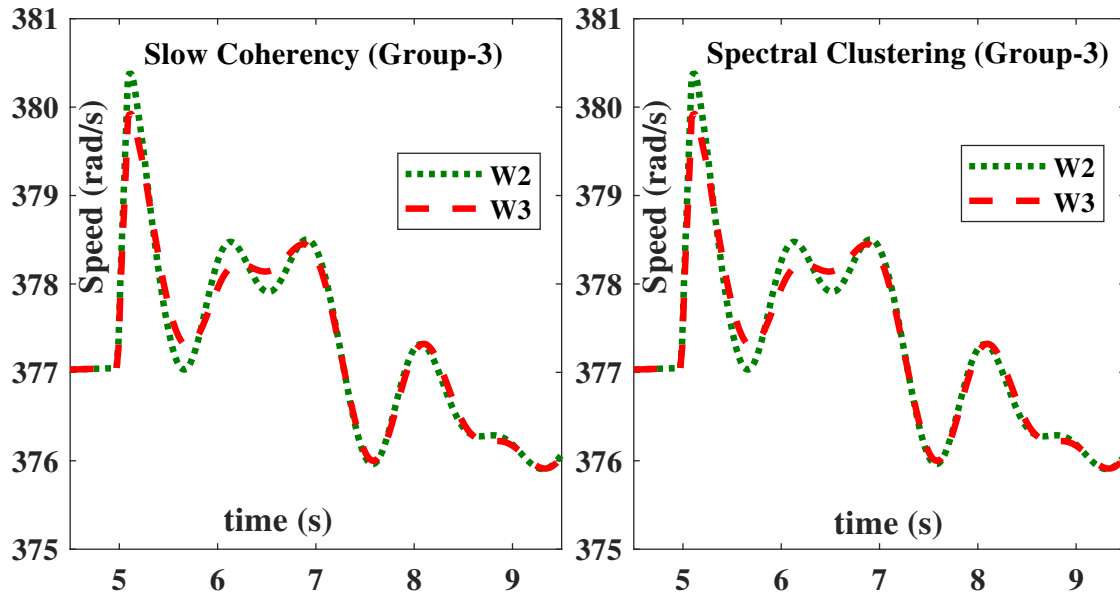


Fig. 3.7. Coherency group-3

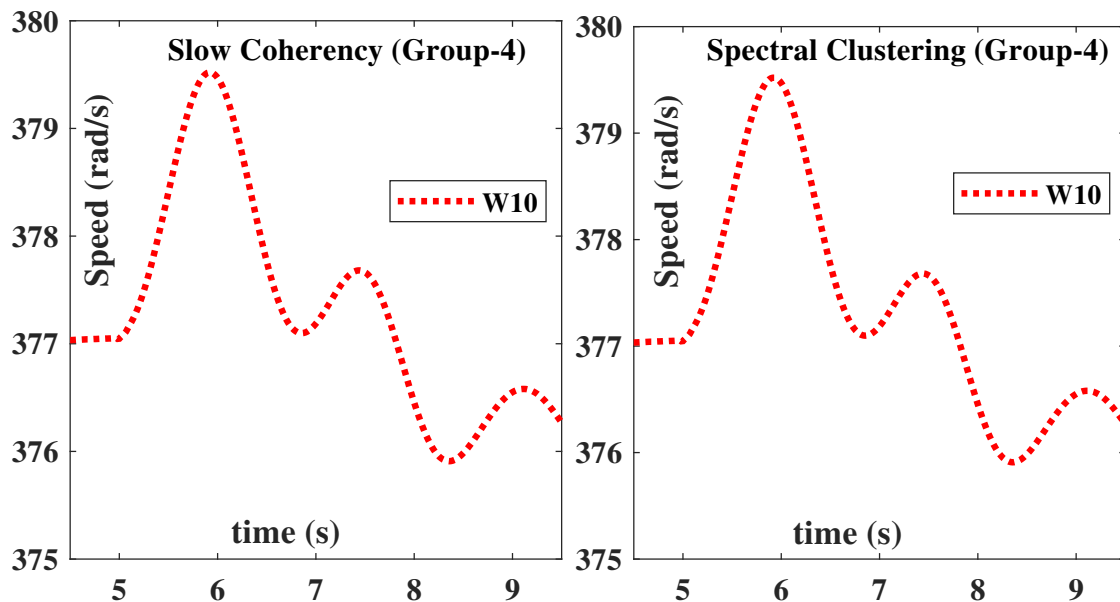


Fig. 3.8. Coherency group-4

of 39-bus system for various operating conditions. Fig. 3.9 shows the coherency grouping for various operating conditions for the IEEE-39 bus system. It can be observed that with the proposed coherency grouping method the generators can be grouped based on current operating condition whereas in offline methods like slow

coherency the generator grouping does not change irrespective of changing operating conditions. The dynamics observed at different operating conditions in Fig. 3.9 supports this statement. It is also worth noting that the computational time required for the proposed online coherency grouping method is much less confirming that the algorithm is feasible to implement on a real-life system.

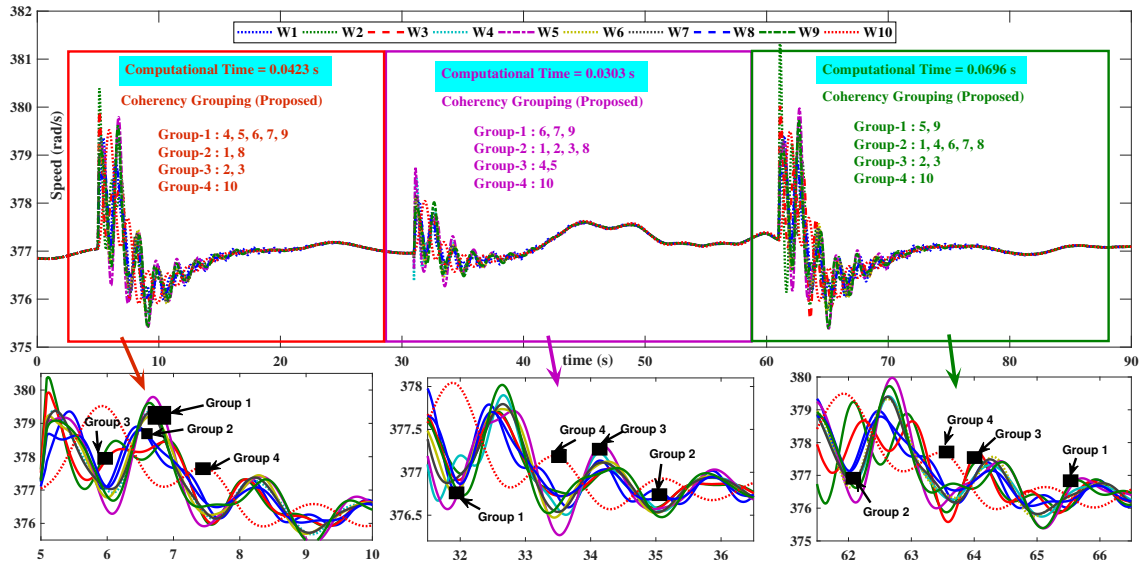


Fig. 3.9. Coherency grouping for different operating conditions.

Table 3.2

Coherency grouping of IEEE-39 bus system (spectral clustering) fault on bus-14

No of Clusters (k)	Groups
4	Computational Time = 0.0423s Group-1:4,5,6,7,9 Group-2:1,8 Group-3:2,3 Group-4:10

### 3.2.2 MIMO Identification

The MIMO identification and signal selection are discussed in Section 2.3 and 2.5 respectively.

Table 3.3  
Coherency grouping of IEEE-39 bus system (spectral clustering) fault on bus-19

No of Clusters (k)	Groups
4	Computational Time = 0.0303s Group-1:6,7,9 Group-2:1,2,3,8 Group-3:4,5 Group-4:10

Table 3.4  
Coherency grouping of IEEE-39 bus system (spectral clustering) fault on bus-6

No of Clusters (k)	Groups
4	Computational Time = 0.0696s Group-1:5,9 Group-2:4,6,7,8 Group-3:2,3 Group-4:10

Table 3.5  
Control loop based on residue approach

Type	Residue analysis using MIMO identification				Residue analysis of state space matrices			
	Group 1		Group 2		Group 1		Group 2	
Speed/Field voltage	$u_1$	$u_2$	$u_3$	$u_4$	$u_1$	$u_2$	$u_3$	$u_4$
$\Delta\omega_1$	0.5640	0.5280	0.6398	0.6323	0.4973	0.6081	0.5263	0.6537
$\Delta\omega_2$	0.4323	0.6571	1.0000	0.6385	0.3551	0.4342	0.3758	0.4668
$\Delta\omega_3$	0.8758	0.7143	0.7366	0.9602	0.7608	0.9303	0.8051	1.0000
$\Delta\omega_4$	0.7093	0.6609	0.8584	0.7826	0.6733	0.8232	0.7125	0.8850
Computational Time (Signal Selection) = 1.28s					Computational Time (Signal Selection) = 0.078s			
Computational Time (WAC Output Signal) = 0.0116s								

### 3.2.3 Order reduction

In general, the order  $k$  is not known a priori, so  $k$  is assumed to be a large number which is limited by the number of samples  $l$  and computational burden. Then, modes with negligible residues are discarded [74] and new order  $p$  is identified (i.e the order of (2.13) is reduced from  $k$  to  $p$ ).

### 3.2.4 Signal selection

The validity of the proposed algorithm for signal selection is verified by implementing this approach on a wind integrated two-area power system model. For this, a dominant mode of 0.6038 Hz is observed. Table 3.5 shows the comparison of proposed signal selection algorithm with the residue analysis [54] of state space matrices corresponding to the dominant mode. Since there are two coherent groups in the two-area system, two WAC are required; one in each group. Generators 1 and 2 are in one coherent group, and the remaining generators are in a second coherent group. It is worth noting that, as the value of residue gets larger, the stronger is the control loop to damp oscillations.

The control loop required to damp the observed mode can be derived from Table 3.5 as follows. In coherent group-1 the residue value is largest between the speed of generator-3 ( $\Delta\omega_3$ ) and the input signal of generator-1 ( $u_1$ ), so generator-1 is the most controllable machine. Likewise, in coherent group-2 the most observable signal is  $\Delta\omega_2$ , and generator 4 is the most controllable machine. Table 4.3 shows the WAC control loop for the case of the IEEE-39 bus system with a fault on bus-14 and with four clusters. In group-1, generator 8 is the most controllable machine and the most observable signal is  $\Delta\omega_7$ , in group-2, generator 10 is the most controllable machine, and the most observable signal is  $\Delta\omega_1$ , in group-3, generator 2 is the most controllable machine and the most observable signal is  $\Delta\omega_6$ , and in group-4, generator 7 is the most controllable machine and the most observable signal is  $\Delta\omega_{10}$ . However, the residue of the control loop for group-2 is very low, which can be verified from the fact

that the inertia of generator-10 is very high compared to other generators and so it is the less controllable machine. Hence the controller for group-2 is ignored.

### 3.2.5 WAC design architecture

The proposed WAC algorithm has three parts 1) identification of control loop transfer function, 2) Discrete-time Linear Quadratic Regulator (DLQR), and 3) state estimation using Kalman filtering. The details are discussed in Section 2.6. Fig. 2.15 shows the architecture of the proposed WAC design.

## 3.3 Simulation Results

The proposed controller is implemented on the two-area (Fig. 1) and IEEE 39-bus (Fig. 2) system interconnected with a 150MW WTG [85] with each WTG is rated at 2MW. The experimental test-bed is as shown in Fig. 3.10.

### 3.3.1 Implementation test results using two-area system

Based on coherency grouping as shown in Table 3.1, it can be seen that generators 1 and 2 are in one group and generators 3 and 4 are in the other group, so two WACs are required which are to be placed one in each group. The signal selection for WAC control loop is discussed in section II. The simulation results with the proposed architecture are compared with the results from a system with both Exciter and PSS, and with Exciter only. Fig. 3.11 shows the wind speed profile used for simulations. Fig. 3.12 shows the active power. It is seen that (see Fig. 3.12) injection of the variable active power of WTG into the grid changes operating condition of the power system, which initiates synchronous generators to oscillate. At this time, a disturbance is created by initiating a fault on bus-8 at 13 sec for 0.1 sec, and another

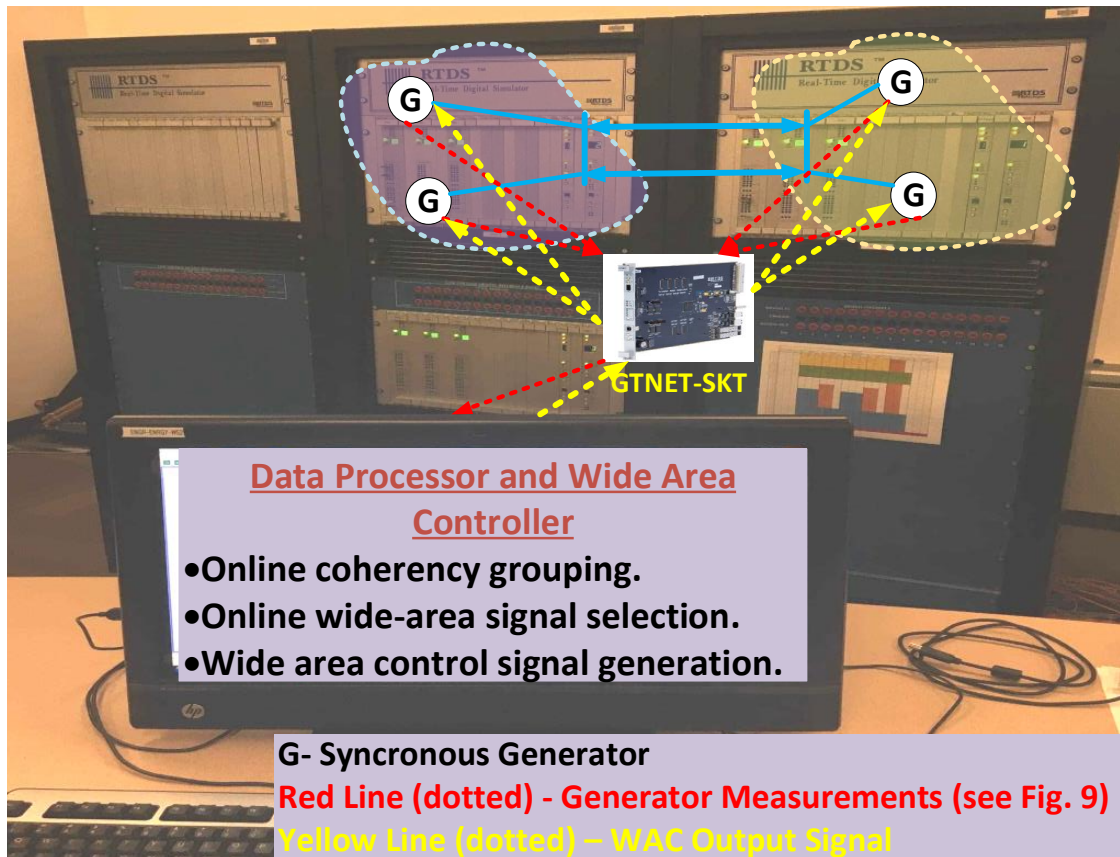


Fig. 3.10. Experimental test bed.

disturbance is created at 33 sec by dropping load connected to bus-9 for 0.1 sec. Fig. 3.13 shows the relative speed of generator 2 w.r.t generator 3, Fig. 3.14 show the speed of generator 1 w.r.t generator 4, Fig. 3.15 shows the relative speed of generator 2 w.r.t generator 4, and Fig. 3.16 shows the WAC controlling signal to generator 1 and generator 3.

From the above results, with the WAC controlling signal (Fig. 3.16) to generator 1 and generators 3, it is observed that the oscillations are effectively damped (Fig. 3.13 to Fig. 3.15). From Fig. 3.13, it is seen that the frequency of inter-area oscillation is 0.6135Hz (approx.). Since the control loop is selected for inter-area oscillation

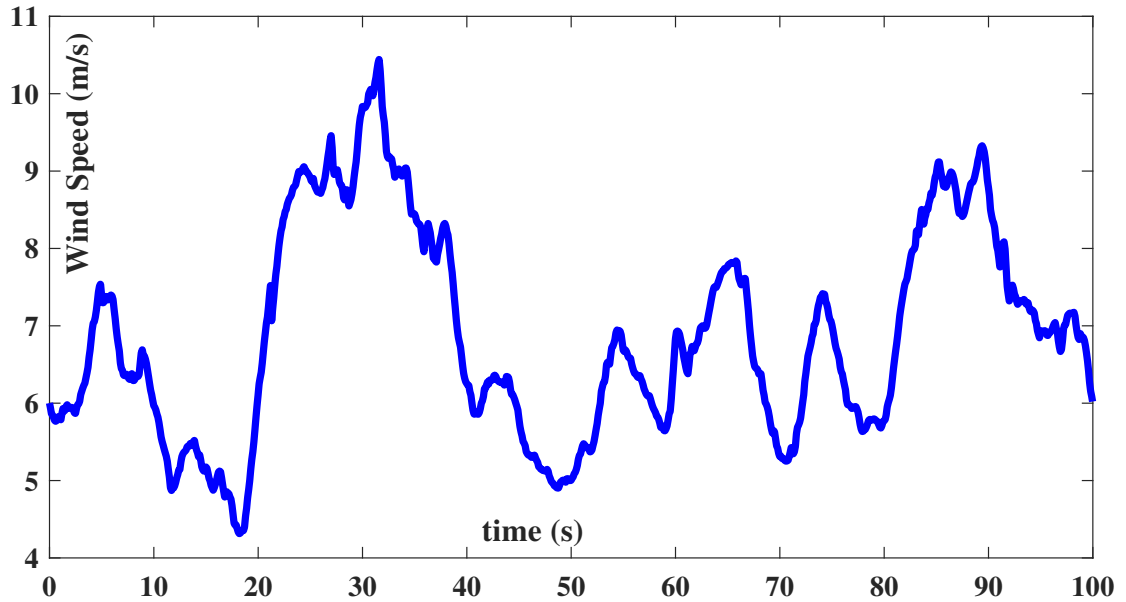


Fig. 3.11. Wind Speed.

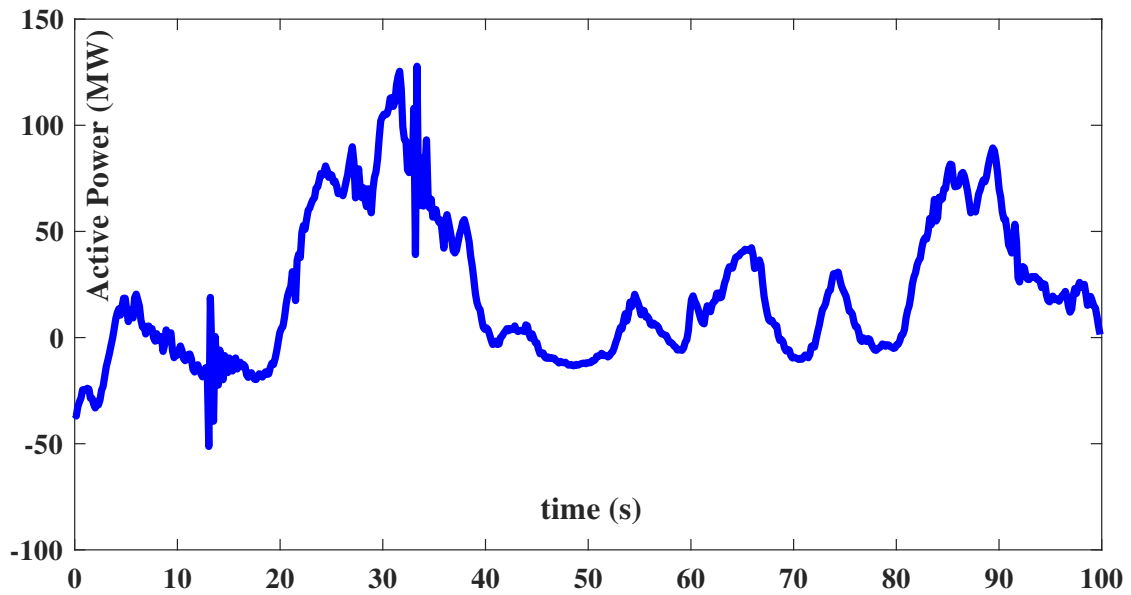


Fig. 3.12. WTG Active Power.

(0.6038Hz), the inter-area oscillations are damped out effectively. From these results, it can be concluded that the proposed algorithm based on the online coherency grouping performs very effective when compared to PSS working alone, and can be implemented online.

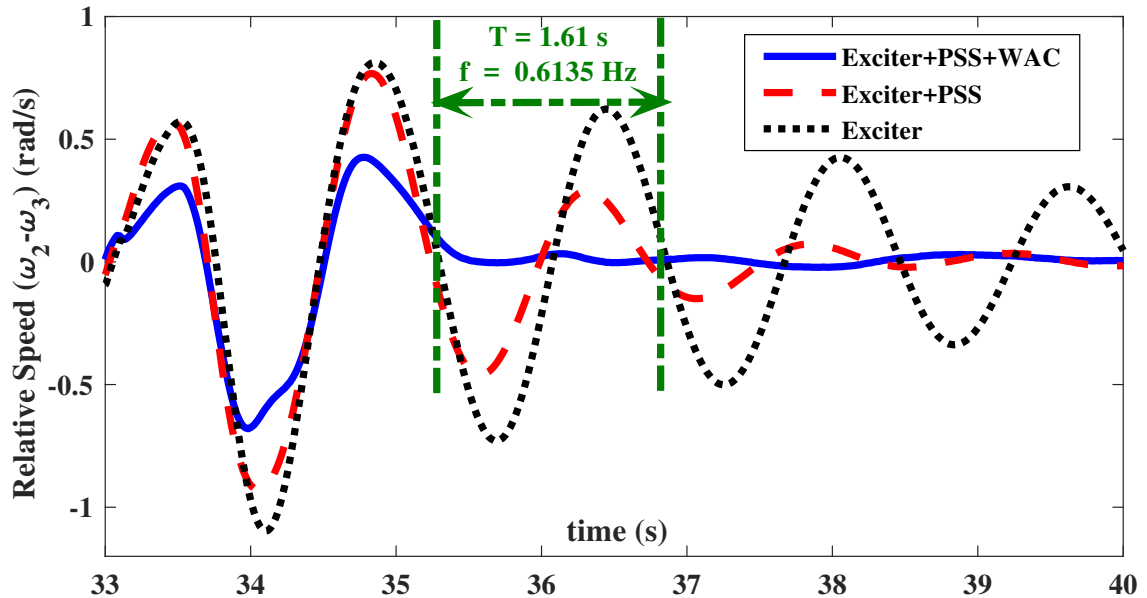


Fig. 3.13. Relative speed of generator 2 w.r.t generator 3.

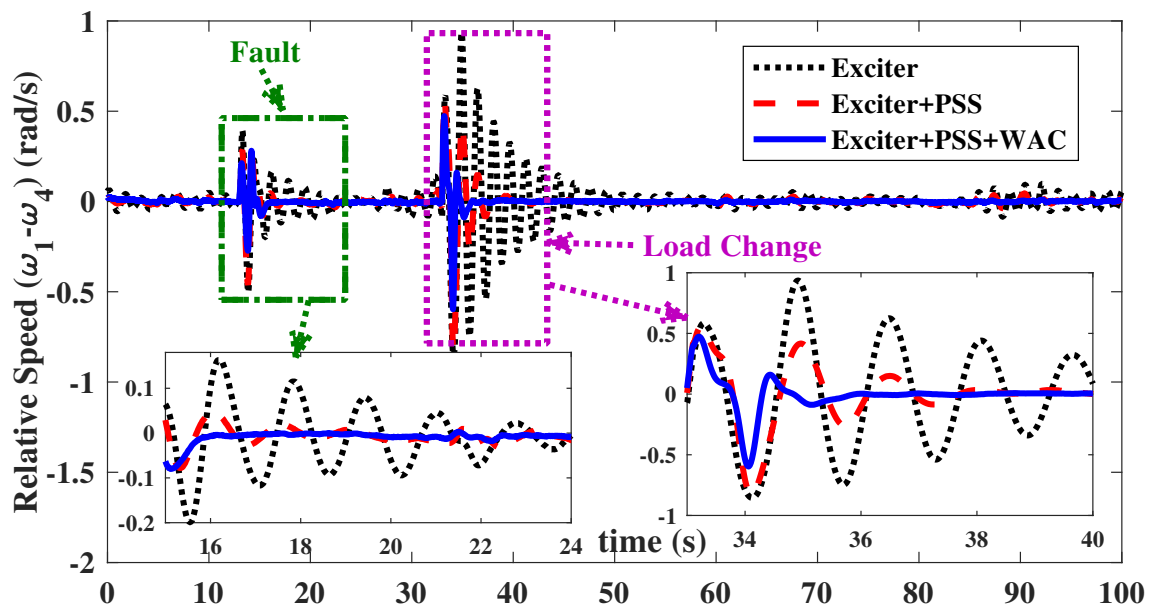


Fig. 3.14. Relative speed of generator 1 w.r.t generator 4.

### 3.3.2 Implementation test results on IEEE 39-bus system

Based on coherency grouping as shown in Table 3.1, generators 4, 5, 6, 7, and 9 are in one group (group-4), generators 1, and 8 are in group-1, generators 2, 3

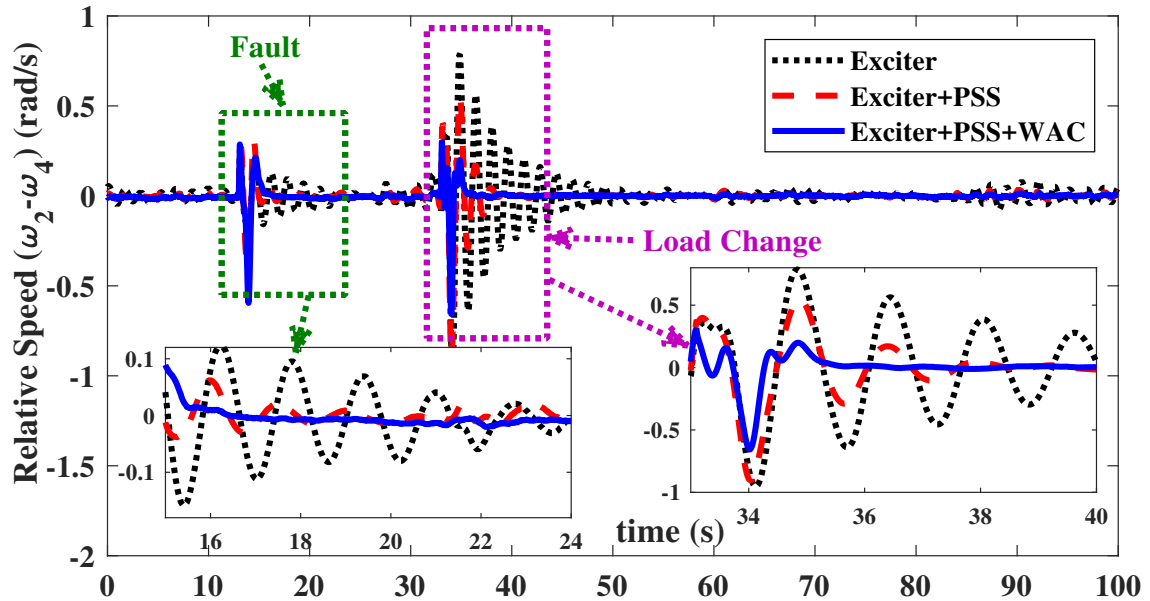


Fig. 3.15. Relative speed of generator 2 w.r.t generator 4.

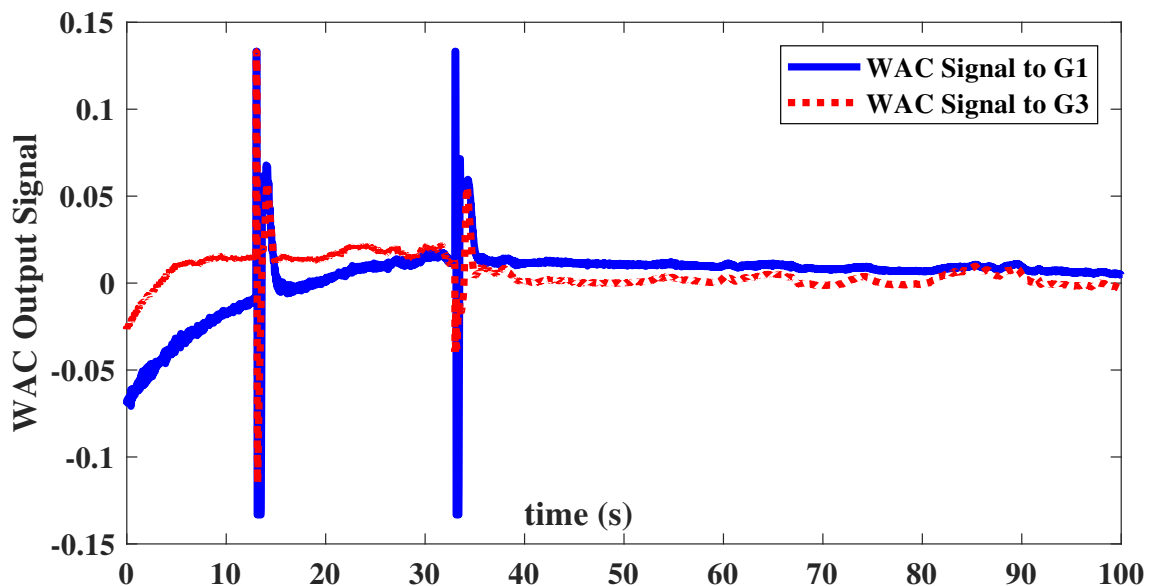


Fig. 3.16. WAC input signal to generator 1 and 3.

are in group-3, so three WAC controllers are required which are to be placed one in each group. The signal selection for WAC control loop is shown in Table 4.3. The simulation results with the proposed controller are compared with the results from a system with both Exciter and PSS, and with Exciter only. Fig. 3.17 shows the

Table 3.6  
IEEE 39-bus control loop  
(fault on bus-14)

	Control Loop	Residue
Group-1	$\Delta\omega_{10} \rightarrow u_7$	0.678
Group-2	$\Delta\omega_7 \rightarrow u_8$	0.49
Group-3	$\Delta\omega_6 \rightarrow u_2$	1
Group-4	$\Delta\omega_1 \rightarrow u_{10}$	0.027
Computational Time (Signal Selection) = 3.16s		
Computational Time (WAC Output Signal) = 0.0192s		

wind speed profile used for simulations. Fig. 3.18 shows active power. It is seen that (see Fig. 3.18), injection of the variable active power of WTG into the grid changes the operating condition of the power system initiating oscillations in synchronous generators. At this time, a disturbance is created by initiating a fault on bus-14 at 5 sec for 0.1 sec, and another disturbance is created at 41 sec by dropping load connected to bus 26 for 0.1 sec. Fig. 3.19 shows the relative speed of generator 5 w.r.t generator 2, Fig. 3.20 show the speed of generator 7 w.r.t generator 2, Fig. 3.21 shows the relative speed of generator 8 w.r.t generator 2, and Fig. 3.22 shows the WAC controlling signal to generator 2, 7, and 8. From Fig. 3.19 to Fig. 3.21, it can be seen that after 17sec the oscillations are damped effectively hence the WAC output is dropped.

From the above results, with the WAC controlling signal (Fig. 3.22) to generator 2, 7, and 8, it is observed that the oscillations are effectively damped (Fig. 3.19 to Fig. 3.21). From Fig. 3.19 it is seen that the frequency of inter-area oscillation is 0.683Hz (approx.). Since the control loop is selected for inter-area oscillation (0.6038Hz), the inter-area oscillations are damped out effectively. Hence it can be concluded that the

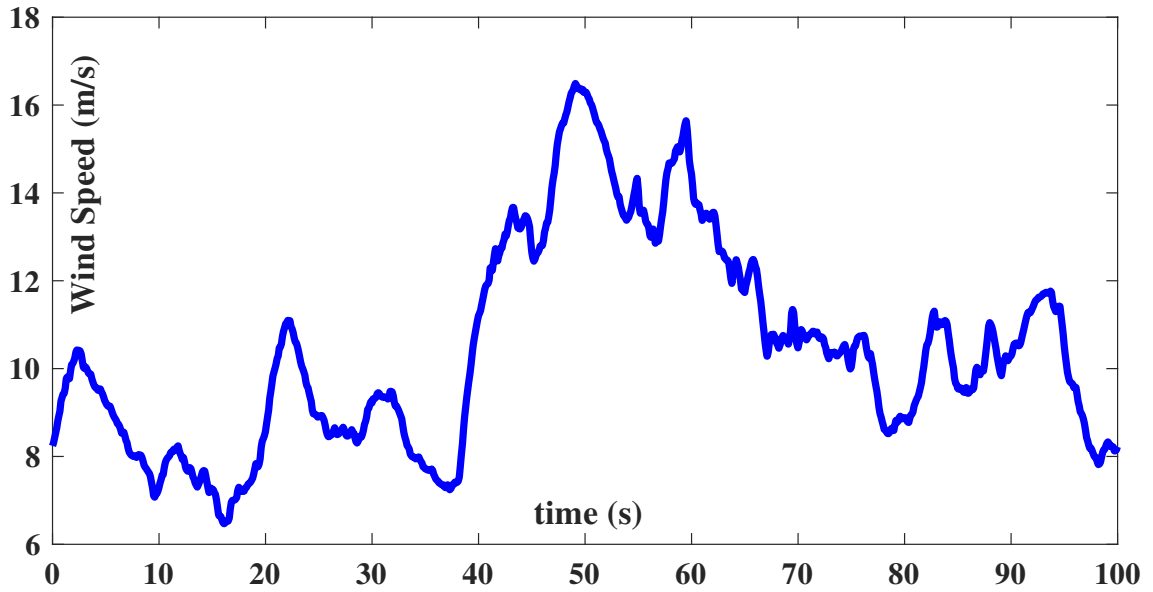


Fig. 3.17. Wind Speed.

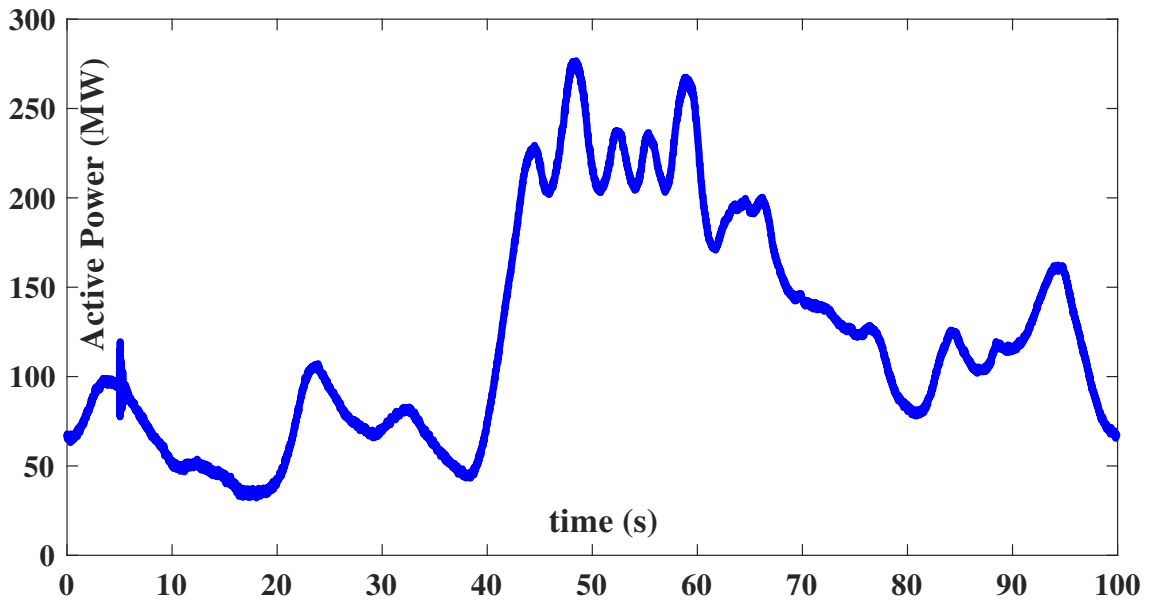


Fig. 3.18. WTG Active Power.

proposed algorithm based on the online coherency grouping performs very effectively when compared to PSS working alone, and can be implemented online.

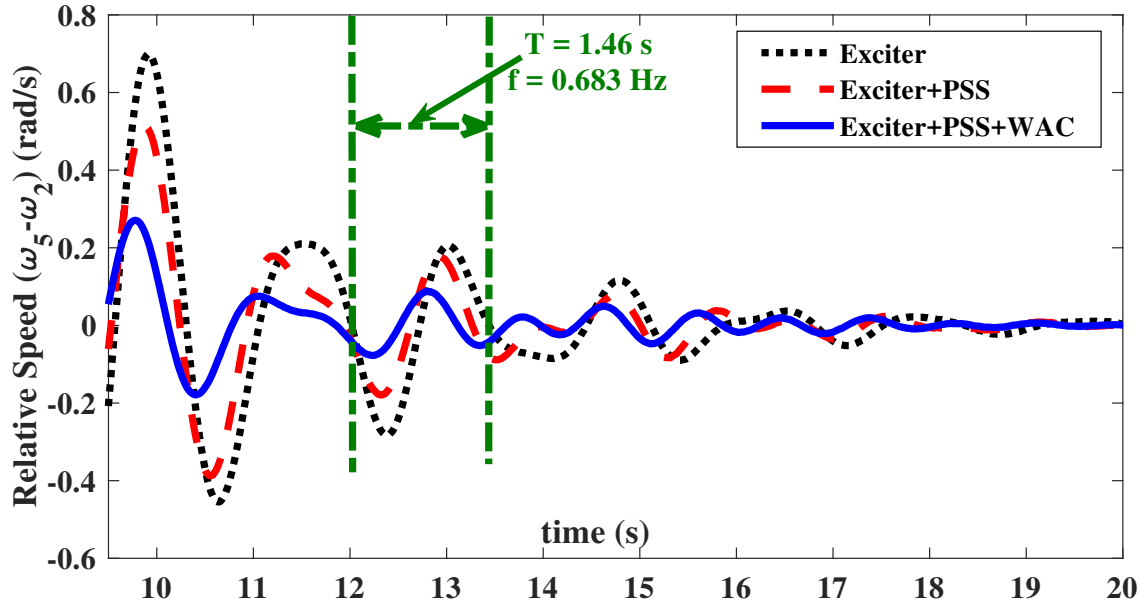


Fig. 3.19. Relative speed of generator 5 w.r.t generator 2.

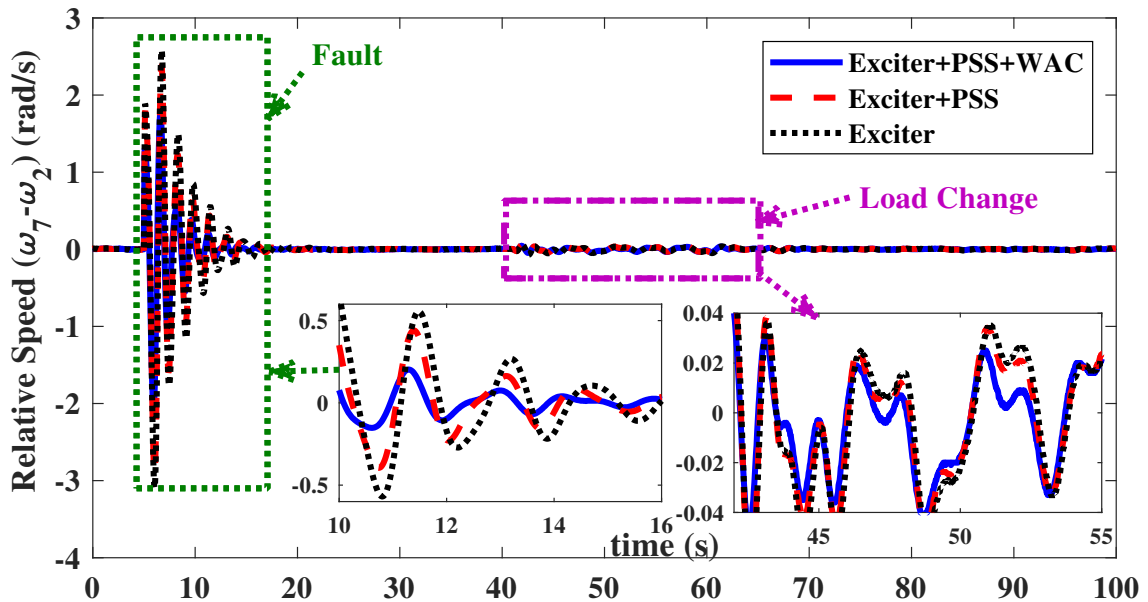


Fig. 3.20. Relative speed of generator 7 w.r.t generator 2.

### 3.4 Summary

In this chapter, an online coherency based WAC is proposed. The proposed WAC algorithm is an efficient way of damping inter-area modes. The location of WAC is

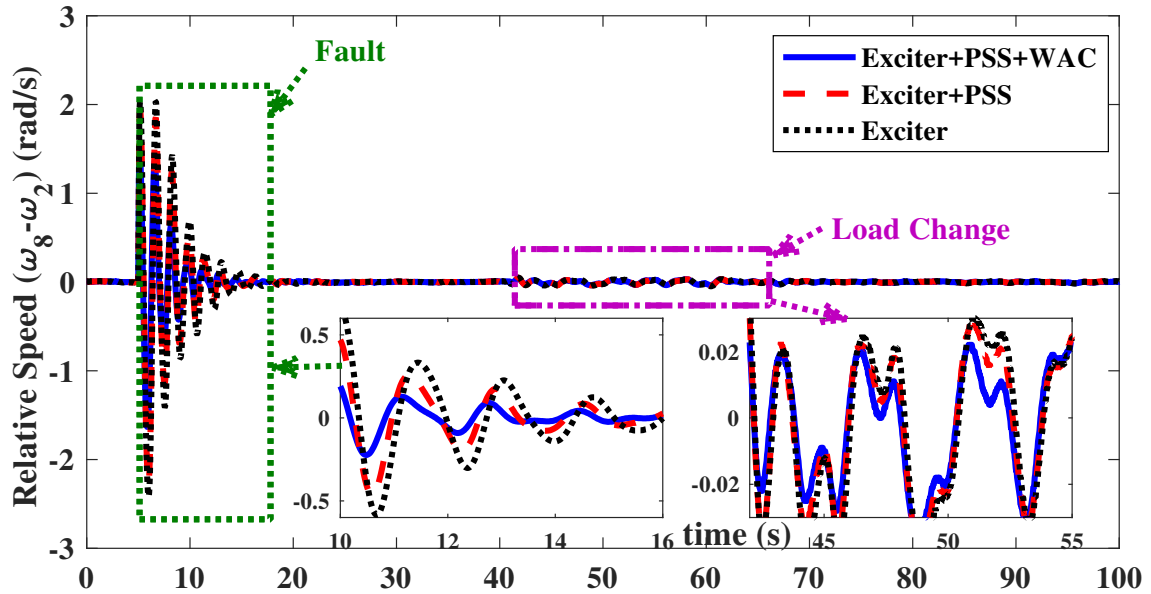


Fig. 3.21. Relative speed of generator 8 w.r.t generator 2.

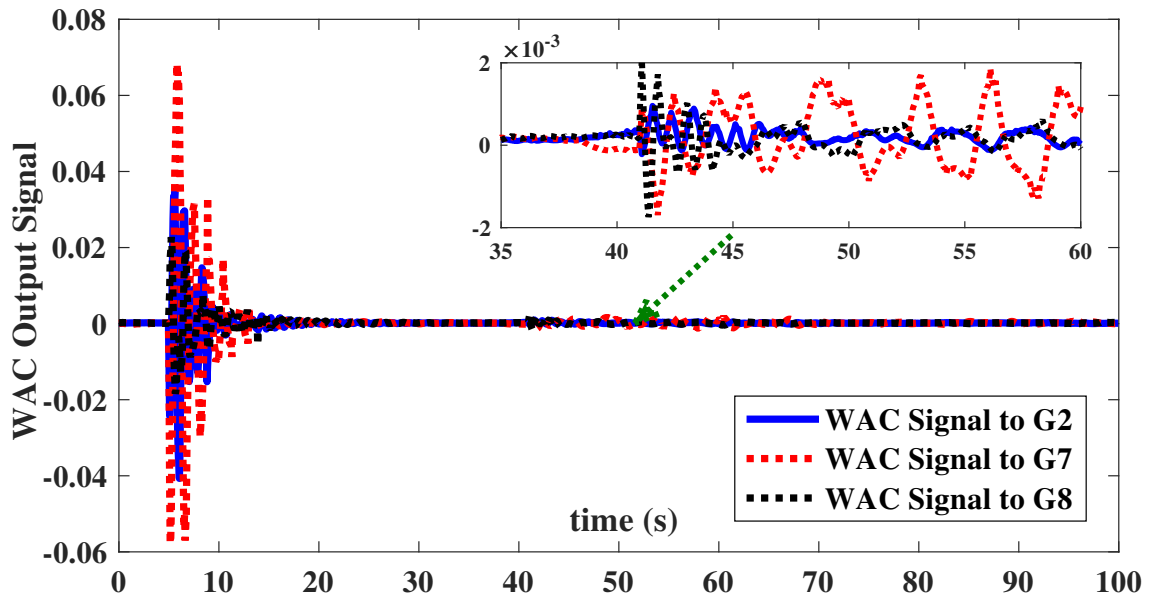


Fig. 3.22. WAC input signal to generator 2, 7, and 8

decided based on online coherency grouping, and signal selection is based on online residue analysis. The spectral clustering and residue using MIMO system identification are computed during the simulation, so any changes in system operating conditions especially due to renewable energy sources are taken into consideration.

The WAC gains calculation and state estimation are performed online; hence the controller parameters are updated based on system conditions. The efficacy of the proposed architecture is verified by testing it on WTG integrated two-area and IEEE 39-bus power system, models. The proof of concept illustrates that with the proposed WAC, inter-area modes can be damped much effectively. In the next chapter, Alternating Direction Method of Multipliers (ADMM) based approach for wide-area control is proposed.

## CHAPTER 4: ALTERNATING DIRECTION METHOD OF MULTIPLIERS (ADMM) BASED DISTRIBUTED APPROACH FOR WIDE-AREA CONTROL

In this chapter, a novel distributed wide-area control architecture based on ADMM is proposed for damping the inter-area oscillations. For this, first, an interconnected power system is divided into areas based on coherency grouping. Second, on each area, local processors are assigned that estimates a black-box transfer function model based on Lagrange multipliers using measurements. For consensus, the local area processors communicate with a global processor to estimate a global transfer function model of the power system from which a residue corresponding to the inter-area mode of interest is derived, after convergence. This residue provides information regarding optimal wide area control loop. Finally, a wide-area damping controller is designed based on this information. The efficacy of the controller is validated using two area and IEEE-39 bus test systems on RTDS/RSCAD and MATLAB co-simulation platform.

### 4.1 Introduction

For reliable operation, electro-mechanical oscillations which arise in large interconnected power systems due to disturbance should be damped in a timely manner. The electro-mechanical oscillations of generators with respect to remaining part of the system are called local modes, whereas groups of generators oscillating together against other groups are called inter-area modes [5]. The frequency of inter-area os-

cillations is between 0.1-1.0 Hz. Higher penetration of renewable energy resources and variable loads makes the inter-connected power systems to operate close to limits. This condition increases the stress on the power system and can deteriorate the inherent damping of the system. Thus inter-area oscillation damping is even more critical and difficult in the modern power grid. Unfortunately, inter-area modes are not observable/controllable from generator local measurements and the effectiveness of conventional power system stabilizer (PSS) in damping of inter-area modes is thus limited [114].

Several methodologies to identify and damp inter-area oscillations considering optimal wide area control loop (input/output signal selection) are reported in Section 1.3.3. However, these methods are formulated using state-space matrices obtained through linearizing the system at a particular operating point and analyzing modes at that point which cannot be implemented in real-life as power system is non-linear and dynamic. Thus, the control loop identified by linearizing at an operating point as formulated in these methods may not be effective in damping inter-area modes.

To overcome drawbacks of linearization based signal selection, measurement-based methods have been designed. In these methods, measurement data is analyzed with a centralized controller to identify the optimal control loop. Since measurements are updated as the system operating condition changes, these methods keep track of changing operating conditions while identifying optimal control loop. Several centralized methods using measurements as discussed in Section 1.3.1.2 address only power system identification but not identifying the optimal control loop. In chapter 2 and 3, the measurement-based approach for optimal control loop selection is discussed.

However, for the large-scale network, the centralized approach for wide area signal selection may not be feasible due to various factors like data volume, data transfer capability, computational time, etc.

Considering these factors and to overcome the drawbacks of earlier methods reported in the literature, this chapter [15] introduces a novel method to identify optimal wide area control loop for wide area damping controller (WADC) using ADMM [15] based distributed algorithms. For the proposed study, initially the interconnected power system is divided into areas based on coherency grouping of generators, then each local area processor designed is used to estimate multi-input-multi-output (MIMO) black-box transfer function model based on Lagrange multipliers method using measurements. The local area processors then communicate with the global processor to estimate a global transfer function model of the power system. Upon convergence, the residue corresponding to inter-area mode of interest provides information of optimal wide area control loop obtained from the estimated global transfer function. Further, knowledge of residue and corresponding eigenvalue is also used for WADC design. The effectiveness of the proposed optimal control loop selection methodology and wide area controller design is validated using two area and IEEE-39 bus test systems on RTDS/RSCAD and MATLAB co-simulation platform.

To summarize, the major contributions of this work are:

- Developed a novel experimental test-bed for power system wide-area monitoring techniques using distributed algorithms.
- Developed an algorithm to solve power system MIMO transfer functions using

ADMM.

- Developed a new method for online selection of optimal wide-area control loop using ADMM techniques.
- Validated the applicability of distributed techniques for power system control application.

The rest of the chapter is organized as follows: In Section 4.2 discusses the proposed approach and problem formulation. In Section 4.3, experimental setup for implementing the proposed signal selection method is discussed. In Section 4.4, implementation test results are illustrated and Section 4.5 summarizes the chapter.

## 4.2 Proposed Approach and Problem Formulation

The proposed methodology involves three steps: a) Divide large-scale network into areas, b) Select the appropriate signal for control, and c) Design a wide-area damping controller. The proposed distributed architecture is shown in Fig. 7.1. The flowchart is shown in Fig. 4.2.

### 4.2.1 Dividing Large Scale Network into Areas

Most of the present techniques for wide-area control are based on linearizing the power system model at an operating point and then calculating the eigenvalues and vectors to identify the optimal wide-area control loop. However getting a linearized system for large-scale utility network is complex and impractical. Also as the operating condition of the grid changes, the linearized system changes and thus calculating the linear system model for every time-step is impractical. To overcome this model-

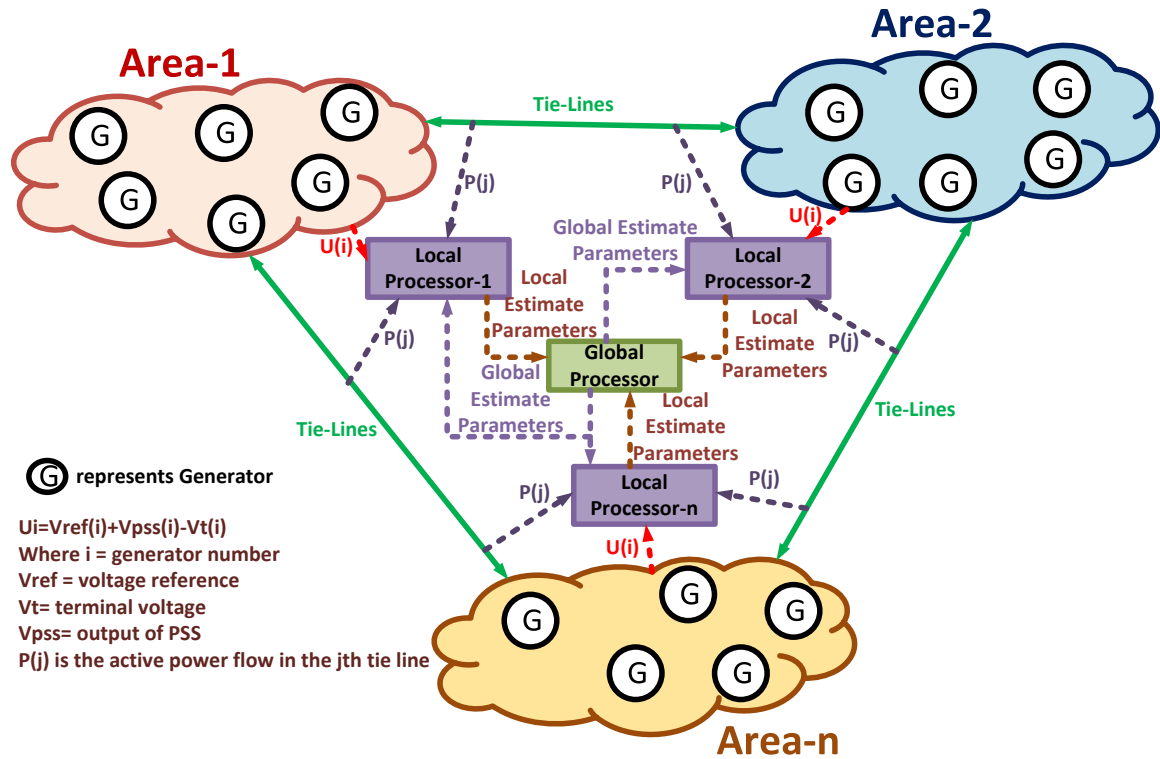


Fig. 4.1. Proposed distributed architecture for wide area control.

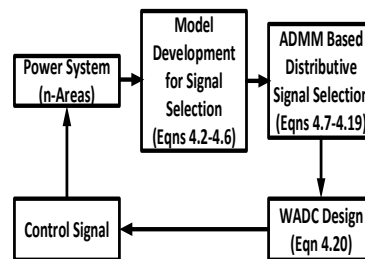


Fig. 4.2. Flowchart of overall methodology.

ing difficulty, in this chapter, a measurement based identification of wide-area control loop is proposed. However analyzing measurements data using centralized data processing framework may not be possible due to data transfer capability, data volume, as well as the availability of communication infrastructure. Also, in reality, different utilities (areas) are combined to a more extensive power system, so for centralized processing, detailed information of other areas may not be readily available at the cen-

tral control center (global processor). To overcome this, the power system is divided into areas based on coherency grouping of generators where each area has one local processor. The local processors estimate a local transfer function of the grid model and communicate with the global processor to estimate a global transfer function.

For the division of the network into areas, an online coherency grouping based on spectral clustering methodology considering the speeds of the generator is used where tie lines connect the areas. Let the speed data points  $\omega_1, \omega_2, \dots, \omega_n$  for a window length of  $n$  are considered for clustering. Using these data points a similarity matrix  $S$  is formulated, where  $S_{ij}$  gives the relation between  $\omega_i$  and  $\omega_j$ . The information from similarity matrix is used to group  $\omega_1, \omega_2, \dots, \omega_n$  into  $k$  clusters. The similarity matrix is based on a Gaussian function represented as in (4.1)

$$S_{ij} = e^{-\frac{\|\omega_i - \omega_j\|}{2\sigma^2}} \quad (4.1)$$

where  $\sigma$  is a scaling factor. Here  $S$  is dense and is of the order  $n \times n$ . The size of  $S$  increases with an increase in the number of data points under consideration, but this slows the simulation speed. To increase the online coherency grouping speed, Nystrom method is used which uses sub-matrix of the dense matrix  $\mathbf{S}$  [19]. The details regarding online coherency grouping methodology are discussed in [109].

#### 4.2.2 Proposed Architecture for Signal Selection

The proposed architecture for optimal wide-area signal selection involves the following steps: a) Model development, and b) ADMM based distributive signal selection.

## 4.2.2.1 Model Development

First, the power system is divided into areas. It is assumed that each area has a local processor which communicates with the global processor as the local processor of one area may not have complete information of other areas for determining optimal wide area control loop. The inter-area oscillations (0.1 to 1 Hz) are between two-areas connected through tie-lines. Since the tie-line information is common to multiple areas and local processors use tie-line power flow to reach a consensus, this information is used for reaching controller convergence. For this, a local transfer function is estimated with an input signal ( $u_n$ ) as shown in Fig. 4.3 and output signal as tie-line power flow as output.

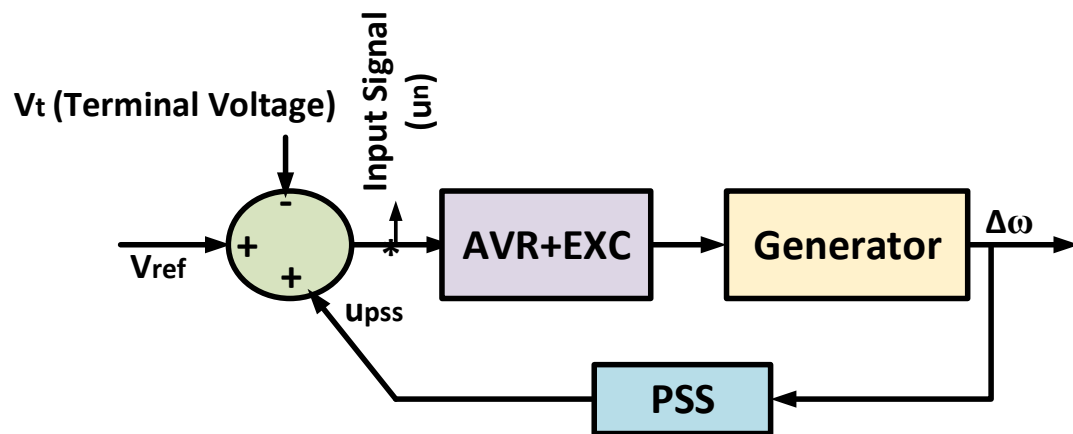


Fig. 4.3. Input signal for transfer function estimation.

For example, if there are  $m$  tie lines and  $n$  generators in the system, then the

MIMO transfer function of the power system can be written as

$$\begin{bmatrix} P_1(z) \\ \vdots \\ P_m(z) \end{bmatrix} = \begin{bmatrix} G_{11}(z) & \dots & G_{1n}(z) \\ \vdots & \dots & \vdots \\ G_{m1}(z) & \dots & G_{mn}(z) \end{bmatrix} \begin{bmatrix} u_1(z) \\ \vdots \\ u_n(z) \end{bmatrix} \quad (4.2)$$

and generalized as

$$P(z) = G(z)U(z) \quad (4.3)$$

where  $u_n$  is the input signal (see Fig. 4.3) and  $P_m$  is the tie-line power flow. Based on the MIMO transfer function of the power system, (7.1)-(7.2) can be represented as  $G_{mn}(z)$  [106, 111]

$$G_{mn}(z) = \frac{P_m(z)}{u_n(z)} = \frac{b_0^h + b_1^h z^{-1} + \dots + b_k^h z^{-k}}{1 + a_1 z^{-1} + \dots + a_k z^{-k}} \quad (4.4)$$

where  $h$  is the element number in the matrix, and  $k$  is the order of transfer function.

It can be seen from (7.3) that, for capturing inter-area modes in the power system, the denominator coefficients need to be the same however numerator coefficients should be different. This gives information regarding inter-area modes in the system as seen from different inputs but their corresponding residues differ. For  $j$  samples and  $N$  observation window length, (7.3) can be rewritten as shown in (4.5). The least

---


$$\begin{bmatrix} P_m(j) \\ P_m(j-1) \\ \vdots \\ P_m(j-N+1) \end{bmatrix} = \begin{bmatrix} P_m(j-1) & \dots & P_m(j-k) & u_n(j) & \dots & u_n(j-k) \\ P_m(j-2) & \dots & P_m(j-k-1) & u_n(j-1) & \dots & u_n(j-k-1) \\ \vdots & \dots & \vdots & \vdots & \dots & \vdots \\ P_m(j-N) & \dots & P_m(j-N+1-k) & u_n(j-N+1) & \dots & u_n(j-N+1-k) \end{bmatrix} \begin{bmatrix} a_1 \\ \vdots \\ a_k \\ b_0^n \\ b_1^n \\ \vdots \\ b_k^n \end{bmatrix} \quad (4.5)$$

squares technique is used to estimate (7.3) in discrete time-domain.  $G(z)$  in (7.2) is formulated after estimating the entire system with different inputs and outputs. Now, (7.3) can be transformed into partial fraction expansion and can be written as (7.4).

$$G_{mn}(z) = \frac{P_m(z)}{u_n(z)} = \frac{R_{(mn)k}}{z - p_{(mn)k}} + \dots + \frac{R_{(mn)2}}{z - p_{(mn)2}} + \frac{R_{(mn)1}}{z - p_{(mn)1}} + k(z) \quad (4.6)$$

where  $k(z)$  is a polynomial in  $z$  and  $R_{(mn)k}$  is the residue of corresponding to the pole  $p_{(mn)k}$ . The residue  $R_{(mn)k}$  provides information about how the mode  $p_{(mn)k}$  is affected by input  $u_n$  and how observable is it from  $P_m$ . This shows that residue is a measure of joint controllability and observability index, where larger the value of residue, the stronger is the optimal control loop. However, solving (7.1) using centralized techniques may not be possible because of computational burden, data volume, etc. For example, if there are 20 tie-lines and 200 generators, using a centralized method the processor must solve 4000 transfer functions which may not be feasible in real-time. On the other hand, the power system is divided into areas either based on geographical location (utilities) or coherency grouping, and each area has its local processor which reports to global processor. Thus local processor of one area (utility) may not have complete information of other areas for wide area control. In the proposed distributed architecture, a distributed consensus-based approach using ADMM can be used to overcome this problem by solving (7.1) in a distributed architecture. In this approach, using Lagrange multipliers method a black-box transfer function model is estimated locally for each area, and then a local processor is used to share

information with the global processor so that a global transfer function of the power system can be estimated. The eigenvalue and corresponding residue information obtained from the global transfer function is used in identifying the wide-area control loop and controller design.

#### 4.2.2.2 ADMM Based Distributive Signal Selection

Large power system comprises of different areas, so (7.1) can be divided into parts and then solved using ADMM. The distributed algorithm is proposed here using an example for simplicity and ease of understanding. Suppose there are four generators ( $n = 4$ ) divided into two areas such that generators 1 and 2 are in one area and generators 3 and 4 are in the other area, both these areas are connected by two tie-lines ( $m = 2$ ). Then (7.1) can be written as follows:

$$\begin{bmatrix} P_1(z) \\ P_2(z) \end{bmatrix} = \begin{bmatrix} G_{11}(z) & \cdots & G_{14}(z) \\ G_{21}(z) & \cdots & G_{24}(z) \end{bmatrix} \begin{bmatrix} u_1(z) \\ u_2(z) \\ u_3(z) \\ u_4(z) \end{bmatrix} \quad (4.7)$$

The centralized equation (7.5) can be distributed and reformulated as follows:

**Step-1:** Divide the above MIMO transfer function into two areas:

- *For Area-1*

$$\begin{bmatrix} P_1(z) \\ P_2(z) \end{bmatrix} = \begin{bmatrix} G_{11}(z) & G_{12}(z) \\ G_{21}(z) & G_{22}(z) \end{bmatrix} \begin{bmatrix} u_1(z) \\ u_2(z) \end{bmatrix} \quad (4.8)$$

Further  $G_{11}(z)$ ,  $G_{12}(z)$ ,  $G_{21}(z)$ , and  $G_{22}(z)$  can be written as follows:

$$\begin{aligned}
 G_{11}(z) &= \frac{P_1(z)}{u_1(z)} = \frac{b_0^1 + b_1^1 z^{-1} + \dots + b_k^1 z^{-k}}{1 + a_1 z^{-1} + \dots + a_k z^{-k}} \\
 G_{12}(z) &= \frac{P_1(z)}{u_2(z)} = \frac{b_0^2 + b_1^2 z^{-1} + \dots + b_k^2 z^{-k}}{1 + a_1 z^{-1} + \dots + a_k z^{-k}} \\
 G_{21}(z) &= \frac{P_2(z)}{u_1(z)} = \frac{b_0^3 + b_1^3 z^{-1} + \dots + b_k^3 z^{-k}}{1 + a_1 z^{-1} + \dots + a_k z^{-k}} \\
 G_{22}(z) &= \frac{P_2(z)}{u_2(z)} = \frac{b_0^4 + b_1^4 z^{-1} + \dots + b_k^4 z^{-k}}{1 + a_1 z^{-1} + \dots + a_k z^{-k}}
 \end{aligned} \tag{4.9}$$

where  $b_0^h, b_1^h, \dots, b_k^h$  are numerator coefficients which are different for each transfer function,  $a_1, a_2, \dots, a_k$  are the denominator coefficients which are equal for all the transfer functions in the power system and  $h = 1, \dots, 4$ .

- *For Area-2*

$$\begin{bmatrix} P_1(z) \\ P_2(z) \end{bmatrix} = \begin{bmatrix} G_{13}(z) & G_{14}(z) \\ G_{23}(z) & G_{24}(z) \end{bmatrix} \begin{bmatrix} u_3(z) \\ u_4(z) \end{bmatrix} \tag{4.10}$$

Further  $G_{13}(z)$ ,  $G_{14}(z)$ ,  $G_{23}(z)$ , and  $G_{24}(z)$  can be written as follows:

$$\begin{aligned}
 G_{13}(z) &= \frac{P_1(z)}{u_3(z)} = \frac{b_0^5 + b_1^5 z^{-1} + \dots + b_k^5 z^{-k}}{1 + a_1 z^{-1} + \dots + a_k z^{-k}} \\
 G_{14}(z) &= \frac{P_1(z)}{u_4(z)} = \frac{b_0^6 + b_1^6 z^{-1} + \dots + b_k^6 z^{-k}}{1 + a_1 z^{-1} + \dots + a_k z^{-k}} \\
 G_{23}(z) &= \frac{P_2(z)}{u_3(z)} = \frac{b_0^7 + b_1^7 z^{-1} + \dots + b_k^7 z^{-k}}{1 + a_1 z^{-1} + \dots + a_k z^{-k}} \\
 G_{24}(z) &= \frac{P_2(z)}{u_4(z)} = \frac{b_0^8 + b_1^8 z^{-1} + \dots + b_k^8 z^{-k}}{1 + a_1 z^{-1} + \dots + a_k z^{-k}}
 \end{aligned} \tag{4.11}$$

where  $b_0^h, b_1^h, \dots, b_k^h$  are numerator coefficients which are different for each transfer function,  $a_1, a_2, \dots, a_k$  are the denominator coefficients which are equal for all the transfer functions in the power system and  $h = 5, \dots, 8$ .

**Step-2:** Writing the (7.7) and (6.8) in least squares format

- For Area-1

$$\begin{aligned}
 \begin{bmatrix} L_1 & M_1 \end{bmatrix} \begin{bmatrix} a^1 \\ b^1 \end{bmatrix} &= [B_{11}] \\
 \begin{bmatrix} L_1 & M_2 \end{bmatrix} \begin{bmatrix} a^2 \\ b^2 \end{bmatrix} &= [B_{12}] \\
 \begin{bmatrix} L_2 & M_1 \end{bmatrix} \begin{bmatrix} a^3 \\ b^3 \end{bmatrix} &= [B_{21}] \\
 \begin{bmatrix} L_2 & M_2 \end{bmatrix} \begin{bmatrix} a^4 \\ b^4 \end{bmatrix} &= [B_{22}]
 \end{aligned} \tag{4.12}$$

- For Area-2

$$\begin{aligned}
 \begin{bmatrix} L_1 & M_3 \end{bmatrix} \begin{bmatrix} a^5 \\ b^5 \end{bmatrix} &= [B_{13}] \\
 \begin{bmatrix} L_1 & M_4 \end{bmatrix} \begin{bmatrix} a^6 \\ b^6 \end{bmatrix} &= [B_{14}] \\
 \begin{bmatrix} L_2 & M_3 \end{bmatrix} \begin{bmatrix} a^7 \\ b^7 \end{bmatrix} &= [B_{23}] \\
 \begin{bmatrix} L_2 & M_4 \end{bmatrix} \begin{bmatrix} a^8 \\ b^8 \end{bmatrix} &= [B_{24}]
 \end{aligned} \tag{4.13}$$

where  $a$  is vector of denominator coefficients,  $b$  is vector of numerator coefficients,  $L$  is matrix of previous samples of  $P_m$ , and  $M_n$  is matrix of current and previous samples of  $u_n$ .

**Step-3:** The objective here is to make  $a^1 = a^2 = \dots = a^8 = z$  for a global consensus problem so that with the given initial conditions numerator and denominator coefficients can be calculated iteratively until objective is achieved.

- *For Area-1 and Area-2 (Calculating a using b)*

$$\begin{aligned}
[L_1] [a^1] &= [B_{11}] - [M_1] [b^1] \\
[L_1] [a^2] &= [B_{12}] - [M_2] [b^2] \\
[L_2] [a^3] &= [B_{21}] - [M_1] [b^3] \\
[L_2] [a^4] &= [B_{22}] - [M_2] [b^4] \\
[L_1] [a^5] &= [B_{13}] - [M_3] [b^5] \\
[L_1] [a^6] &= [B_{14}] - [M_4] [b^6] \\
[L_2] [a^7] &= [B_{23}] - [M_3] [b^7] \\
[L_2] [a^8] &= [B_{24}] - [M_4] [b^8]
\end{aligned} \tag{4.14}$$

---

**Algorithm 4.1** ADMM-Algorithm

---

- 1: Each local processor ( $q$ ) initializes  $a_0^q, b_0^q$  using (6.9) and (6.10).  $z_0$  and  $w_0^q$  are also initialized
  - 2: At iteration  $j$ :
  - 3: Local processors updates  $a^q$  as  $a_{j+1}^q = \underset{a^q}{\operatorname{argmin}} L_\rho$
  - 4: Local processor transmits  $a_{j+1}^q$  to the global processor
  - 5: Global processor calculates  $z_{j+1} = \frac{1}{2} \sum_{q=1}^2 a_{j+1}^q$
  - 6: Global processor transmits  $z_{j+1}$  to all local processors.
  - 7: Local processor updates  $w^q$  as  $w_{j+1}^q = w_j^q + \rho(a_{j+1}^q - z_{j+1})$
  - 8: Local processor updates  $b_{j+1}^q$  using (6.12)
- 

- *For Area-1 and Area-2 (Calculating b using a)*

$$\begin{aligned}
[M_1] [b^1] &= [B_{11}] - [L_1] [a^1] \\
[M_2] [b^2] &= [B_{12}] - [L_1] [a^2] \\
[M_1] [b^3] &= [B_{21}] - [L_2] [a^3] \\
[M_2] [b^4] &= [B_{22}] - [L_2] [a^4] \\
[M_3] [b^5] &= [B_{13}] - [L_1] [a^5] \\
[M_4] [b^6] &= [B_{14}] - [L_1] [a^6] \\
[M_3] [b^7] &= [B_{23}] - [L_2] [a^7] \\
[M_4] [b^8] &= [B_{24}] - [L_2] [a^8]
\end{aligned} \tag{4.15}$$

More generically (6.11) and (6.12) can be rewritten as follows:

$$[L^q] [a^q] = [B^q] - [M^q] [b^q] \tag{4.16}$$

$$[M^q] [b^q] = [B^q] - [L^q] [a^q] \tag{4.17}$$

Where  $q$  is area number.

**Step-4:** Global consensus optimization problem is formulated using equations (6.13)

and (6.14) as follows:

$$\min_{a^1, \dots, a^q, z} \sum_{q=1}^2 \frac{1}{2} \|[L^q] [a^q] - [B^q] + [M^q] [b^q]\|^2 \tag{4.18}$$

subject to  $a^q - z = 0$ , for  $q = 1, 2$

$z$  is the global consensus solution, that is obtained when the local estimates of all local processors denoted by  $a^q$ ,  $q = 1, 2$  reach the same value.

It can be seen that the ADMM estimation method uses Lagrange multiplier approach in an iterative distributed methodology. The augmented Lagrange is computed

as follows [74]

$$L_\rho = \sum_{q=1}^2 \frac{1}{2} \|[L^q] [a^q] - [B^q] + [M^q] [b^q]\| + w_q^T (a^q - z) + \frac{\rho}{2} \|a^q - z\|^2 \quad (4.19)$$

where  $a$  and  $z$  are the vectors of the primal variables,  $w$  is the vector of the dual variables or the Lagrange multipliers associated with (6.15), and  $\rho > 0$  denotes a penalty factor. ADMM implementation to solve distributed MIMO system is shown in below algorithm.

---

**Algorithm 4.2** ADMM-Algorithm

---

- 1: Each local processor ( $q$ ) initializes  $a_0^q, b_0^q$  using (6.9) and (6.10).  $z_0$  and  $w_0^q$  are also initialized
  - 2: At iteration  $j$ :
  - 3: Local processors updates  $a^q$  as  $a_{j+1}^q = \underset{a^q}{\operatorname{argmin}} L_\rho$
  - 4: Local processor transmits  $a_{j+1}^q$  to the global processor
  - 5: Global processor calculates  $z_{j+1} = \frac{1}{2} \sum_{q=1}^2 a_{j+1}^q$
  - 6: Global processor transmits  $z_{j+1}$  to all local processors.
  - 7: Local processor updates  $w^q$  as  $w_{j+1}^q = w_j^q + \rho(a_{j+1}^q - z_{j+1})$
  - 8: Local processor updates  $b_{j+1}^q$  using (6.12)
- 

### 4.2.3 Wide Area Damping Controller Design

To provide increased damping of inter-area oscillations supplementary control is required. The supplementary control is to be applied to the controllable generator, and it should work in parallel with other local controls of the generator. This supplementary control is called wide-area damping control. The input-output signal selection methodology for wide area damping controller is as discussed in Section-4.2.2. In the literature various wide area control are reported, however in this chapter wide-area damping controller design based on residue as reported in [5, 92] is adapted since the primary focus of this chapter is to study distributed approach for signal selection.

Fig. 4.4 shows the block diagram of the closed loop system with PSS and wide area

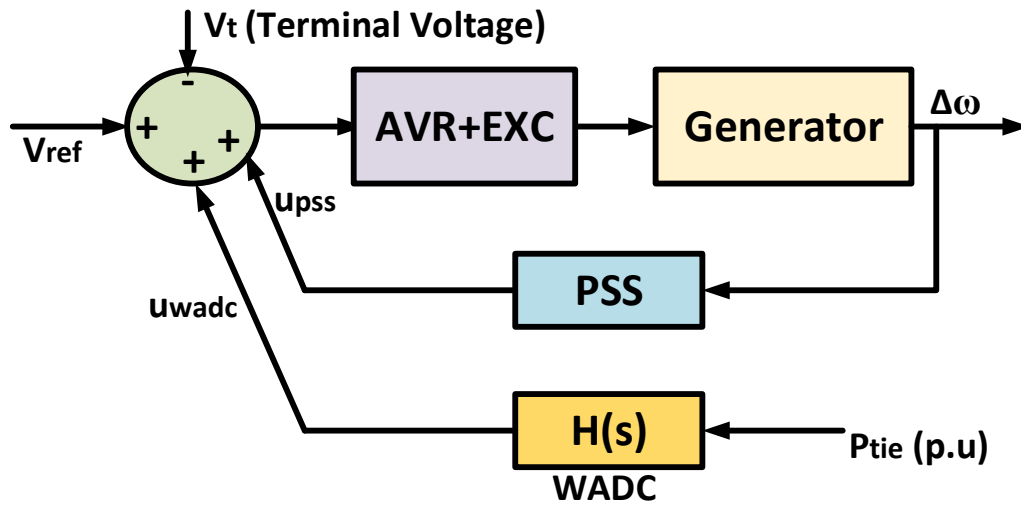


Fig. 4.4. Wide area control implementation.

controller  $H(s)$ .  $H(s)$  is represented as in (6.18).

$$H(s) = K_{WADC} \frac{sT_w}{1 + sT_w} \left[ \frac{1 + sT_{lead}}{1 + sT_{lag}} \right]^m \quad (4.20)$$

where  $K_{WADC}$  is the wide area controller gain,  $T_w$  is the washout time constant (usually 5 - 10 sec),  $T_{lag}$  and  $T_{lead}$  are the lag and lead time constant respectively, and  $m$  is the number of compensating blocks. Fig. 4.5 shows the flowchart for WADC design. The methodology of designing parameters for WADC is discussed in [5, 92], so further details are not presented here.

### 4.3 Experimental Setup for Implementing the Proposed Signal Selection Method

The proposed algorithm for signal selection and damping controller is implemented using RTDS/RSCAD and MATLAB co-simulation platform [107]. The power system is modeled and simulated in RTDS/RSCAD whereas MATLAB sessions act as local

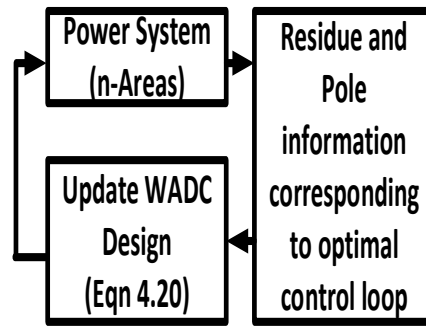


Fig. 4.5. Flowchart for WADC design.

and global processors. Both the MATLAB and RTDS communicate with each other using GTNET-SKT hardware interface. Each area sends the required generator input ( $u_n$ ) and tie-line power flow data to the local processors through the GTNET-SKT connection. Local processors will process the data, estimate a local transfer function, and then communicates with the global processor to obtain a consensus-based global transfer function. Based on the global transfer function the wide area control loop and design of WADC are updated. Using the updated WADC design, the local areas will send control actions to the generators. The simulation time step in RTDS is  $50\mu s$  (20000 samples/sec) but for the small signal stability analysis simulation time step of 20ms (50 samples/sec) is sufficient to preserve inter-area modes (0.1Hz to 1Hz). To reduce the data processing and computational time the data is down-sampled from 20000/sec to 50 samples/sec such that inter-area modes are preserved for small signal stability analysis. The experimental testbed is as shown in Fig. 4.6.

#### 4.4 Implementation Test Results

The proposed algorithm is initially implemented on the two-area power system model which consists of four generators each 900 MVA. Then to further validate the

algorithm on a larger system, IEEE 39 bus system which consists of 39 buses, 10 generators is used. The first step in implementing the algorithm is to identify/divide the system into areas based on coherency grouping or based on the real physical geography of the larger power system. Using the online coherency grouping technique two-area (Fig. 4.7) and IEEE 39 bus system (Fig. 4.8) are divided into groups as shown in Table. 6.1.

Table 4.1  
Coherency grouping of generators

Test System	Grouping
Two Area	Group-1: 1,2
	Group-2: 3,4
IEEE 39-BUS	Group-1: 4,5,6,7,9
	Group-2: 1,8
	Group-3: 2,3
	Group-4: 10

#### 4.4.1 Implementation test results using two-area system

In this case, the two-area system as shown in Fig. 4.7 is used. With an input signal as shown in Fig. 4.3 and tie line power flow as the output, MIMO transfer function is estimated locally for each area, and then local processor communicates with the global processor to arrive at a global solution. To validate the algorithm during an inter-area oscillation, a fault is created on bus 8 at 0.25sec and cleared at 0.45sec. In this case, residue analysis is performed by solving the global consensus problem. With estimation based on global consensus, it is found that the frequency of oscillation is 0.6667 Hz which is in consensus with the tie-line power oscillation frequency as shown in Fig. 4.9. The frequency and residue (magnitude and angle) information give the

optimal wide area control loop, and this information is also critical for damping controller design. From Table. 5.2 it can be seen that the control loop between  $P_{tie1}$  and Gen-3 has the highest value of residue for the inter-area mode of 0.6548 Hz. Based on this it can be concluded that Generator-3 is most controllable and tie-line (Bus7-Bus8-Bus9) power flow is the most observable signal. This means input to WADC should be the tie-line power flow and output should be fed to Generator-3.

To study the effectiveness of the proposed algorithm, the performance is tested with the presence of different generator controllers like:

- With exciter
- With exciter and PSS
- With exciter and WADC
- With exciter, PSS, and WADC

Table 4.2  
Residue analysis of two-area system

	Residue		Frequency (Hz)	
	$P_{tie1}$	$P_{tie2}$	$P_{tie1}$	$P_{tie2}$
Gen-1	1.4649	1.3823	0.6563	0.6562
Gen-2	0.7893	0.7463	0.6572	0.6571
Gen-3	14.4958	13.3761	0.6548	0.6548
Gen-4	4.16	3.9402	0.6577	0.6578

Fig. 4.10 and Fig. 4.11 shows the relative speeds of generators-1 and generator-3 with respect to generator-2 (swing) respectively. Fig. 4.12 shows the active power flow deviation through tie-lines and Fig. 4.13 shows the wide area controller action.

Table 4.3  
IEEE 39-bus control loop  
(fault on bus-14)

	Observable	Controllable	Residue
	Line (Bus15-Bus14)	Gen-6	5.5871
High	Line (Bus9-Bus39)	Gen-3	4.6915
	Line (Bus1-Bus39)	Gen-1	2.4572
	Line (Bus26-Bus25)	Gen-5	0.2753
Low	Line (Bus4-Bus3)	Gen-3	0.1512
	Line (Bus3-Bus4)	Gen-1	0.1175

Based on the above results it can be seen that WADC is effective in damping inter-area oscillations using the optimal wide area control loop. It can be seen that the proposed approach provides better damping of oscillations.

#### 4.4.2 Implementation test results using 39-bus system

To further validate the proposed algorithm on the larger system and to test the algorithm for various fault scenarios IEEE 39-bus system is used. Further, the effect of selecting a wrong control loop is also analyzed here. Here WADC (Strong) represents a strong wide-area control loop, and WADC (Weak) represents weak wide-area control loop.

##### 4.4.2.1 Scenario:1 Fault on Bus-14

A three-phase fault is created on Bus-14 for 0.1 sec at 2 sec. Table. 4.3 shows the three control loops for each area with high and low residues. Using this information the effect of strong and weaker control loops are analyzed. Fig. 4.14 shows the strong and weak control loops for the fault on bus-14.

Fig. 4.15 and Fig. 4.16 shows the active power deviation of the lines connected

Table 4.4  
Controller performance comparison  
(fault on bus-14)

Controller	Active Power Deviation (MW) at 4.3s (Fig. 4.15)	Relative Speed (rad/s) at 3.9s (Fig. 4.17)
Exciter	-187.54	-1.4952
Exciter+PSS	-132.1754	-1.1272
Exciter+WADC (Strong)	-46.044	-0.6330
Excite+PSS+WADC (Strong)	-68.37	-0.4670
Exciter+WADC (Weak)	-171.7852	-1.4570
Exciter+PSS+WADC (Weak)	-129.5395	-1.1267

between Bus17-Bus18 and Bus1-Bus39 respectively. Fig. 4.17 and Fig. 4.18 shows the relative speed between generator 4 and generator 6 w.r.t swing generator-2 respectively. Fig. 4.19 shows the wide area control output for the case with PSS. Table. 4.4 shows the active power deviation and relative speed at a sample point (trough of oscillation here). From the Table. 4.4 it can be seen that when compared to Exciter only case, addition of a PSS reduced oscillations by 29.52%, addition of WADC (Strong) reduce the oscillation by 63.54%, addition of PSS and WADC (Strong) reduce the oscillation by 75.45%, with the addition of WADC (Weak) the oscillations reduce by 8.4%, and with the addition of PSS and WADC (Weak) the oscillations reduce by 30.93%. Whereas the relative speed oscillations with PSS, WADC (Strong), PSS and WADC (Strong), WADC (Weak), PSS and WADC (Weak) are reduced by 24.61%, 57.66%, 68.77%, 2.55%, and 24.65% respectively. It can be concluded that with WADC the oscillations are damped much more effectively; however, it can also be seen that with WADC the oscillations are damped effectively if the optimal control loop is strong.

Table 4.5  
IEEE 39-bus control loop  
(fault on bus-25)

	Observable	Controllable	Residue
	Line (Bus39-Bus1)	Gen-10	7.8621
High	Line (Bus39-Bus9)	Gen-10	6.9582
	Line (Bus1-Bus39)	Gen-8	4.1673
	Line (Bus15-Bus14)	Gen-5	0.5836
Low	Line (Bus26-Bus25)	Gen-9	0.3949
	Line (Bus4-Bus3)	Gen-2	0.3936

#### 4.4.2.2 Scenario:2 Fault on Bus-25

Similarly, in this scenario, a three-phase fault is created on Bus-25 for 0.1 sec at 2 sec. Table. 4.5 shows the three control loops for each area with high and low residues. Using this information the effect of strong and weaker control loops are analyzed.

Fig. 4.20 and Fig. 4.21 shows the active power deviation of the lines connected between Bus17-Bus18 and Bus1-Bus39 respectively. Fig. 4.22 and Fig. 4.23 shows the relative speed between generator 4 and generator 6 w.r.t swing generator-2 respectively. Fig. 4.24 shows the wide area control output for the case with PSS. Table. 4.6 shows the active power deviation and relative speed at a sample point (trough of oscillation here). From the Table. 4.4 it can be seen that when compared to Exciter only case, addition of a PSS reduced oscillations by 19.68%, addition of WADC (Strong) only reduce the oscillation by 63.27%, addition of PSS and WADC (Strong) reduce the oscillation by 74.04%, with the addition of WADC (Weak) the oscillations reduce by 3.4%, and with the addition of PSS and WADC (Weak) the oscillations reduce by 28.62%. Whereas the relative speed oscillations with PSS, WADC (Strong),

Table 4.6  
Controller performance comparison  
(fault on bus-25)

Controller	Active Power Deviation (MW) at 4.3s (Fig. 4.20)	Relative Speed (rad/s) at 3.9s (Fig. 4.22)
Exciter	-192.39	-1.52
Exciter+PSS	-154.52	-1.26
Exciter+WADC (Strong)	-70.67	-0.73
Excite+PSS+WADC (Strong)	-49.95	-0.57
Exciter+WADC (Weak)	-185.78	-1.4894
Exciter+PSS+WADC (Weak)	-137.3218	-1.2321

PSS and WADC (Strong), WADC (Weak), PSS and WADC (Weak) are reduced by 17.11%, 51.97%, 62.50%, 2.01%, and 18.94% respectively. It can be concluded that with WADC the oscillations are damped much more effectively; however, it can also be seen that with WADC the oscillations are damped effectively if the optimal control loop is strong.

Further to compare the effectiveness of the proposed algorithm, the norms of different oscillation cases are compared with exciter only case. The relative error metric is given by (5.7).

$$relative\ error = \frac{\|y_{exc} - y_{act}\|_2}{\|y_{exc}\|_2} \quad (4.21)$$

where  $y_{exc}$  is the data with exciter only,  $y_{act}$  is the data with other cases as shown in Table. 4.7, and  $\| \cdot \|$  is the 2-norm of a vector. Using the relative error metric, it can be observed that the larger the error between with exciter only case and other cases with supplementary controls like PSS and WADC, more effective is the damping.

Table 4.7  
Relative error comparison

Variable	Case-1	Case-2	Case-3	Case-4	Case-5
Fig. 4.17	0.7146	0.6732	0.4107	0.4230	0.3137
Fig. 4.18	0.7587	0.6667	0.4232	0.4403	0.3
Fig. 4.15	0.6831	0.6014	0.3773	0.3704	0.2327
Fig. 4.16	0.6552	0.5687	0.3388	0.3368	0.1733
Fig. 4.22	0.6228	0.5519	0.2061	0.2543	0.1013
Fig. 4.23	0.6254	0.5391	0.1998	0.2545	0.1021
Fig. 4.20	0.6093	0.54061	0.1938	0.2728	0.1003
Fig. 4.21	0.6004	0.5367	0.1906	0.2125	0.1320

Case1: Exciter+PSS+WADC (Strong), Case2: Exciter+WADC (Strong)

Case3: Exciter+PSS, Case4: Exciter+WADC (Weak)

Case5: Exciter+PSS+WADC (Weak)

#### 4.5 Summary

The proposed method for selection of optimal control loop for wide area control using ADMM based distributed algorithms overcome the drawbacks of earlier methods reported in the literature. In this approach, the interconnected power system is divided into areas, and then using measurements a multi-input-multi-output (MIMO) black-box transfer function model is estimated locally for each area based on the Lagrange multipliers method. The local area processors will then communicate with the global processor to estimate a global transfer function model of the power system. The information of residue corresponding to inter-area mode pole obtained from global transfer function is used for selecting an optimal wide area control loop and to design WADC. The efficacy of the proposed distributed approach is validated using two-area and IEEE 39 bus power system models on RTDS/RSCAD and MATLAB

co-simulation platform. From the simulation results, it is found that the proposed distributive method applicability in damping inter-area oscillations effectively. In the next chapter, frequency-based reduced order modeling is introduced.

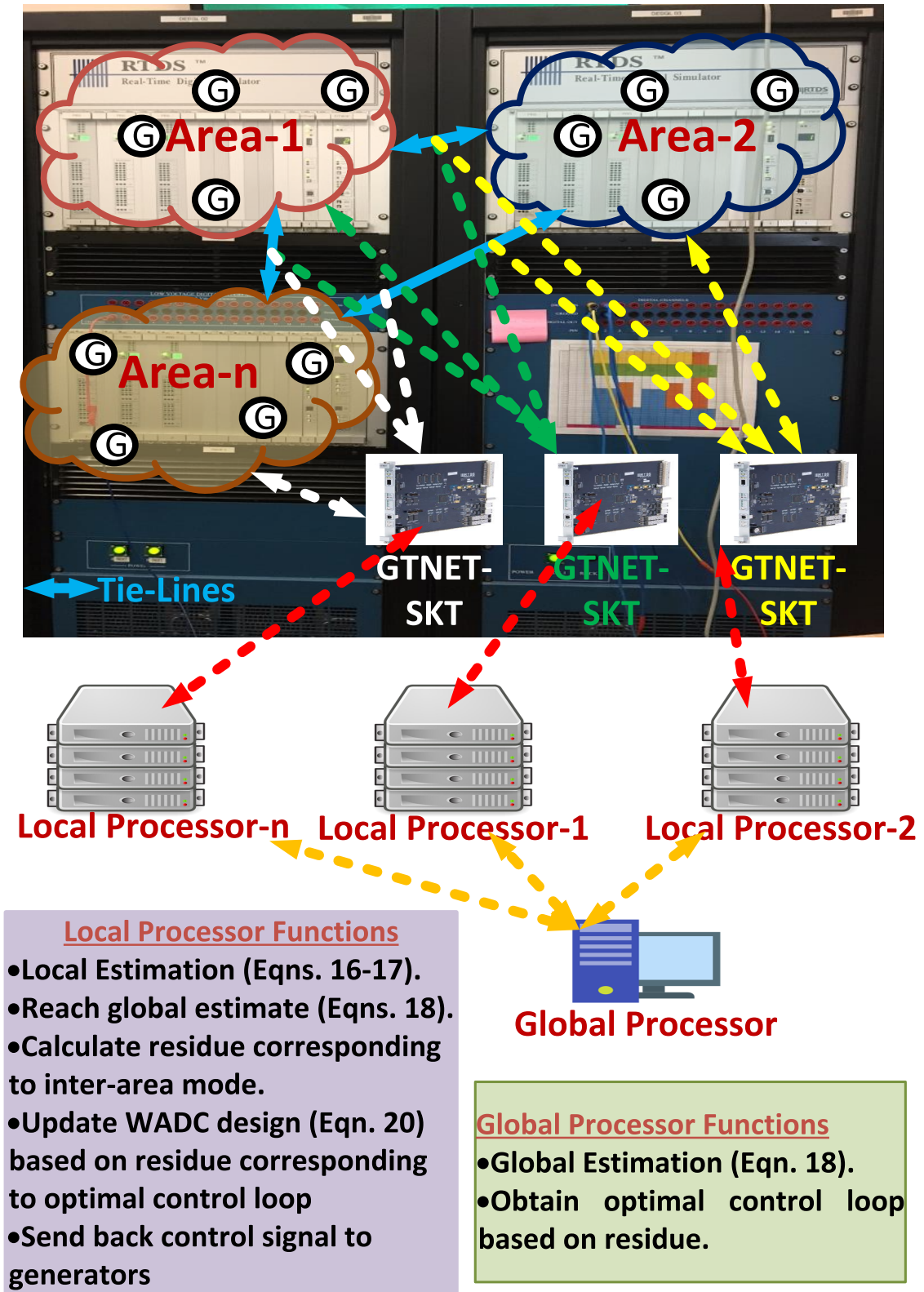


Fig. 4.6. Experimental test bed.

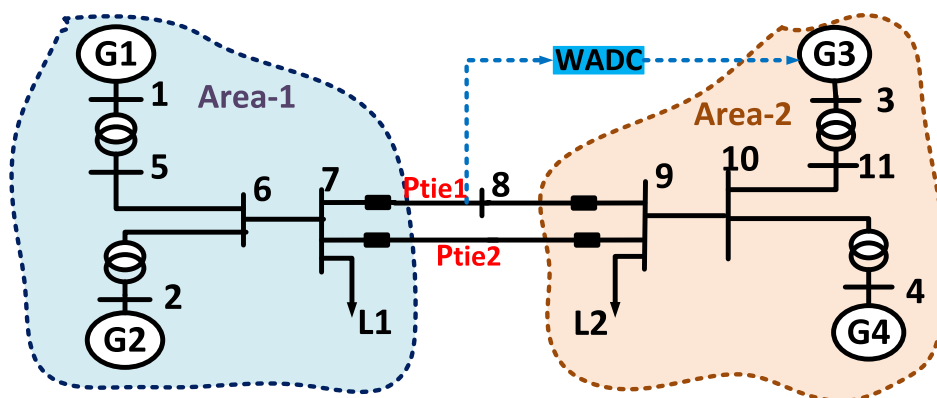


Fig. 4.7. Two area test system.

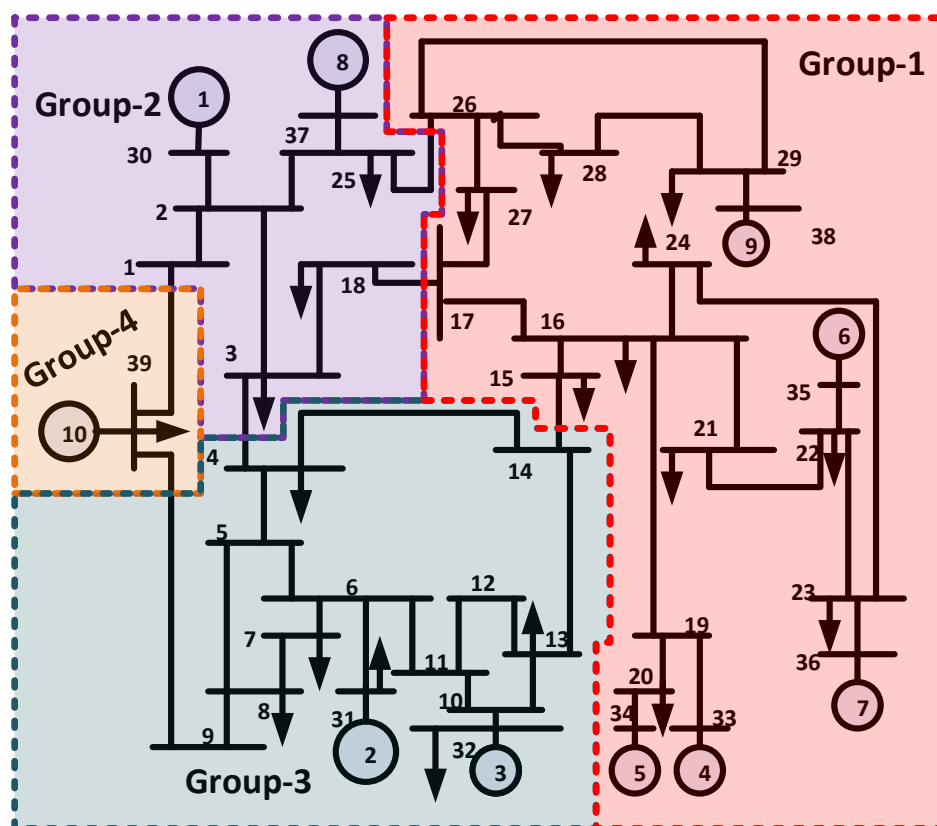


Fig. 4.8. IEEE-39 bus test system model.

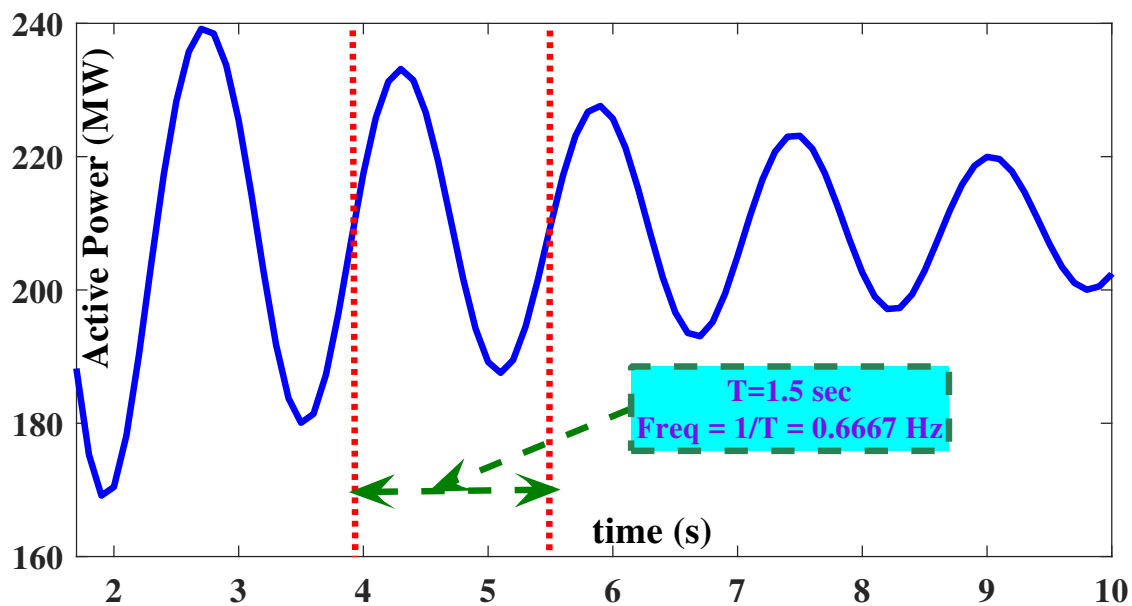


Fig. 4.9. Tie-line power flow (Bus7-Bus8-Bus9).

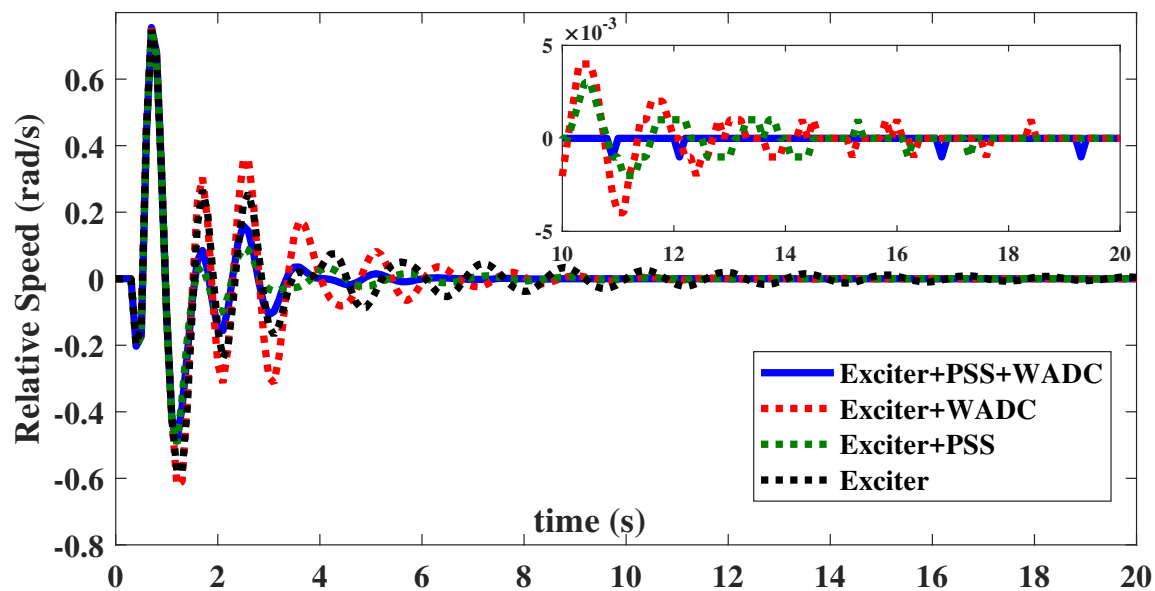


Fig. 4.10. Relative speed between generator-1 and generator-2.

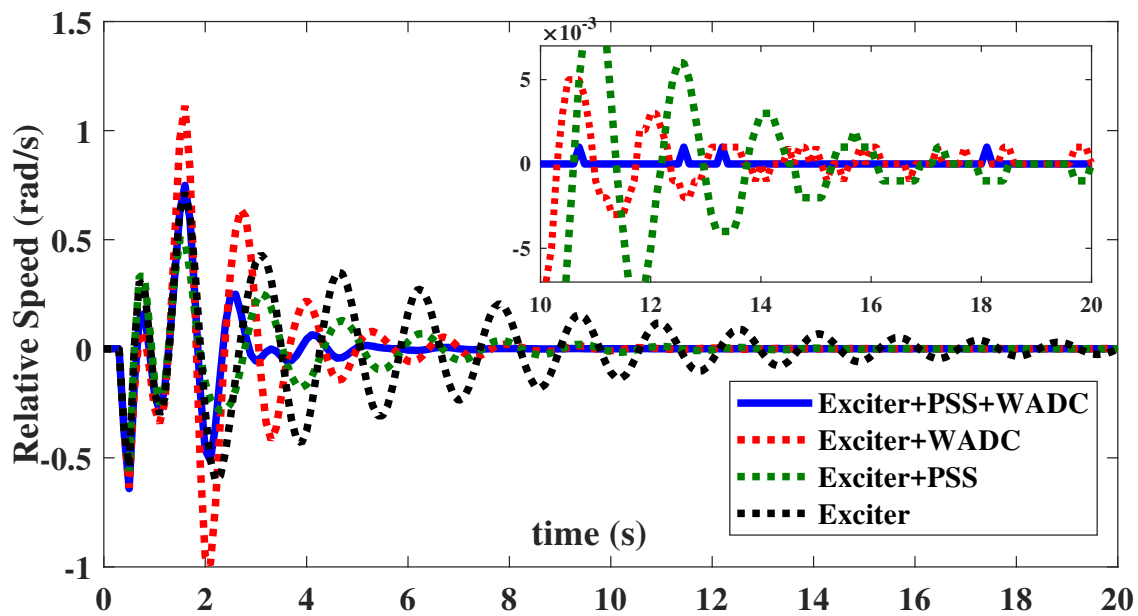


Fig. 4.11. Relative speed between generator-3 and generator-2.

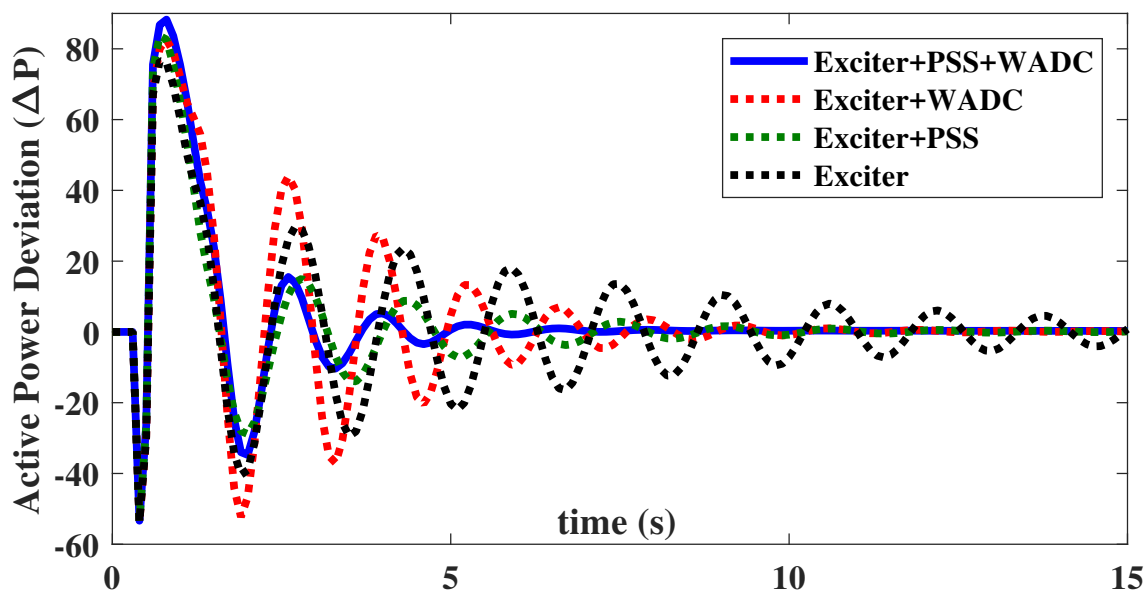


Fig. 4.12. Active power deviation through tie-line (Bus7-Bus8-Bus9).

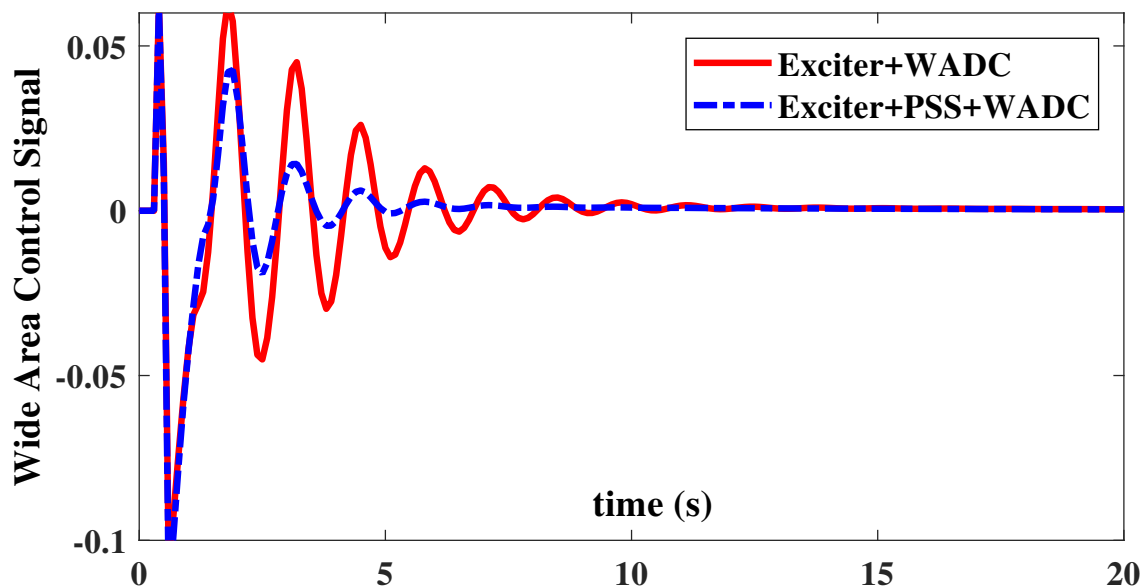


Fig. 4.13. Wide area control signal to generator-3.

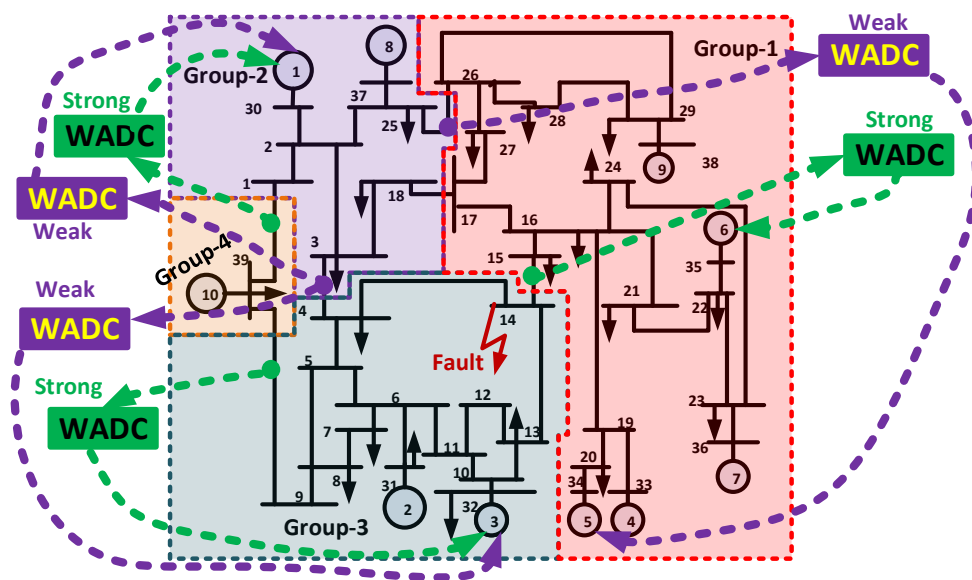


Fig. 4.14. Control Loops for IEEE-39 Bus (Bus-14 fault).

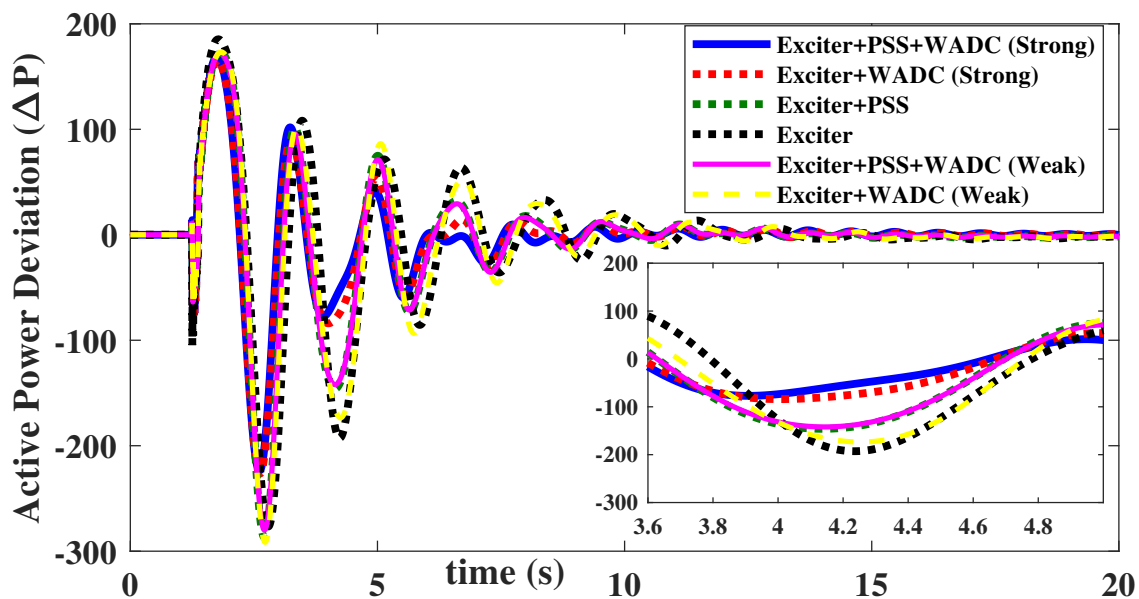


Fig. 4.15. Active power deviation (Bus17-Bus18).

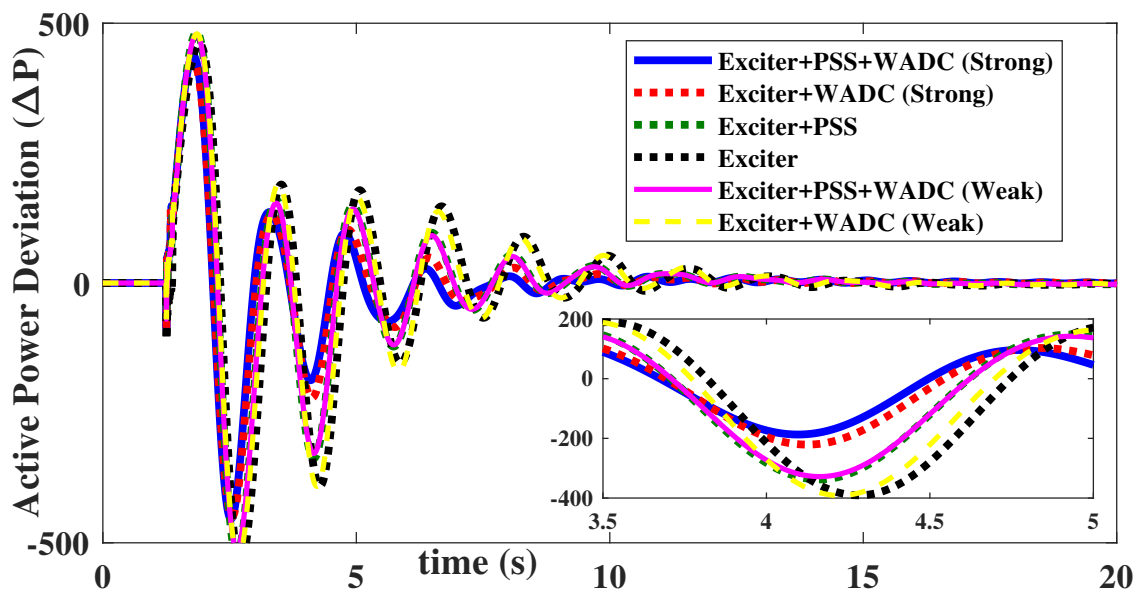


Fig. 4.16. Active power deviation (Bus1-Bus39).

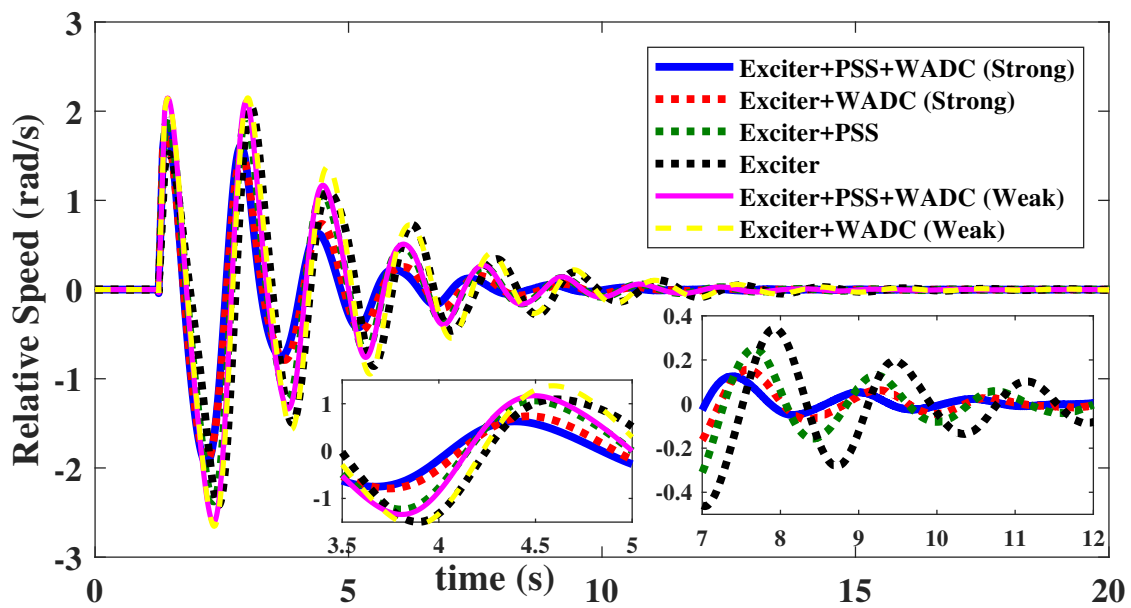


Fig. 4.17. Relative speed between generator 2 and generator 4.

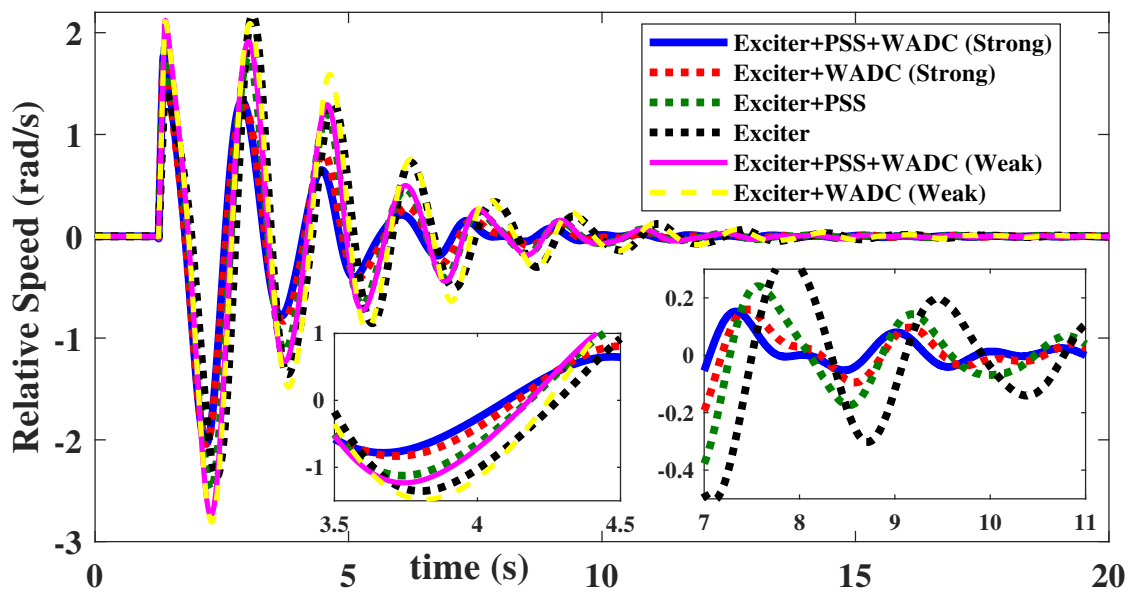


Fig. 4.18. Relative speed between generator 2 and generator 6.

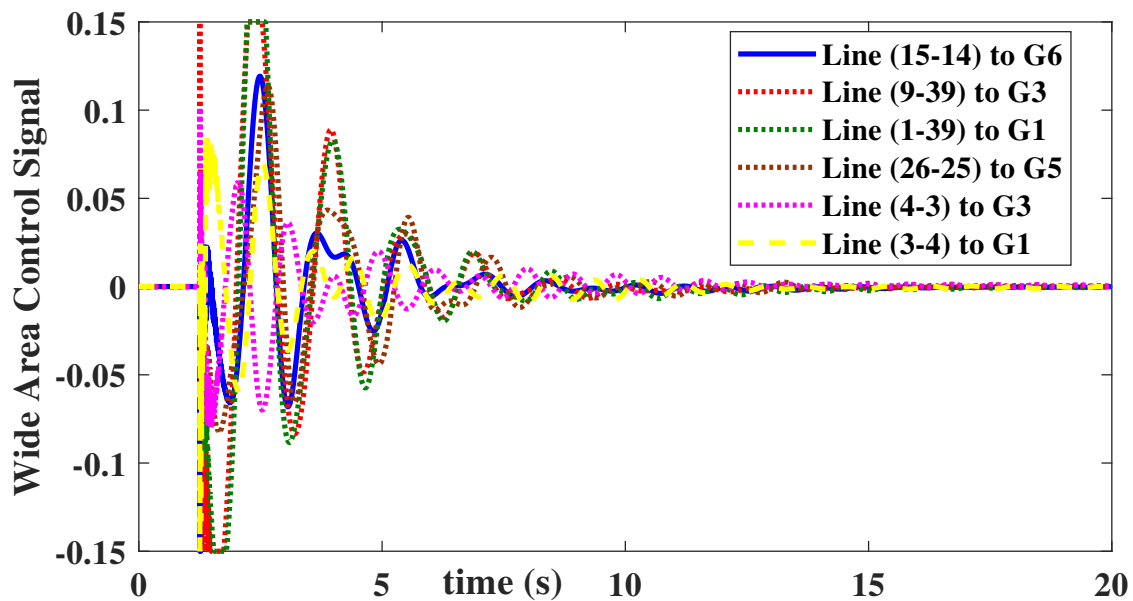


Fig. 4.19. Wide area control output with PSS.

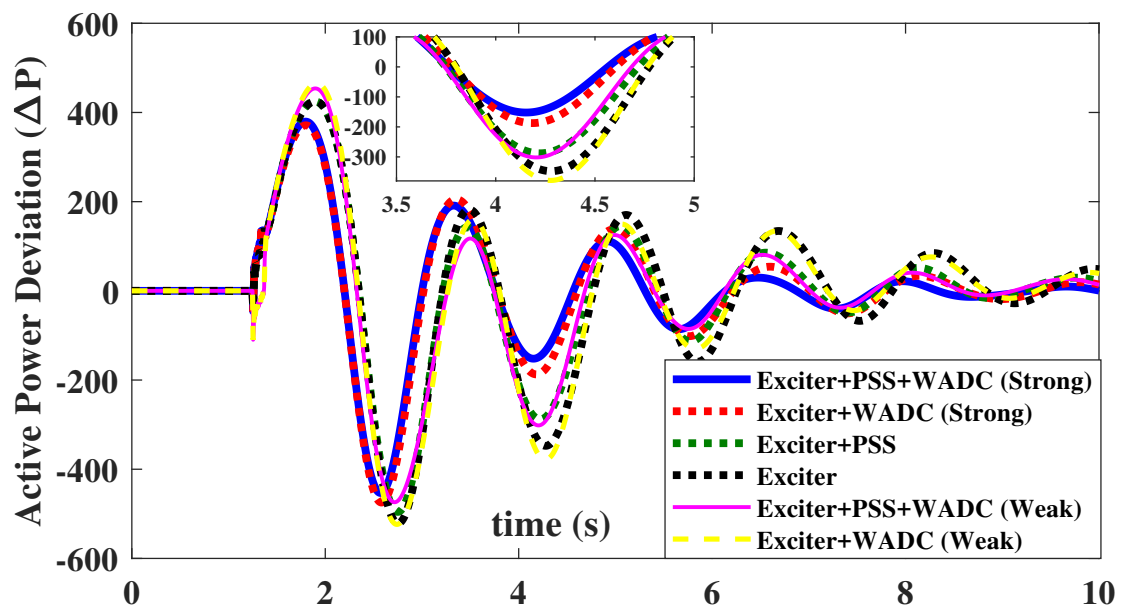


Fig. 4.20. Active power deviation (Bus1-Bus39).

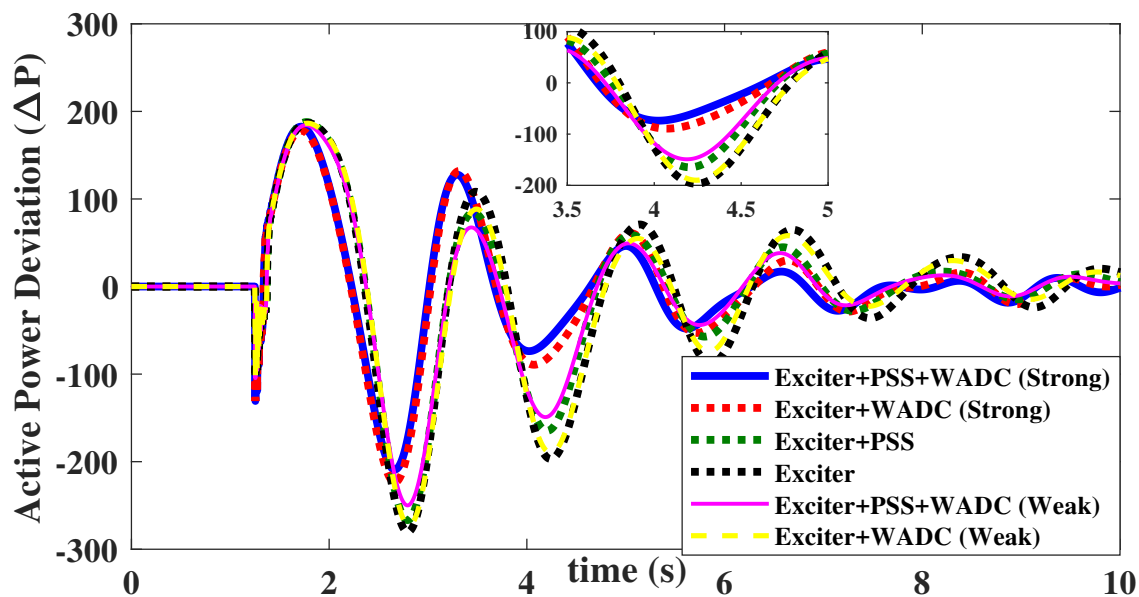


Fig. 4.21. Active power deviation (Bus17-Bus18).

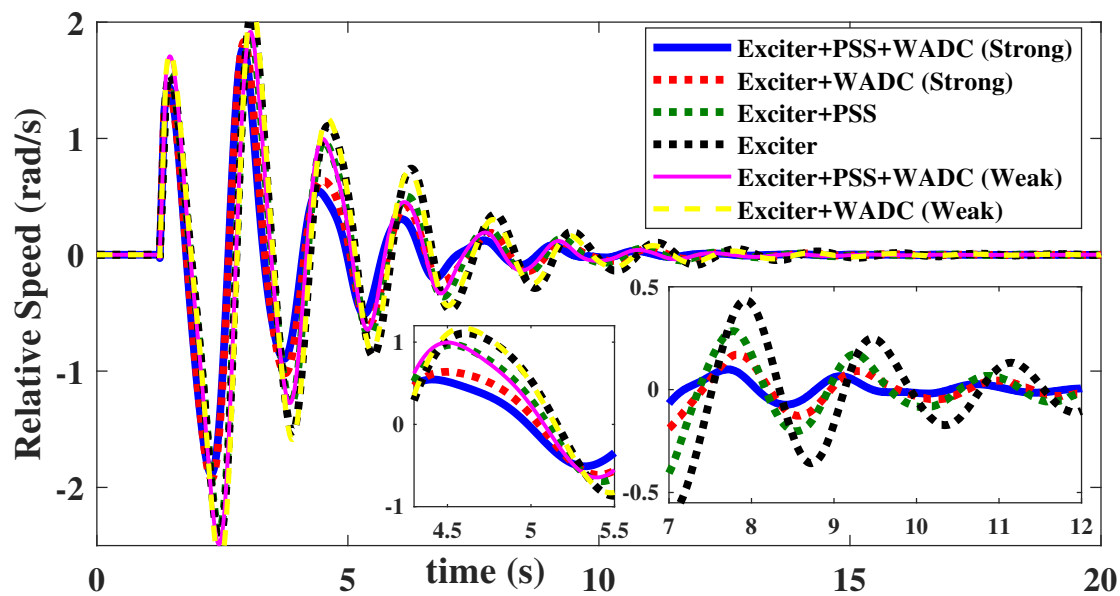


Fig. 4.22. Relative speed between generator 2 and generator 4.

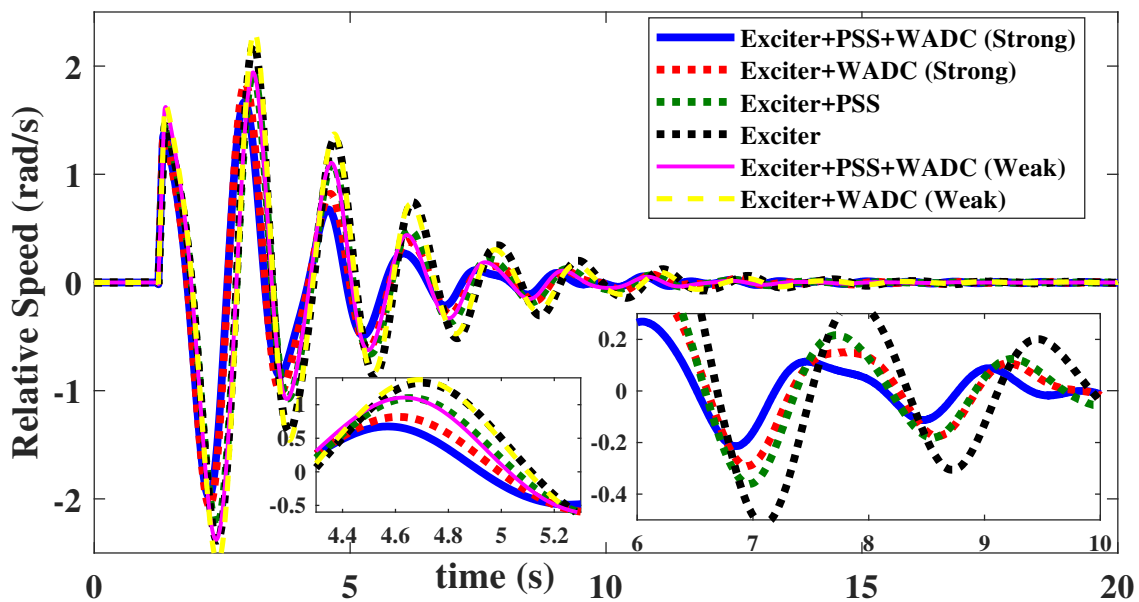


Fig. 4.23. Relative speed between generator 2 and generator 6.

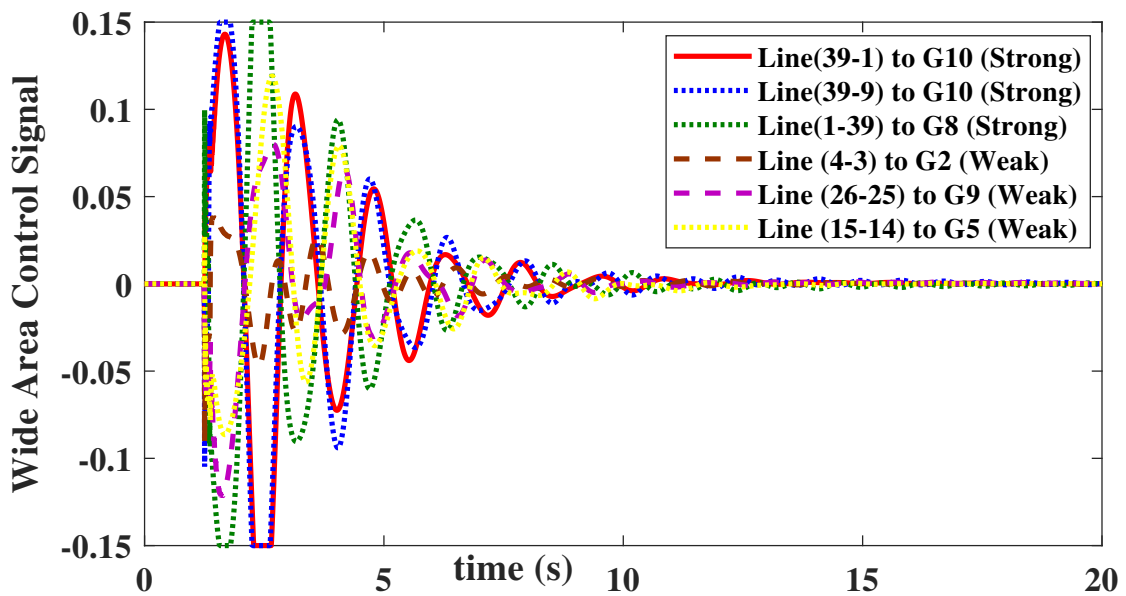


Fig. 4.24. Wide area control output with PSS.

## CHAPTER 5: DEVELOPMENT AND APPLICABILITY OF ONLINE PASSIVITY ENFORCED WIDE-BAND MULTI-PORT EQUIVALENTS FOR HYBRID TRANSIENT SIMULATION

This chapter presents a method for developing single and multi-port Frequency Dependent Network Equivalent (FDNE) based on a passivity enforced online recursive least squares (RLS) identification algorithm which identifies the input admittance matrix in  $z$ -domain. Further, with the proposed architecture, a real-time hybrid model of the reduced power system is developed that integrate Transient Stability Analysis (TSA) and FDNE. Main advantages of the proposed architecture are, it identifies the FDNE even with unknown network parameters in the frequency range of interest, and yet can be implemented directly due to discrete formulation while maintaining desired accuracy, stability and passivity conditions. The accuracy and characteristics of the proposed method are verified by implementing on two area and IEEE 39-bus power system models.

### 5.1 Introduction

Real-time electromagnetic (EMT) simulation requires detailed modeling of transmission systems to understand the effect of transients and harmonics arising due to varying operating conditions and disturbances in power grid. Effect of power electronic components associated with renewable energy sources on the power grid and performance of different controllers can be analyzed using EMT simulations. Typi-

cally, integration time step of EMT simulation is in microseconds ( $\mu s$ ). This makes modeling of a large transmission system for EMT studies impractical as detail modeling increases complexity and computational burden. One solution is to model the transmission system as TSA type simulations with larger integration time as TSA simulations can run faster than EMT. However, in TSA type, due to large integration time, the high-frequency behavior of the system is not preserved making this approach not very accurate.

Another approach is to model the large transmission network as frequency dependent reduced order systems that can represent the power grid under any operating condition. One way to reduce large power grid is to model part of the network which is of interest (study area) in detail and the remainder of the system (external area) by an efficient equivalent such as FDNE. In this process, initially, the network is divided into study and external area based on the coherency grouping of generators such that all coherent generators are present in the external area. The boundary between the study and external area is divided considering the fact that interconnecting points should have the least minimum number of ports. Generally, in TSA type equivalent, the network admittance is evaluated only at the fundamental frequency; hence this representation ignores high-frequency oscillations. The high-frequency behavior of the external area can be preserved by using FDNE; however, FDNE ignores electromechanical oscillations. To cover both electromechanical and high-frequency response, the external area should be modeled as a combination of TSA equivalent and FDNE.

FDNEs are generally formulated as frequency-dependent black-box terminal equivalents based on rational functions. The methodologies reported in the literature are

discussed in Section 1.4.

However, state-of-the-art algorithms formulate FDNE with continuous domain transfer function which makes it very complicated to implement in the real-time simulator (EMT based). Also, in many of these methods FDNE formulation is dependent on the availability of admittance data over a wide range of frequency; however, the availability of data is not guaranteed. Further, off-line calculation of admittance over a wide frequency range, and storing and retrieving of the data for curve fitting is tedious and time-consuming. For example, if the frequency range of interest is from 0 to 5000 Hz with a step size of 0.1 Hz, one should construct 50001 admittance matrices at each frequency sample which is extremely complicated to compute. This complexity increases with the sample size of frequencies, the number of ports, and the size of the network under consideration.

This chapter introduces a novel method for formulating FDNEs based on the online recursive least square identification. In this method, the external area is energized with constant voltage source at the boundary buses after all the voltage sources, and current sources in the network are short-circuited and open circuited respectively. Subsequently, by tracking input voltage and output current, FDNE is formulated. The proposed method simplifies FDNE formulation which is independent of the availability of network parameters over a wide frequency range and reduces complexity in implementing FDNE by formulating it in discrete domain directly. Also by using Kron's node elimination method external area network size is reduced and all generators are aggregated for further reduction in computational burden. The advantages of the proposed architecture are:

- FDNE formulation is independent of the availability of network parameters over a wide frequency range.
- The architecture formulates FDNE in discrete domain, which reduces complexity in interfacing FDNE with the real-time simulator.
- The architecture formulates coherency based network equivalents of complex networks with the less computational burden and desired accuracy.
- The methodology enforces stability and passivity conditions to ensure stable EMT simulations.
- The methodology can be directly implemented for real-time control [108].

The rest of the chapter is organized as follows: In Section 5.2 overall architecture is discussed. In Section 5.3 implementation test on the interconnected power grid is discussed and Section 5.5 summarizes the chapter.

## 5.2 Proposed Methodology

In large power grids, it has been frequently observed that after disturbances the generators swing together in groups, meaning units near a disturbance respond faster and together, whereas distant machines show relatively damped oscillatory behavior. This physical property is known as *coherency* and a group of machines with similar responses are termed coherent generators. In our work, the generators are coherently grouped based on a localness index. Further, the power system model order reduction is performed by dividing the original system into a *study* area and an *external* area. The proposed method further divides the external area into two parts. The first one

is a low-frequency equivalent (TSA) and the second one is high-frequency equivalent (FDNE). The reduced order modeling of power system involves the following steps:

### 5.2.1 Aggregation of External Area for TSA type modeling and Real-time Integration

For retaining the electromechanical behavior of the system under consideration aggregated TSA model is used. Fig. 7.2 shows the flowchart for TSA type modeling.

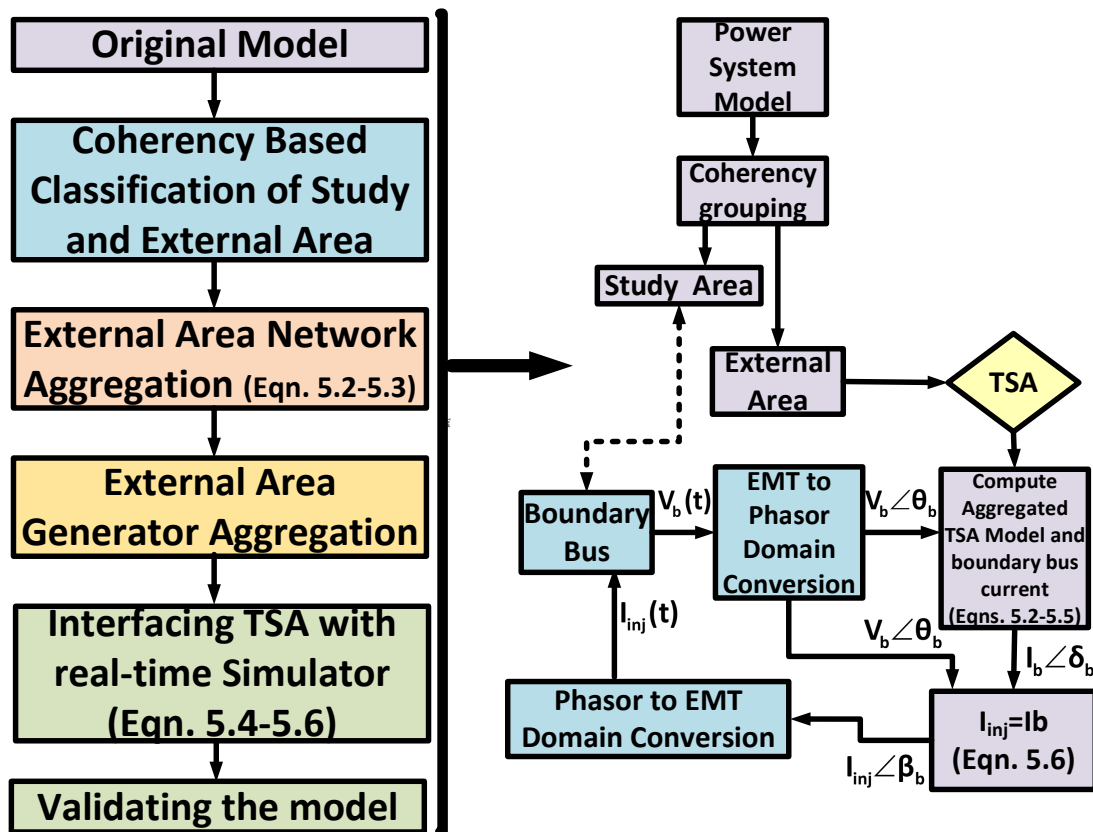


Fig. 5.1. The conceptual and functional flowchart for TSA type modeling

### 5.2.1.1 Coherency Based Classification of Study and External Area

For coherency grouping of the power system under study, initially the small signal stability study of the power grid model is performed, and the generator electromechanical modes of oscillation are evaluated. Further, based on the participation factors of all the generators, a localness index is calculated as follows:

$$L_{index} = \sum_{i=1}^n (1 - P_{ki})^n \quad (5.1)$$

where  $n$  is a number of synchronous generators connected in the system and,  $P_{ki}$  is the normalized participation factor of the  $k^{th}$  machine in the  $i^{th}$  mode. For example, Table. 6.1 shows the coherency grouping of generators for IEEE 39 bus system based on the localness index. More details of the localness index are discussed in [36].

Table 5.1  
Coherency grouping of generators for IEEE 39 bus system

<b>Group</b>	I	II	III	IV
Generators	4,5,6,7,9	1,10,8	3	2

### 5.2.1.2 Network Aggregation

For aggregating the external area network, the admittance matrix ( $Y_{n \times n}$ ) of the external area is formulated using the bus and line data (at 60Hz). For example, if there are  $n$  number of buses in the external area and we want to retain  $m$  buses (i.e.  $m = i + j$ , where  $j$  be the number of boundary buses and  $i$  is the number of generator buses) and eliminate the remaining  $n - m$  buses in the external area, then using Kron

node elimination method [3], reduced admittance matrix ( $Y_{red}$ ) can be obtained as:

$$Y_{red(m \times m)} = [Y_{m \times m} - Y_{m \times n} Y_{n \times n}^{-1} Y_{n \times m}] \quad (5.2)$$

$$\begin{bmatrix} I_{b(j \times 1)} \\ I_{g(i \times 1)} \end{bmatrix} = Y_{red(m \times m)} \begin{bmatrix} V_{b(j \times 1)} \\ V_{g(i \times 1)} \end{bmatrix} \quad (5.3)$$

where subscript  $b$  and  $g$  represents the boundary and generator buses respectively.

### 5.2.1.3 Generator and Associated Controller Aggregation

After network aggregation and generators are left intact, the reduced admittance matrix is of the size  $m \times m$  ( $m = i + j$ , i.e. there are  $j$  boundary buses and  $i$  generator buses). To further reduce computational burden and to reduce complexity in modeling, generators and associated controllers can be aggregated. With generator aggregation, the reduced admittance matrix is of the size  $(m - i + 1) \times (m - i + 1)$  ( $m = i + j$ , i.e.  $i$  coherent generators can be aggregated into one generator). Method of generator and controller aggregation is discussed in [21]. Thus additional details are not explained in the chapter.

### 5.2.1.4 Interfacing TSA type modeling with real-time simulator

In this step, voltages at the boundary buses is the input to the TSA block, where output currents from the TSA block is injected back to the boundary buses. Here, the generators are modeled in detail to observe the electromechanical behavior. Conversion of boundary bus voltage from time domain to phasor domain is then performed using discrete sequence analyzer [124]. The result gives magnitude  $|V_b|$  and, phase angle  $\angle V_b$ . Also, phase angle of  $V_b$  with reference to  $I_b$  can be determined as

$\theta_b = \angle\delta_b - \angle V_b$ , where  $\angle\delta_b$  is the angle of  $I_b$ . Then, using (7.4) the generator bus voltage is calculated.

$$V_g \angle\theta_g = (I_g \angle\delta_g - Y_{bb} V_b \angle\theta_b) Y_{gg}^{-1} \quad (5.4)$$

where,  $I_g$  is the generator current injection,  $\angle\delta_g$  is the angle of generator current,  $V_b$  is the boundary bus voltage,  $V_g$  is the generator bus voltage and,  $\angle\theta_g$  is the angle of generator bus voltage. Generator voltage  $V_g$  is calculated recursively every time step. From calculated  $V_g$  and boundary bus voltage  $V_b$ , boundary bus current injection  $I_{inj}$  is calculated as shown in (7.5)-(7.6).

$$I_b \angle\delta_b = Y_{bb} V_b \angle\theta_b + Y_{bg} V_g \angle\theta_g \quad (5.5)$$

$$I_{inj} \angle\beta_b = I_b \angle\delta_b \quad (5.6)$$

After calculating boundary bus current  $I_{inj} \angle\beta_b$  in phasor form, it is converted into the time domain and injected into the boundary bus. The overall implementation is shown in Fig. 7.2.

### 5.2.2 Study and analysis of TSA type equivalent modeling

For study and preliminary analysis, the TSA type equivalent is implemented on two area power system model as shown in Fig. 6.4. In this test system, area-1 consists of generators G1, G2, and area-2 consists of generators G3, G4 [106]. For analysis purpose, area-2 is considered as the external area with boundary bus as bus 10. Two cases are considered for the study. In the first case, the external area is modeled as TSA type equivalent with only network aggregation (*EMT+TSA Based Model*), and in the second case external area is modeled as TSA type equivalent with network and

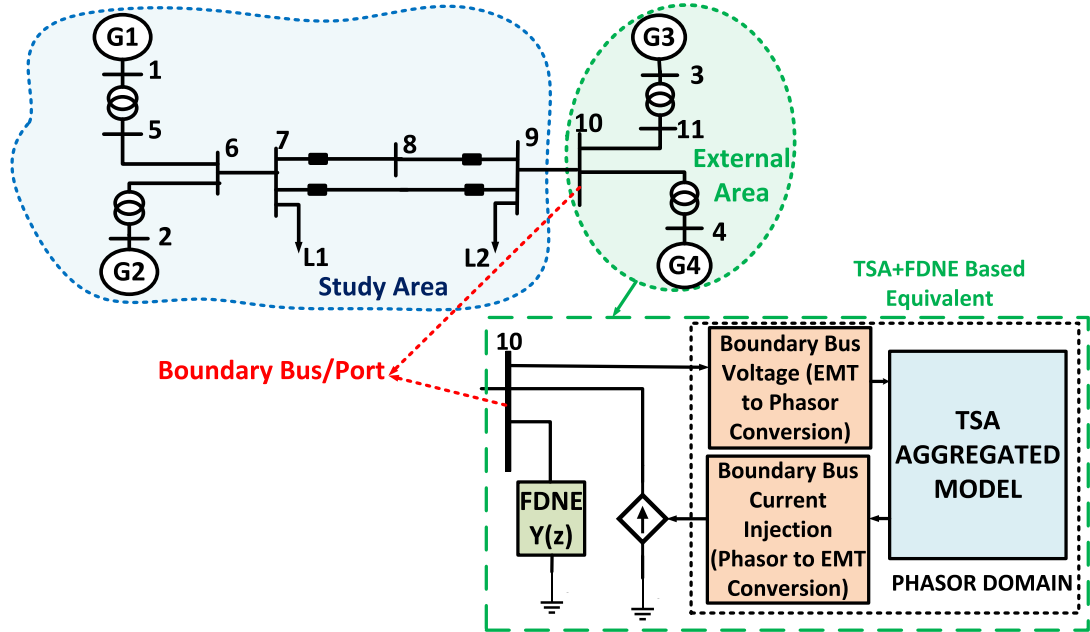


Fig. 5.2. Proposed dynamic equivalent of two area system

generator aggregation (*EMT+TSA Based Model (AGG)*). For both cases, the study area is modeled as full EMT. For benchmarking, both the test cases are compared with the full EMT model of external and study area (*EMT Based Model*).

Fig. 6.3 shows the comparison of the relative speed of Gen. 2 with respect to (w.r.t) gen. 1, and Fig. 6.6 shows the comparison of active power flow from bus 10 to bus 9. From Fig. 6.3, it can be observed that TSA type equivalent can preserve electro-mechanical oscillations, but high-frequency oscillations are not preserved as it can be seen from Fig. 6.6.

For quantitative analysis, relative error between the two cases and full EMT type model is calculated using (5.7). The results are tabulated in Table. 5.2.

$$relative\ error = \frac{\|y_{ref} - y_{act}\|_2}{\|y_{ref}\|_2} \quad (5.7)$$

where  $y_{ref}$  represents the output from full EMT model (*EMT Based Model*) and  $y_{act}$

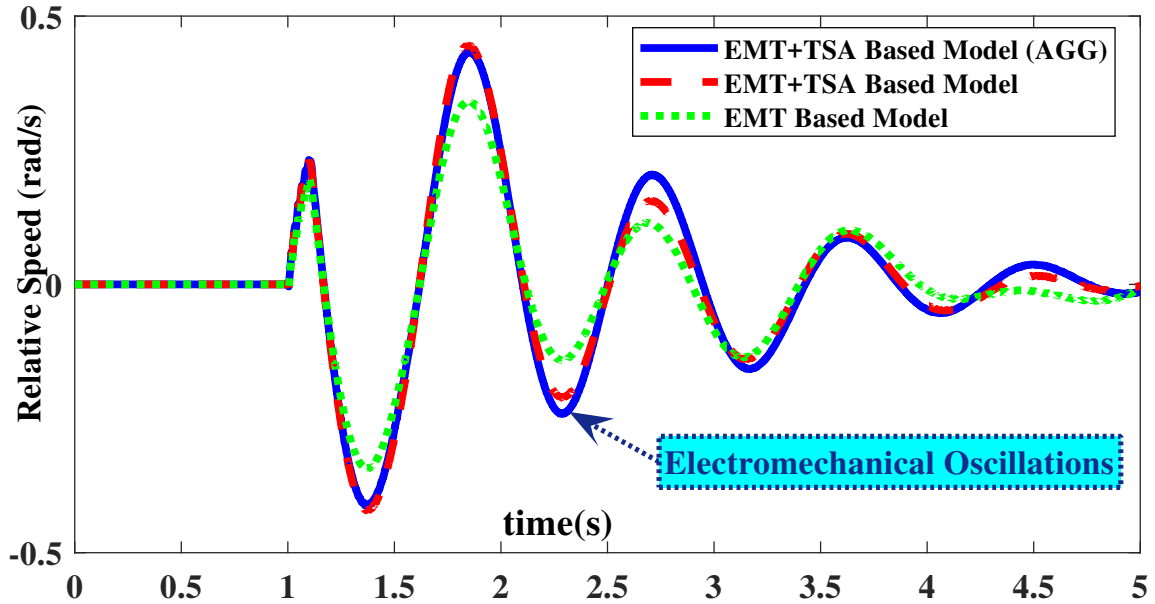


Fig. 5.3. The relative speed of Gen.2 w.r.t Gen.1

represents the output obtained in each case (*EMT+TSA Based Model (AGG)* and (*EMT+TSA Based Model*) respectively)

Table 5.2  
Comparison of reduced (EMT+TSA) and original (EMT) models

	EMT+TSA(AGG)	EMT+TSA
Fig. 6.3	0.3589	0.2998
Fig. 6.6	0.0356	0.0351

It can be seen that the aggregated model has a significant error. This motivates the use of FDNE representations.

### 5.2.3 FDNE Formulation and Real-time simulator Integration

For retaining the high frequency behavior of the system under consideration, FDNE is formulated. Fig. 6.7 shows the FDNE modeling flowchart. In this method, the external area is energized with constant voltage source with varying frequency in steps (from few Hz to kHz) after short circuiting all voltage sources, and open circuiting

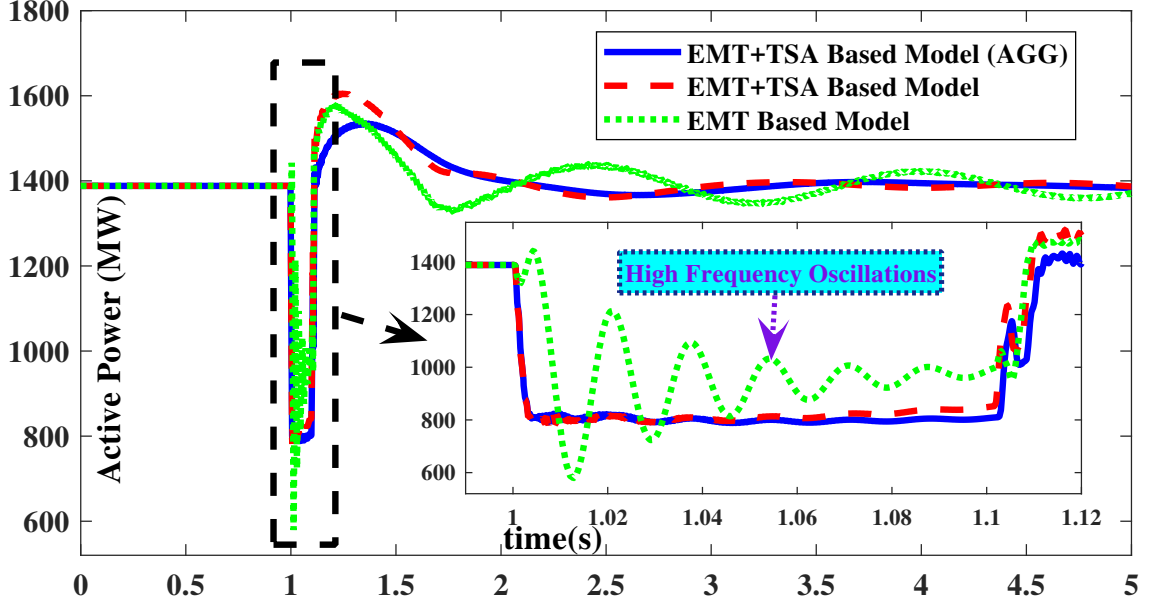


Fig. 5.4. Active power flow from bus 10 to bus 9

all current sources. By tracking input voltage and output current, FDNE is then formulated in  $z$ -domain using RLS. The basic principle is as follows. If  $V_F$  is the voltage input to the boundary bus and  $I_F$  is the current output from the boundary bus, then frequency dependent admittance ( $Y_{fit}$ ) can be written as

$$Y_{fit}(z^{-1}) = \frac{I_F(k)}{V_F(k)} = \frac{b_1 z^{-1} + b_2 z^{-2} + \dots + b_n z^{-n}}{1 + a_1 z^{-1} + a_2 z^{-2} + \dots + a_n z^{-n}} \quad (5.8)$$

where  $k$  is the number of samples. For a  $m$ -port network (that means  $m$  boundary buses),  $Y_{fit}$  can be represented as in (6.7), where  $Y_{fit(m,p)}$  and  $Y_{fit(m,m)}$  in (6.7) are the self and mutual admittance respectively. FDNE model formulation and validation involves the following steps.

#### 5.2.3.1 Recursive Least Square Estimation

Identification of a dynamic process is performed every sample period using the process input  $u(k)$  and the process output  $y(k)$  at every sample  $k$ . Considering the

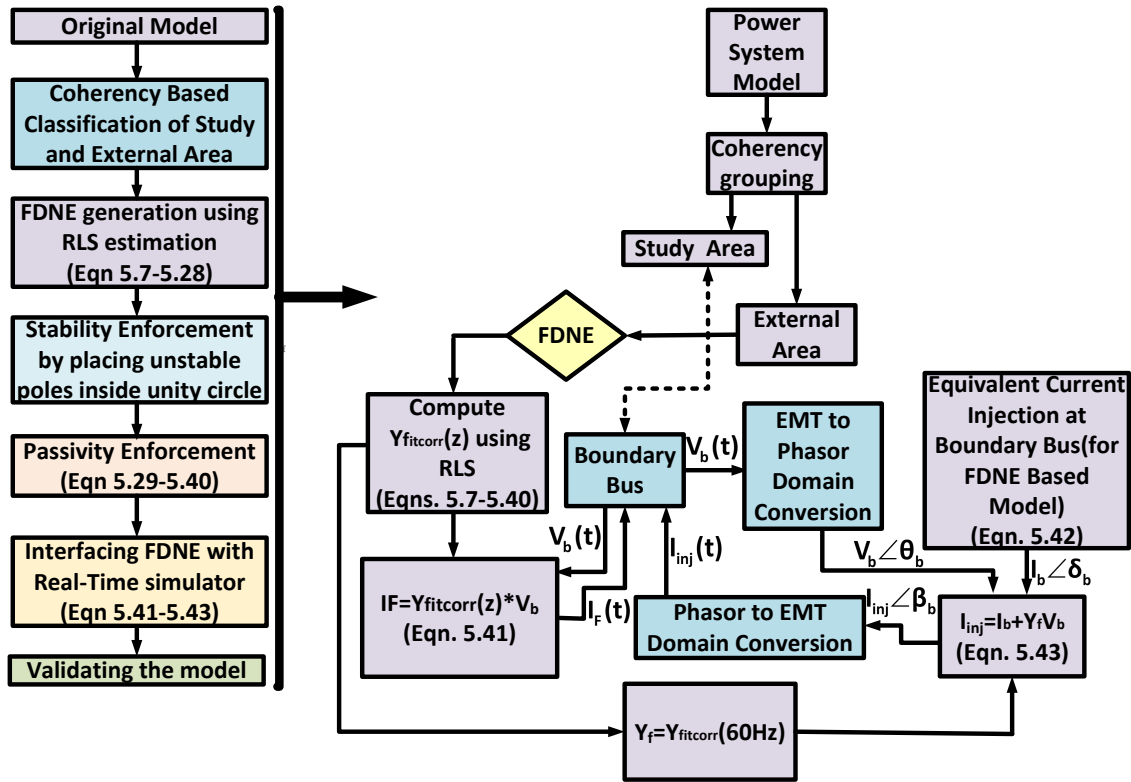


Fig. 5.5. The conceptual and functional flowchart for FDNE modeling

$z$ -domain model of an  $n^{th}$  order process, this can be represented as

$$\frac{y(k)}{u(k)} = \frac{b_1 z^{-1} + b_2 z^{-2} + \dots + b_n z^{-n}}{1 + a_1 z^{-1} + a_2 z^{-2} + \dots + a_n z^{-n}} \quad (5.10)$$

$$Y_{fit}(z^{-1})_{m \times m} = \begin{bmatrix} Y_{fit(1,p)} + Y_{fit(1,1)} + \dots + Y_{fit(1,m)} & -Y_{fit(1,2)} & \dots & -Y_{fit(1,m)} \\ Y_{fit(2,1)} & \dots & \dots & -Y_{fit(2,m)} \\ \dots & \dots & \dots & \dots \\ -Y_{fit(m,1)} & \dots & \dots & Y_{fit(m,p)} + Y_{fit(m,1)} + \dots + Y_{fit(m,m)} \end{bmatrix} \quad (5.9)$$

where  $a$ 's and  $b$ 's are the transfer function denominator and numerator coefficients respectively. For  $N$  observation window length, (6.8) can be rewritten as

$$\begin{bmatrix} y(k) \\ y(k-1) \\ \cdot \\ \cdot \\ \cdot \\ y(k-N+1) \end{bmatrix}_{N \times 1} = [X_{N \times 2n}] \begin{bmatrix} a_1 \\ \cdot \\ \cdot \\ a_n \\ b_1 \\ \cdot \\ \cdot \\ b_n \end{bmatrix}_{2n \times 1} \quad (5.11)$$

Equation (6.9) can be written in the generic form as

$$\Phi_{model(N \times 1)} = X_{N \times 2n} \Theta_{2n \times 1} \quad (5.12)$$

where  $X$  a matrix of past inputs and outputs,  $\Phi$  is a matrix of past and present outputs, and  $\Theta$  is the coefficient matrix of the transfer function.

Assume that the model identified is different from measurements, then

$$\epsilon = \Phi_{measured} - \Phi_{model} \quad (5.13)$$

where  $\epsilon$  is the error between the performance of the system measurement (subscript measured) and the model (subscript model). For reducing this error, a criteria  $J$  can be defined as

$$J = \epsilon^t \epsilon \quad (5.14)$$

By letting  $dJ/d\Theta = 0$ , we get

$$\Theta = [X^t X]^{-1} X^t \Phi_{measured} \quad (5.15)$$

From (6.13) it can be seen that, in order to calculate the measured variable the inverse of the state matrix should be determined. This can drastically slow down the process and some time may even not be achievable. To circumvent this issue, a recursive least squares technique is used. RLS is a computational algorithm that eliminates the matrix inversion. Let  $S = X^t X$ , then (6.13) can be written as

$$\Theta = S^{-1} X^t \Phi \quad (5.16)$$

where  $\Phi = \Phi_{measured}$

Then,

$$\Theta(k) = S^{-1} [x(k)X^t(k-1)] \begin{bmatrix} \Phi(k) \\ \Phi(k-1) \end{bmatrix} \quad (5.17)$$

$$\Theta(k) = S^{-1} [X(k)\Phi(k) + X^t(k-1)\Phi(k-1)] \quad (5.18)$$

Using (6.10)

$$\Theta(k) = S^{-1} [X(k)\Phi(k) + X^t(k-1)X(k-1)\Theta(k-1)] \quad (5.19)$$

$$\Theta(k) = S^{-1} [X(k)\Phi(k) + S(k-1)\Theta(k-1)] \quad (5.20)$$

$$S(k) = S(k-1) + X(k)X^t(k) \quad (5.21)$$

Substituting (6.19) in (6.18)

$$\Theta(k) = S^{-1} [X(k)\Phi(k) + \{S(k) - X(k)X^t(k)\}\Theta(k-1)] \quad (5.22)$$

$$\begin{aligned} \Theta(k) = \Theta(k-1) + [S(k-1) + X(k)X'(k)]^{-1}X(k) \\ [\Phi(k) - X'(k)\Theta(k-1)] \end{aligned} \quad (5.23)$$

Let  $P(k) = S^{-1}(k)$ ,. Then by using matrix inversion lemma,  $P(k)$  can be represented as

$$P(k) = P(k-1) \left[ I - \frac{X(k)X'(k)P(k-1)}{1 + X'(k)P(k-1)X(k)} \right] \quad (5.24)$$

Let

$$K(k) = \frac{X(k)}{1 + X'(k)P(k-1)X(k)} \quad (5.25)$$

Then,  $P(k)$  can be re-written as

$$P(k) = [I - K(k)X'(k)] P(k-1) \quad (5.26)$$

Substituting (6.24) in (6.21), (6.21) can be represented as

$$\Theta(k) = \Theta(k-1) + K(k) [\Phi(k) - X'(k)\Theta(k-1)] \quad (5.27)$$

With weighted least square, (6.23) and (6.24) can be presented as

$$K(k) = \frac{P(k-1)X(k)}{\gamma + x'(k)P(k-1)X(k)} \quad (5.28)$$

$$P(k) = \frac{[I - K(k)X'(k)] P(k-1)}{\gamma} \quad (5.29)$$

where  $\gamma$  is the weighting factor.

Thus with a given process input  $V_F(k)$  and process output  $I_F(k)$ ,  $Y_{fit}$  can be computed using RLS estimation [10, 109]. The validity of the proposed algorithm is verified by implementing on different test systems. In the first case, the proposed algorithm is implemented on two area test system with a 1-port network. Fig. 6(a)

and Fig. 6(b) shows the magnitude and angle of admittance of the external area and Table. 6.2 shows the comparison of FDNE formulation for two area system. It can be observed that even though this approach uses a lower order transfer function (meaning less computational burden), this method gives a similar error compared to higher order VF method.

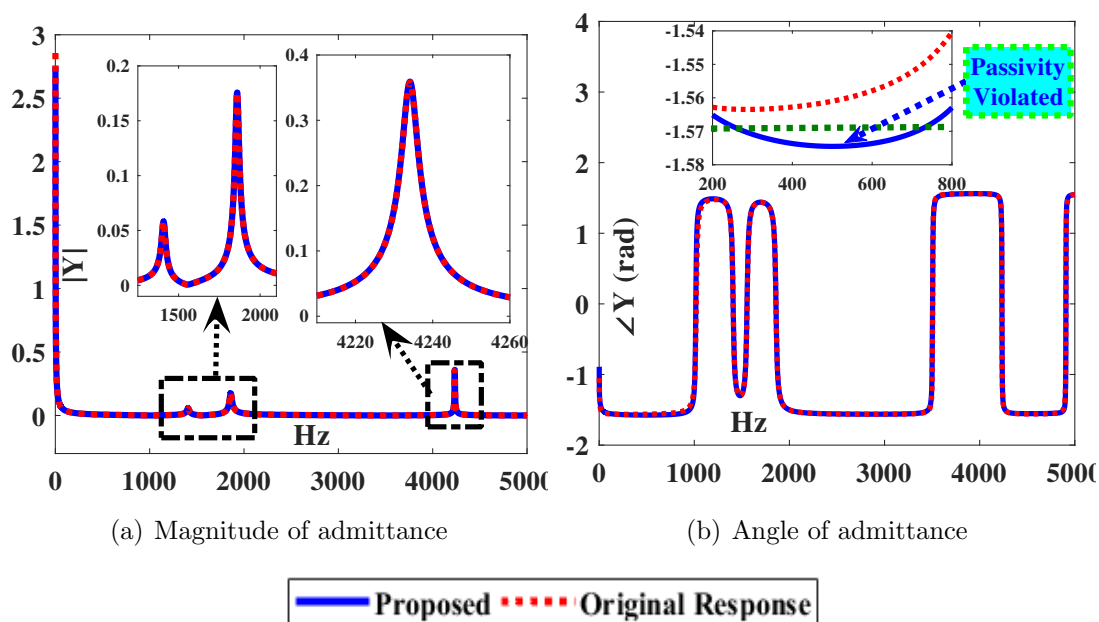


Fig. 5.6. Admittance vs frequency of external area (two area system)

Table 5.3  
FDNE formulation comparison

Type	Proposed Method	Vector Fitting(VF)
FDNE Order	17	21
RMS Error	2.176e-6	2.0101e-6

### 5.2.3.2 Passivity Enforcement

For a stable EMT simulation, the admittance matrix should be passive. Presence of negative resistance (i.e., the angle of admittance  $> \pm 1.57$  rad in phasor form) in the

frequency range of interest due to inherent approximations in identification violates passivity. For instance, from Fig. 6(b) it can be seen that for the previous test case, passivity is violated. For enforcing passivity, an algorithm is developed as shown in Algorithm 5.1. The details are as follows.

---

**Algorithm 5.1** Algorithm for Passivity Enforcement

---

- 1: Calculate  $Y_{fit}(z^{-1})$  using RLS
  - 2:  $z = e^{j2\pi f T_s}$  where  $f = 1 : f_{max}$ ,  $f_{max}$  is the maximum frequency of interest, and  $T_s$  is the sampling time
  - 3: Obtain admittance matrix ( $Y_{fitdata}$ ) by substituting step-2 in step-1
  - 4: Calculate  $G_{fitdata} = \Re[Y_{fitdata}]$  from step-3
  - 5: Calculate  $G_{fit}(z^{-1})$  and  $B_{fit}(z^{-1})$  (eqns. 6.31 – 6.33)
  - 6: Assume initial  $G_{fitcorr}(z^{-1}) = G_{fit}(z^{-1})$
  - 7: **for**  $k = 1$  to  $length(f)$  **do**
  - 8:     **if** minimum eigenvalue of  $G_{fitdata}(k) < 0$  **then**
  - 9:         using SDP calculate  $G_{fitcorrdata}$
  - 10:          $\Delta G(k) = G_{fitcorrdata}(k) - G_{fitdata}(k)$
  - 11:     **else**
  - 12:          $\Delta G(k) = 0$
  - 13:     **end if**
  - 14:      $G_{fitcorr}(z^{-1}) = G_{fitcorr}(z^{-1}) + \Delta G(k)$
  - 15: **end for**
  - 16: Finally  $Y_{fitcorr}(z^{-1}) = G_{fitcorr}(z^{-1}) + B_{fit}(z^{-1})$  is obtained
- 

From (6.7), let  $Y_{fit}(z^{-1})$  is the fitted admittance transfer function matrix which of the size  $m \times m$  (where  $m$  is the number of ports). By substituting  $z = e^{i2\pi f T_s}$  in (6.7), the fitted admittance matrix for  $k$  frequency samples can be represented as

$$[Y_{fitdata}]_{m \times m \times k} = [Y_{fit}(z^{-1})]_{m \times m} \quad (5.30)$$

where  $f \in 1 : f_{max}$  ( $f_{max}$  being the maximum frequency under consideration) and,  $T_s$  is the sampling time. Let  $G_{fitdata}$  is the real part of the admittance matrix ( $Y_{fitdata}$ ).

Then

$$[G_{fitdata}]_{m \times m \times k} = \Re [Y_{fitdata}]_{m \times m \times k} \quad (5.31)$$

For a function to be passive

$$eig(G_{fitdata}) > 0 \quad (5.32)$$

This implies that, if the admittance transfer function matrix is positive definite then it is also passive, if the fitted function  $Y_{fit}$  violates (6.30), then a new transfer function matrix  $Y_{fitcorr}$  is obtained. The conductance transfer function ( $G_{fit}$ ) and susceptance transfer function ( $B_{fit}$ ) are calculated as follows.

$$Y_{fit}(z^{-1}) = G_{fit}(z^{-1}) + B_{fit}(z^{-1}) \quad (5.33)$$

$$G_{fit}(z^{-1}) = \frac{1}{2} [Y_{fit}(z^{-1}) + Y_{fit}(z^{-1})^*] \quad (5.34)$$

$$B_{fit}(z^{-1}) = \frac{1}{2} [Y_{fit}(z^{-1}) - Y_{fit}(z^{-1})^*] \quad (5.35)$$

where \* stands for complex conjugate.

Since passivity is related to real part of admittance matrix ( $G_{fit}$ ), correcting  $G_{fit}$  without affecting imaginary part ( $B_{fit}$ ) is sufficient. The corrected transfer function matrix ( $Y_{fitcorr}$ ) is represented as follows

$$Y_{fitcorr}(z^{-1}) = G_{fitcorr}(z^{-1}) + B_{fit}(z^{-1}) \quad (5.36)$$

where

$$G_{fitcorr}(z^{-1}) = G_{fit}(z^{-1}) + \Delta G \quad (5.37)$$

The objective here is to calculate  $\Delta G$ . A real, symmetric matrix  $G_{fitcorrdata}$  is said to be positive definite if  $x^T G_{fitcorrdata} x > 0 \forall x \neq 0$ . Thus  $x^T G_{fitcorrdata} x$  can be

written as

$$\begin{aligned} x^T G_{fitcorrdata} x &= \frac{1}{2} (x^T G_{fitcorrdata} x + x^T G_{fitcorrdata}^T x) \\ &= \frac{1}{2} x^T (G_{fitcorrdata} + G_{fitcorrdata}^T) x \end{aligned} \quad (5.38)$$

This shows  $G_{fitcorrdata}$  is positive definite if and only if  $G_{fitcorrdata} + G_{fitcorrdata}^T$  is positive definite. This can be achieved by minimizing an objective function through optimization as:

$$\min \|G_{fitdata} - G_{fitcorrdata}\|_F \quad (5.39)$$

$$\text{s.t. } G_{fitcorrdata} + G_{fitcorrdata}^T > 0 \quad (5.40)$$

where  $F$  stands for frobenius norm of a matrix. We propose a convex optimization formulation to find  $G_{fitcorrdata}$  using semi definite programming (SDP) [39]. The optimization solution is then used to calculate  $\Delta G$  using (5.41).

$$\Delta G = G_{fitcorrdata} - G_{fitdata} \quad (5.41)$$

The validity of the proposed algorithm is implemented for enforcing passivity of 1-port network formulated previously. From Fig. 5.7 it can be seen that the passivity is enforced.

### 5.2.3.3 Interfacing FDNE with real time simulator

FDNE can be directly implemented since it is computed in  $z$ -domain. The implementation process is as follows. With boundary bus voltage ( $V_b$ ) as input to FDNE,

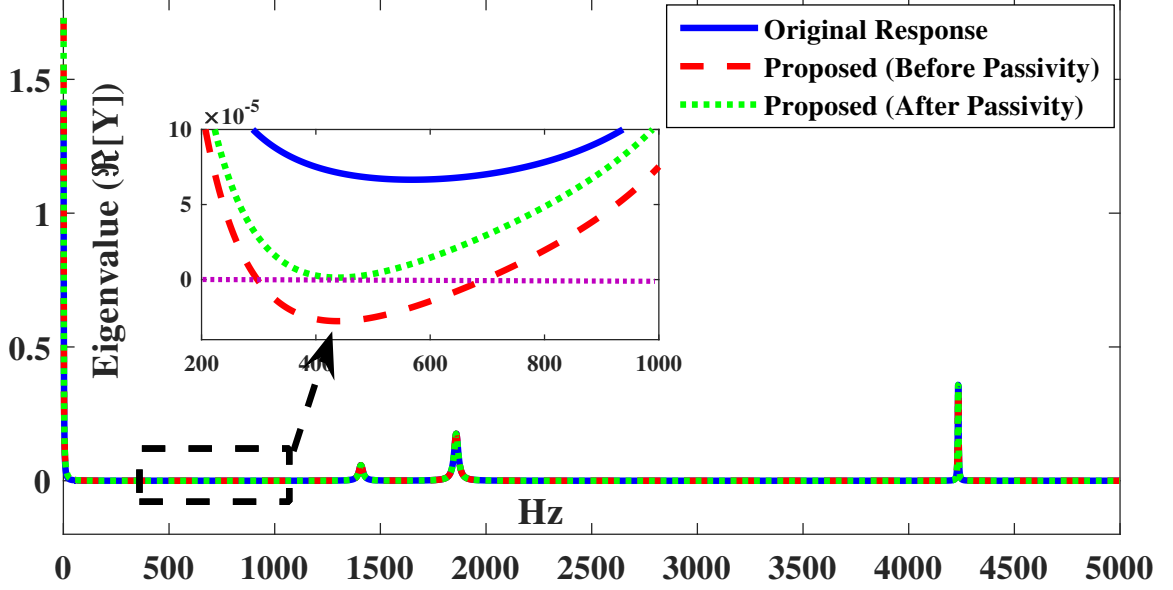


Fig. 5.7. The eigenvalue of real-part of admittance matrix (1-port)

and with  $n^{th}$  order estimation, (7.7) can be written as

$$\begin{aligned}
 I_F(k) = & -a_1 I_F(k-1) - a_2 I_F(k-2) \cdots - a_n I_F(k-n) \\
 & + b_1 V_b(k-1) + b_2 V_b(k-2) \cdots + b_n V_b(k-n)
 \end{aligned} \tag{5.42}$$

where  $I_F$  is current output from FDNE. For observing high frequency transients only FDNE part is required. To maintain boundary bus parameters at initial steady state, a constant current source is injected into the boundary bus as calculated from (6.27) [63, 65]. This can be represented as,

$$I_b \angle \delta_b = \left( \frac{P_b + jQ_b}{V_b \angle \theta_b} \right)^* \tag{5.43}$$

$$I_{binj} \angle \beta_{inj} = I_b \angle \delta_b - Y_{fitcorr}(60Hz) V_b \angle \theta_b \tag{5.44}$$

where  $P_b$  and  $Q_b$  are the active and reactive power flow respectively from the boundary bus,  $V_b$  and  $\theta_b$  are the voltage and angle respectively of the boundary bus. Since admittance at a fundamental component of frequency ( $Y_{fitcorr}(60Hz)$ ) is included

either in (7.5) for *EMT+FDNE+TSA Based Model* or in (5.43) for *EMT+FDNE Based Model*, the fundamental frequency component must be eliminated from FDNE. This is performed by adding a  $Y(60Hz)V_b\angle\theta_b$  term in (5.44) before injecting boundary bus current to remove fundamental frequency component from FDNE.

#### 5.2.4 Study and analysis of FDNE type equivalent modeling

For study and preliminary analysis, the proposed FDNE algorithm is implemented on two area test system. In the first case, the external area is modeled as FDNE type using the proposed algorithm (*EMT+FDNE Based Model (Proposed)*), and in the second case, the external area is modeled as FDNE type using vector fitting (VF) algorithm (*EMT+FDNE Based Model(VF)*). Fig. 5.8 shows the comparison of the relative speed of Gen. 2 w.r.t gen. 1, and Fig. 5.9 shows the comparison of active power flow from bus 10 to bus 9.

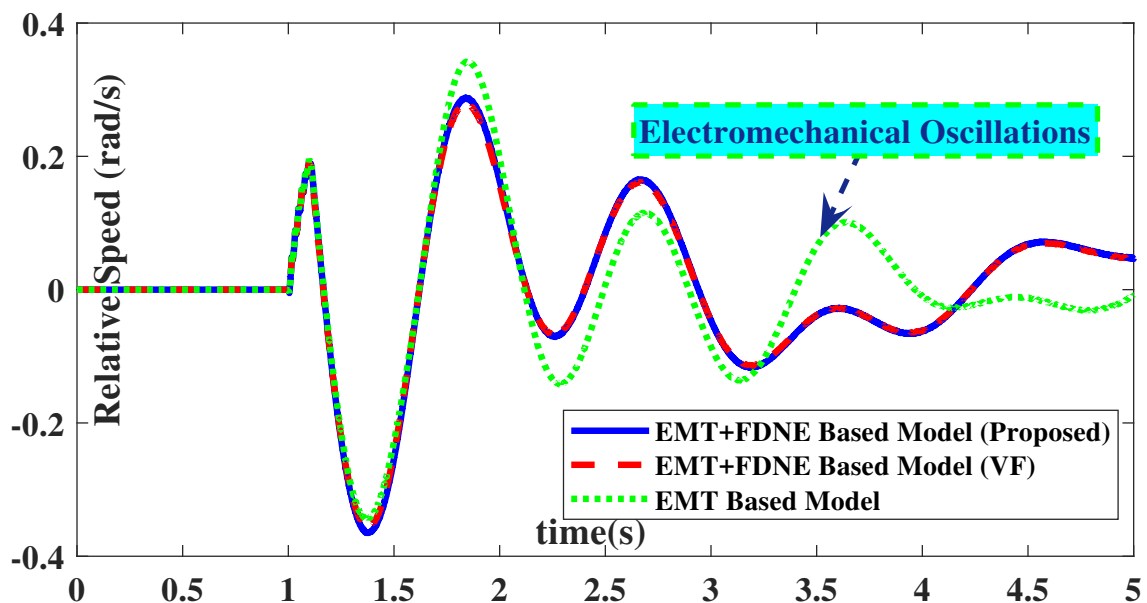


Fig. 5.8. Relative speed of Gen.2 w.r.t Gen.1

Table 5.4 shows the comparisons between proposed FDNE and an offline VF based

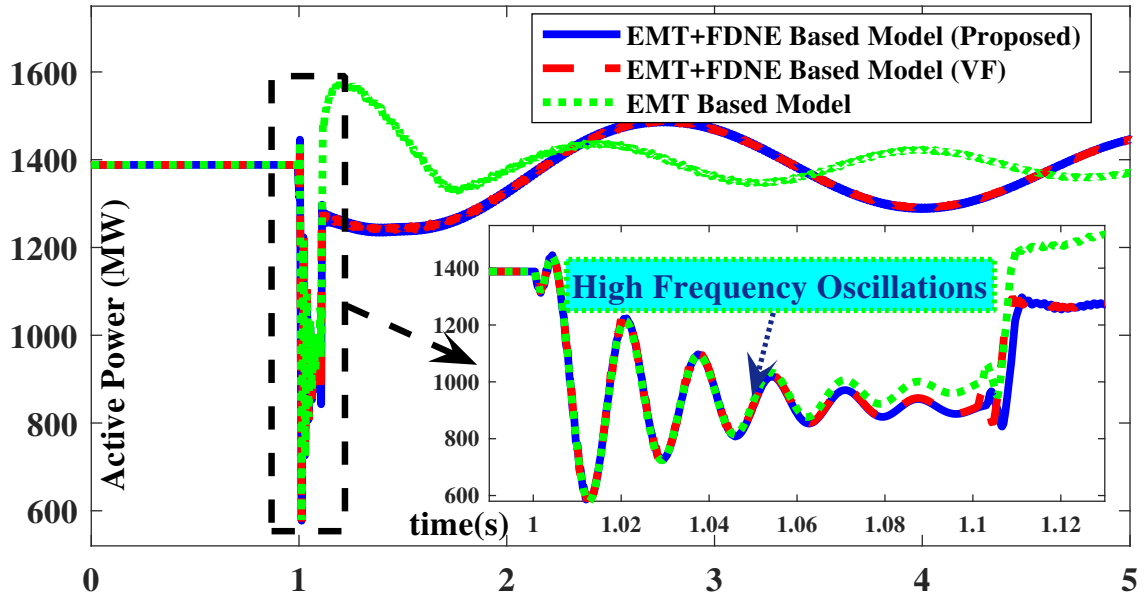


Fig. 5.9. Active power flow from bus 10 to bus 9 (Boundary Bus)

Table 5.4  
Comparison of reduced (EMT+FDNE) and original (EMT) models

	EMT+FDNE(Proposed)	EMT+FDNE(VF)
Fig. 5.8	0.481261	0.4827015
Fig. 5.9	0.077046	0.0771309

algorithm. Both algorithms gives similar results, proving that FDNE can be formulated online with less computational effort and lower order of transfer function when compared to offline algorithms. From Fig. 5.8 and Fig. 5.9 it can be seen that with this approach, high frequency oscillations are preserved whereas electromechanical oscillations are not preserved, proving the need to have combined FDNE models with TSA equivalents.

### 5.2.5 Implementing TSA and FDNE on two area power system

Fig. 5.10 shows the implementation approach for combined TSA and FDNE type equivalents. Table. 5.5 shows the comparison of frequency and damping factor for the

original model and various reduced order model using eigenvalue realization algorithm for generator-3 speed data. In the table case *EMT+FDNE+TSA Based Model (AGG)* represents modeling external area as a combination of FDNE and TSA type with both network and generator aggregation, whereas *EMT+FDNE+TSA Based Model* represents modeling external area as a combination of FDNE and TSA type with only network aggregation. The other cases are described before. It can be seen that the proposed approach provides very close results compared to full EMT based model.

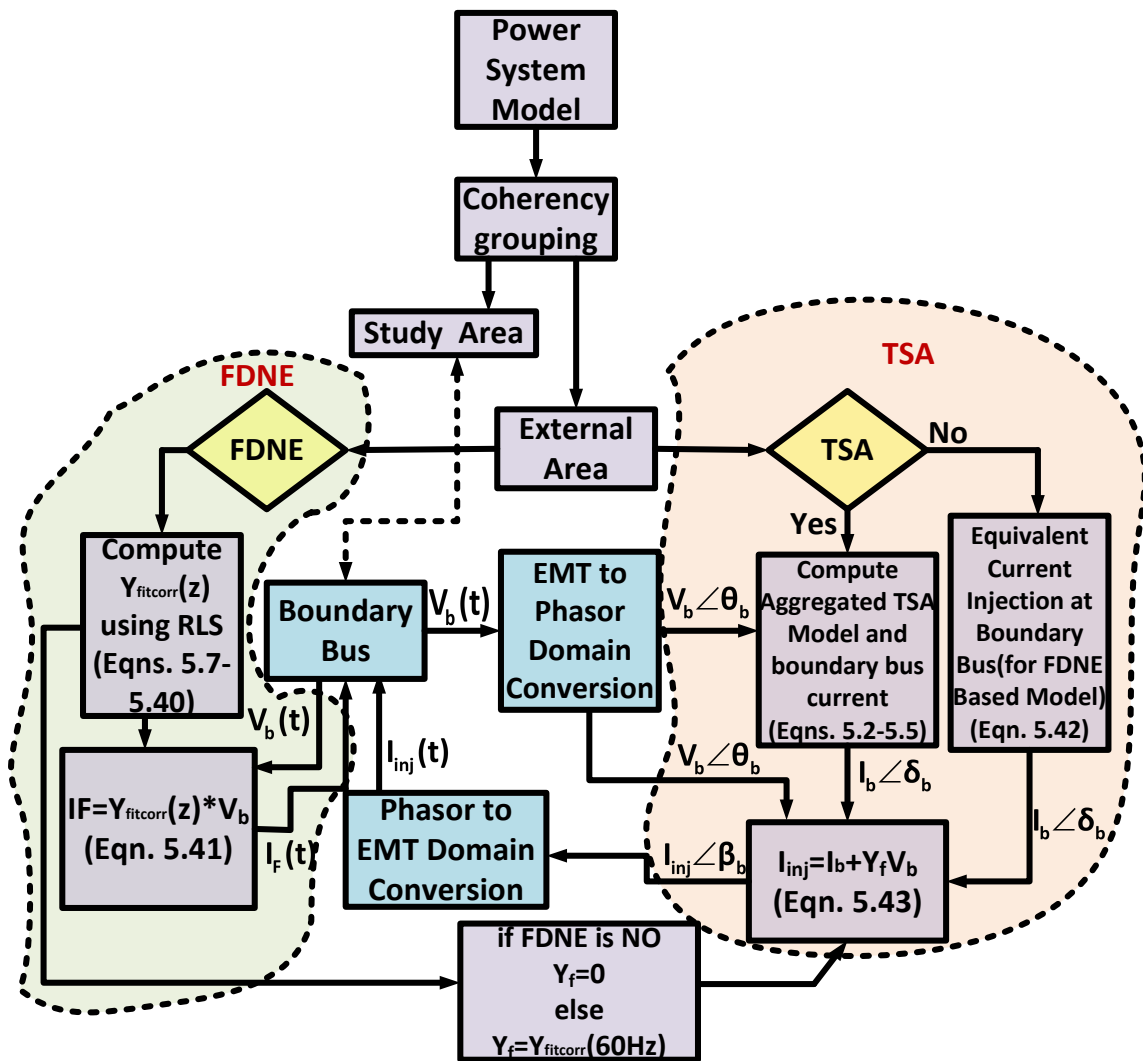


Fig. 5.10. Implementation flowchart for TSA and FDNE type models.

Table 5.5  
Comparison of reduced order (FDNE only) models

Case	Eigen Value	Frequency(Hz)	Damping(%)
EMT Based Model	$-1.323 \pm i7.544$	0.6566	21.92
	$-0.880 \pm i5.157$	0.8327	16.82
EMT+TSA Based Model(AGG)	$-0.906 \pm i7.096$	0.5494	43.09
	$-1.381 \pm i6.537$	1.0634	20.67
EMT+TSA Based Model	$-1.306 \pm i7.583$	0.6501	5.7543
	$-0.598 \pm i5.014$	0.8038	11.8466
EMT+FDNE Based Model	$-0.664 \pm i6.993$	0.3822	61.26
	$-0.373 \pm i2.507$	0.4034	61.26
EMT+FDNE+TSA Based Model(AGG)	$-1.321 \pm i7.652$	0.6623	4.1457
	$-0.670 \pm i4.984$	0.8804	13.336
EMT+FDNE+TSA Based Model	$-1.325 \pm i7.601$	0.6518	5.2343
	$-0.610 \pm i5.002$	0.8021	12.1216

Fig. 5.11 shows the comparison of the relative speed of Gen. 2 w.r.t gen. 1, and Fig. 5.12 shows the comparison of active power flow from bus 10 to bus 9. From Fig. 5.11 and Fig. 5.12, it can be seen that both high frequency and electromechanical oscillations are well preserved. Table. 5.6 shows the error comparison for reduced and original model using (5.7).

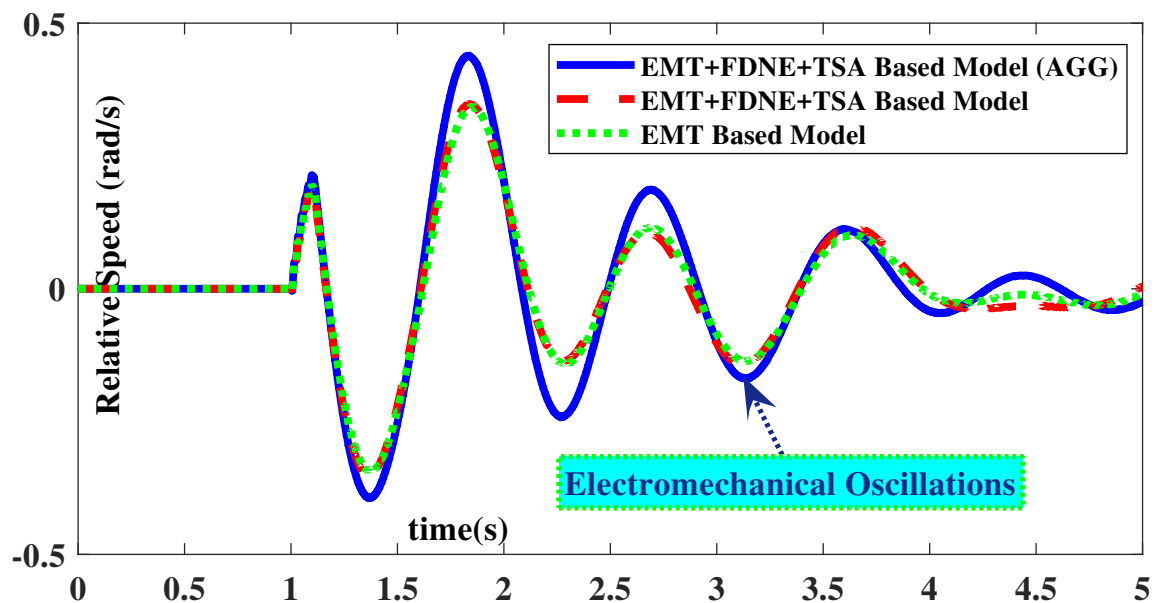


Fig. 5.11. Relative speed of Gen.2 w.r.t Gen.1

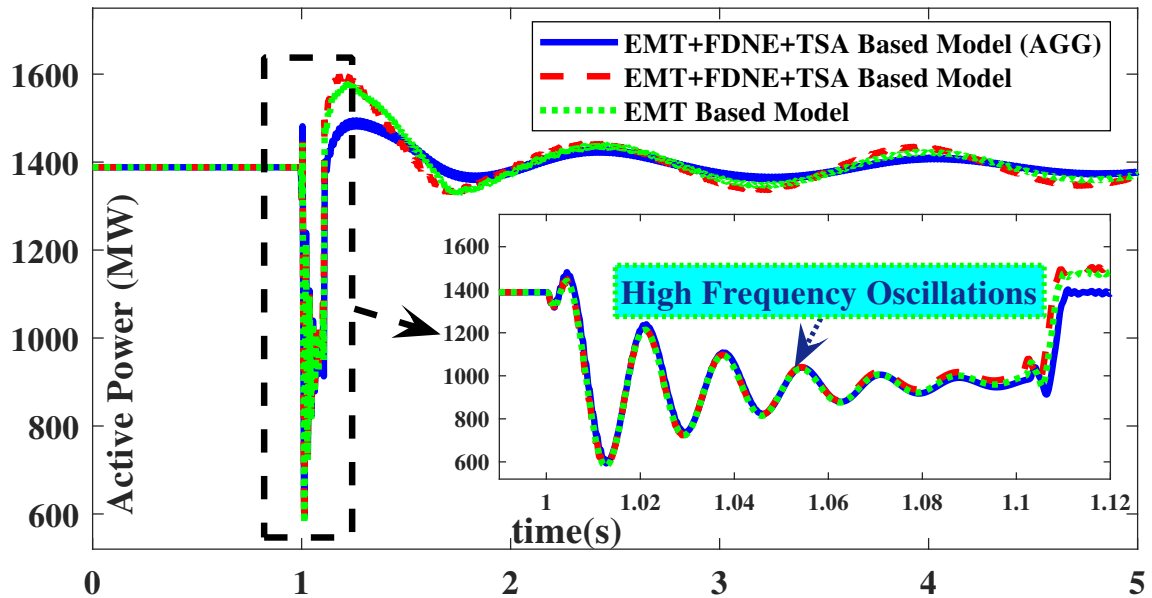


Fig. 5.12. Active power flow from bus 10 to bus 9 (Boundary Bus Power)

Table 5.6  
Comparison of reduced (EMT+FDNE+TSA) and original (EMT) models

	EMT+FDNE+TSA(AGG)	EMT+FDNE+TSA
Fig. 5.11	0.2286	0.0923
Fig. 5.12	0.0163	0.0076

### 5.3 Implementation Test on Interconnected Power Grid

To prove scalability and implementation using a multi-port network, IEEE 39 bus power system model (3-port) as shown in Fig. 6.12 is considered [20, 46]. Here based on the coherency grouping of the generators the test system is divided into *study* and *external* area. To assess the performance of proposed *EMT+FDNE+TSA* based reduced order model, Group-I which consists of generators 4, 5, 6, 7, 9 is considered as *external* area and the rest of the power system as *study* area. The *study* and *external* area is divided at bus 16, bus 17, and bus 26 (boundary buses). Fig. 14(a) and Fig. 14(b) shows the admittance magnitude and angle of port-3. Fig. 5.15 shows

the passivity enforcement for 3-port network.

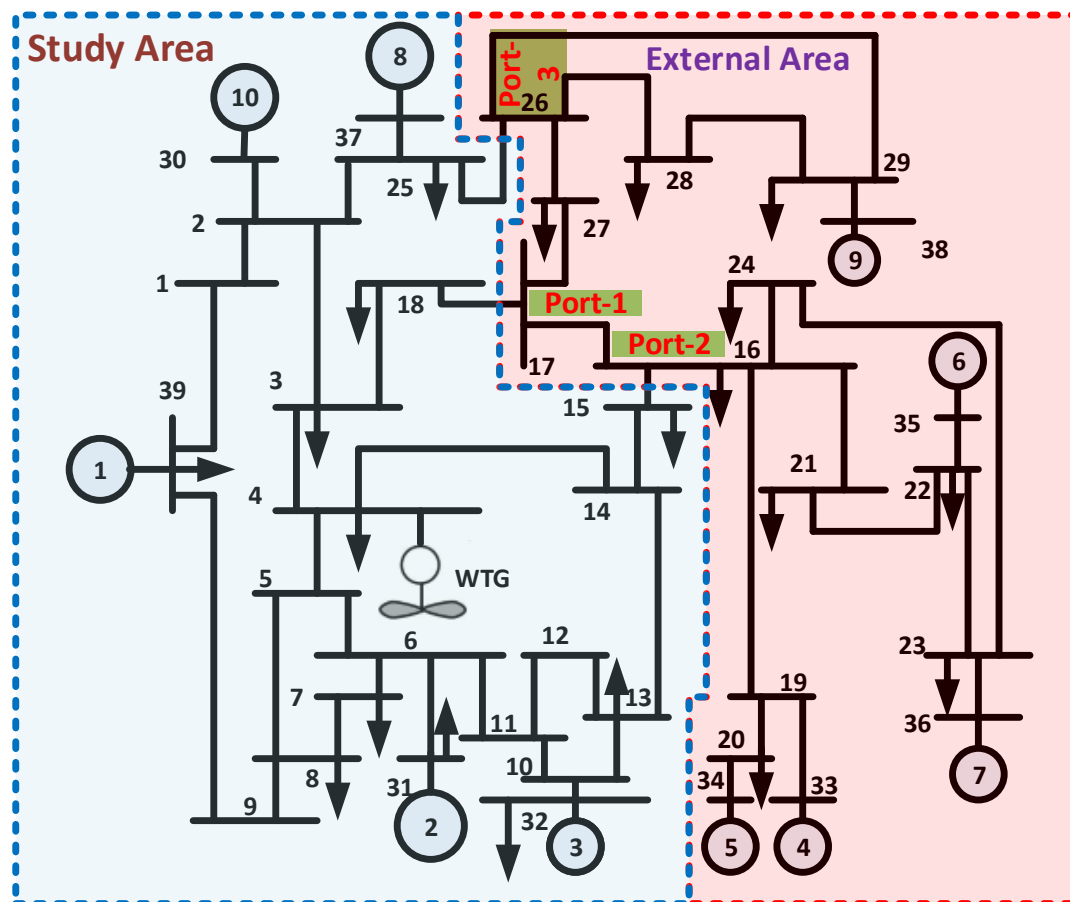


Fig. 5.13. IEEE 39 bus test system

Table 5.7  
Comparison of reduced (EMT+FDNE+TSA) and original (EMT) models

	EMT+FDNE+TSA(AGG)	EMT+FDNE+TSA
Fig. 5.16	0.1634	0.0489
Fig. 5.17	0.0112	0.0081
Fig. 5.18	0.0905	0.0433

For analysis, a three-phase fault is initialized for a duration of 0.1s, and the simulation results are compared with the original model. Fig. 5.16 to Fig. 5.18 shows the

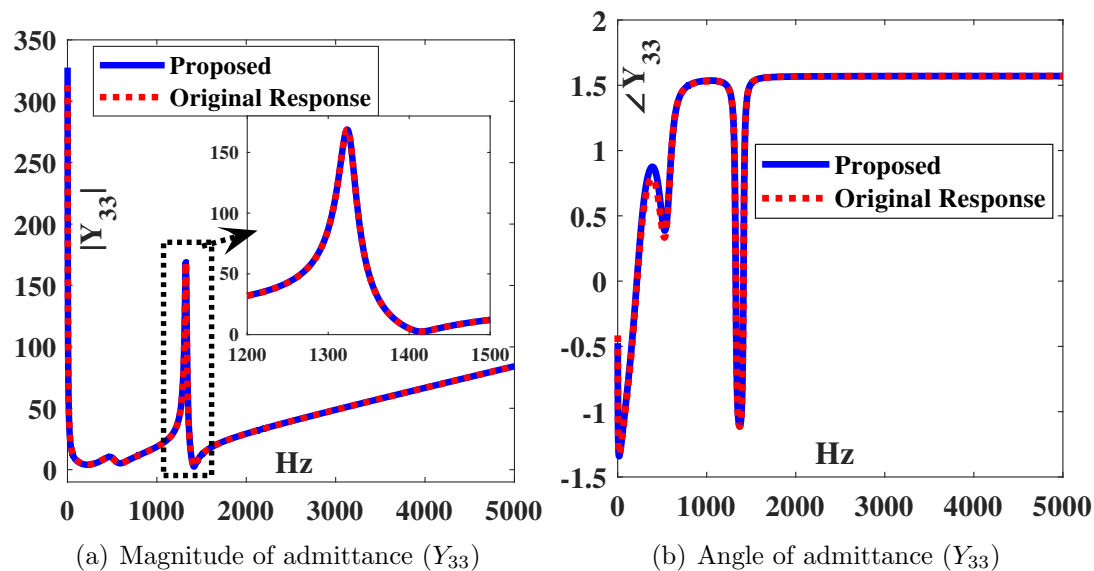


Fig. 5.14. Admittance vs frequency of external area (39 Bus System)

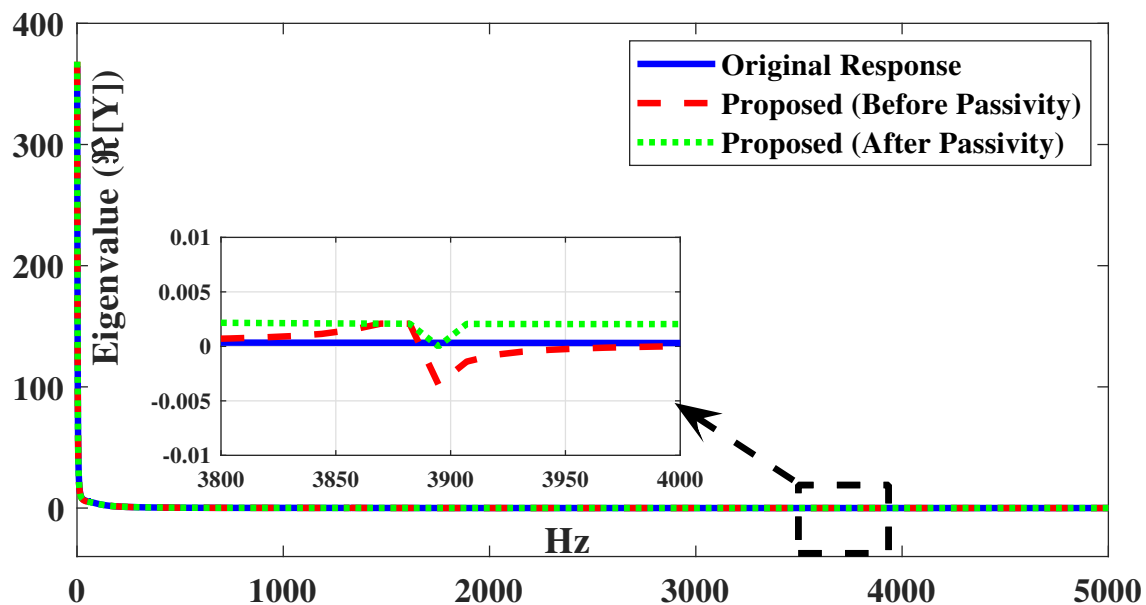


Fig. 5.15. The corrected eigenvalue of real-part of admittance matrix (3-port)

validation results of the proposed algorithm. Table 5.7 shows the relative error (5.7) comparison of reduced models with original model.

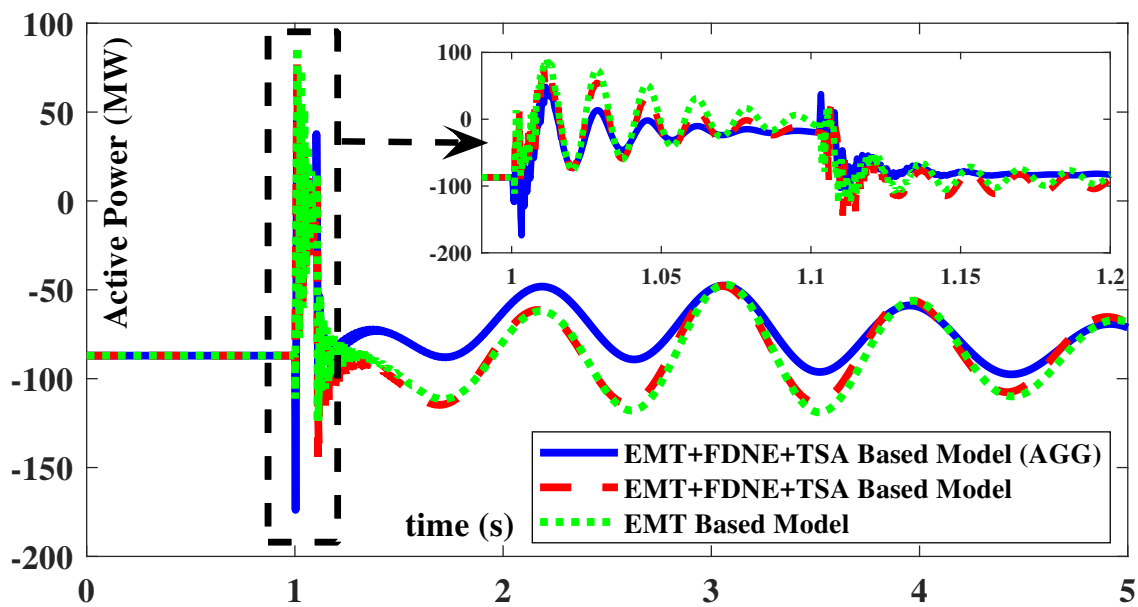


Fig. 5.16. Bus 26 Active Power

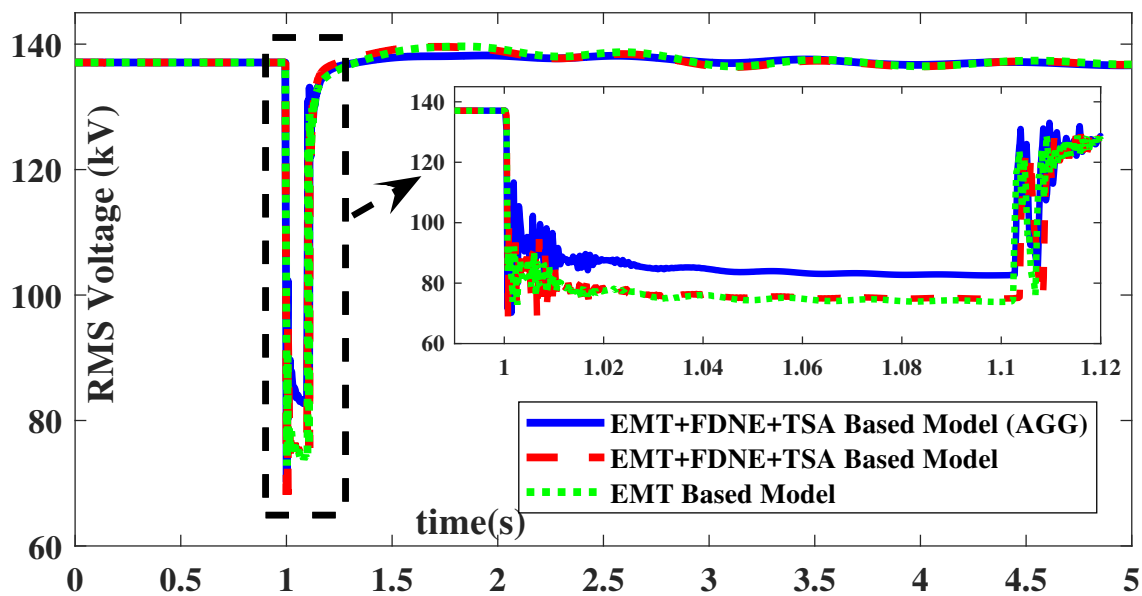


Fig. 5.17. Bus 17 Voltage

#### 5.4 Application of Reduced Order Model for Wide Area Control

In this case, a large power system with multiple utilities, designing and validating the wide-area controller requires detailed EMT model of the large power system.

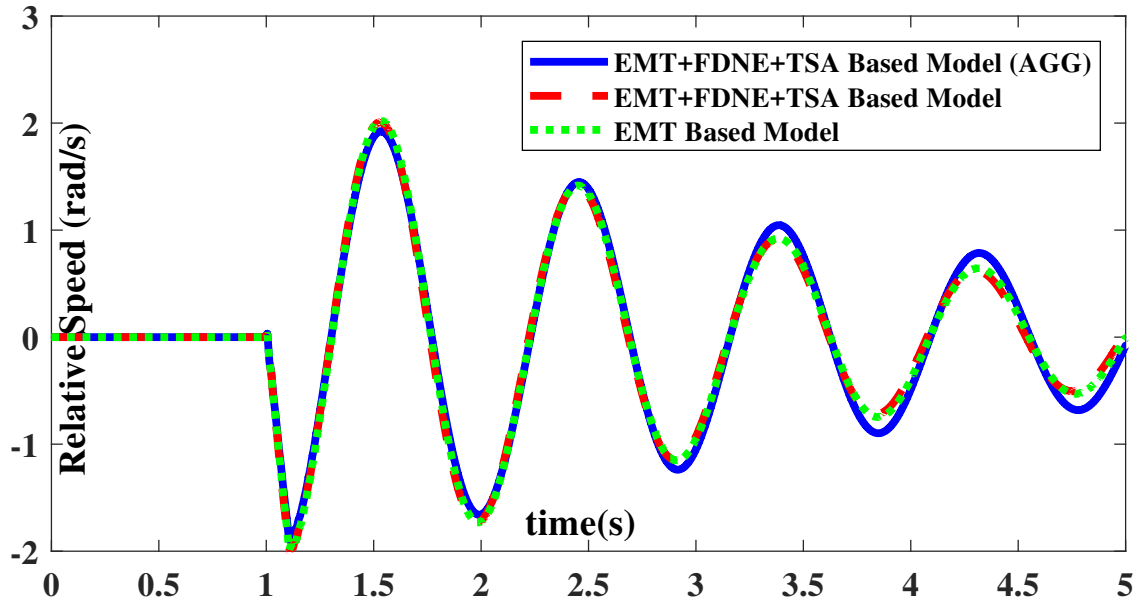


Fig. 5.18. Relative speed of generator gen.1 w.r.t gen.2

In the conventional methods, the utility or the study area is modeled in detail and the remaining part of the network as an aggregated source. However, this type of modeling does not capture the exact dynamics of a large power system. Fig. 5.19 shows the IEEE 68 bus power system model which is a combination of multiple areas. In literature NETS area is represented as the IEEE 39 bus system and the remaining areas (NYPS, Area-3, Area-4, and Area-5) is modeled as an aggregated generator-10 as shown in Fig. 5.19. This type of aggregation ignores the important dynamics of the system, and the WADC designed with such modeling may not be accurate if implemented in the field.

To this effect, in this chapter, the NETS area in the 68-bus system is considered as the study area and remaining part of the network as the external area as shown in Fig.5.19 with boundary buses as Bus 61 and Bus 47. The study area is modeled in detail whereas the external area is modeled as a combination of FDNE+TSA based

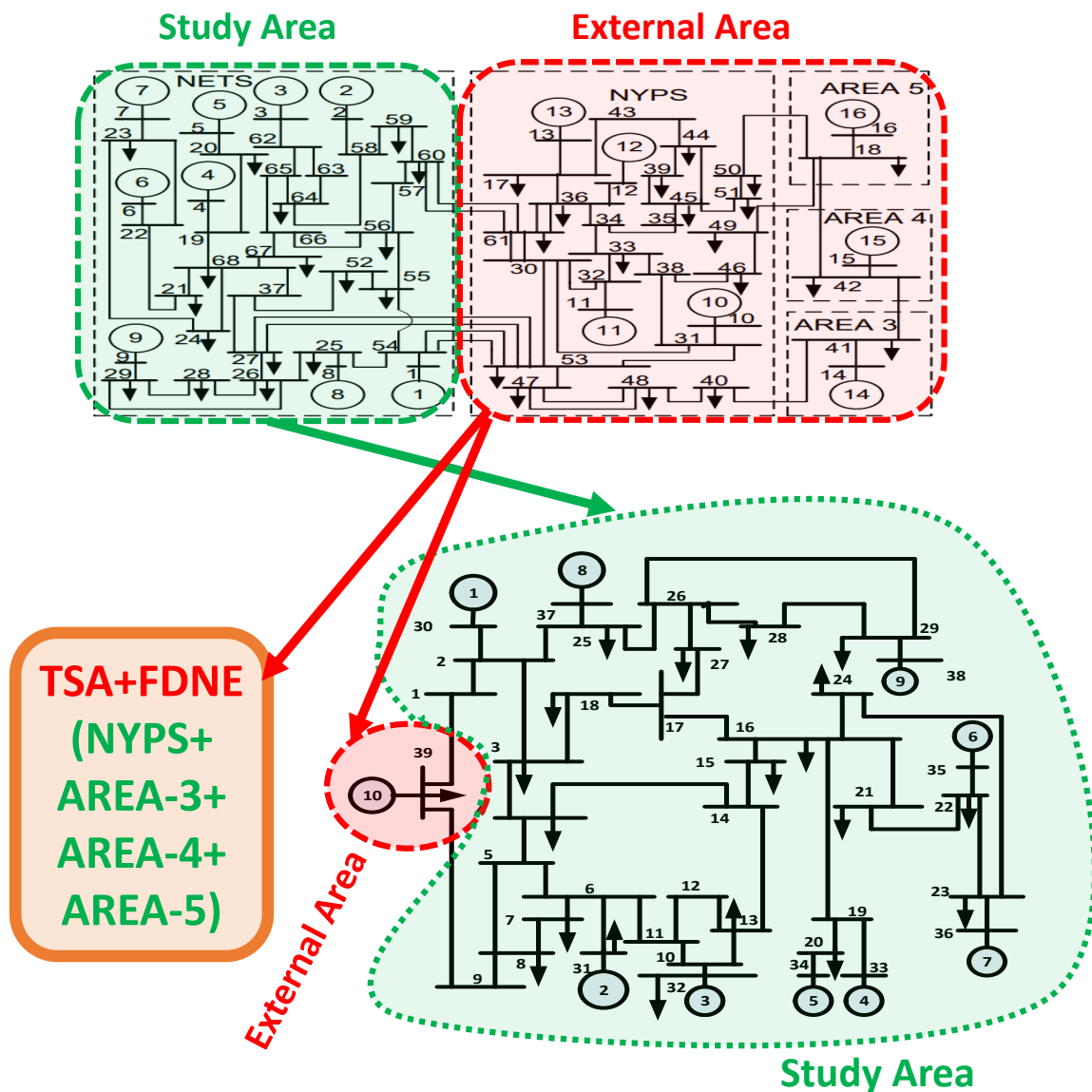


Fig. 5.19. IEEE 68 bus system

equivalent as shown in Fig. 5.20.

The WADC algorithm is implemented using the architecture discussed in chapter 2. The same type of sequential disturbances are created here; however, Bus-14 in 39 bus system is Bus-66 in 68 bus system; likewise, Bus-19 in 39 bus system is same as Bus-19 in 68 bus system.

The chapter is organized as follows: Section 5.4.1 discusses the validation of reduced

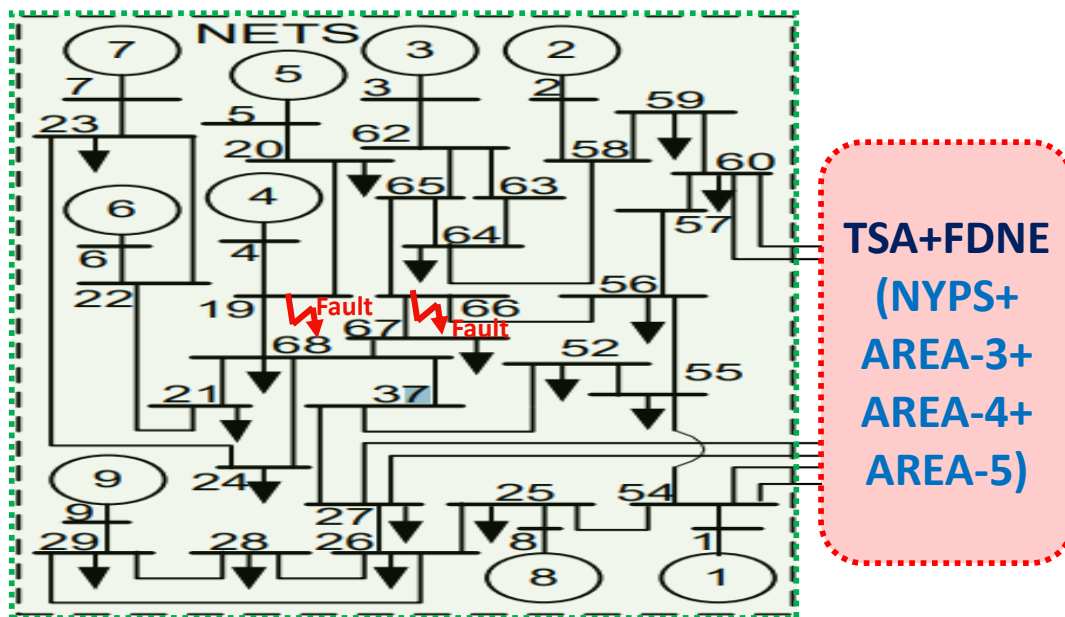


Fig. 5.20. The equivalent representation of 68 bus system

68 bus system. Section 5.4.2 discusses the simulation results for application of reduced order model for wide-area control.

#### 5.4.1 Reduced Model Validation for IEEE 68 system

For validating the reduced order model the response of reduced 68 bus system is compared with IEEE 68 bus system and IEEE 39 bus system, for this, a fault is created on Bus-66 for a duration of 0.1s at 13.9s. Fig. 5.21 and Fig. 5.22 shows the speeds of generators 7 and 9 respectively. Fig. 5.23 shows the RMS voltage of the boundary bus-61. From the above figures, it can be seen that the dynamics of reduced 68 bus is closer to IEEE 68 bus system than IEEE 39 bus system. For quantitative analysis, relative error between the reduced 68 bus and IEEE 39 bus is compared with IEEE 68 bus EMT type model using (5.45). The results are tabulated in Table. 5.8. From this, we can conclude the need for frequency based reduced models rather

than an aggregated source.

$$relative\ error = \frac{\|y_{ref} - y_{act}\|_2}{\|y_{ref}\|_2} \quad (5.45)$$

where  $y_{ref}$  represents the output from 68 bus system and  $y_{act}$  represents the output obtained in each case of reduced 68 and 39 bus system.

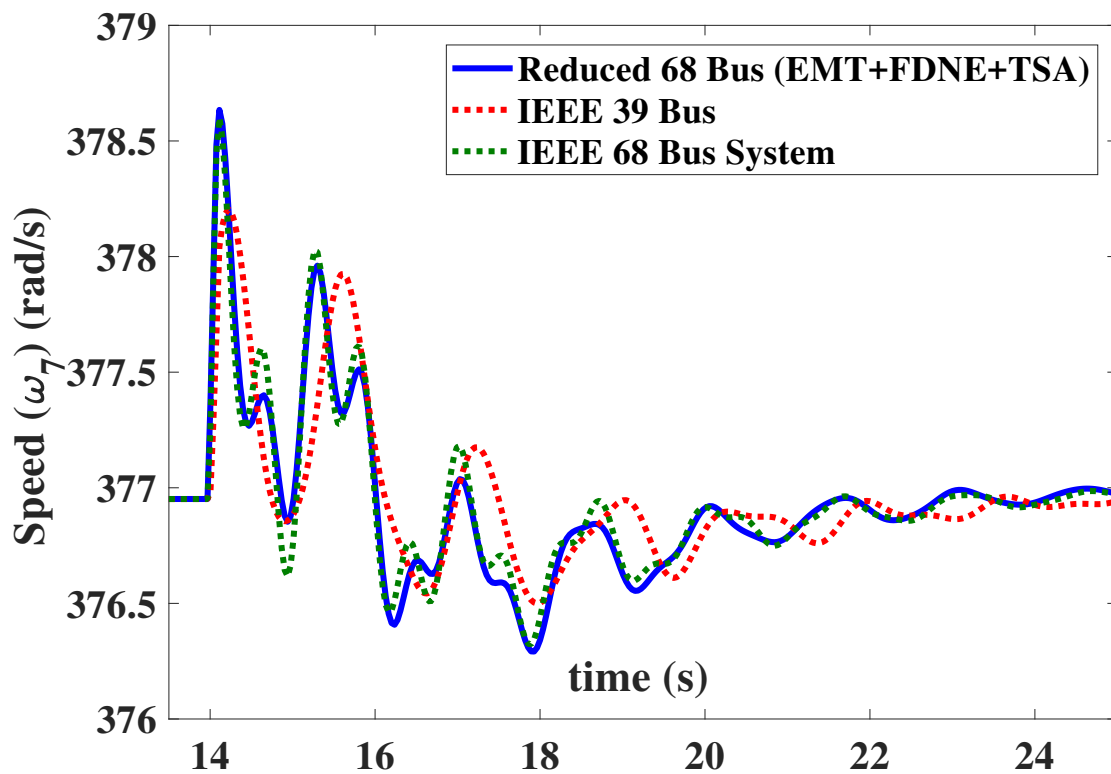


Fig. 5.21. Generator-7 speed (rad/s)

Table 5.8  
Comparison of reduced 68 bus, IEEE 39 and 68 bus models

	Reduced 68 Bus	IEEE 39 Bus
Fig. 5.21	0.019423	0.0629
Fig. 5.22	0.016391	0.052166

#### 5.4.2 Simulation Results of Wide Area Control

For this system two cases are analyzed for different disturbances.

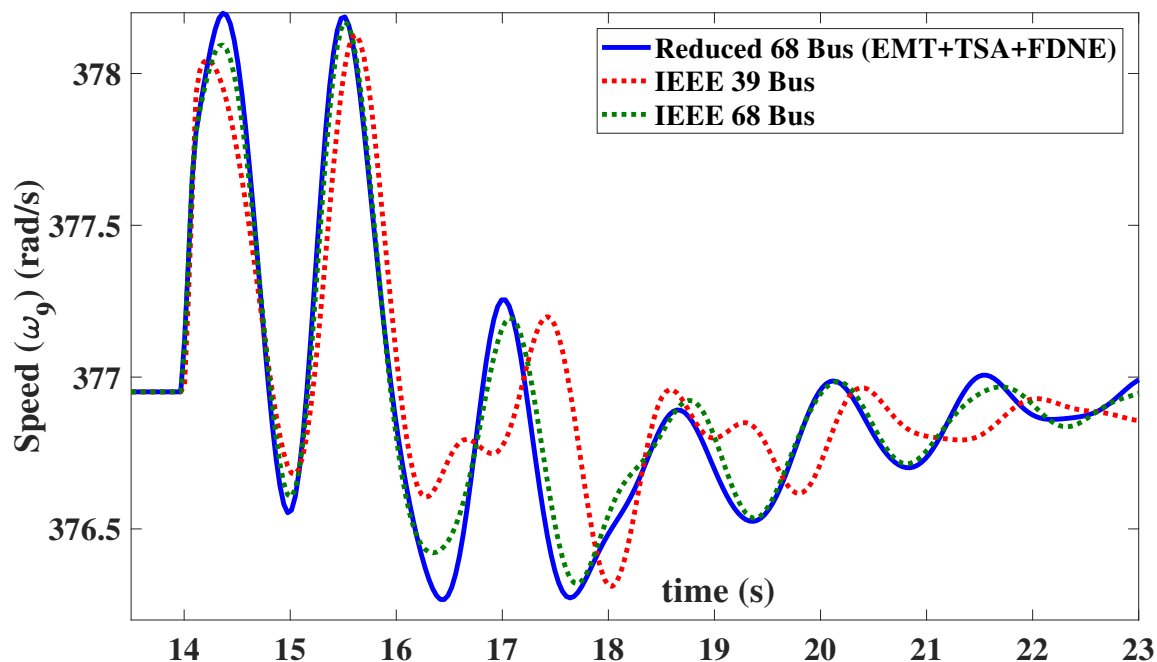


Fig. 5.22. Generator-9 speed (rad/s)

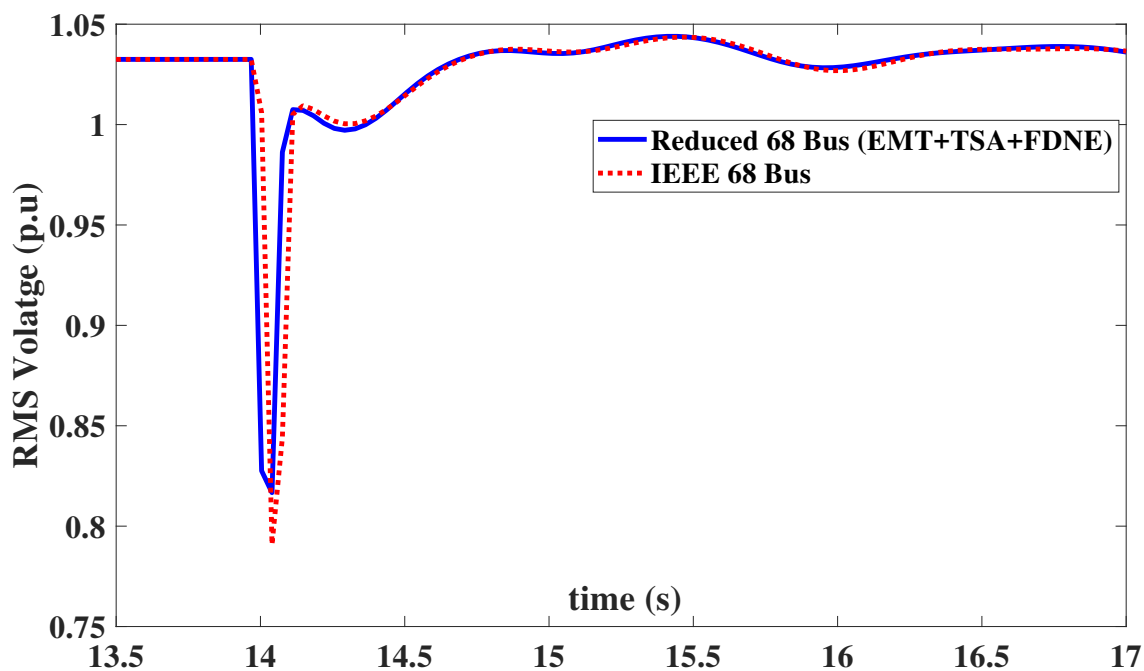


Fig. 5.23. Boundary bus voltage (Bus-61) (rad/s)

#### 5.4.2.1 Case:1 Fault on Bus-66

For the same disturbance scenario as discussed in Section 7.5.1.1, Table 5.9 shows the optimal wide-area control loop for fault on Bus-66. Here for same coherency

grouping as discussed in chapter 2, generator-2 speed is the most observable and generator-7 is the most controllable in group-1, generator-1 speed is the most observable and generator-9 is the most controllable in group-2, and generator-4 speed is the most observable and generator-2 is the most controllable in group-3. Since group-4 belongs to other utilities, no WADC is designed. Fig. 5.24, Fig. 5.25, and Fig. 5.26 shows the speed deviations of generator 2, 7, and 9 with and without WADC respectively. Fig. 5.27 shows the WADC output sent to the most controllable generator. From the above figures, it can be seen that the with the proposed approach the oscillations are damped effectively. Table 5.10 shows the damping improvement comparison of speed deviations with and without wide-area controller using reduced 68 bus and IEEE 39 bus power system models. For this, the same metric in (5.45) is used. Here  $y_{ref}$  is the speed deviation without WADC and  $y_{act}$  is the speed deviation with WADC.

Table 5.9  
IEEE 39-bus control loop  
(fault on bus-66)

	Control Loop	Residue
Group-1	$\Delta\omega_2 \rightarrow u_7$	0.7854
Group-2	$\Delta\omega_1 \rightarrow u_9$	1
Group-3	$\Delta\omega_4 \rightarrow u_2$	0.8565

Table 5.10  
Damping improvement comparison (Case:1)

	Reduced 68 bus	IEEE 39 bus
Fig. 5.24	0.4899	Fig. 2.20 0.4301
Fig. 5.25	0.5809	Fig. 2.21 0.4330
Fig. 5.26	0.5815	Fig. 2.22 0.4332

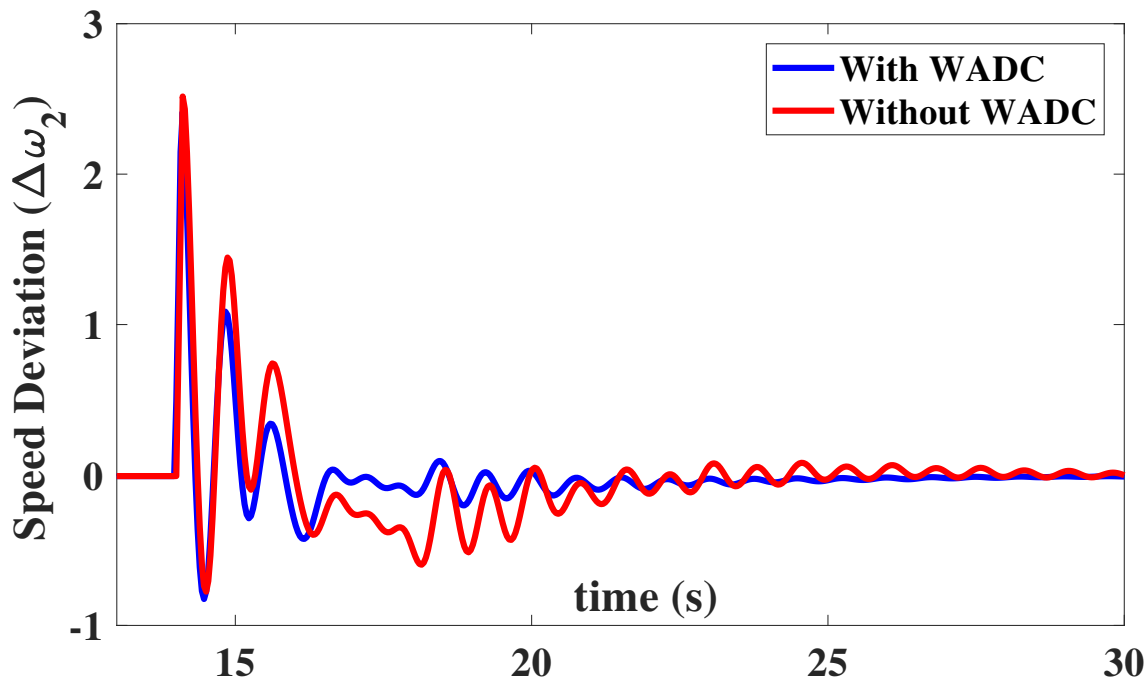


Fig. 5.24. Generator-2 speed deviation (rad/s)

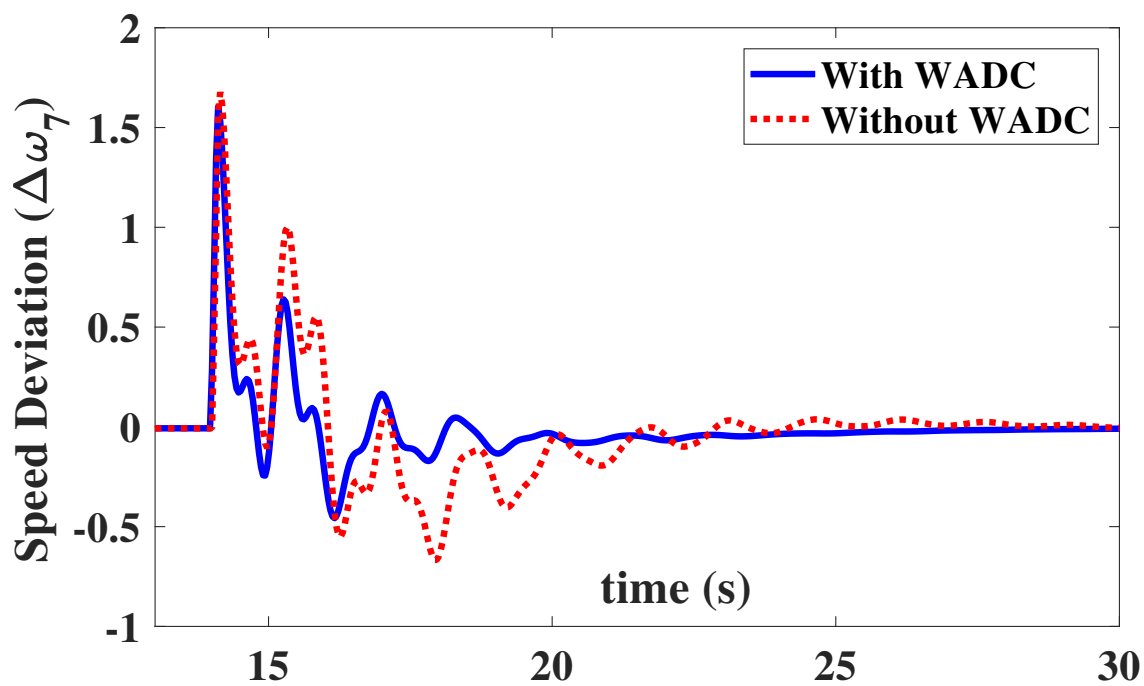


Fig. 5.25. Generator-7 speed deviation (rad/s)

#### 5.4.2.2 Case:2 Fault on Bus-19

For the same disturbance scenario as discussed in Section 7.5.1.2, Table 5.11 shows the optimal wide-area control loop for fault on Bus-19. Here for same coherency

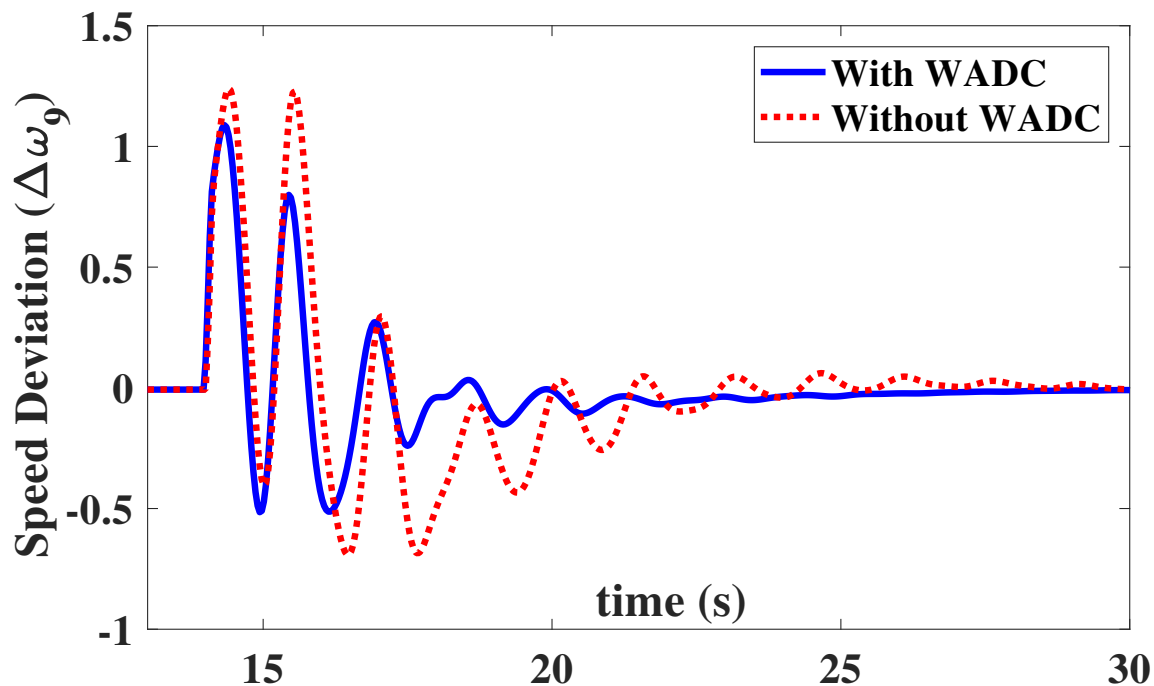


Fig. 5.26. Generator-9 speed deviation (rad/s)

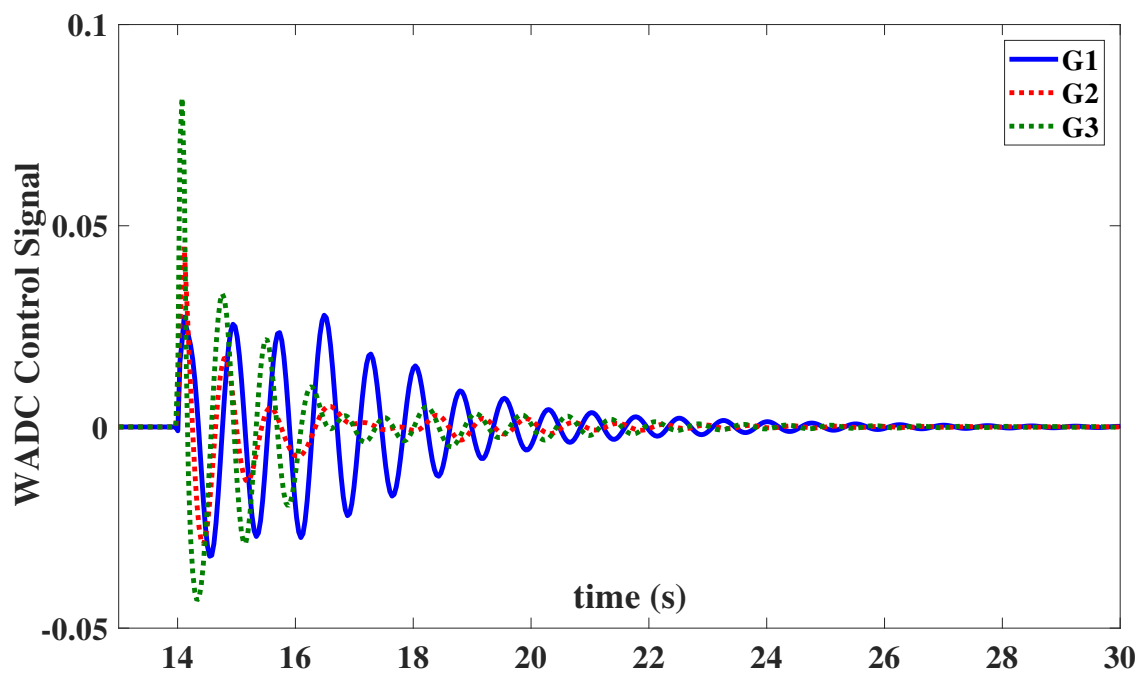


Fig. 5.27. WADC output signal

grouping as discussed in chapter 2, generator-1 speed is the most observable and generator-6 is the most controllable in group-1, generator-4 speed is the most observ-

able and generator-9 is the most controllable in group-2, and generator-5 speed is the most observable and generator-2 is the most controllable in group-3. Since group-4 belongs to other utilities, no WADC is designed. Fig. 5.28, Fig. 5.29, and Fig. 5.30 shows the speed deviations of generator 2, 6, and 9 with and without WADC respectively. Fig. 5.31 shows the WADC output sent to the most controllable generator. From the above figures, it can be seen that the with the proposed approach the oscillations are damped effectively. Table 5.12 shows the damping improvement comparison of speed deviations with and without wide-area controller using reduced 68 bus and IEEE 39 bus power system models. For this, the same metric in (5.45) is used. Here  $y_{ref}$  is the speed deviation without WADC and  $y_{act}$  is the speed deviation with WADC.

Table 5.11  
IEEE 39-bus control loop  
(fault on bus-19)

	Control Loop	Residue
Group-1	$\Delta\omega_1 \rightarrow u_6$	1
Group-2	$\Delta\omega_4 \rightarrow u_9$	0.9785
Group-3	$\Delta\omega_5 \rightarrow u_2$	0.5475

Table 5.12  
Damping improvement comparison (Case:2)

	Reduced 68 bus	IEEE 39 bus		
Fig. 5.28	0.5429	Fig. 2.25	0.4611	
Fig. 5.29	0.4928	Fig. 2.26	0.4375	
Fig. 5.30	0.5268	Fig. 2.27	0.4738	

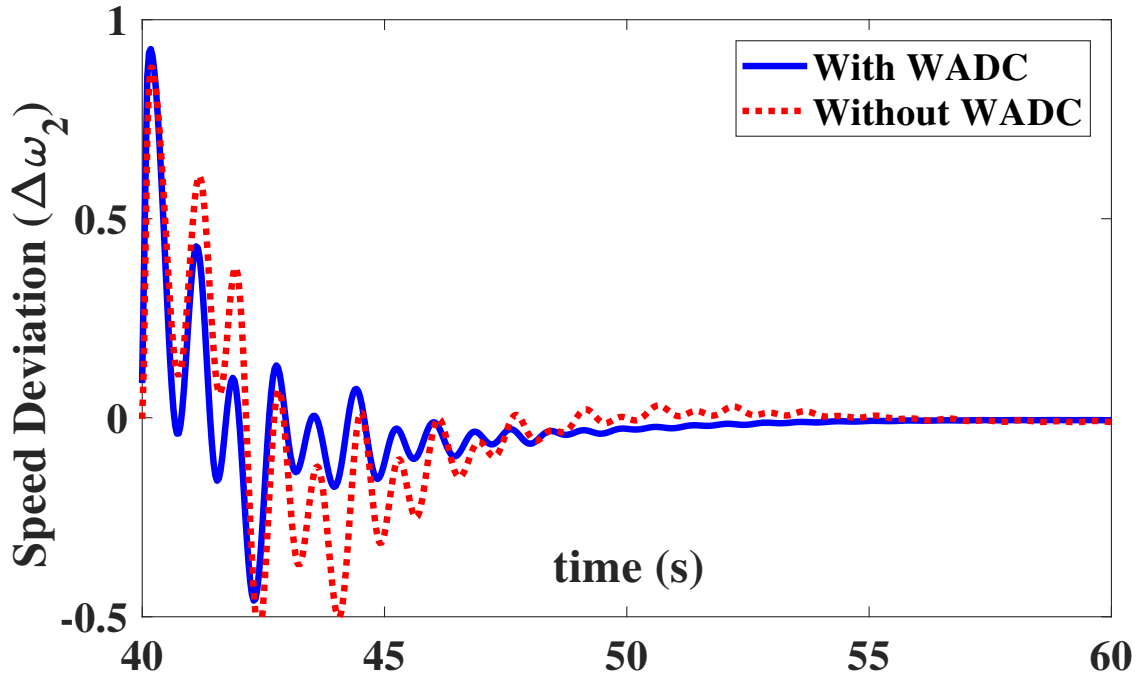


Fig. 5.28. Generator-2 speed deviation (rad/s)

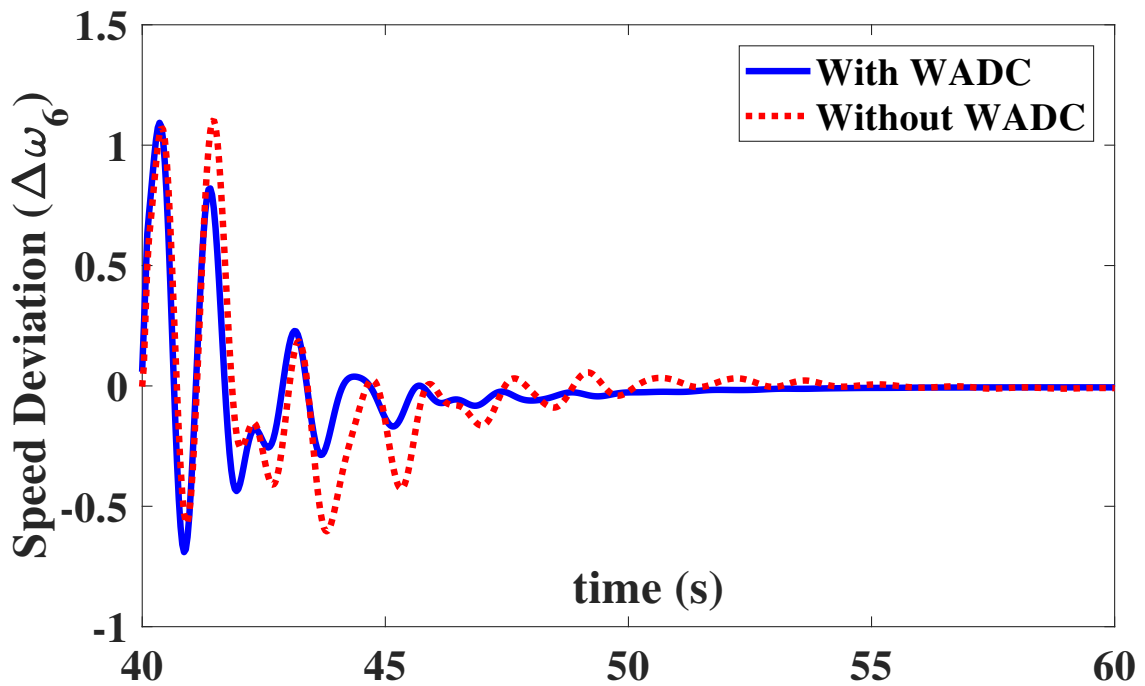


Fig. 5.29. Generator-6 speed deviation (rad/s)

## 5.5 Summary

In this chapter, a novel real-time frequency based reduced order modeling of the large power system for EMT simulation is proposed. In the proposed architecture,

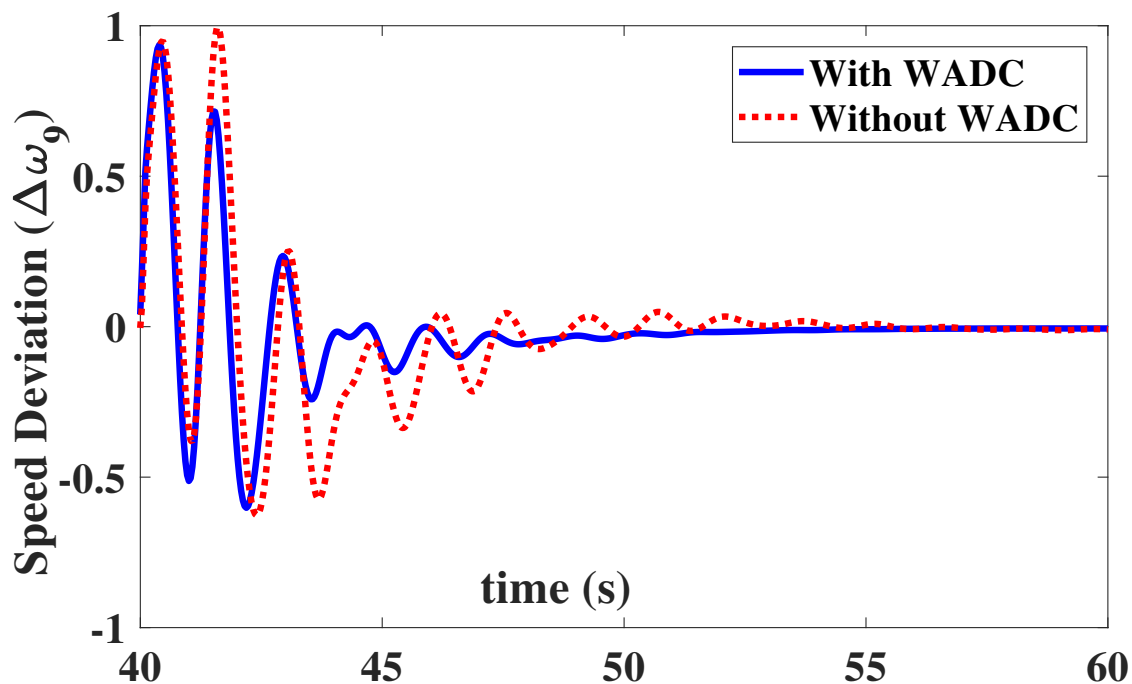


Fig. 5.30. Generator-9 speed deviation (rad/s)

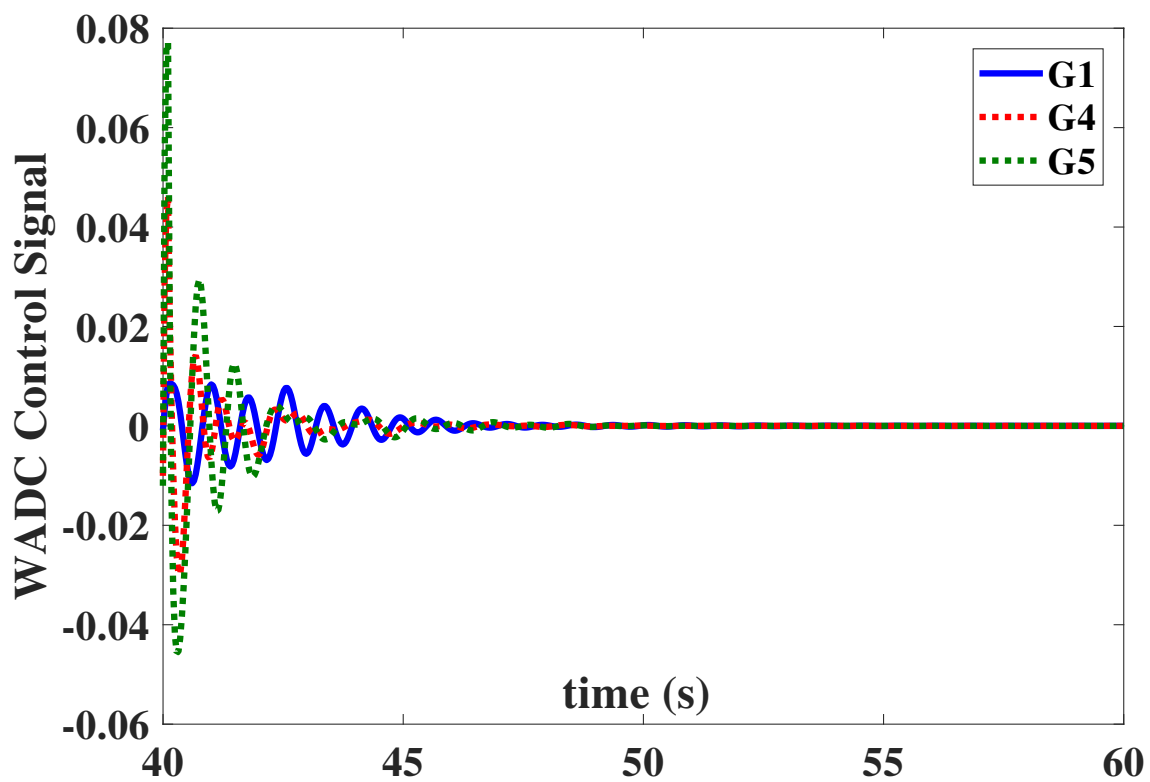


Fig. 5.31. WADC output signal

'external area' is modeled as a combination of FDNE and TSA. FDNE is formulated using a discrete online RLS which can preserve high-frequency behavior, whereas TSA preserves the electromechanical (low frequency) behavior of the system under consideration. The approach also enforced passivity conditions. Implementation results in two area and IEEE 39 bus power system models shows that the proposed reduced order model is in close agreement with the full model and the advantage of the reduced order model is that it can accurately aggregate large power grid for EMT simulations. In the next chapter, the reduced order modeling based control methodology of wind farms is proposed.

## CHAPTER 6: SENSORLESS REAL-TIME REDUCED ORDER MODEL-BASED ADAPTIVE MAXIMUM POWER TRACKING PITCH CONTROLLER FOR GRID-CONNECTED WIND TURBINES

This chapter presents a sensor-less maximum power tracking (MPT) pitch controller for grid-connected Wind Turbine (WT). The main advantage of the proposed architecture is that the approach ensures smooth operation and thus minimizes the mechanical stress and damage on the WT during high wind speed and grid transient conditions. Simultaneously, it also: a) reduces transients in Point of Common Coupling (PCC) bus voltage, b) reduces rotor speed oscillations, and c) controls the output power of the wind turbine without exceeding its thermal limits. The approach can work without wind speed measurements. To consider the effect of grid variations at the PCC, the affected area in the grid is modeled as a study area (area of interest), and remaining area (external area) is modeled as frequency dependent reduced order model (FDROM). The reduced order model (ROM) is then used to estimate the reference speed. The proposed controller is designed using the error between the actual speed of the generator and the reference speed, to ensure smooth operation and limit the speed and aerodynamic power at the rated values. The architecture is evaluated using wind farm integrated Kundur's two-area and IEEE-39 bus test systems using the real-time digital simulator (RTDS).

## 6.1 Introduction

In recent years, the move towards eliminating fossil fuel dependency and embracing sustainable energy based power generation has increased interest in integrating renewable energy sources (RES) into the power grid. In 2016, WTG provided almost 6% of U.S. electricity generation (about 37% of electricity generation from RES) [81]. However, WTGs operate under varying wind conditions and depends on time and geographical location, which may be above or below rated values, thus varying their output power. During high wind speed conditions, the controller should limit the speed of the generator not crossing the rated value by limiting the rotation rate of the rotor, since pitch system contributes to 21.3% of the overall failure rate of wind turbines [6]. This can be achieved by controlling the blade pitch angle [125]. However, in practical systems, WTG operations are also influenced by the dynamics of the entire power grid. Thus, the design of WTG controllers should take into consideration of grid dynamics. Wind speed conditions are generally measured using anemometers, failure of which can cause deterioration in tracking performance. This should be addressed in the controller design as well [35].

Grid level interactions of the wind farms/turbines are generally controlled considering a constant voltage at the PCC even though electro-mechanical dynamics are included in such simulations. This ignores response of the wind farms with the electromagnetic transients in the grid. The effect is on the mechanical fatigue that happens on the wind generators. If one should design a controller considering grid dynamics, detailed Electro-Magnetic Transient (EMT) based grid models with dynamic

models of WTG including DFIG are required. However, detail modeling of the large-scale power grid is impractical due to computational complexity [129]. In [117, 129], to reduce computational burden several model order reduction techniques based on linearized models have been developed, but these models are effective only during low-frequency oscillations. A possible method to reduce computational burden while retaining accuracy is to model part of WTG integrated grid (study area) in detail and the remainder of the network (external area) [64] as an equivalent. For this, the external area is modeled as a combination of low frequency (Transient Stability Assessment -TSA type) and high frequency (FDNE type) equivalents. In TSA type, the network is formulated as an admittance matrix at the fundamental frequency, and the generators are aggregated and modeled in detail such that low-frequency electromechanical oscillations are preserved, whereas FDNE preserves the high-frequency oscillations.

In the literature, several WTG pitch control strategies for limiting the aerodynamic power and generator speed are proposed. An individual pitch control scheme with a proportional-integral (PI) controller with two resonant compensators is proposed in [128]. However, the PI controllers are designed based on a specific operating point. A pitch angle controller based on fuzzy logic is proposed in [115], in which generator output power and speed are used as input to the controller. However, determining exact, fuzzy rules and membership functions for dynamically changing conditions are considered. In [58], a fuzzy predictive algorithm coupled with conventional PI controllers is proposed for wind-turbine collective-pitch control. In [88], a method of nonlinear PI control for variable pitch wind turbine is proposed. The non-linearities

and disturbances are evaluated and compensated using extended order state and perturbation observer. However, this method uses only one set of PI parameters for various speeds. Ref. [23] investigated determining the pitch angle when wind speed exceeds rated value using particle swarm optimization (PSO), and [101] proposed a method for blade pitch angle control using PID control.

In this chapter, a novel sensor-less method for smoothly controlling the transients of WTG during high wind speed is introduced. The architecture uses an online dynamic network model of the power grid that is computationally tractable, to calculate reference speed for tracking. Then an adaptive controller is designed for smooth tracking and limiting the mechanical stress on the turbine. The control variables used are the algebraic error between the calculated reference speed and actual generator speed. For controller adaptation, a model identification method based on Recursive Least Square (RLS) method is also designed [108]. RLS identification is performed online to estimate the transfer function with the difference between the reference and actual speed as the process output and the controlling signal as the process input. Then using the identified transfer function, the controller gains of the controller are calculated online. If there is a change in operating point, the controller auto-tunes as the transfer function is identified every sample time. This auto-tuning feature allows the proposed controller to provide an efficient way for adjusting the pitch angle during changing system operating conditions, as opposed to the conventional PI controller where gains are constant irrespective of the system conditions.

The advantages of the proposed architecture are it,

- auto-tunes based on the wind speed and grid conditions and thus can higher precision.
- can be implemented in practical systems as the online grid models are computationally tractable.
- provides dynamic control capabilities as opposed to conventional controllers.
- can eliminate the requirement of the anemometer.
- reduces mechanical stress on the turbine, voltage transients, and speed oscillations.

The rest of the chapter is organized as follows. In Section 6.2 the wind turbine and generator modeling are discussed. In Section 6.3, frequency dependent reduced-order modeling of the large power grid is discussed. Section 6.4 discusses the proposed adaptive pitch controller and example case study. Section 6.5 shows the implementation of the proposed controller. Section 6.6 discusses the real-time simulation results and Section 6.7 summarizes the chapter.

## 6.2 Wind Turbine and Generator Modeling

The variable speed WTGs are more frequently involved in providing grid reliability as they are more controllable provides reactive power support and harvests optimum energy over a wide wind speed range [37]- [93]. In this chapter, a two-mass variable speed model of WTG is designed and scaled up to represent 200 MW of rated power at the VSC interface transformer for modeling purposes.

### 6.2.1 The Wind Turbine

The mechanical power output ( $P_m$ ) of the turbine in kW [100] can be represented as

$$P_m = C_p(\lambda, \beta) \frac{\rho A}{2} v_{wind}^3 \quad (6.1)$$

where  $C_p(\lambda, \beta)$  is the coefficient of performance of the turbine which can be determined from the  $C_p$  vs  $\lambda$  curve for different blade pitch angle ( $\beta$ ),  $\lambda$  is the tip speed,  $\rho$  is the density of air in  $kg/m^3$ ,  $A$  is the area swept by the turbine blades in  $m^2$ , and  $v_{wind}$  is the velocity of the wind in m/s. From this,  $\lambda$  can be represented as [17, 18]

$$\lambda = \frac{R\omega_t}{v_{wind}} \quad (6.2)$$

where  $R$  and  $\omega_t$ , are the radius of the turbine ( $m$ ) and the rotational speed of the turbine ( $rad/s$ ) respectively.

### 6.2.2 The Coefficient of Performance

The turbine coefficient of performance describes the power extraction efficiency of the WT and is generally less than 0.5. This can be represented as [70]

$$C_p(\lambda, \beta) = c_1 \left[ \frac{c_2}{\lambda_i} - c_3\beta - c_4 \right] e^{-\frac{c_5}{\lambda_i}} + c_6\lambda \quad (6.3)$$

where

$$\frac{1}{\lambda_i} = \frac{1}{\lambda + 0.08\beta} - \frac{0.035}{\beta^3 + 1}$$

For the proposed design,  $c_1 = 0.5176$ ,  $c_2 = 116$ ,  $c_3 = 0.4$ ,  $c_4 = 5$ ,  $c_5 = 21$  and  $c_6 = 0.0068$ . The value of tip speed ratio  $\lambda$  is constant for all maximum power points. The maximum value for power coefficient  $C_p$  for a particular wind turbine can be

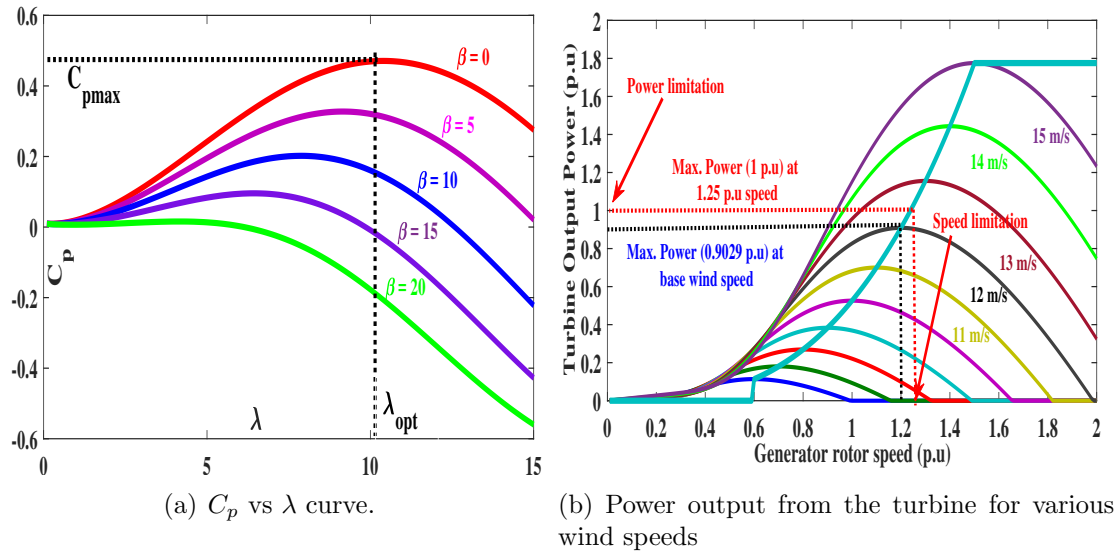


Fig. 6.1. Wind turbine characteristics.

obtained from  $C_p$  vs  $\lambda$  curve for different values of  $\beta$ . For the wind turbine selected for this work, the optimum value and the maximum value of  $\lambda$  are 10.4 and 0.48 respectively at  $\beta = 0^\circ$ . A characteristic plot of  $C_p$  vs.  $\lambda$  for the proposed turbine based on (7.3) is as shown in Fig. 1(a). From Fig. 1(a), it can be observed that as  $\beta$  increases,  $\lambda$  decreases due to a decrease of turbine speed, and simultaneously  $C_p$  becomes less. This feature is used in pitch angle control to limit the speed of the rotor for wind speeds greater than the rated value. Fig. 1(b) shows the turbine output power (p.u) vs rotor speed (p.u) for various wind speeds.

### 6.2.3 Wind Generator

In the proposed study, type III DFIG with conventional vector control based Grid Side and Rotor Side Controllers is considered. The detailed nonlinear model of DFIG is developed in RSCAD<sup>TM</sup>. Modeling details of DFIG are discussed in several previous works [85], [38, 120].

### 6.2.4 Maximum Power Point Tracking (MPPT)

At any speed, from (7.1)

$$P_m = k_p c_p v_w^3 = k_p c_p \left( \frac{\omega_r}{r_{gear} \lambda} \right)^3 \quad (6.4)$$

$$\omega_r = r_{gear} \lambda \left( \frac{P_m}{k_p c_p} \right)^{\frac{1}{3}} \quad (6.5)$$

where  $\omega_t$  and  $\omega_r$  [p.u] are the angular speed of the turbine and rotor respectively, and  $P_m$  is the turbine mechanical power in [p.u]. The scaling factor  $k_p \left( = \frac{\rho A c_{pmax} \times v_{\omega BASE}}{2 P_{BASE}} \right)$  indicates maximum output power at base wind speed. The angular speed of the turbine,  $\omega_t$  [p.u], is related to the generator rotor speed by the gear ratio, ( $r_{gear} = 1.2$ ), i.e.  $\omega_t = \frac{\omega_r}{r_{gear}}$ .

### 6.3 Frequency-Dependent Reduced Order Modeling of Power Grid

Large power systems can be modeled as an equivalent to reducing complexity and computational burden while preserving the high and low-frequency behavior of the system under consideration. To this effect, the proposed frequency dependent reduced-order power system models the area of interest (study) area in detail and the remaining part as a combination of FDNE and coherency based TSA equivalent. First, FDNE is formulated based on online RLS identification, by short and open circuiting all voltage and current sources respectively and energizing the external area with constant voltage and varying frequency. The FDNE is represented as a discrete

transfer function and rearranged as shown in (7.7).

$$\begin{aligned}
 I_b(k) = & -a_1 I_b(k-1) - a_2 I_b(k-2) \cdots - a_n I_b(k-n) \\
 & + b_1 V_b(k-1) + b_2 V_b(k-2) \cdots + b_n V_b(k-n)
 \end{aligned}
 \tag{6.6}$$

where  $I_b$  and  $V_b$  are the boundary bus current and voltages respectively,  $k$  is the current sample, and  $n$  is the order.

For designing the TSA equivalent and to further reduce the complexity and computational burden, all generating units and nodes in external area are aggregated using coherency based inertial aggregation [20, 109] and the admittance matrix ( $Y$ ) of external area is reduced to  $Y_{red}(2 \times 2)$  matrix by Kron node reduction method represented as follows:

$$\begin{bmatrix} I_b \\ I_e \end{bmatrix} = \begin{bmatrix} Y_{bb} & Y_{be} \\ Y_{eb} & Y_{ee} \end{bmatrix} \begin{bmatrix} V_b \\ V_e \end{bmatrix}
 \tag{6.7}$$

where  $I_e$  and  $V_e$  are the generator bus current and voltage respectively. The generator bus voltage is calculated as shown in (6.8) and generator bus is energized with  $V_e$  as shown in Fig. 6.2.

$$V_e = [I_e - Y_{eb} V_b] Y_{ee}^{-1}
 \tag{6.8}$$

Finally,  $I_b$  is calculated as shown in (6.9) and injected into the boundary bus.

$$I_b = Y_{bb} V_b + Y_{be} V_e
 \tag{6.9}$$

The advantage of this method is that the reduced power system model behaves as the original system and can replace the original system for further dynamic assessment of renewable energy sources. Further details regarding reduced order modeling are

discussed in [106, 111].

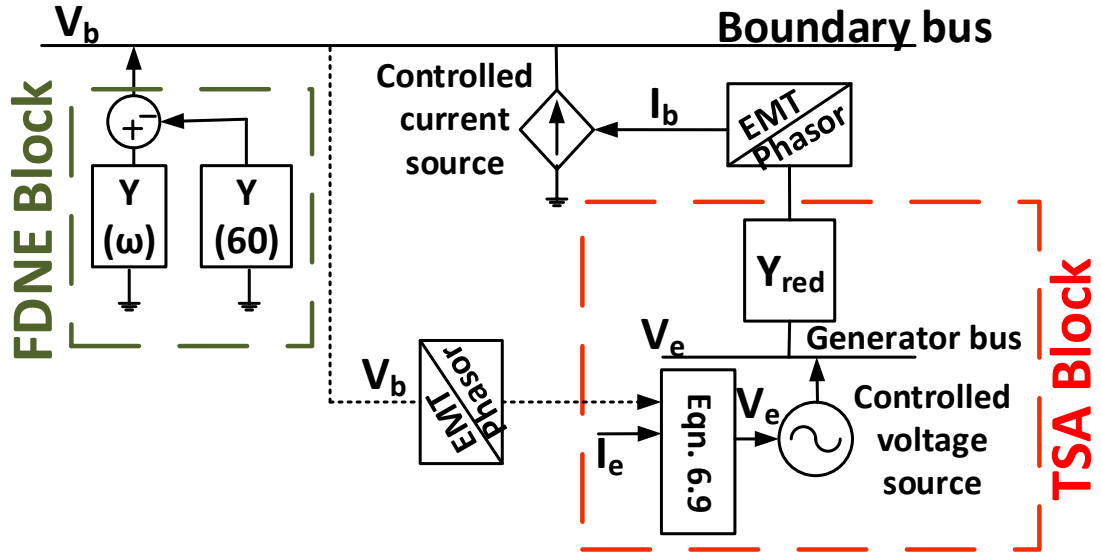


Fig. 6.2. FDNE and TSA block diagram for a power network.

#### 6.4 Proposed Adaptive Pitch Controller

The proposed adaptive pitch controller involves two steps: 1) Recursive Least Square Identification and 2) Calculating gains of the controller.

##### 6.4.1 Recursive Least Square Identification

The RLS identification with the process input  $u(k)$  and the process output  $y(k)$  is performed dynamically at every sample  $k$ . The  $n^{\text{th}}$  order process of the model in  $z$ -domain can be represented as

$$\frac{y(k)}{u(k)} = \frac{b_1 z^{-1} + b_2 z^{-2} + \dots + b_n z^{-n}}{1 + a_1 z^{-1} + a_2 z^{-2} + \dots + a_n z^{-n}} \quad (6.10)$$

where  $a$ 's and  $b$ 's are the denominator and numerator coefficients of the transfer function respectively. Let  $N$  be the observation window length, then (6.10) can be

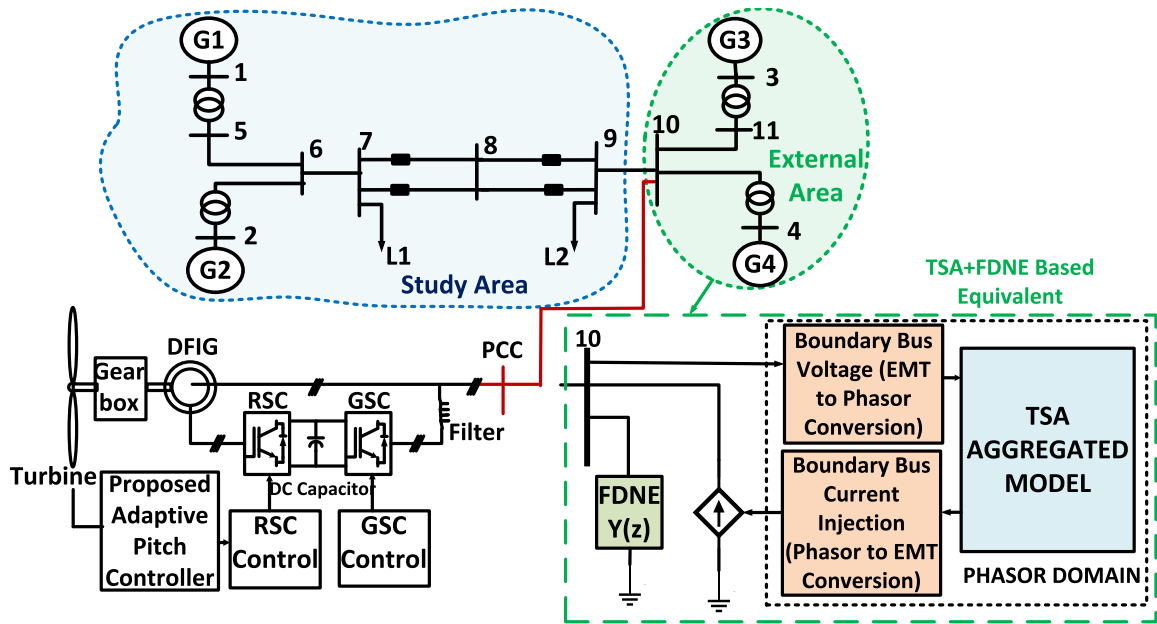


Fig. 6.3. Proposed dynamic equivalent of two-area test system.

rewritten as

$$\begin{bmatrix} y(k) \\ y(k-1) \\ \cdot \\ \cdot \\ y(k-N+1) \end{bmatrix}_{N \times 1} = [X_{N \times 2n}] \begin{bmatrix} a_1 \\ \cdot \\ \cdot \\ a_n \\ b_1 \\ \cdot \\ \cdot \\ b_n \end{bmatrix}_{2n \times 1} \quad (6.11)$$

Equation (6.11) can be represented in the generic form as follows

$$\Phi_{model(N \times 1)} = X_{N \times 2n} \Theta_{2n \times 1} \quad (6.12)$$

where  $\Phi$  is a matrix of past and current outputs ( $y$ ),  $X$  is a matrix of past inputs and outputs and,  $\Theta$  is a matrix of the numerator and denominator coefficients of the transfer function. If the identified model is different from measurements, then

$$\epsilon = \Phi_{measured} - \Phi_{model} \quad (6.13)$$

where  $\epsilon$  is the error between the measurements from the system (subscript measured) and the identified model (subscript model) for which criteria  $J$  can be defined as

$$J = \epsilon^t \epsilon \quad (6.14)$$

By letting  $dJ/d\Theta = 0$ , we get

$$\Theta = [X^t X]^{-1} X^t \Phi_{measured} \quad (6.15)$$

From (6.15), to identify the coefficients of the transfer function the inverse of the state matrix should be computed. If the size of the state matrix is large, inverting a large matrix will slow down the process and sometimes may be even not achievable. To overcome this issue, a recursive least squares technique is used. RLS is a computational algorithm that recursively finds the coefficients of the model and eliminates the matrix inversion. Let  $S = X^t X$  then (6.15) can be written as

$$\Theta = S^{-1} X^t \Phi \quad (6.16)$$

where  $\Phi = \Phi_{measured}$

$$\Theta(k) = S^{-1} [x(k)X^t(k-1)] \begin{bmatrix} \Phi(k) \\ \Phi(k-1) \end{bmatrix} \quad (6.17)$$

$$\Theta(k) = S^{-1} [x(k)\Phi(k) + X^t(k-1)\Phi(k-1)] \quad (6.18)$$

Using (6.12)

$$\Theta(k) = S^{-1} [x(k)\Phi(k) + X^t(k-1)X(k-1)\Theta(k-1)] \quad (6.19)$$

$$\Theta(k) = S^{-1} [x(k)\Phi(k) + S(k-1)\Theta(k-1)] \quad (6.20)$$

$$S(k) = S(k-1) + x(k)x'(k) \quad (6.21)$$

Substituting (6.21) in (6.20)

$$\Theta(k) = S^{-1} [x(k)\Phi(k) + \{S(k) - x(k)x'(k)\}\Theta(k-1)] \quad (6.22)$$

$$\begin{aligned} \Theta(k) &= \Theta(k-1) + [S(k-1) + x(k)x'(k)]^{-1}x(k) \\ &\quad [\Phi(k) - x'(k)\Theta(k-1)] \end{aligned} \quad (6.23)$$

Let  $P(k) = S^{-1}(k)$ , and by matrix inversion lemma  $P(k)$  can be represented as

$$P(k) = P(k-1) \left[ I - \frac{x(k)x'(k)P(k-1)}{1 + x'(k)P(k-1)x(k)} \right] \quad (6.24)$$

Substituting (6.21) in (6.20) and letting

$$K(k) = \frac{P(k-1)x(k)}{1 + x'(k)P(k-1)x(k)} \quad (6.25)$$

where  $P(k)$  can be written as

$$P(k) = [I - K(k)x'(k)] P(k-1) \quad (6.26)$$

Therefore, (6.23) can be represented as

$$\Theta(k) = \Theta(k-1) + K(k) [\Phi(k) - x'(k)\Theta(k-1)] \quad (6.27)$$

With weighted least square, (6.25) and (6.26) can be presented as

$$K(k) = \frac{P(k-1)x(k)}{\gamma + x'(k)P(k-1)x(k)} \quad (6.28)$$

$$P(k) = \frac{[I - K(k)x'(k)]P(k-1)}{\gamma} \quad (6.29)$$

Finally, using the process input  $u(k)$  and process output  $y(k)$ , the numerator and denominator coefficients of the transfer function (6.10) can be computed using RLS identification [10].

#### 6.4.2 Calculating Gains of the Controller

For calculating the gains of the controller, the process model is always restricted to second order. This algorithm calculates the proportional, integral, and derivative gains  $K_p$ ,  $K_i$ , and  $K_d$  every sample period. In this process, the closed loop pole shifting factor  $\alpha$  is the only adjustment or tuning that is required. Using (6.10) 2<sup>nd</sup> order model can be represented as

$$\frac{y}{u} = \frac{b_1q^{-1} + b_2q^{-2}}{1 + a_1q^{-1} + a_2q^{-2}} = \frac{B}{A}(\text{open loop}) \quad (6.30)$$

From (6.27), the open loop characteristic equation is given by

$$1 + a_1q^{-1} + a_2q^{-2} = 0 \quad (6.31)$$

Thus, the closed loop characteristic equation using pole shifting by a factor  $\alpha$  can be represented as

$$(1 + \alpha q^{-1})(1 + a_1\alpha q^{-1} + a_2\alpha^2 q^{-2}) = 0 \quad (6.32)$$

where,  $0 \leq \alpha \leq 1$  and  $q$  is a shift operator. From the above, the control structure is given by

$$u(k) = \frac{T(q^{-1})}{R(q^{-1})}y_r(k) - \frac{S(q^{-1})}{R(q^{-1})}y(k) \quad (6.33)$$

If in (6.33) we let

$$R(q^{-1}) = (1 - q^{-1})(1 + r_1q^{-1}) \quad (6.34)$$

$$S(q^{-1}) = s_0 + s_1q^{-1} + s_2q^{-2} \quad (6.35)$$

where

$$\begin{aligned} s_0 &= T_s K_i + \frac{K_d}{T_s} + K_p \\ s_1 &= -\frac{2K_d}{T_s} - K_p + r_1 K_p \\ s_2 &= \frac{K_d}{T_s} - r_1 K_p \end{aligned}$$

The architecture can be represented in terms of PID gains, which can be calculated using the following set of equalities:

$$K_i = \frac{-(s_0 + s_1 + s_2)}{T_s} \quad (6.36)$$

$$K_p = \frac{(s_1 + 2s_2)}{1 + r_1} \quad (6.37)$$

$$K_p = T_s \left[ \frac{r_1 s_1 - (1 - r_1) s_2}{1 + r_1} \right] \quad (6.38)$$

As the system operating conditions changes, the coefficients of the transfer function get updated and hence the STR PID controller auto-tunes in real-time. The derivative part in PID controller helps in reducing the overshoot. Fig. 6.4 shows the architecture of the proposed controller.

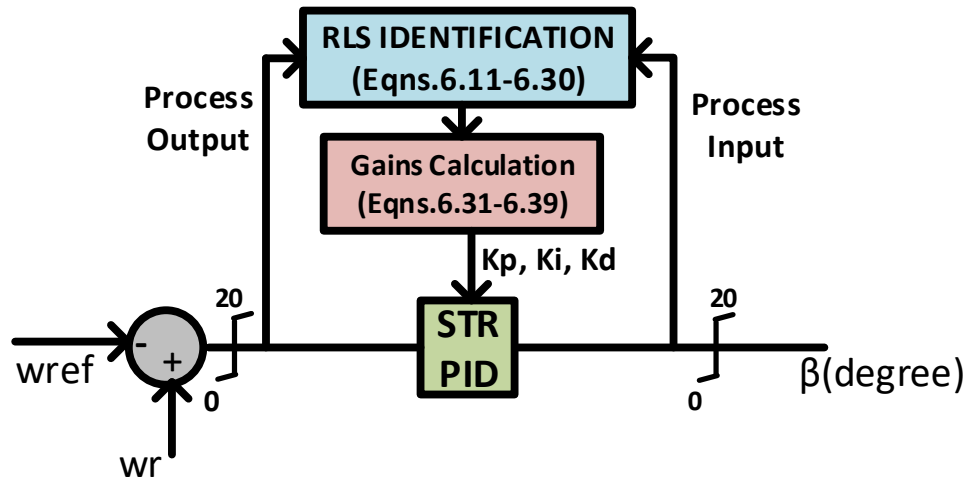


Fig. 6.4. Proposed STR Controller.

### 6.5 Implementation of the Proposed Controller

The proposed adaptive pitch angle controller uses the difference between the reference speed ( $\omega_{ref}$ ) and the actual speed ( $\omega_r$ ) for estimating the control signal. The  $\omega_{ref}$  is calculated as follows:

**Step:1** Initialize  $\omega_r$  and estimate  $P_m$  from (7.4) and represented as:

$$P_m(t) = k_p c_p \left( \frac{\omega_r(t)}{r_{gear} \lambda} \right)^3 \quad (6.39)$$

At MPPT,  $\lambda, c_p = 1$  [p.u] and using (6.39), the mechanical power is represented as

$$P_m(t) = k_p \left( \frac{\omega_r(t)}{r_{gear}} \right)^3 \quad (6.40)$$

where  $t$  is the current iteration.

**Step:2** The electrical power delivered  $P_e$  is calculated using grid conditions at boundary and PCC bus to include the grid transient effects in the controller action, whereas

conventional pitch controller doesn't account for this calculation.

$$P_e(t) = \frac{V_{pcc}(t)V_B(t)}{X} \sin(\delta_B(t) - \delta_{pcc}(t)) \quad (6.41)$$

where  $V_{pcc}$  and  $V_B$  is the voltage of the WTG bus and boundary bus respectively,  $\delta_{pcc}$  and  $\delta_B$  are the voltage angle at PCC and boundary bus respectively, and  $X$  is the reactance between PCC and boundary bus. Generally, stator resistance is small enough to ignore power loss associated with it and when the converter power loss is neglected, the total real power (here  $P_e$ ) injected into the grid equals to the sum of the rotor power and the stator power [59, 73].

**Step:3** Using the  $P_m$  in (6.40) and  $P_e$  in (6.41), the  $\omega_r$  is calculated as follows:

$$\omega_r(t+1) = \frac{P_m(t) - P_e(t)}{J \left( \frac{\omega_r(t) - \omega_r(t-1)}{\Delta t} \right)} \quad (6.42)$$

where  $J$  is the moment of inertia,  $\Delta t$  is the simulation time step. Steps 1, 2 and 3 are repeated until  $P_m$  and  $\omega_r$  is converged and the converged value of  $\omega_r$  is taken as the  $\omega_{ref}$  (Fig. 6.5). The integrated implementation flowchart is as shown in Fig. 6.6.

## 6.6 Experimental Test Bed and Results

The proposed framework in Fig. 6.6 is using a lab real-time simulator set up on Kundur's two-area [82] and IEEE 39-bus [46] test system models with WTGs. Table 6.1 and 6.2 show the simulation parameters of the wind turbine and DFIG. The real-time testbed consists of a) Reduced order RTDS/RSCAD<sup>TM</sup> models of Kundur two area and IEEE 39-bus test systems, b) RTDS/RSCAD<sup>TM</sup> model of WTGs and, c) GTNET-SKT connection between RTDS and MATLAB for interfacing TSA type equivalent with EMT type simulation (Fig. 6.7). The grid models are an actual

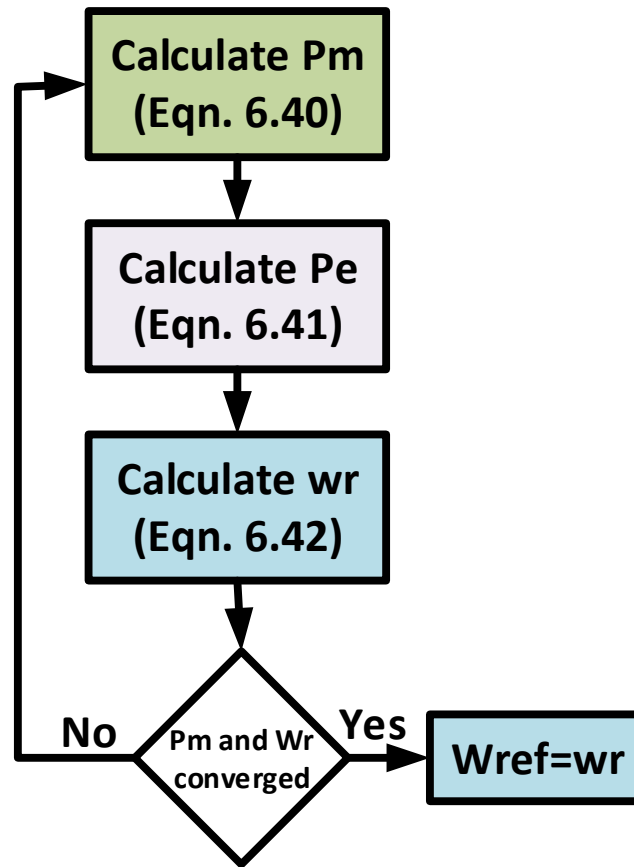


Fig. 6.5. Flowchart for  $\omega_{ref}$  calculation.

representation of the wind farms and characterize real-time closed-loop control with real-life verified generator and control models with GE controllers. The operating principle of the test-bed is the rules that guide the machine model to work based on the grid changes.

#### 6.6.1 Validation of the algorithm using Kundur's test system

First, for validating the algorithm using grid integrated WTGs, two-area test system (see Fig. 6.3) is used. The test system consists of four 900MVA synchronous generators and a WTG at bus-10. Based on the location of WTG, the test system

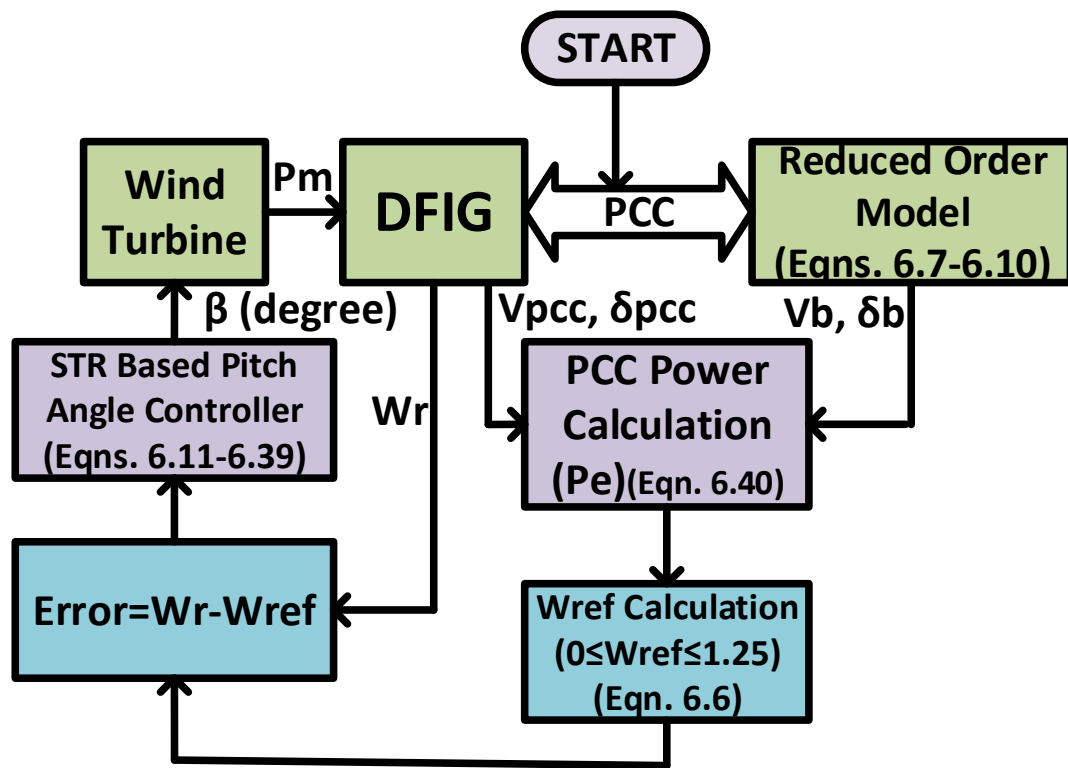


Fig. 6.6. Flowchart of the proposed controller.

is divided into study and external area as shown in Fig. 6.3. The external area is modeled as a wide-band equivalent, which is the combination of TSA and FDNE. The TSA type equivalent is modeled in MATLAB<sup>®</sup> in phasor domain and FDNE type equivalent is modeled in RSCAD<sup>™</sup> in EMT domain. The reduced order model of the test system is validated by comparing its behavior under transient response with the original test system. For this, 3-phase bolted faulted created at 0.1 sec for 0.1 sec. Fig. 8(a) and Fig. 8(b) shows the comparison of RMS voltage at bus 7 and the relative speed of Gen-3 w.r.t Gen-2 respectively. From the above results, it can be observed that the reduced order model behaves similarly as the full model under transient condition. Several other event analyses have been studied, and similar

Table 6.1  
Simulation parameters of wind turbine

<b>Parameter Name</b>	<b>Value</b>
Rated generator power	2.2 MVA
Rated turbine power	2.0 MW
Generator speed at rated turbine speed (p.u.)	1.2 p.u.
Rated wind speed	12.0 m/s
Cut-in wind speed	6.0 m/s
Cut-out wind speed	25 m/s
Rate of change of pitch angle	$\pm 10^0/s$

Table 6.2  
Simulation parameters of DFIG

<b>Parameter Name</b>	<b>Value</b>
Rated stator voltage (L-L RMS)	0.69 kV
Turn ratio (rotor over stator)	2.6377
Rated MVA	2.2 MVA
Stator resistance	0.00462 p.u.
Stator leakage reactance	0.102 p.u.
Unsaturated magnetizing reactance	4.348 p.u.
First cage rotor resistance	0.006 p.u.
First cage rotor leakage reactance	0.08596 p.u.
Inertia constant	1.5 MWs/MVA

results are obtained.

To validate the controller under rapidly varying realistic wind conditions Fig. 9(a) has been extracted from the ERCOT data along with a 3-phase bolted fault on Bus-8 for a duration of 6 cycles at 13 sec, and the performance is compared with conventional PI and no controller systems. Figs. 9(b)-10(a) show the active power and rotor speed of the DFIG. It shows that with the conventional controller the rating of the DFIG

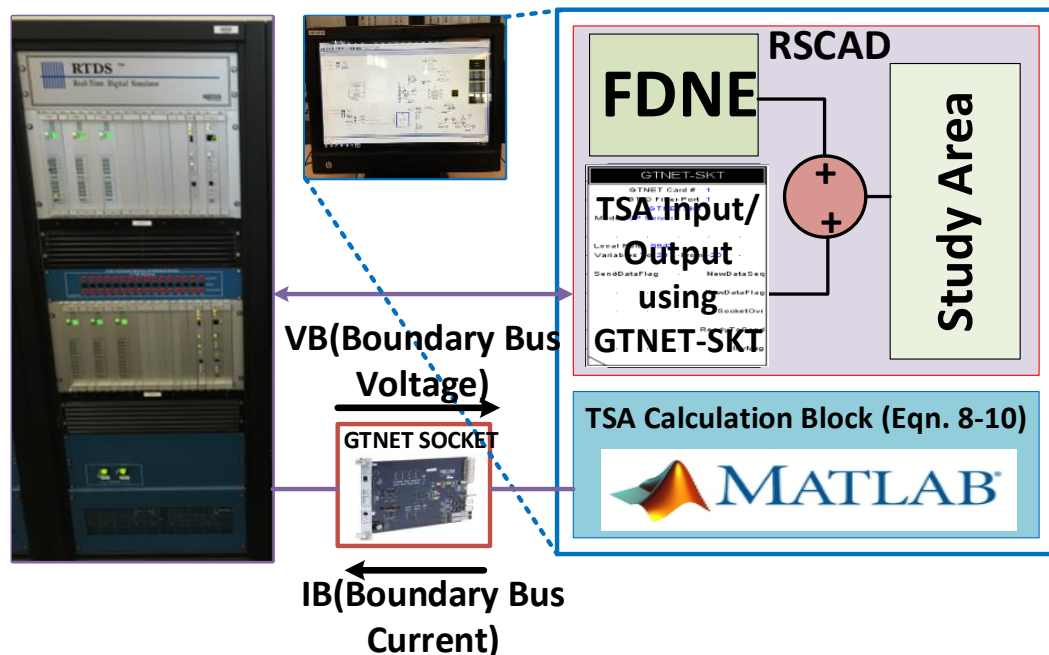


Fig. 6.7. Experiment setup in RTDS.

exceeds its limit and effectively increases stress on all connected electrical equipment. For example, the active power at 30sec with a proposed controller is 219.6 MW, whereas with a conventional controller it is 264.06 MW. So, with the conventional controller, the active power is 20% more than the rated value which increases the stress on electrical equipment. Even the rotor speed crosses its limit when controlled by the conventional PI controller (For example, it crosses 1.35 p.u at 30 sec while the limit is 1.25 p.u). So it can be concluded that the proposed controller controls the output power and at the same time limits the rotor speed. Additionally, other conventional generators (for example  $G_1$  here) connected to the grid has less rotor oscillations with the proposed controller (See Fig. 10(b)).

Also, it can be seen from Fig. 11(a) that the rate of change of pitch angle is within its limit (10 deg/s). Additionally, Fig. 11(b) illustrates that the proposed

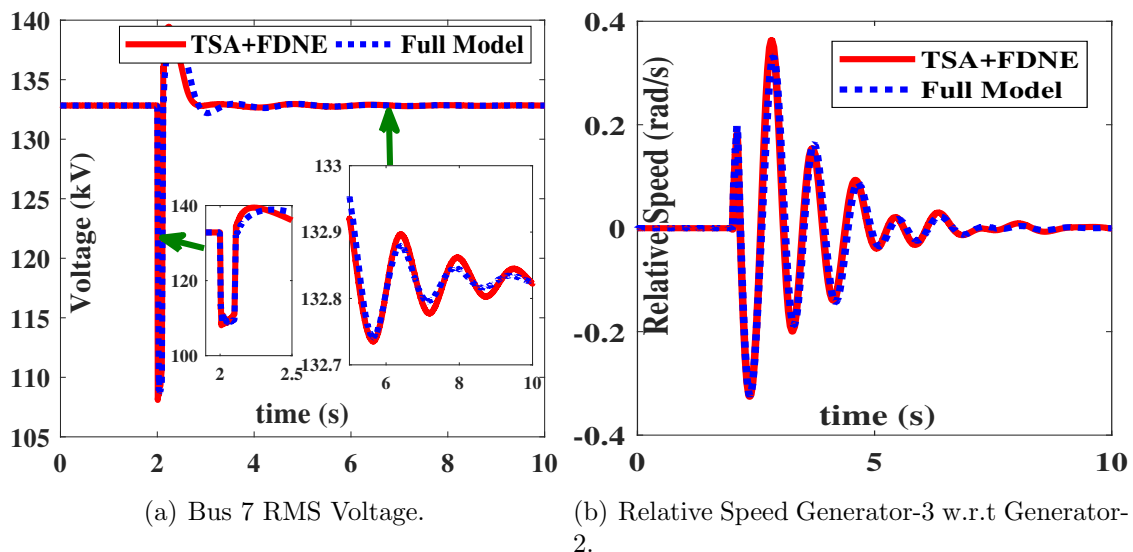


Fig. 6.8. FDNE validation

controller is effectively limiting the mechanical torque. It can be observed that at 90 sec the mechanical torque with a conventional controller is 0.9266 p.u. Hence, the conventional controller provides fatigue caused by increased mechanical stress on the turbine due to torque overrun by 11.20%.

The RLS identification is performed for  $\omega_r - \omega_{ref}$  and  $\beta$  as shown in Fig. 6.4. The controller gains  $K_i$ ,  $K_p$ , and  $K_d$  are calculated at every time step using online identification routine. The conventional PI controller gains are adapted from GE wind turbine field implemented values [35].

Fig. 6.12 shows the comparison of gains of STR and the conventional PI controller for the two-area system. From Fig. 6.12, it can be seen that STR controller auto-tunes as the operating condition changes whereas the conventional PI controller has fixed gains irrespective of operating condition. For reliable operation, the generator should be operated below the maximum speed limit (1.25 p.u) and thus tuning is

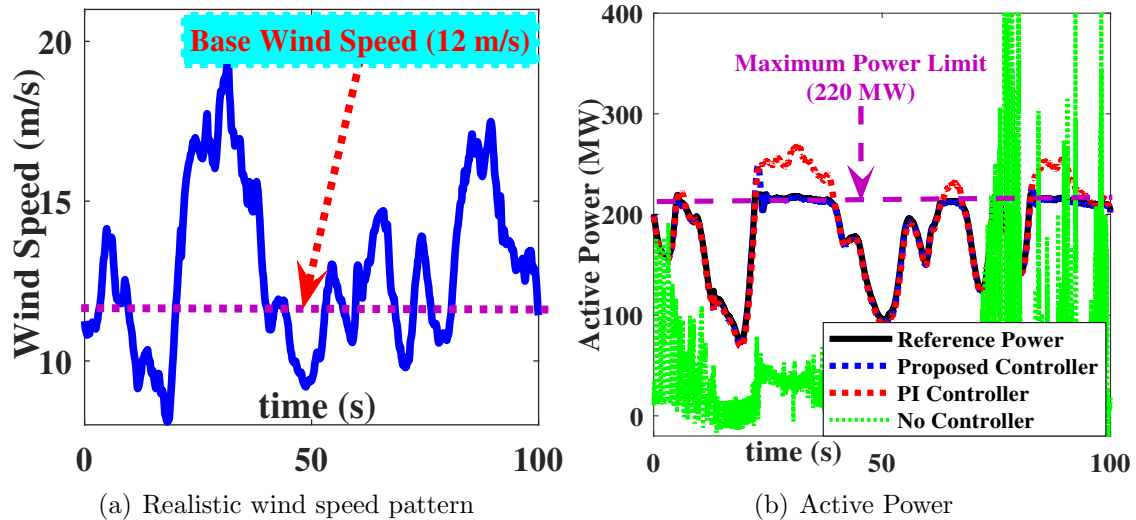


Fig. 6.9. Wind Speed and DFIG Active Power

necessary.

#### 6.6.2 Validation of the algorithm with IEEE 39-bus test system

For further validation, the algorithm is also implemented on the IEEE 39-bus system with WTGs connected at bus 17 and bus 26. The test system is divided into study and external area based on the location of the WTGs as shown in Fig. 6.13. The external area is modeled as a combination of TSA and FDNE.

In this case, the proposed controller is tested and validated for variable wind speed pattern (Fig. 14(a)) along with a 3-ph bolted fault on Bus-14 for 0.1 sec at 13sec. With the proposed controller, PCC voltage is much smoother and within allowable limit during high wind speed conditions when compared to PCC voltage with the conventional PI controller (Fig. 14(b)). For example, the voltage at 40sec proposed controller is 1.017 p.u, whereas with the conventional controller it is 0.9692 p.u. So, with the conventional controller, the voltage is 6.266% less than the steady state value (1.034 p.u). Hence, the proposed controller improves the voltage by 4.93% and can

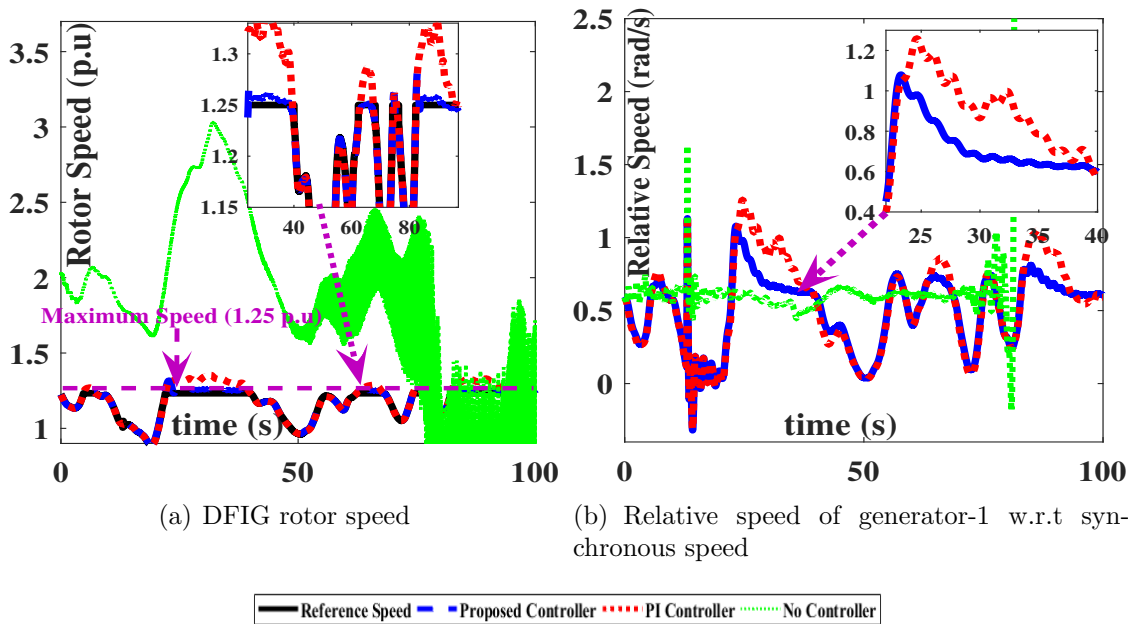


Fig. 6.10. DFIG rotor speed and relative speed comparison.

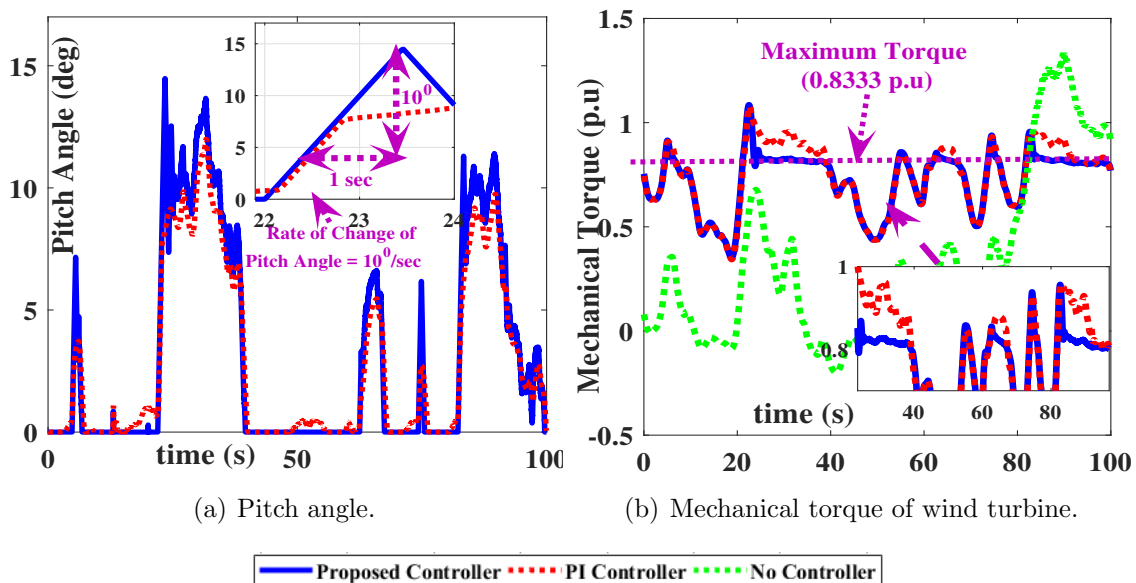


Fig. 6.11. Pitch angle and mechanical torque comparison.

keep the voltage at the PCC within stable regions during high wind speed conditions.

Fig. 15(a) shows the comparison of DFIG rotor speed of WTG-2 and Fig. 15(b) shows the comparison of the active power of WTG-1. Fig. 16(a) shows the relative

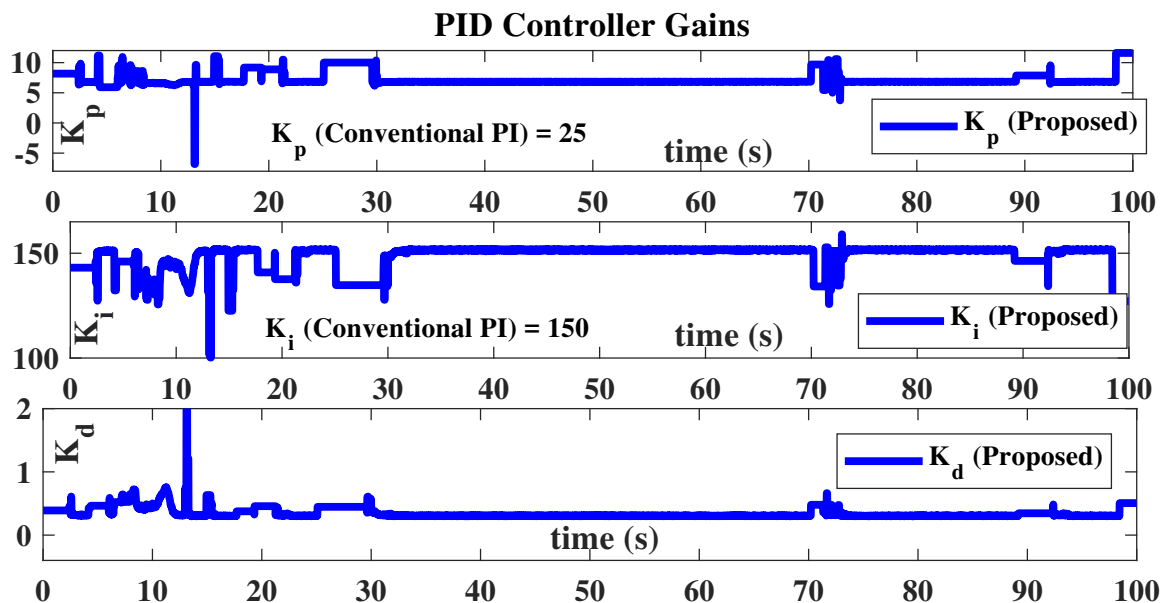


Fig. 6.12. STR and conventional PI controller gains.

speed of synchronous generator-3. Fig. 16(b) shows the mechanical torque of WTG-2.

It can be seen that the active power at 45sec with the proposed controller is 218.7 MW, whereas with the conventional controller it is 285.8 MW. So, with the conventional controller, the active power is 29.9% more rated value which stresses on electrical equipment. Also, the rotor speed crosses its limit using the conventional controller (for example, it crosses 1.37p.u at 45 sec where the limit is 1.25 p.u). The WTG control helps to keep the speed, and active power under control and yet can keep the voltage at the PCC and other buses within the stable operating region during high wind speed conditions. It can be observed that at 40 sec the mechanical torque with the conventional controller is 0.9968 p.u, so the conventional controller provides fatigue caused by increased mechanical stress on the turbine due to torque overrun by 19.62%. Hence, with the proposed controller, during high wind speed conditions, all electrical and mechanical parameters are within the rated limits, so

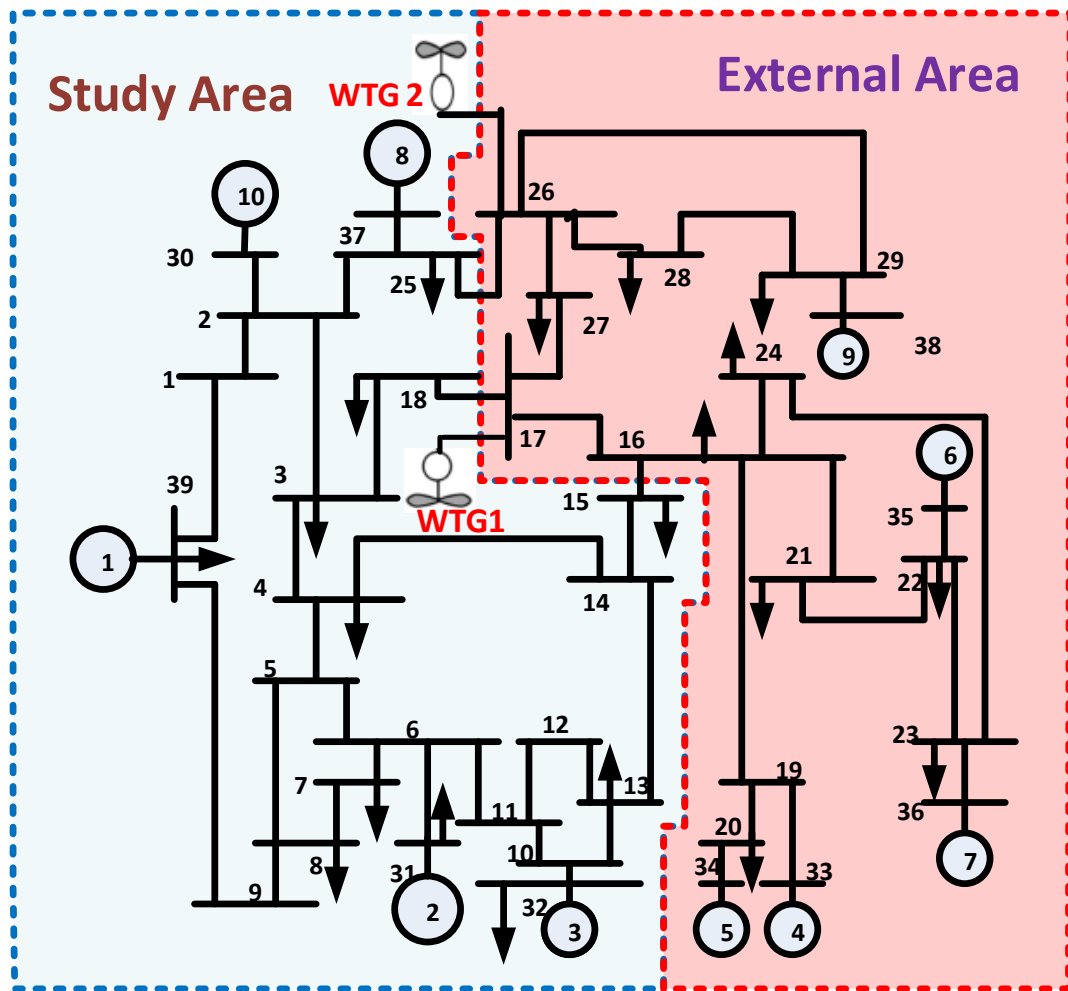


Fig. 6.13. IEEE 39-Bus system.

actions that are otherwise required to protect the electrical and mechanical equipment during these conditions is not a primary concern. Further with the proposed controller synchronous machine oscillations in the grid are damped out much faster when compared to the conventional PI controller. The proposed architecture also ensures that the active power transfer is smooth thus maintaining the required power balance during high wind speed conditions.

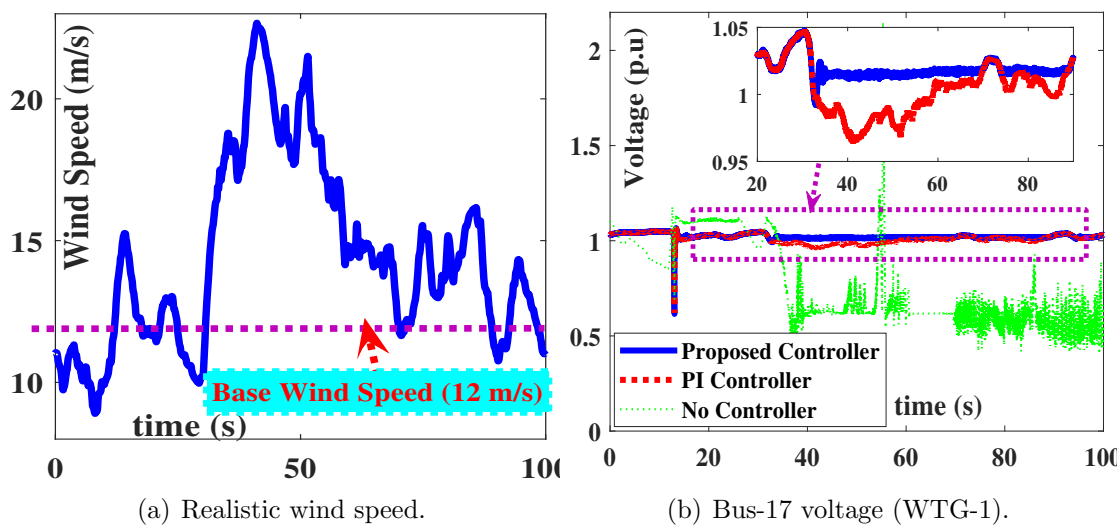


Fig. 6.14. Wind speed and PCC voltage comparison.

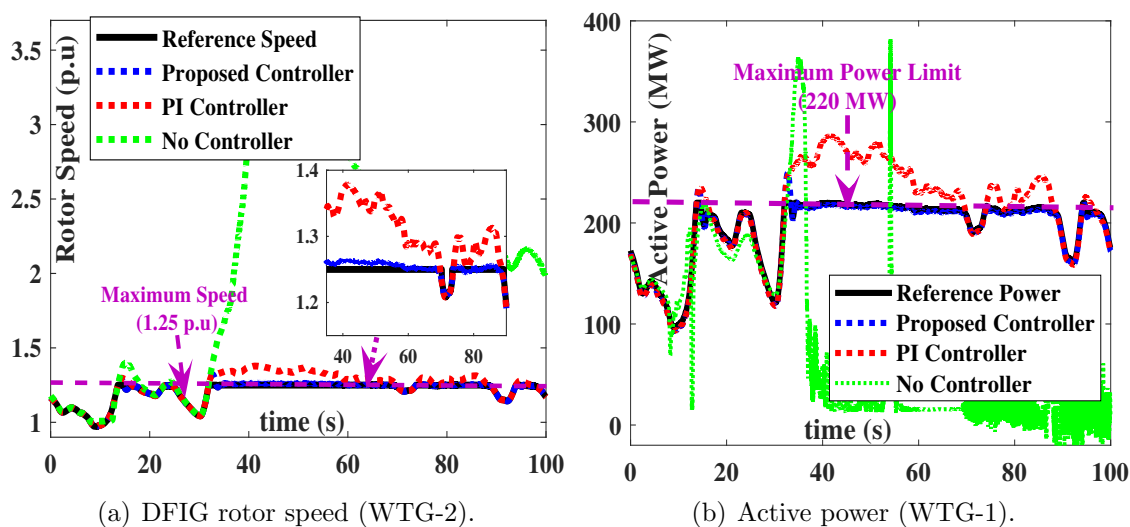


Fig. 6.15. DFIG rotor speed and active power comparison.

## 6.7 Summary

The proposed sensor-less pitch angle control of WTG, considering the grid dynamics at the wideband frequency and using the STR controller is an efficient way of controlling the speed of the turbine during high wind speed. WTG is connected to reduced order model of the power grid, the area in which WTG connected is modeled

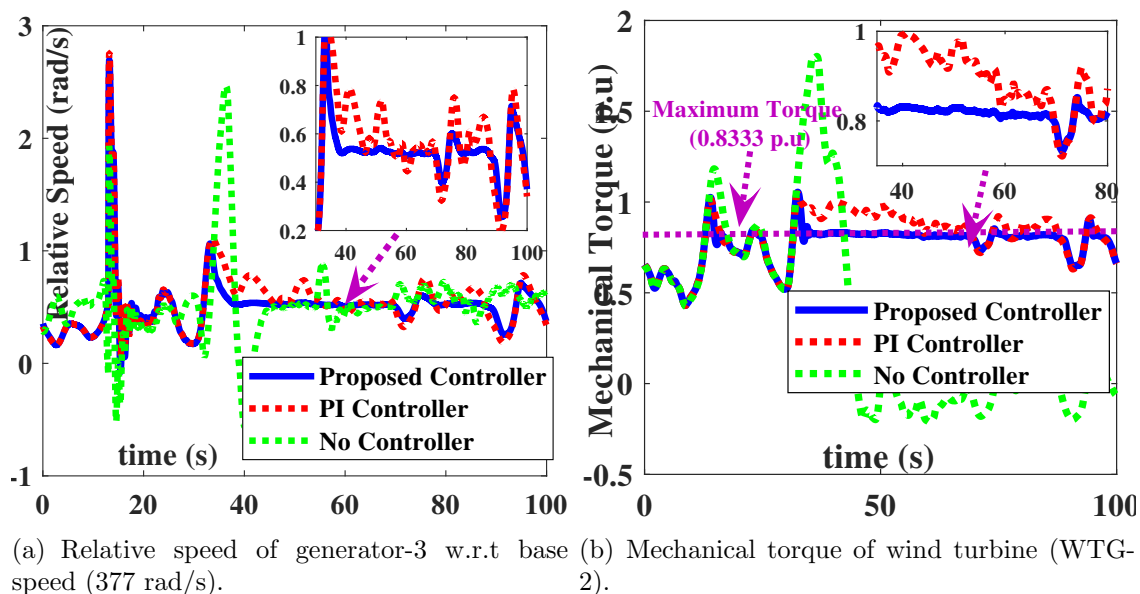


Fig. 6.16. Relative speed and mechanical torque comparison.

in detail while the remaining part is modeled as a combination of FDNE and coherency based TSA equivalent. The proposed method is validated in RTDS/RSCAD using WTG integrated reduced order models of Kundur two-area and IEEE-39 bus test systems. The results clearly illustrate that the proposed pitch angle controller provides better power balance, voltage regulation and reduces fatigue on the turbine. Additionally, the proposed architecture can work without anemometer, thus avoiding any malfunctioning of the device. It has also been demonstrated that the architecture can be implemented in real-life as demonstrated using real-time simulators. In the next chapter, the distributed coherency grouping of generators is proposed.

## CHAPTER 7: DISTRIBUTED COHERENCY GROUPING OF GENERATORS BASED ON SPECTRAL CLUSTERING USING MEASUREMENTS

The availability of synchrophasor measurements from the PMU data enhanced wide area measurement systems (WAMS). One of the important tasks of such situational awareness system is coherency grouping of generators after a transient condition in the system. For coherency grouping, data corresponding to all generators should be transmitted to a central control center for processing. Dealing with a large amount of data, acquiring, and processing requires most advanced communication and super-computing facilities. In reality, the areas are divided based on geography/utility, in this case, the generator in one area may have a coherent generator in another area. To identify coherent groups of data the processor should require data from all the generators, but the part of the network owned by one utility may not be completely observable from other utility. To this effect, this chapter proposes a distributed coherency grouping of generators based on spectral clustering. In this method initially generators of each area are clustered locally, and the optimal number of clusters are identified using Elbow method. The cluster centers corresponding to each group are transmitted to the global control center and at the global control center these centers from all local control centers are grouped which gives the indices of global clusters. The global indices are transmitted to the local area for regrouping based on global indices. The proposed algorithm is validated using IEEE 39-bus power system model

on RSCAD/RTDS<sup>®</sup> and MATLAB<sup>®</sup> real-time co-simulation platform.

## 7.1 Introduction

With ever-increasing demand and penetration of intermittent renewable energy sources, the power system is operating at near rated value and has posed an immediate challenge for power system operators. For reliable grid operations, an efficient situational awareness system is vital. Synchrophasor measurements from PMU enhanced the effectiveness of situational awareness systems as measurements are readily available and also power system states can be estimated using PMU data [34]. Coherency identification of the generators is one of the important tasks of situational awareness system for efficient power system operation. In literature several coherency identification methods are reported, many of these methods are based on either power system model or measurements from data acquisition systems.

The modal based approaches are discussed in Section 1.3.2.1. However model-based methods are based on the linearized power system model at a particular operating point, and the accuracy depends on the accuracy of the model. The practical applications of model-based methods are not-accurate since real power system is non-linear and operating point changes w.r.t time (i.e., network topology, load changes, contingencies, etc.).

The shortcomings of the model-based method can be over-come by measurement based methods. Since the model-based methods are solely dependent on measurements, these methods are independent of contingencies, accurate network parameters, or a detailed dynamic model. Recently PMU based measurements are used for

coherency identification, and the current research methodologies are focusing in this direction [66]. Coherency based on measurements are discussed in Section 1.3.2.2.

However, apart from the inherent pros and cons of the measurement based methods, most of the current methods have the following physical limitations:

- Dealing with a large amount of data requires most advanced communication and super-computing facilities.
- The areas are divided based on geography/utility, in this case, the generator in one area may have a coherent generator in another area. To identify coherent groups of data the processor should require data from all the generators, but the part of the network owned by one utility may not be completely observable from other utility.

To overcome this limitation, this chapter proposes a distributed coherency grouping of generators based on spectral clustering. In this method, initially the optimal number of clusters in each area are pre-determined based on Elbow method [14], then generators are clustered in local control centers using Nystrom method based spectral clustering [109, 110] and assigned local cluster indices. The cluster centers corresponding to each group are transmitted from the local control center to a global control center. These cluster centers are grouped using Elbow method to estimate the optimal clusters at global control centers. The corresponding global cluster indices are transmitted back to local control centers and used to re-index the local cluster indices. The final cluster indices after re-indexing local cluster indices based on global-cluster indices provide information of coherent generator groups/clusters. The proposed

algorithm is validated using IEEE 39-bus power system model on RSCAD/RTDS and MATLAB real-time co-simulation platform.

To summarize, the major contributions of this work are:

- Developed a novel real-time co-simulation test bed for power system wide-area monitoring techniques using distributed algorithms.
- Developed a distributed algorithm for coherency grouping of generators.
- The applicability of distributed techniques for coherency grouping of generators is validated.

The chapter is organized as follows: Section 7.2 discusses the proposed algorithm, Section 7.3 discusses the implementation of the proposed algorithm, Section 7.4 discusses the experimental setup, the implementation test results are discussed in Section 7.5, and Section 7.6 concludes the chapter.

## 7.2 Proposed Algorithm

The proposed algorithm for distributed clustering of generators involves following steps: a) Determine an optimal number of clusters, b) Clustering of generators at local control centers using Nystrom spectral clustering, and c) Clustering of local cluster centers at the global control center.

### 7.2.1 Optimal number of clusters

The optimal number of clusters at local and global control centers are determined using the Elbow method combined with k-means clustering.

### 7.2.1.1 $K$ -means Clustering

The  $k$ -means clustering is a simple clustering algorithm in which  $k$  initial cluster centers are chosen, where  $k$  is the number of clusters which is either optimally determined or user-specific parameter.  $k$  clusters are formed by assigning each point to its closest cluster center. Then the cluster centers are recomputed based on the points assigned to each cluster, and this process continues till the cluster centers do not change. The  $k$ -means clustering is shown in Algorithm. 7.1.

---

#### **Algorithm 7.1** $k$ -means Clustering

---

- 1: Select  $k$  initial cluster centers
  - 2: **repeat**
  - 3:   By assigning each point to its closest cluster centers  $k$  clusters are formed.
  - 4:   The cluster centers are recomputed based on the points assigned to each cluster.
  - 5: **until** The cluster centers do not change
- 

### 7.2.1.2 Elbow Method

For estimating the optimal number of clusters in each local and global center Elbow method is used. In this method, start with  $k = 2$  and increase in step of 1. This method looks at percentage variance w.r.t number of clusters, the optimal number of clusters is when adding more clusters will explain a lot of variance and the point at which the marginal gain drop giving an angle in the graph gives the optimal number of clusters. So,  $k$  is the optimal number of clusters corresponding to 90% percentage of % variance. Algorithm. 7.2 shows the methodology of Elbow method. Further details on Elbow method are reported in [14, 22].

---

**Algorithm 7.2** Elbow Method
 

---

- 1: Set initial no of clusters  $k = 1$  and the maximum number of clusters is equal to number of points.
  - 2: **repeat**
  - 3:   Compute sums of point-to-cluster center distances in the  $k$ -by-1 vector using k-means (Algorithm 7.1).
  - 4:   Increment  $k$  in steps of 1.
  - 5: **until**  $k =$  no of points
  - 6:   Compute variance of sums of point-to-cluster center distances and percentage variance.
  - 7:   The optimal number of clusters ( $k$ ) corresponds to 90% of percentage variance.
- 

### 7.2.2 Clustering of generators at local control centers

The generators has to be clustered into  $k$  optimal clusters using the generator speed data. This can be achieved using spectral clustering.

#### 7.2.2.1 Spectral clustering using Nystrom method

The proposed distributed clustering of generators is performed using spectral clustering. Initially the generators in each area are clustered using spectral clustering based on Nystrom method, for this generator speed data  $\omega_1, \dots, \omega_n$  is used, where  $n$  is the length of data window. A similarity matrix  $S \in R^{n \times n}$  which gives the relation between  $\omega_i$  and  $\omega_j$  is formulated. The similarity matrix is based on Gaussian and represented as (7.1).

$$S_{ij} = e^{-\left(\frac{\|\omega_i - \omega_j\|^2}{2\sigma^2}\right)} \quad (7.1)$$

where  $\sigma$  is the scaling factor.

The objective of the algorithm is to use similarity matrix information to group  $\omega_1, \dots, \omega_n$  into  $k$  clusters. However, the similarity matrix  $S$  is dense and the size is

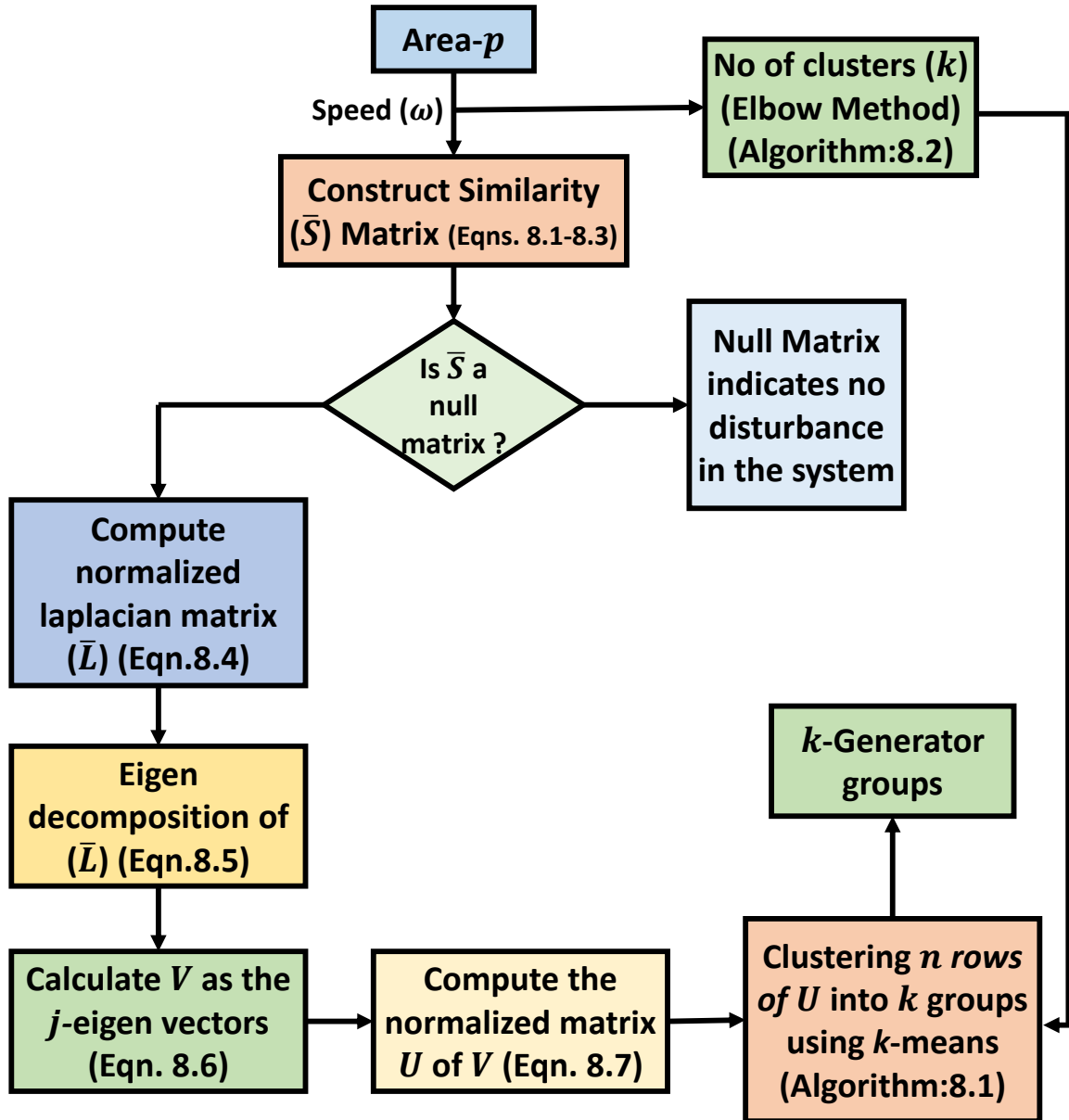


Fig. 7.1. Flow chart of spectral clustering algorithm.

large i.e.  $n \times n$ . To increase the speed of clustering and reduce the computational burden during online clustering a Nystrom method is used, which analyzes sub-matrix of the dense matrix  $S$ . Let  $A$  represents a matrix of the size  $l \times l$  matrix (where  $l \ll n$ ),  $B$  represents a matrix of size  $l \times (n - l)$  and  $C$  represents a matrix of size  $(n - l) \times (n - l)$ . The matrices  $A$ ,  $B$ ,  $C$ , and  $D$  are sub-matrices of dense matrix  $S$

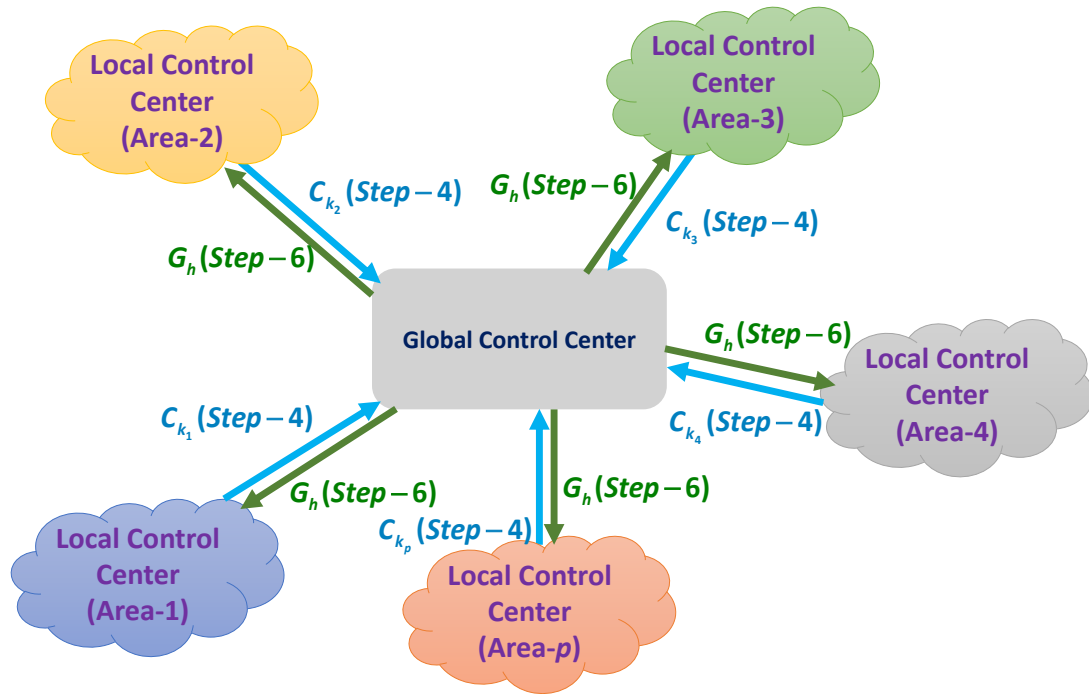


Fig. 7.2. Implementation of the proposed algorithm.

and represented as (7.2).

$$S = \begin{bmatrix} A & B \\ B^T & C \end{bmatrix}, W = \begin{bmatrix} A \\ B^T \end{bmatrix} \quad (7.2)$$

Using  $A$  and  $B$ , the dense matrix  $S$  is approximated by Nystrom method and the approximation  $\bar{S}$  is represented as (7.3)

$$S \approx \bar{S} = WA^{-1}W^T = \begin{bmatrix} A & B \\ B^T & B^T A^{-1} B \end{bmatrix} \quad (7.3)$$

Using the approximated similarity matrix  $\bar{S}$ , the normalized laplacian matrix is written as (7.4)

$$\bar{L} = I - D^{-\frac{1}{2}} \bar{S} D^{-\frac{1}{2}} \quad (7.4)$$

where  $D = \sum_{j=1}^n \bar{S}_{ij}$  is a diagonal matrix.

The eigenvalues and corresponding eigen-vectors of  $\bar{L}$  are obtained from eigenvalue decomposition as follows

$$\bar{L} = \bar{V}\bar{\Sigma}\bar{V}^T \quad (7.5)$$

where  $\bar{\Sigma}$  and  $\bar{V}$  are the eigenvalues and the corresponding eigen-vectors respectively.

If  $j$  slow eigenvalues are considered in the clustering process, then the eigen-vectors corresponding to  $j$  eigenvalues, represented as a  $R^{n \times j}$  matrix, are

$$V = [\vec{v}_1, \vec{v}_2, \dots, \vec{v}_j] \quad (7.6)$$

where  $\vec{v}_i \in R^n, i = 1, \dots, j$  and  $j$  is the number of eigen-vectors. The normalized eigen-vector matrix can then be represented as

$$U_{im} = \frac{\bar{V}_{im}}{\sqrt{\sum_{r=1}^k \bar{V}_{ir}^2}}, i = 1, \dots, n \quad \text{and} \quad m = 1, \dots, j \quad (7.7)$$

The rows of can easily be clustered into groups using k-means method [19,77]. Fig. 7.1 shows the flowchart of the proposed clustering algorithm.

### 7.2.3 Clustering of local cluster centers at global control center

The cluster centers from all local control centers are transmitted to the global center, so the input data to the global center are the cluster centers. Since these cluster centers are not dense Elbow method accompanied with k-means will suffice for global center clustering. These cluster centers are grouped into  $h$  optimal clusters, and the global cluster indices are transmitted back to local control centers for estimating final indices based on global-cluster indices. The final cluster indices give information

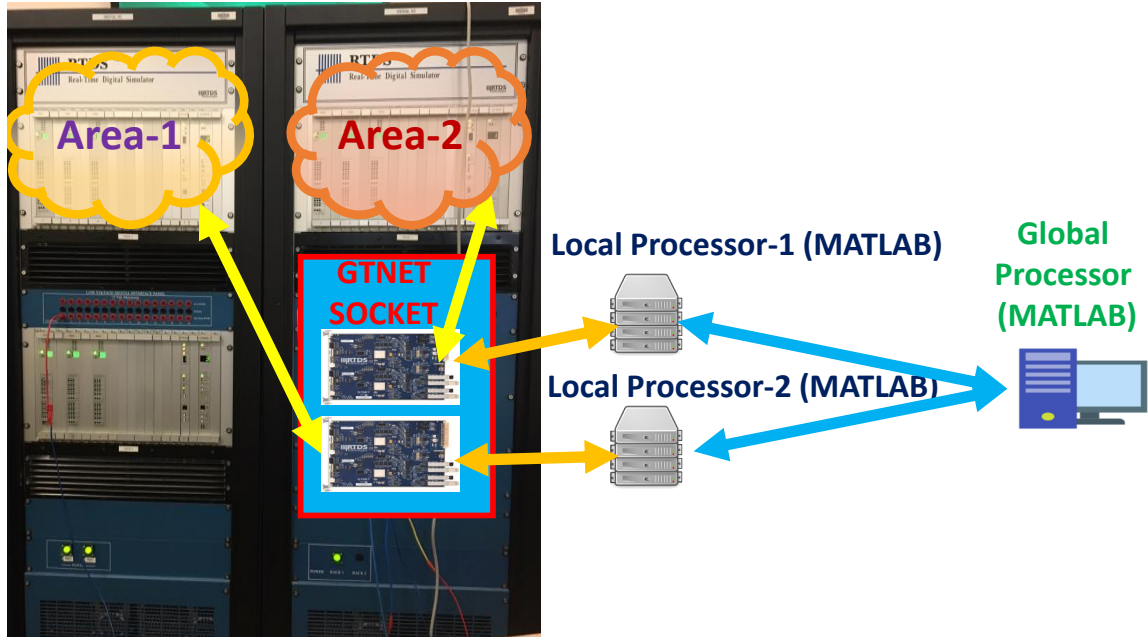


Fig. 7.3. Real-time experimental setup.

about the coherent generator groups for the system as a whole.

### 7.3 Implementation of the Proposed Algorithm

The implementation of the proposed algorithm has following steps:

Step 1: Determine no of areas ( $p$ ) and no of generators in each area ( $q_r$ ) where  $r = 1, \dots, p$ .

Step 2: Optimal number of clusters ( $k_r$ ) in each local control center is determined using Elbow method.

Step 3: Using generator speed data ( $\omega \in R^{q \times n}$ ),  $q_r$  generators in area  $r$  are clustered into  $k_r$  groups which gives cluster centers ( $C_{k_r}$ ) and local cluster indices ( $L_{k_r}$ ).

Step 4: The cluster centers are transmitted to global control center and concatenated

$$\text{as } C_G = [C_{k_1}, C_{k_2}, \dots, C_{k_p}].$$

Step 5:  $C_G$  which is global cluster center matrix is clustered into user defined or optimal number of clusters ( $h$ ) and global cluster indices ( $G_h$ ) are obtained. Since the size of  $C_G$  is very low compared to full speed data matrix, Elbow method accompanied with  $k$ -means method can be directly used for clustering.

Step 6: Global cluster indices are transmitted back to local control centers and generators are assigned final cluster indices based on global cluster indices.

Fig. 7.2 shows the implementation of the proposed algorithm.

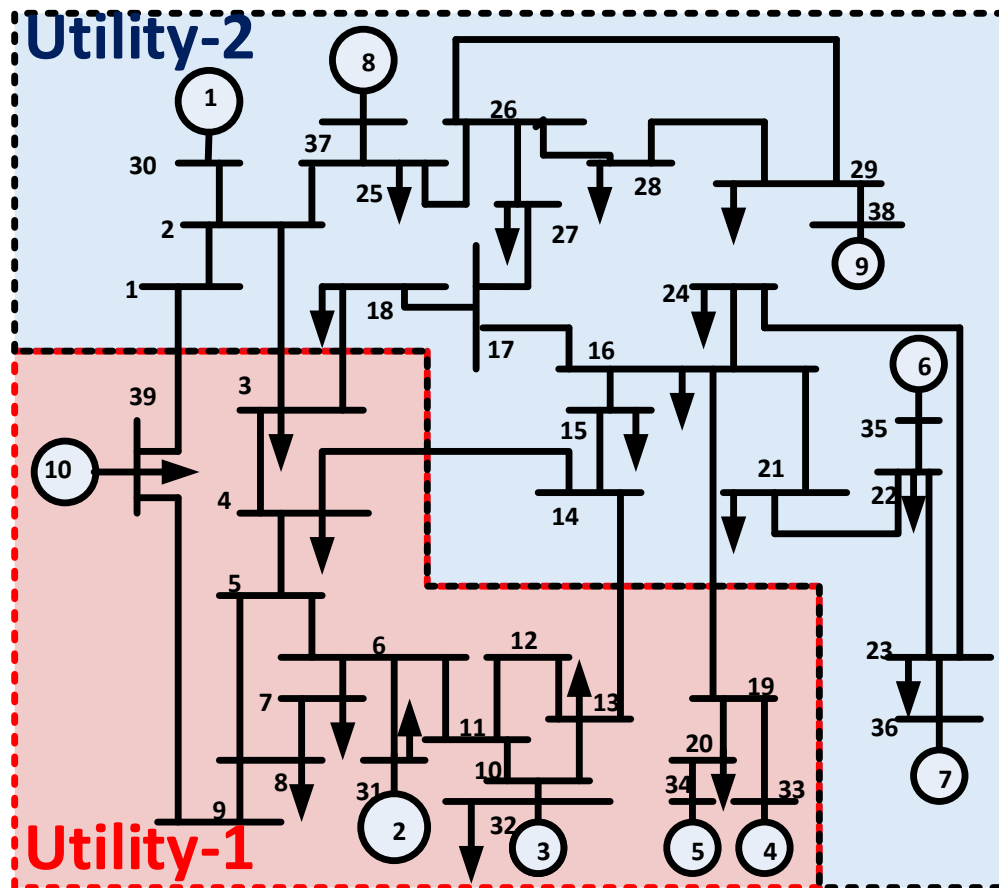


Fig. 7.4. IEEE 39 bus system.



## 7.5 Implementation Test Results

The IEEE-39 bus system is assumed to be consisting of two utilities as shown in Fig. 7.4. The utility-1 consists of generators 1 to 5 and utility-2 consists of generators 6 to 10. The utility-1 is modeled in rack-1 whereas utility-2 is modeled in rack-2 to emulate the scenario of different utilities. The RTDS transmits the speed data to MATLAB through the GTNET-SOCKET connection. To validate the proposed online distributed clustering algorithm and to demonstrate how the generator grouping changes w.r.t change in system operating conditions a sequence of events are created. Initially a 3-ph fault is created at 4.9s on Bus-14 for a duration of 0.1s, then another fault is created at 30.9s on Bus-19 for a duration of 0.1s, and finally, another fault is created at 60.9s on Bus-6 for a duration of 0.1s. The response of generators after the sequence of events is as shown in Fig. 7.5.

The objective is to cluster the coherent group of generators for various operating conditions; this can be achieved by analyzing the generator dynamics from all the utilities in real-time using the proposed algorithm. The input data to the clustering algorithm is speed data for a 20s window. Each time block is the 20s and updated every 10s as represented in Fig. 7.5, hence the coherency groups of generators are updated every 10s. The update frequency can be less than or greater than 10s based on the user computational resources and requirement. The generators are grouped every time block in this case in 90s duration the generators are grouped 9 times.

The first step in this proposed algorithm involves estimating the optimal number of clusters (groups) using Elbow method.

### 7.5.1 Estimation of Optimal Number of Clusters

The optimal number of clusters for local centers are estimated for a sequence of events as shown in Fig. 7.5. For demonstration purpose, three 20s windows are shown here.

#### 7.5.1.1 Case:1 (From 0s to 20s)

For this case, the utility-1 the speed data of generators 1 to 5 from 0s to 20s is used for analysis. Using the Elbow method, the optimal number of clusters for local area-1 are 3. Similarly, the utility-2 the speeds of generator 6 to 10 from 0 to 20s is analyzed. From the Elbow method, the optimal number of clusters in this local area is 3. Fig. 7.6 shows the percentage variance w.r.t no of clusters.

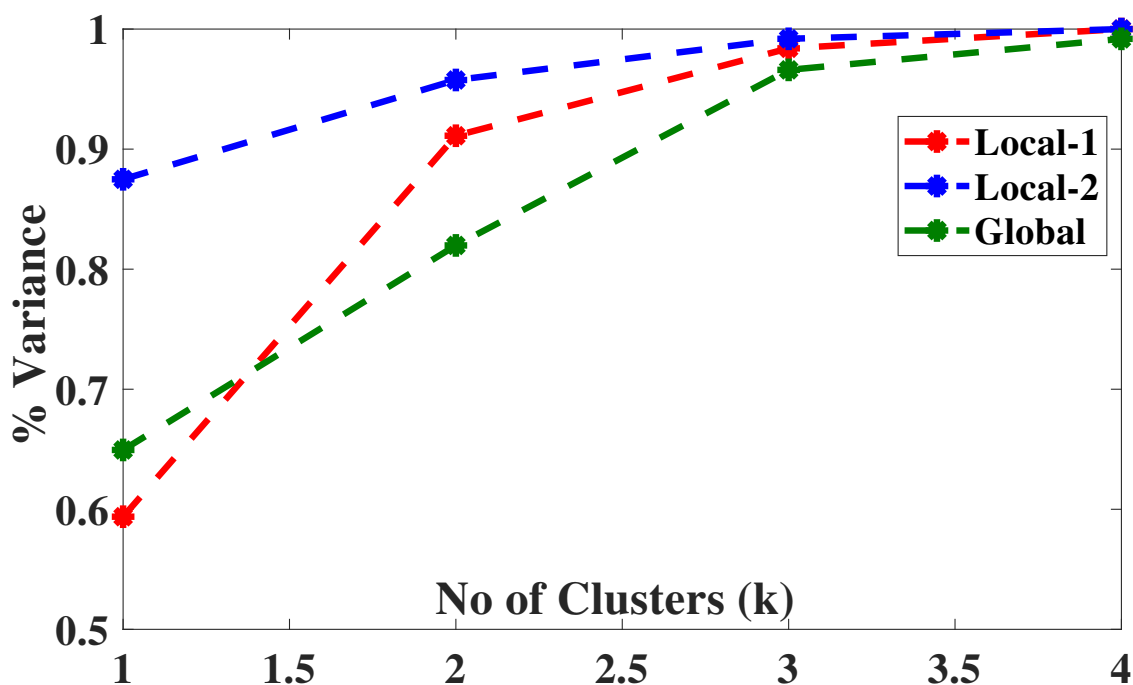


Fig. 7.6. Optimal number of clusters (Case: 1).

## 7.5.1.2 Case:2 (From 30s to 50s)

For this case, the utility-1 the speed data of generators 1 to 5 from the 30s to 50s is used for analysis. Using the Elbow method the optimal number of clusters is 4 for local area-1. Similarly, the utility-2 the speeds of generator 6 to 10 from 30s to 50s is analyzed. From the Elbow method, the optimal number of clusters in this area are 3 for local area-2. Fig. 7.7 shows the percentage variance w.r.t no of clusters.

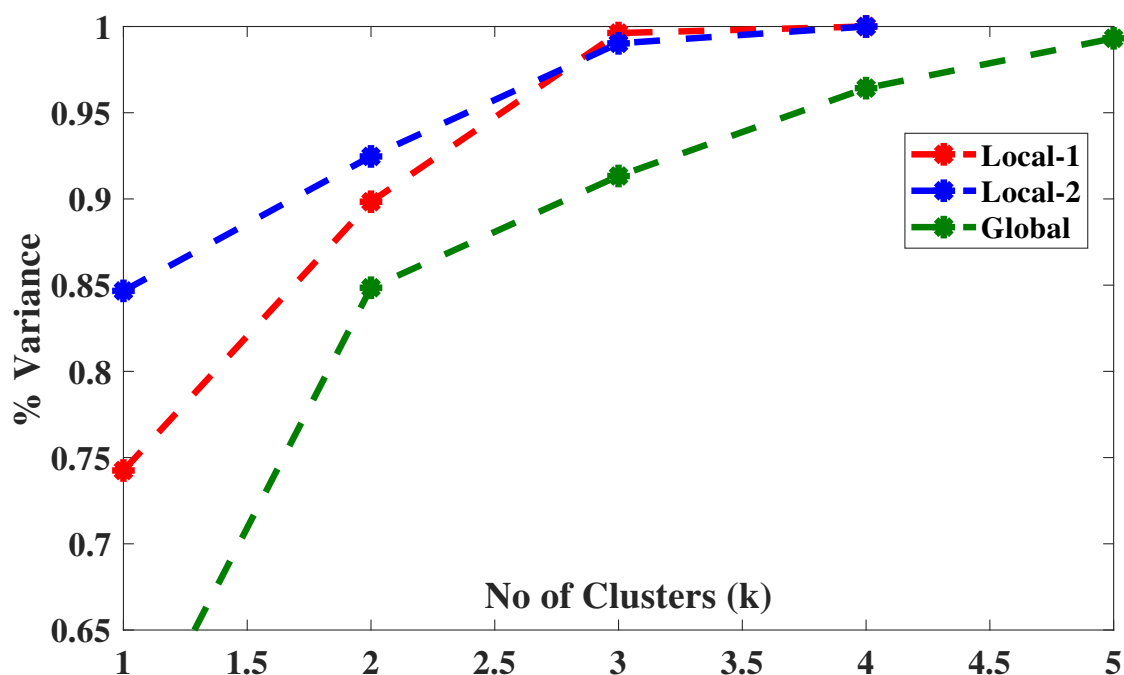


Fig. 7.7. Optimal number of clusters (Case: 2).

## 7.5.1.3 Case:3 (From 60s to 80s)

For this case, the utility-1 the speed data of generators 1 to 5 from 30s to 50s is used for analysis. Using the Elbow method the optimal number of clusters is 4 for local area-1. Similarly, the utility-2 the speeds of generator 6 to 10 from 60s to 80s is analyzed. From the Elbow method, the optimal number of clusters in this area are 3

for local area-2. Fig. 7.8 shows the percentage variance w.r.t no of clusters.

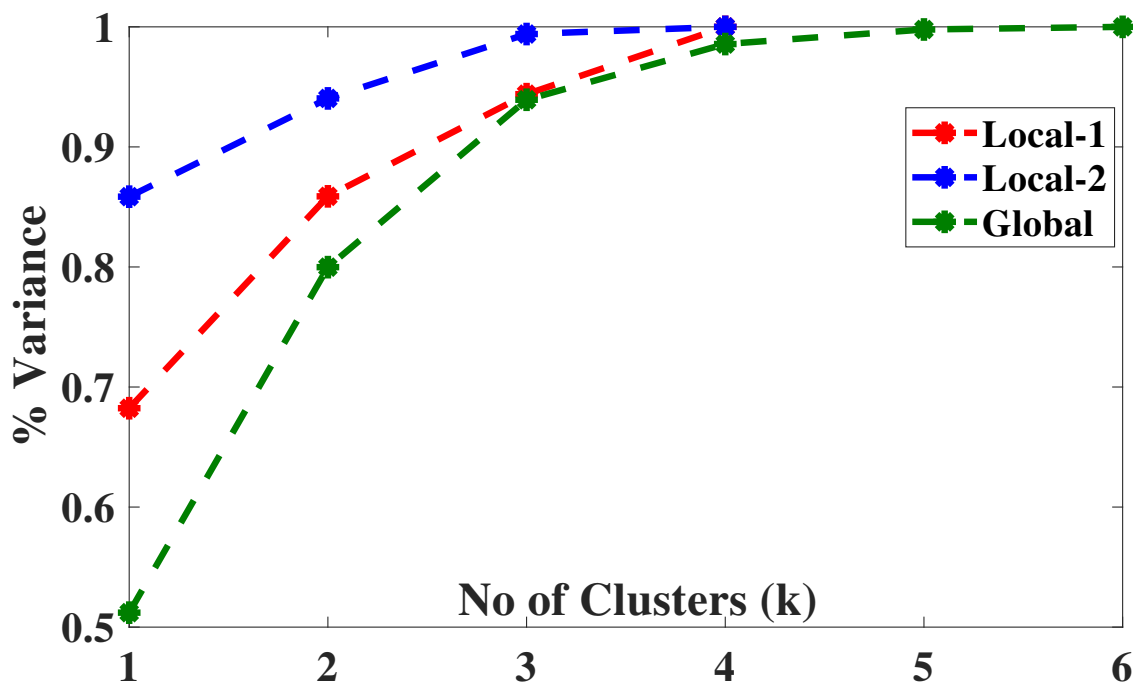


Fig. 7.8. Optimal number of clusters (Case: 3).

### 7.5.2 Distributed Coherency Grouping

In this, after identifying the optimal number  $k$  of clusters in each local area, the speed data is grouped into  $k$  clusters using spectral clustering method. Then cluster centers from all local areas are transmitted to the global centers. The input data to the global control center are the cluster centers, and at the global center, this data is grouped into a new optimal number of clusters  $h$  using Elbow method. At the global center, the size of data is very small, so Elbow method suffice. The algorithm is implemented for different scenarios.

## 7.5.2.1 Case:1

The optimal number of clusters obtained using Elbow method in Section. 7.5.1.1 are used. Then utility-1 is grouped locally into three clusters based on spectral clustering. From Table 7.1, it can be seen that after local area clustering generators 2 and 3 with index 1 is in group-1, generator 1 is in group-2, and generators 4 and 5 with index 3 are in group-3. Likewise, utility-2 is grouped locally into three clusters based on spectral clustering. From Table 7.1, it can be seen that generator 8 with index 1 is in group-1, generators 6, 7, 9 with index 2 are in group-2, and finally, generator 10 with index 3 is in group-3. Here the local cluster indices (LI) for each local area are independent and have no commonality. Then the 3 cluster centers from utility-1 and 3 cluster centers from utility-2 are transmitted to the global control for further grouping. At the global control center, the 6 cluster centers are grouped using Elbow method accompanied with k-means. It is found that there are four optimal clusters  $h$  as shown in Fig. 7.6. The global cluster indices (GI) are transmitted back to the local control center for regrouping.

The regrouping for obtaining final cluster indices of generators is as follows, in utility-1, cluster center for generator 1 is with LI 2. Then after global clustering, the cluster center with LI 2 is assigned GI 1, so the FI of generator 1 is 1, i.e. generator 1 is in group-1. Likewise, generator 2 and 3 belong to group-2, generator 4 and 5 belong to group-4. In utility-2 the local cluster center for generator 6 is with LI 2, whereas after global clustering the index changed GI 4, so the FI of generator 6 is 4, i.e. generator 6 belongs to group-4. Likewise, generator 7 and 9 also belongs to group

Table 7.1  
Distributed clustering (Case:1)

	Utility-1					Utility-2				
	G1	G2	G3	G4	G5	G6	G7	G8	G9	G10
LI	2	1	1	3	3	2	2	1	2	3
GI	2 1 4					1 4 3				
FI	1	2	2	4	4	4	4	1	4	3

LI= local cluster indices, GI= global cluster indices, FI= final cluster indices

4, generator 8 belong to group-1, and generator 10 belong to group-3. It can be seen that the generator in one area has a coherent group of generator in another area, like in group-4 generators 4 and 5 from utility-1 and generators 6, 7 and 9 from utility-2.

This grouping is validated from actual dynamic response following a disturbance. Fig. 7.9, Fig. 7.10, and Fig. 7.11 shows the speed of generators in group-1,2,3 respectively. The generator frequency vectors which verifies above results is shown in Fig. 7.5

#### 7.5.2.2 Case:2

The optimal number of clusters is obtained using Elbow method in Section. 7.5.1.2 are used. Then utility-1 is grouped locally into four clusters based on spectral clustering. From Table 7.2, it can be seen that after local area clustering generator 1 with LI 1 is group-1, generator 5 with LI 2 is group-2, generators 2 and 3 with LI 3 is in group-3, and generator 4 with LI 4 is group-4. Likewise, utility-2 is grouped locally into three clusters based on spectral clustering. From Table 7.2, it can be seen that after local area clustering generator 6, 7, and 9 with LI 1 is group-1, generator 10 with LI 2 is group-2, and generator 8 with LI 3 is group-3. Here the LI for each local area

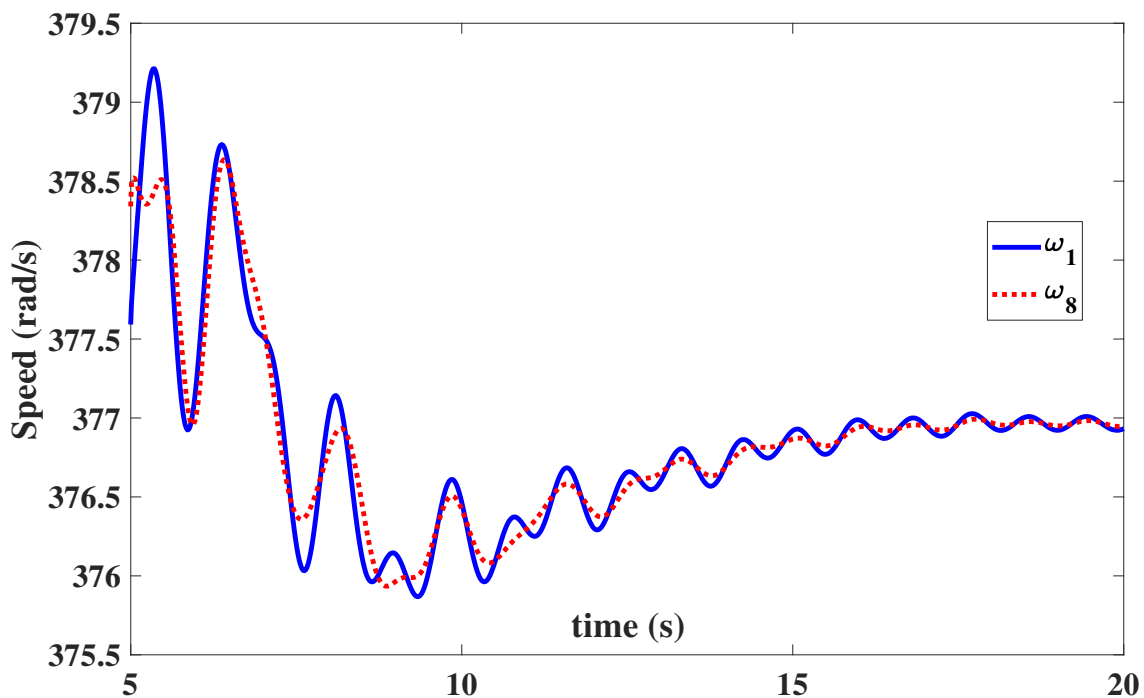


Fig. 7.9. Coherency group-1 (Case:1).

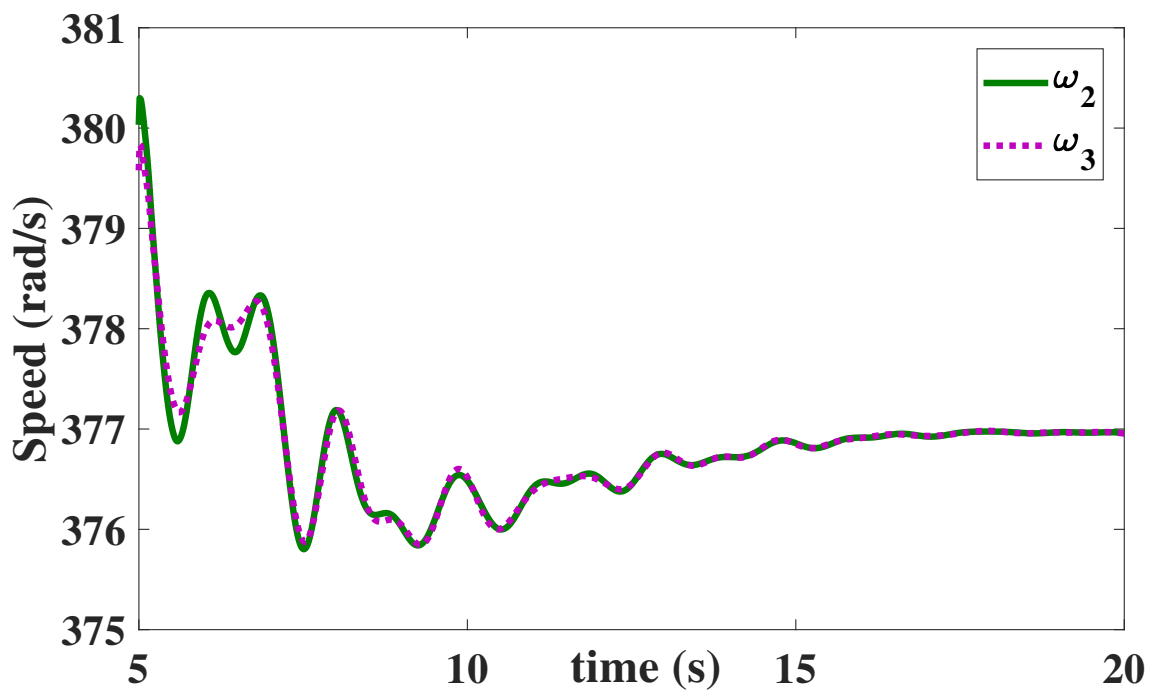


Fig. 7.10. Coherency group-2 (Case:1).

are independent and have no commonality. Then the 4 cluster centers from utility-1 and 3 cluster centers from utility-2 are transmitted to the global control for further

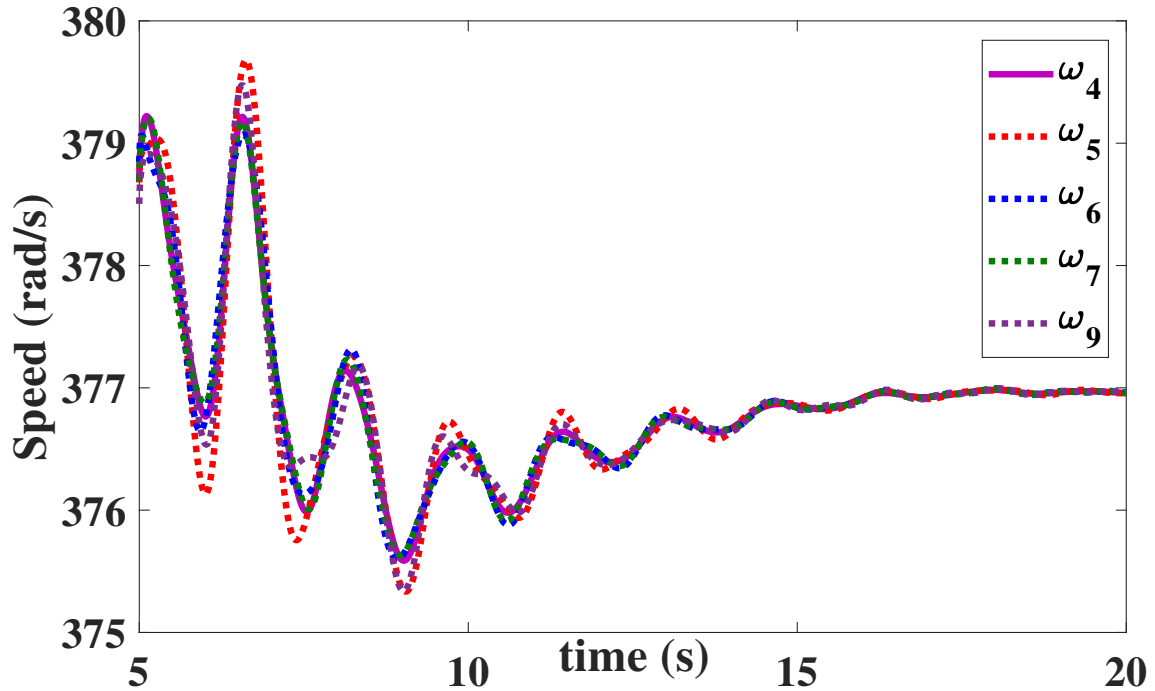


Fig. 7.11. Coherency group-3 (Case:1).

grouping. At the global control center, the 7 cluster centers are grouped using Elbow method accompanied with k-means. It is found that there are four optimal clusters  $h$  as shown in Fig. 7.7. The newly updated grouping indices are transmitted back to the local control center for regrouping.

The regrouping for obtaining FI of generators is as follows, in utility-1, cluster center for generator 1 is with LI 1. Then after global clustering, the cluster center with LI 1 is assigned GI 3, so the FI of generator 1 is 3, i.e. generator 1 is in group-3. Likewise, generator 2 and 3 also belong to group-3, generator 4 and 5 belong to group-4. In utility-2 the local cluster center for generator 6 is with FI 1, whereas after global clustering the index changed GI 1, so the FI of generator 6 is 1, i.e. generator 6 is in group-1. Likewise, generator 7 and 9 belong to group-1, generator 8 belong to group-3, and generator 10 belong to group-2. It can be seen that the generator in one

Table 7.2  
Distributed clustering (Case:2)

	Utility-1					Utility-2				
	G1	G2	G3	G4	G5	G6	G7	G8	G9	G10
LI	1	3	3	4	2	1	1	3	1	2
GI	3 4 3 4					1 2 3				
FI	3	3	3	4	4	1	1	3	1	2

LI= local cluster indices, GI= global cluster indices, FI= final cluster indices

area has a coherent group of generator in another area, like in group-3 generators 1, 2, and 3 are from utility-1 and generators 8 from utility-2.

This grouping is validated from actual dynamic response following a disturbance. Fig. 7.12, Fig. 7.13, and Fig. 7.14 shows the speed of generators in group-1, 3, and 4 respectively. The generator frequency vectors which verifies above results is shown in Fig. 7.5

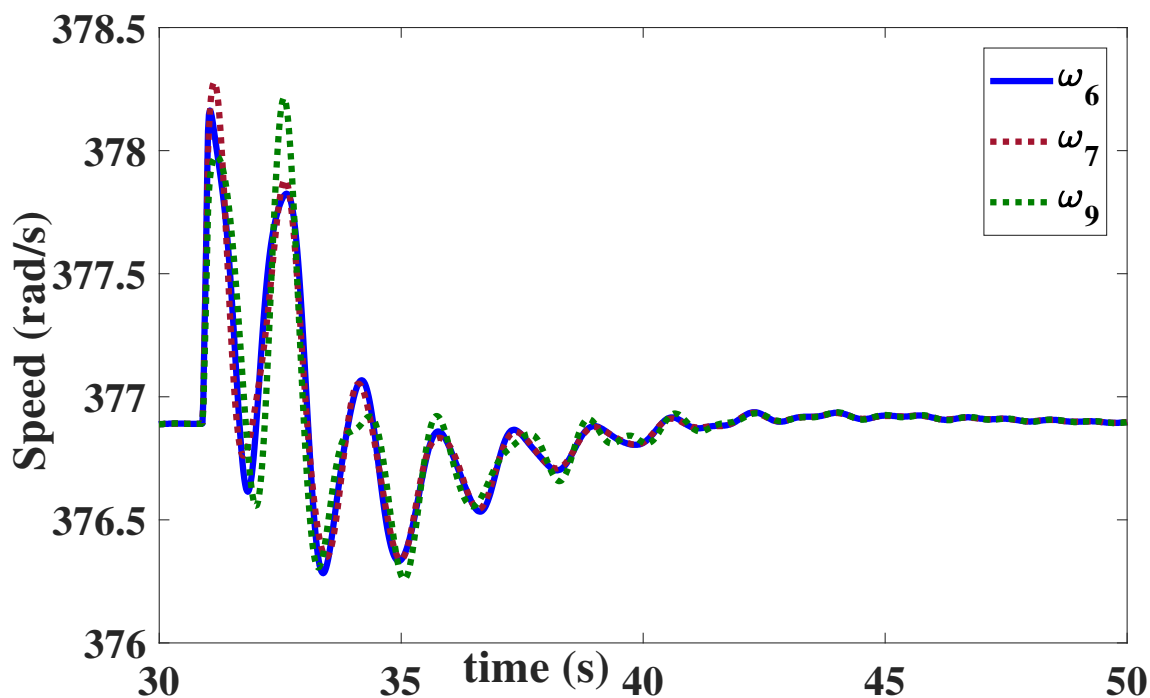


Fig. 7.12. Coherency group-1 (Case:2).

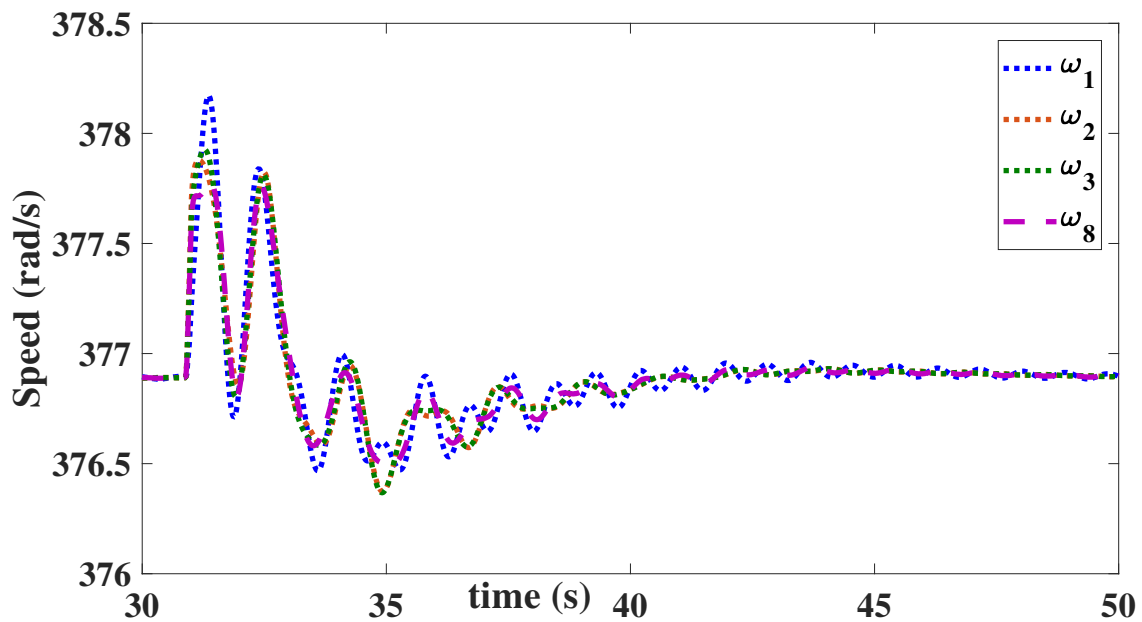


Fig. 7.13. Coherency group-3 (Case:2).

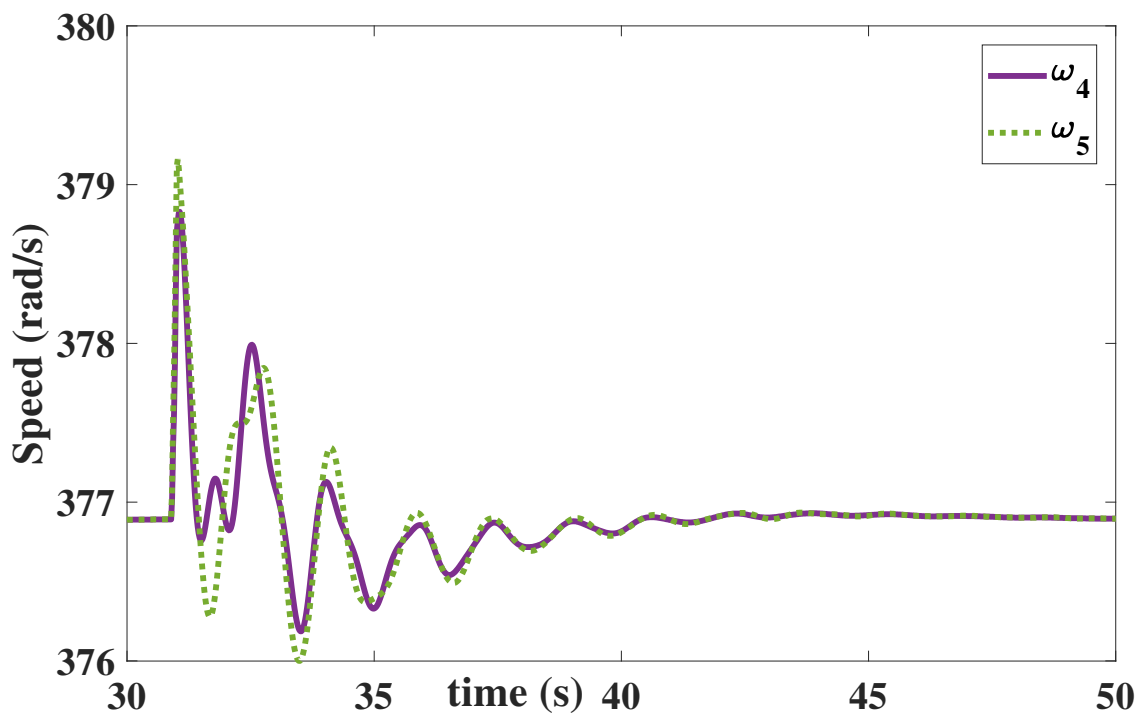


Fig. 7.14. Coherency group-4 (Case:2).

### 7.5.2.3 Case:3

The optimal number of clusters is obtained using Elbow method in Section. 7.5.1.3 are used. Then utility-1 is grouped locally into four clusters based on spectral clus-

tering. From Table 7.3, it can be seen that after local clustering, generator 2 and 3 with index 1 is group-1, generator-4 with index 2 is group-2, generator-3 with index 3 is group-3, and generator 5 with index-4 is group-4. Likewise, utility-2 is grouped locally into three clusters based on spectral clustering. From Table 7.3, it can be seen that after local clustering, generator 10 with index 1 is group-1, generator-9 with index 2 is group-2, and generators 6, 7, and 8 with index 3 is group-3. Here the LI for each local area are independent and have no commonality. Then the 4 cluster centers from utility-1 and 3 cluster centers from utility-2 are transmitted to the global control for further grouping. At the global control center, the 7 cluster centers are grouped using Elbow method accompanied with k-means. It is found that there are four optimal clusters  $h$  as shown in Fig. 7.8. The GI is transmitted back to the local control center for regrouping.

The regrouping for obtaining FI of generators is as follows, in utility-1, cluster center for generator 1 is with LI 3. Then after global clustering, the cluster center with LI 3 is assigned GI 2, so the FI of generator 1 is 2, i.e. generator 1 is in group-2. Likewise, generator 2 and 3 also belong to group-4, generator 4 belong to group-2, and generator 5 belong to group-3. In utility-2 the local cluster center for generator 6 is with LI 3, whereas after global clustering the index changed to GI 2, so the FI of generator 6 is 2, i.e. generator 6 is in group-2. Likewise, generator 7 and 8 belong to group-2, generator 9 belong to group-3, and generator 10 belong to group-1. It can be seen that the generator in one area has a coherent group of generator in another area, like in group-2 generators 1 and 4 are from utility-1 and generators 6, 7, and 8 from utility-2.

Table 7.3  
Distributed clustering (Case:3)

	Utility-1					Utility-2						
	G1	G2	G3	G4	G5	G6	G7	G8	G9	G10		
LI	3	1	1	2	4	3	3	3	2	1		
GI						4	2	2	3	1	3	2
FI	2	4	4	2	3	2	2	2	3	1		

LI= local cluster indices, GI= global cluster indices, FI= final cluster indices

This grouping is validated from actual dynamic response following a disturbance. Fig. 7.15, Fig. 7.16, and Fig. 7.17 shows the speed of generators in group-2, 3, and 4 respectively. The generator frequency vectors which verifies above results is shown in Fig. 7.5

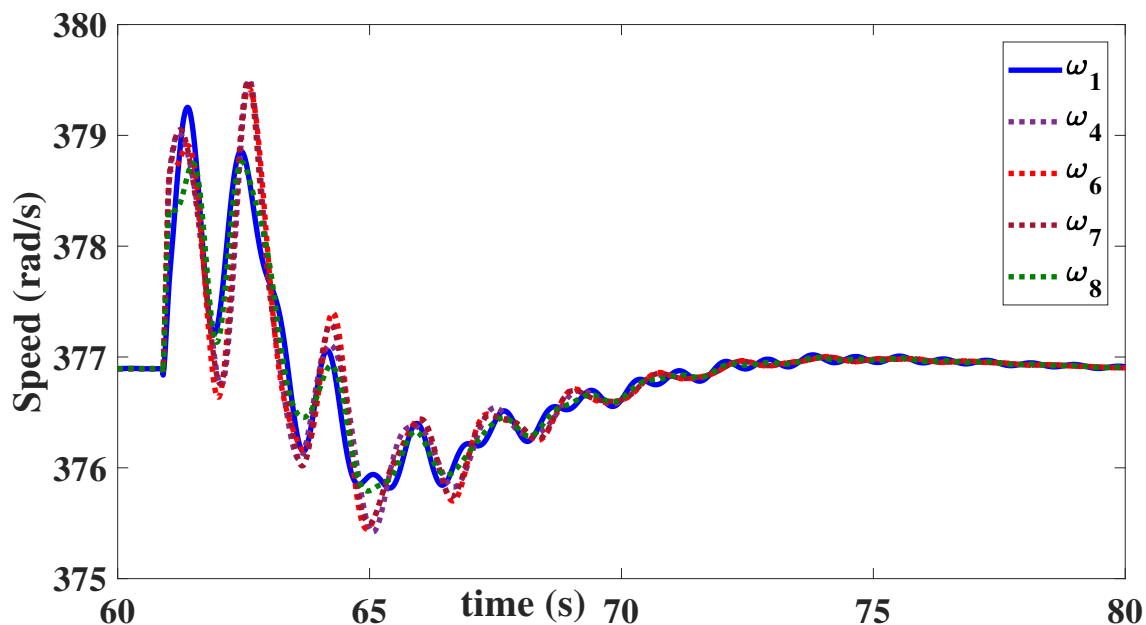


Fig. 7.15. Coherency group-2 (Case:3).

## 7.6 Summary

In this chapter, a distributed online coherency grouping algorithm is proposed. The proposed algorithm is an efficient way to group generators in different utilities using

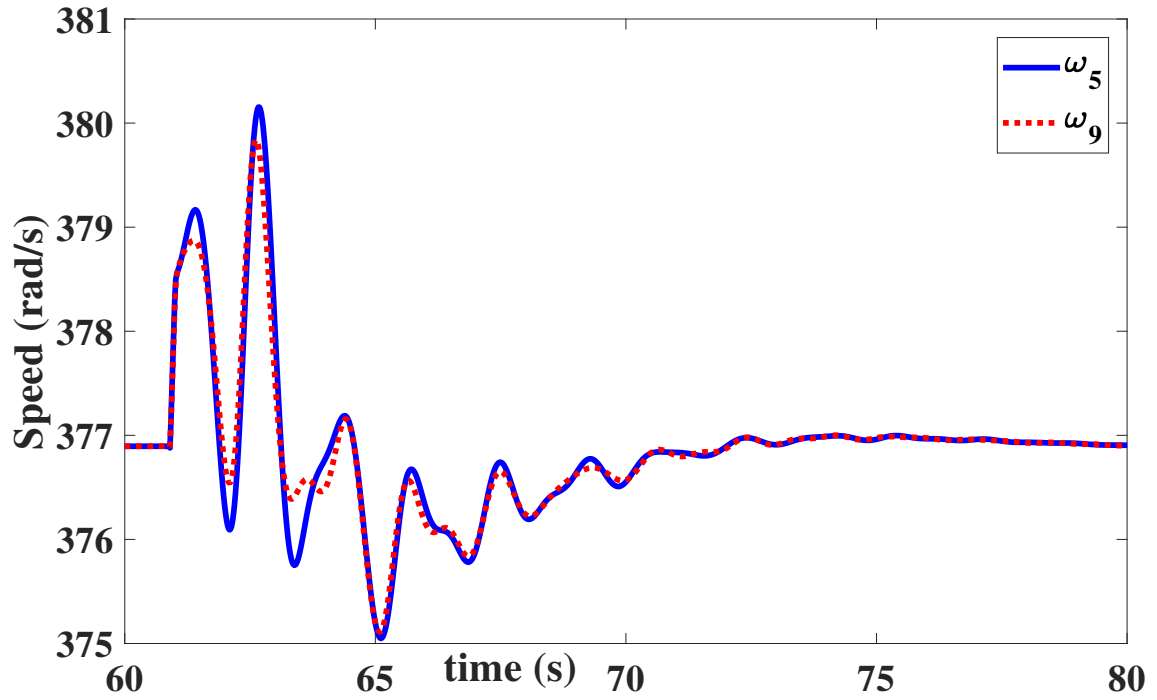


Fig. 7.16. Coherency group-3 (Case:3).

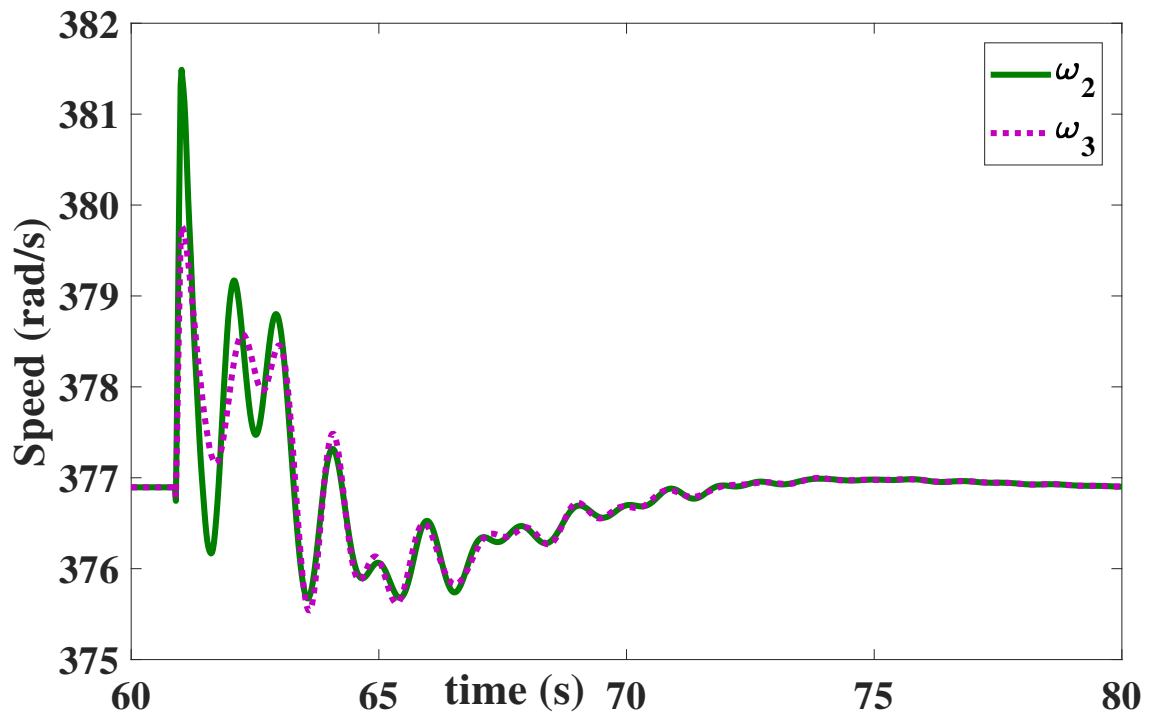


Fig. 7.17. Coherency group-4 (Case:3).

a distributed approach based on spectral clustering. The proposed algorithm use generator speed data and the optimal number of clusters in each area are determined using Elbow method, then the spectral clustering based on Nystrom method is used to cluster generators into an optimal number of groups, and each generator is assigned a local cluster index. The cluster centers in each area are transmitted to the global control center, and these cluster centers from all areas are grouped into an optimal number of clusters and assigned a global cluster index. The global cluster indices are transmitted to the local control centers and based on which final clustering indices are obtained. The final cluster indices will provide information on coherent groups of generators. The efficacy of the proposed algorithm is verified by testing it on an IEEE 39-bus power system model on a real-time co-simulation platform for different operating conditions. In the next chapter, overall conclusions and future works are presented.

## CHAPTER 8: CONCLUSION

### 8.1 Concluding Remarks

In this dissertation, new approaches for real-time wide-area damping of inter-area oscillations in renewable energy integrated power grid based on measurements are presented. Towards this, initially, an algorithm for centralized wide-area damping control is developed, in which the WADC is designed based on DLQR and Kalman filtering. Further, this methodology is enhanced by incorporating an online coherency grouping algorithm in the wide area control process. The drawbacks of the centralized WADC methodology is mitigated by decentralizing the approach using ADMM. Further, to reduce complexities and large-scale implementation, frequency-based reduced order model algorithm is proposed in which study area is modeled in detail, and the external area is represented as a combination of FDNE and TSA equivalent. This reduced order model is used for the design and validation of various power system control approaches including 1) Pitch control of wind farms, and 2) Wide-area control. Further, a decentralized version of the online coherency grouping algorithm is designed that can improve the scalability issue of real-time controller implementation. The effectiveness of the proposed algorithms are verified by implementing on two-area, IEEE 39 bus, and IEEE 68 bus power system models on RTDS/RSCAD and MATLAB based real-time co-simulation platform.

## 8.2 Future Work Directions

The developed algorithms for distributed wide-area control and reduced order modeling can be further extended. Some of the considerations for future work are listed below:

- The decentralized wide-area control based on ADMM can be further improved by incorporating distributed coherency into the controller framework.
- The reduced order model is a combination of low frequency and high-frequency equivalent. This can be upgraded to a hybrid reduced order model by including generator dynamics in FDNE so that, FDNE will cover high frequency and low-frequency electromechanical oscillations, i.e. TSA can be eliminated.
- The frequency dependent reduced order modeling can be further extended to distribution systems/microgrid. Using the reduced order model of the microgrid, renewable energy planning studies can be performed.

## REFERENCES

- [1] Control systems/MIMO systems. [https://en.wikibooks.org/wiki/Control\\_Systems/MIMO\\_Systems](https://en.wikibooks.org/wiki/Control_Systems/MIMO_Systems).
- [2] GTNETx2: the powerful new network interface card. <https://www.rtds.com/gtnetx2-the-powerful-new-network-interface-card/>.
- [3] Power system analysis. [http://nptel.ac.in/courses/Webcourse-contents/IIT-Kanpur/power-system/chapter\\_3/3\\_6.html](http://nptel.ac.in/courses/Webcourse-contents/IIT-Kanpur/power-system/chapter_3/3_6.html).
- [4] M. Abd-El-Rehim, I. D. Helal, and M. A. H. Omar. Multi-machine power system dynamic equivalents using artificial intelligence. In *Power Systems Conference, 2006. MEPCON 2006. Eleventh International Middle East*, pages 255–260, Dec 2006.
- [5] M. E. Aboul-Ela, A. A. Sallam, J. D. McCalley, and A. A. Fouad. Damping controller design for power system oscillations using global signals. *IEEE Trans. on Power Syst.*, 11:767–773, 1996.
- [6] L. Alhmoud. Reliability improvement for high-power IGBT in wind energy applications. *IEEE Trans. Ind. Electron.*, PP:1–9, Jan. 2018.
- [7] H. Y. Altalib and P. C. Krause. Dynamic equivalents by combination of reduced order models of system components. *IEEE Transactions on Power Apparatus and Systems*, 95:1535–1544, Sep 1976.
- [8] U. D. Annakkage et al. Dynamic system equivalents: A survey of available techniques. *IEEE Trans. on Power Delivery*, 27:411–420, Jan 2012.
- [9] M. A. M. Ariff and B. C. Pal. Coherency identification in interconnected power system An independent component analysis approach. *IEEE Trans. on Power Syst.*, 28:1747–1755, May 2013.
- [10] K. Åström and B. Wittenmark. *Adaptive Control: Second Edition*. Dover Books on Electrical Engineering. Dover Publications, 2013.
- [11] S. Avdakovi, E. Beirovi, A. Nuhanovi, and M. Kuljugi. Generator coherency using the wavelet phase difference approach. *IEEE Trans. on Power Syst.*, 20:271–278, Jan 2014.
- [12] S. P. Azad, R. Iravani, and J. E. Tate. Damping inter-area oscillations based on a model predictive control (MPC) HVDC supplementary controller. *IEEE Transactions on Power Systems*, 28(3):3174–3183, Aug 2013.
- [13] M. Beiraghi and A. M. Ranjbar. Adaptive delay compensator for the robust wide-area damping controller design. *IEEE Transactions on Power Systems*, 31(6):4966–4976, Nov 2016.

- [14] P. Bholowalia and A. Kumar. EBK-means: A clustering technique based on elbow method and K-means in WSN. *International Journal of Computer Applications*, 105, Nov 2014.
- [15] S. Boyd, N. Parikh, E. Chu, B. Peleato, and J. Eckstein. Distributed optimization and statistical learning via the alternating direction method of multipliers. *Found. Trends Mach. Learn.*, 3:1–122, 2010.
- [16] D. Chaniotis and M. A. Pai. Model reduction in power systems using Krylov subspace methods. *IEEE Trans. on Power Syst.*, 20:888–894, May 2005.
- [17] J. Chen, J. Chen, and C. Gong. New overall power control strategy for variable-speed fixed-pitch wind turbines within the whole wind velocity range. *IEEE Trans. Ind. Electron.*, 60:2652–2660, July 2013.
- [18] J. Chen, T. Lin, C. Wen, and Y. Song. Design of a unified power controller for variable-speed fixed-pitch wind energy conversion system. *IEEE Trans. Ind. Electron.*, 63:4899–4908, Mar. 2016.
- [19] W. Y. Chen, Y. Song, H. Bai, C. J. Lin, and E. Y. Chang. Parallel spectral clustering in distributed systems. *IEEE Transactions on Pattern Analysis and Machine Intelligence*, 33(3):568–586, March 2011.
- [20] J. Chow. *Power System Coherency and Model Reduction*. Power Electronics and Power Systems. Springer New York, 2014.
- [21] J. Chow, P. Accari, and W. Price. Inertial and slow coherency aggregation algorithms for power system dynamic model reduction. *IEEE Trans. on Power Syst.*, 10(2):680–685, May 1995.
- [22] A. Coates and A. Y. Ng. *Learning feature representations with K-means*. in *Neural Networks: Tricks of the Trade*. Springer New York, 2012.
- [23] K. K. Das and M. Buragohain. An algorithmic approach for maximum power point tracking of wind turbine using particle swarm optimization. *IJAREEIE*, 4:4099–4106, May 2015.
- [24] E. Davison. A method for simplifying linear dynamic systems. *IEEE Transactions on Automatic Control*, 11:93–101, Jan 1966.
- [25] M. Davodi, H. R. Modares, E. Reihani, and A. Sarikhani. Coherency approach by hybrid PSO, K-Means clustering method in power system. In *IEEE 2nd International Power and Energy Conference, 2008*, pages 255–260, Jan 2008.
- [26] S. E. M. de Oliveira and A. G. Massaud. Modal dynamic equivalent for electric power systems i: Theory. *IEEE Transactions on Power Systems*, 3:1731–1737, Nov 1988.

- [27] S. E. M. de Oliveira and A. G. Massaud. Modal dynamic equivalent for electric power systems. ii: Stability simulation tests. *IEEE Transactions on Power Systems*, 3:1731–1737, Nov 1988.
- [28] D. Deschrijver, B. Gustavsen, and T. Dhaene. Advancements in iterative methods for rational approximation in the frequency domain. *IEEE Trans. on Power Delivery*, 22:1633–1642, July 2007.
- [29] V. Q. Do and M. M. Gavrilovic. An iterative pole removal method for synthesis of power system equivalent networks. *IEEE Trans. on Power Apparatus and Systems*, 103:2065–2070, Aug 1984.
- [30] V. Q. Do and M. M. Gavrilovic. A synthesis method for one-port and multi-port equivalent networks for analysis of power system transients. *IEEE Trans. on Power Apparatus and Systems*, 1:103–113, Apr 1986.
- [31] J. L. Dominguez-Garcia, C. E. Ugalde-Loo, F. Binachi, and O. GomisBellmunt. Input and output signal selection for damping of power system oscillations using wind power plants. *Int. J. Electr. Power Energy Syst.*, 58:75–84, Jun 2014.
- [32] R. J. Galarza, J. H. Chow, W. W. Price, A. W. Hargrave, and P. M. Hirsch. Aggregation of exciter models for constructing power system dynamic equivalents. *IEEE Transactions on Power Systems*, 13:782–788, Aug 1998.
- [33] A. J. Germond and R. Podmore. Aggregation of generating unit models. *IEEE Transactions on Power Apparatus and Systems*, PAS-97:1060–1069, July 1978.
- [34] E. Ghahremani and I. Kamwa. Local and wide-area PMU-based decentralized dynamic state estimation in multi-machine power systems. *IEEE Trans. on Power Syst.*, 31:547–562, Jan 2016.
- [35] S. Ghosh, S. Kamalasan, N. Senroy, and J. Enslin. Doubly fed induction generator (dfig)-based wind farm control framework for primary frequency and inertial response application. *IEEE Trans. Power Syst.*, 31:1861–1871, May 2016.
- [36] S. Ghosh and N. Senroy. The localness of electromechanical oscillations in power systems. *Int. J. Elect. Power Energy Syst.*, 42(1):306–313, Nov 2012.
- [37] S. Ghosh and N. Senroy. Electromechanical dynamics of controlled variable speed wind turbines. *IEEE Syst. Journal*, 9:639–646, 2015.
- [38] A. Gole. Vector controlled doubly fed induction generator for wind applications, 2004.
- [39] M. Grant and S. Boyd. Graph implementations for nonsmooth convex programs. In *in Recent Advances in Learning and Control*, pages 95–110, New York: Springer, 2008.

- [40] B. Gustavsen. Computer code for rational approximation of frequency dependent admittance matrices. *IEEE Trans. on Power Delivery*, 17:1093–1098, Oct 2002.
- [41] B. Gustavsen. Fast passivity enforcement for pole-residue models by perturbation of residue matrix eigenvalues. *IEEE Trans. on Power Delivery*, 23:2278–2285, Oct 2008.
- [42] B. Gustavsen and A. Semlyen. Application of vector fitting to state equation representation of transformers for simulation of electromagnetic transients. *IEEE Trans. on Power Delivery*, 13:834–842, Jul 1998.
- [43] B. Gustavsen and A. Semlyen. Rational approximation of frequency domain responses by vector fitting. *IEEE Trans. on Power Delivery*, 14:1052–1061, July 1999.
- [44] B. Gustavsen and A. Semlyen. Enforcing passivity for admittance matrices approximated by rational functions. *IEEE Trans. on Power Delivery*, 16:97–104, Feb 2001.
- [45] M. H. Haque and A. H. M. A. Rahim. Identification of coherent generators using energy function. In *IEE Proceedings C - Generation, Transmission and Distribution*, pages 255–260, July 1990.
- [46] I. Hiskens. Report: 39-bus system (new england reduced model), 2013.
- [47] J. Hong and J. Park. A time-domain approach to transmission network equivalents via prony analysis for electromagnetic transients analysis. *IEEE Trans. on Power Systems*, 10:1789–1797, Nov 1995.
- [48] P. Jiang, S. Feng, and X. Wu. Robust design method for power oscillation damping controller of STATCOM based on residue and TLS-ESPRIT. *International Transactions on Electrical Energy Systems*, 24(10):1385–1400, Jul 2013.
- [49] T. Jiang, H. Jia, H. Yuan, N. Zhou, and F. Li. Projection pursuit: A general methodology of wide-area coherency detection in bulk power grid. *IEEE Trans. on Power Syst.*, 31:2776–2786, July 2016.
- [50] M. Jonsson, M. Begovic, and J. Daalder. A new method suitable for real-time generator coherency determination. *IEEE Transactions on Power Systems*, 19(3):1473–1482, Aug 2004.
- [51] P. Ju, F. Li, N. G. Yang, X. M. Wu, and N. Q. He. Dynamic equivalents of power systems with online measurements. part 2: Applications. *IEE Proceedings - Generation, Transmission and Distribution*, 151:179–182, Mar 2004.
- [52] P. Ju, L. Q. Ni, and F. Wu. Dynamic equivalents of power systems with online measurements. part 1: Theory. *IEE Proceedings - Generation, Transmission and Distribution*, 151:175–178, Mar 2004.

- [53] W. Juanjuan, F. Chuang, and Z. Yao. Design of WAMS-based multiple HVDC damping control system. *IEEE Trans. Smart Grid*, 2:572–581, Jun 2008.
- [54] I. Kamwa, R. Grondin, and Y. Hebert. Wide-area measurement based stabilizing control of large power systems—a decentralized/hierarchical approach. *IEEE Transactions on Power Systems*, 16(1):136–153, Feb 2001.
- [55] H. Kim, G. Jang, and K. Song. Dynamic reduction of the large-scale power systems using relation factor. *IEEE Trans. on Power Syst.*, 19:1696–1699, Aug 2004.
- [56] M. Klein, G. J. Rogers, and P. Kundur. A fundamental study of inter-area oscillations in power systems. *IEEE Transactions on Power Systems*, 6(3):914–921, Aug 1991.
- [57] L. P. Kunjumammed, R. Singh, and B. C. Pal. Robust signal selection for damping of inter-area oscillations. *Proc. IET Gener. Transm. Distrib.*, 6:404–416, May 2012.
- [58] A. Lasheen and A. L. Elshafei. Wind-turbine collective-pitch control via a fuzzy predictive algorithm. *Renewable Energy*, 87:298–306, 2016.
- [59] Y. Lei, A. Mullane, G. Lightbody, and R. Yacamini. Modeling of the wind turbine with a doubly fed induction generator for grid integration studies. *IEEE Trans. Energy Convers.*, 21:257–264, Mar. 2006.
- [60] E. C. Levy. Complex curve fitting. *IEE Transactions on Automatic Control*, AC-4:37–44, May 1959.
- [61] Y. Li, C. Rehtanz, S. Ruberg, L. Luo, and Y. Cao. Assessment and choice of input signals for multiple HVDC and FACTS wide-area damping controllers. *IEEE Trans. Power Syst.*, 27:1969–1977, Nov 2012.
- [62] Y. Li, C. Rehtanz, S. Ruberg, L. Luo, and Y. Cao. Wide-area robust coordination approach of HVDC and FACTS controllers for damping multiple inter-area oscillations. *IEEE Trans. Power Del.*, 27:1096–1105, Mar 2012.
- [63] Y. Liang, X. Lin, A. M. Gole, and M. Yu. Improved coherency-based wide-band equivalents for real-time digital simulators. *IEEE Trans. on Power Syst.*, 26(3):1410–1417, Jul 2011.
- [64] Y. F. Liang, X. Lin, A. M. Gole, and M. Yu. Improved coherency based wide-band equivalents for real-time digital simulators. *IEEE Trans. Power Syst.*, 26:1410–1417, Aug. 2011.
- [65] X. Lin, A. M. Gole, and M. Yu. A wide-band multi-port system equivalent for real-time digital power system simulators. *IEEE Trans. on Power Syst.*, 24(1):237–249, Feb 2009.

- [66] Z. Lin, F. Wen, Y. Ding, and Y. Xue. Data-driven coherency identification for generators based on spectral clustering. *IEEE Trans. on Industrial Informatics*, 14:1275–1285, Mar 2018.
- [67] H. Liu, L. Zhu, Z. Pan, F. Bai, Y. Liu, Y. Liu, M. Patel, E. Farantatos, and N. Bhatt. ARMAX-based transfer function model identification using wide-area measurement for adaptive and coordinated damping control. *IEEE Transactions on Smart Grid*, 8(3):1105–1115, May 2017.
- [68] Y. Liu. Wide-area measurement system development at the distribution level: An FNET/GridEye example. In *2016 IEEE Power and Energy Society General Meeting (PESGM)*, pages 1–1, July 2016.
- [69] L. Marti. Low-order approximation of transmission line parameters for frequency-dependent models. *IEEE Transactions on Power Apparatus and Systems*, PAS-102:3582–3589, Nov 1983.
- [70] Mathworks. *Wind Turbine, Documentation SimPowerSystems*, 2004.
- [71] J. Milanovic and A. Duque. Identification of electromechanical modes and placement of PSSs using relative gain array. *IEEE Trans. Power Syst.*, 19:410–417, Feb 2004.
- [72] A. S. Morched, J. H. Ottevangers, and L. Marti. Multi-port frequency dependent network equivalents for the EMTP. *IEEE Transactions on Power Delivery*, 8:1402–1412, Jul 1993.
- [73] S. Muller, M. Deicke, and R. W. D. Doncker. Doubly fed induction generator systems for wind turbines. *IEEE Ind. Appl. Mag.*, 8:26–33, May 2002.
- [74] S. Nabavi, J. Zhang, and A. Chakraborty. Distributed optimization algorithms for wide-area oscillation monitoring in power systems using interregional pmu-pdc architectures. *IEEE Transactions on Smart Grid*, 6(5):2529–2538, Sep 2015.
- [75] R. Nath, S. S. Lamba, and K. S. P. Rao. Coherency based system decomposition into study and external areas using weak coupling. *IEEE Transactions on Power Apparatus and Systems*, PAS-104:1443–1449, Jun 1985.
- [76] R. J. Newell, M. D. Risan, L. Allen, I. S. Rao, and D. L. Stuehm. Utility experience with coherency-based dynamic equivalents of very large systems. *IEEE Transactions on Power Apparatus and Systems*, PAS-104:3056–3063, Nov 1985.
- [77] A. Ng. The K-means clustering algorithm. <http://cs229.stanford.edu/notes/cs229-notes7a.pdf>, Dec 2017.

- [78] H. Nguyen-Duc, L. A. Dessaint, A. F. Okou, and I. Kamwa. Selection of input/output signals for wide area control loops. In *IEEE PES General Meeting*, pages 1–7, July 2010.
- [79] T. Noda. Identification of a multiphase network equivalent for electromagnetic transient calculations using partitioned frequency response. *IEEE Transactions on Power Delivery*, 20:1134–1142, Apr 2005.
- [80] T. Noda. A binary frequency-region partitioning algorithm for the identification of a multiphase network equivalent for emt studies. *IEEE Transactions on Power Delivery*, 22:1257–1258, Apr 2007.
- [81] Electricity in the united states. [https://www.eia.gov/energyexplained/index.cfm?page=electricity\\_in\\_the\\_united\\_states](https://www.eia.gov/energyexplained/index.cfm?page=electricity_in_the_united_states).
- [82] P. Kundur. *Power System Stability and Control*. New York: McGraw-Hill, 1994.
- [83] B. B. Padhy, S. C. Srivastava, and N. K. Verma. A coherency-based approach for signal selection for wide area stabilizing control in power systems. *IEEE Systems Journal*, 7(4):807–816, April 2013.
- [84] B. Pal and B. Chaudhuri. *Robust Control in Power Systems*. Power Electronics and Power Systems. Springer US, 2006.
- [85] R. Pena, J. C. Clare, and G. M. Asher. Doubly fed induction generator using back-to-back PWM converters and its application to variable-speed wind-energy generation. *IEE Proceedings - Electric Power Applications*, 143(3):231–241, May 1996.
- [86] J. W. Pierre, N. Zhou, F. K. Tuffner, J. F. Hauer, D. J. Trudnowski, and W. A. Mittelstadt. Probing signal design for power system identification. *IEEE Transactions on Power Systems*, 25(2):835–843, May 2010.
- [87] W. W. Price, A. W. Hargrave, J. H. Chow, B. J. Hurysz, and P. M. Hirsch. Large-scale system testing of a power system dynamic equivalencing program. *IEEE Transactions on Power Systems*, 13:768–774, Aug 1998.
- [88] Y. Ren, L. Li, J. Brindley, and L. Jiang. Nonlinear PI control for variable pitch wind turbine. *Control Engineering Practice*, 50:84–94, May 2016.
- [89] E. F. Report. *Dynamic Reduction*. EPRI TR-102234, Project 2447-01. 1993.
- [90] M. A. Rios and O. Gomez. Identification of coherent groups and PMU placement for inter-area monitoring based on graph theory. In *2011 IEEE PES Conference on Innovative Smart Grid Technologies (ISGT Latin America)*, pages 255–260, Nov 2011.

- [91] G. Rogers. *Power System Oscillations*. Power Electronics and Power Systems. Springer US, 2012.
- [92] R. Sadikovic. Damping controller design for power system oscillations, internal report. In *ETH Zurich*, Dec 2004.
- [93] RTDS Technologies Inc. *Wind-Turbine driven doubly-fed induction generator user manual*, 2015.
- [94] C. K. Sanathanan and J. Koemer. Transfer function synthesis as a ratio of two complex polynomials. *IEE Transactions on Automatic Control*, 8:56–58, Jan 1963.
- [95] J. J. Sanchez-Gasca and J. H. Chow. Performance comparison of three identification methods for the analysis of electromechanical oscillations. *IEEE Trans. on Power Syst.*, 14(3):995–1002, Aug 1999.
- [96] S. A. N. Sarmadi and V. Venkatasubramanian. Electromechanical mode estimation using recursive adaptive stochastic subspace identification. In *2014 IEEE PES T D Conference and Exposition*, pages 1–1, April 2014.
- [97] N. Senroy. Generator coherency using the HilbertHuang transform. *IEEE Transactions on Power Systems*, 23(4):1701–1708, Nov 2008.
- [98] H. Singh and A. Abur. Time domain modelling of external systems for electromagnetic transients programs. *IEEE Trans. on Power Delivery*, 8:671–679, May 1993.
- [99] H. Singh and A. Abur. Multiport equivalencing of external systems for simulation of switching transients. *IEEE Trans. on Power Delivery*, 10:374–382, Jan 1995.
- [100] J. G. Slootweg, S. W. H. de Haan, H. Polinder, and W. L. Kling. General model for representing variable speed wind turbines in power systems dynamics simulations. *IEEE Trans. Power Syst.*, 18:144–151, Feb. 2003.
- [101] S. Soued, M. A. Ebrahim, H. S. Ramadan, and M. Becherif. Optimal blade pitch control for enhancing the dynamic performance of wind power plants via metaheuristic optimisers. *IET Electric Power Application*, 11:1432–1440, Sept. 2017.
- [102] A. O. Soysal and A. Semlyen. Practical transfer function estimation and its application to wide frequency range representation of transformers. *IEEE Transactions on Power Delivery*, 8:1627–1637, July 1993.
- [103] H. Stahl. Transfer function synthesis using frequency response data. *International Journal of Control*, 39:541–550, 1984.

- [104] A. M. Stankovic and A. T. Saric. Transient power system analysis with measurement-based gray box and hybrid dynamic equivalents. *IEEE Transactions on Power Systems*, 19:455–462, Feb 2004.
- [105] R. J. Snchez-Garca, M. Fennelly, S. Norris, N. Wright, G. Niblo, J. Brodzki, and J. W. Bialek. Hierarchical spectral clustering of power grids. *IEEE Trans. on Power Syst.*, 29:2229–2237, Sep 2014.
- [106] A. Thakallapelli, S. Ghosh, and S. Kamalasan. Real-time frequency based reduced order modeling of large power grid. In *2016 IEEE Power and Energy Society General Meeting (PESGM)*, pages 1–5, July 2016.
- [107] A. Thakallapelli, S. Ghosh, and S. Kamalasan. Real-time reduced order model based adaptive pitch controller for grid connected wind turbines. In *Proc. Industry Applications Society Annual Meeting (IAS), IEEE*, Oct 2016.
- [108] A. Thakallapelli, S. Ghosh, and S. Kamalasan. Real-time reduced order model based adaptive pitch controller for grid connected wind turbines. In *2016 IEEE Industry Applications Society Annual Meeting*, pages 1–8, Oct 2016.
- [109] A. Thakallapelli, S. J. Hossain, and S. Kamalasan. Coherency based online wide area control of wind integrated power grid. In *2016 IEEE International Conference on Power Electronics, Drives and Energy Systems (PEDES)*, pages 1–6, Dec 2016.
- [110] A. Thakallapelli, S. J. Hossain, and S. Kamalasan. Coherency and online signal selection based wide area control of wind integrated power grid. *IEEE Transactions on Industry Applications*, 54:3712–3722, Jul 2018.
- [111] A. Thakallapelli and S. Kamalasan. Optimization based real-time frequency dependent reduced order modeling of power grid. In *Proc. IEEE Power Energy Society General Meeting*, Jul 2017.
- [112] J. M. Undrill and A. E. Turner. Construction of power system electromechanical equivalents by modal analysis. *IEEE Transactions on Power Apparatus and Systems*, PAS-90:2049–2059, Sep 1971.
- [113] A. Vahidnia, G. Ledwich, E. Palmer, and A. Ghosh. Generator coherency and area detection in large power systems. *IET Gener. Trans. Distr.*, 6:874–883, Sep 2012.
- [114] A. Vahidnia, G. Ledwich, and E. W. Palmer. Transient stability improvement through wide-area controlled SVCS. *IEEE Trans. on Power Syst.*, 31(4):3082–3089, Jul 2016.
- [115] T. L. Van, T. H. Nguyen, and D. Lee. Advanced pitch angle control based on fuzzy logic for variable-speed wind turbine systems. *IEEE Trans. Energy Convers.*, 30:578–587, 2015.

- [116] L. Wang, M. Klein, S. Yirga, and P. Kundur. Dynamic reduction of large power systems for stability studies. *IEEE Transactions on Power Systems*, 12:889–895, May 1997.
- [117] S. Wang, S. Lu, N. Zhou, G. Lin, M. Elizondo, and M. A. Pai. Dynamic-feature extraction, attribution, and reconstruction (dear) method for power system model reduction. *IEEE Trans. Power Syst.*, 29:2049–2059, Sept. 2014.
- [118] M. Watanabe, M. Yamashita, and Y. Mitani. Wide area measurements based robust power system controller design. In *2014 Power Systems Computation Conference*, pages 1–7, Aug 2014.
- [119] A. H. Whitfield. Transfer function synthesis using frequency response data. *International Journal of Control*, 43:1413–1426, 1986.
- [120] D. Woodford. Determination of main parameters for a doubly fed induction generator for a given turbine rating, 2004.
- [121] W. Yao, L. Jiang, J. Wen, Q. H. Wu, and S. Cheng. Wide-area damping controller of FACTS devices for inter-area oscillations considering communication time delays. *IEEE Transactions on Power Systems*, 29(1):318–329, Jan 2014.
- [122] Y. Yao-nan and M. A. El-Sharkawi. Estimation of external dynamic equivalents of a thirteen-machine system. *IEEE Transactions on Power Apparatus and Systems*, PAS-100:1324–1332, Mar 1981.
- [123] S. B. Yusof, G. J. Rogers, and R. T. H. Alden. Slow coherency based network partitioning including load buses. *IEEE Transactions on Power Systems*, 8:1375–1382, Aug 1993.
- [124] Z. Stojkovic . *Computer aided design in power engineering application of software tools*. Springer, 2012.
- [125] J. Zhang, M. Cheng, Z. Chen, and X. Fu. Pitch angle control for variable speed wind turbines. In *Proc. 3rd Int. Conf. Elect. Utility DRPT*, pages 2691–2696, Nanjing, China, Apr. 2008.
- [126] J. Zhang, G. Welch, G. Bishop, and Z. Huang. A two-stage kalman filter approach for robust and real-time power system state estimation. *IEEE Transactions on Sustainable Energy*, 5(2):629–636, April 2014.
- [127] W. Zhang, J. Hu, and A. Abate. On the value functions of the discrete-time switched LQR problem. *IEEE Transactions on Automatic Control*, 54(11):2669–2674, Nov 2009.
- [128] Y. Zhang, M. Cheng, and Z. Chen. Load mitigation of unbalanced wind turbines using pi-r individual pitch control. *IET Renewable Power Generation*, 9:262–271, Apr. 2015.

- [129] Y. Zhang, A. M. Gole, W. Wu, B. Zhang, and H. Sun. Development and analysis of the applicability of a hybrid transient simulation platform combining tsa and emt elements. *IEEE Trans. Power Syst.*, 28:357–366, Feb. 2013.
- [130] D. Zhou, J. Guo, Y. Zhang, J. Chai, H. Liu, Y. Liu, C. Huang, X. Gui, and Y. Liu. Distributed data analytics platform for wide-area synchrophasor measurement systems. *IEEE Transactions on Smart Grid*, 7(5):2397–2405, Sept 2016.
- [131] N. Zhou, Z. Huang, L. Dosiek, D. Trudnowski, and J. W. Pierre. Electromechanical mode shape estimation based on transfer function identification using pmu measurements. In *2009 IEEE Power Energy Society General Meeting*, pages 1–7, July 2009.
- [132] N. Zhou, J. W. Pierre, and J. F. Hauer. Initial results in power system identification from injected probing signals using a subspace method. *IEEE Transactions on Power Systems*, 21(3):1296–1302, Aug 2006.
- [133] N. Zhou, D. Trudnowski, J. Pierre, and W. Mittelstadt. Electromechanical mode on-line estimation using regularized robust RLS methods. In *IEEE PES General Meeting*, pages 1–1, July 2010.
- [134] C. Zhu, M. Khammash, V. Vittal, and W. Qiu. Robust power system stabilizer design using H-infin; loop shaping approach. *IEEE Transactions on Power Systems*, 18(2):810–818, May 2003.